Charge Asymmetry in Top Quark Pair Production at $\sqrt{s} = 13$ TeV with the ATLAS Detector

Robert Adam Vallance

A thesis submitted to the University of Birmingham for the degree of
Doctor of Philosophy

Abstract

The charge asymmetry in top quark pair production was investigated using $139\,\text{fb}^{-1}$ of proton-proton collision data at $\sqrt{s} = 13\,\text{TeV}$ with the ATLAS experiment. This was undertaken in the dilepton channel, where two oppositely-charge leptons (electrons or muons), two jets and missing transverse energy from two neutrinos were required. Asymmetries were determined in the full truth-level phase space for the reconstructed $t\bar{t}$ events and a reduced phase space for the two leptons, both using the Fully Bayesian Unfolding method. The asymmetries were calculated inclusively across all the data and differentially in bins of $t\bar{t}$ (or dilepton) transverse momentum, mass and longitudinal velocity. The inclusive $t\bar{t}$ asymmetry is 0.0081 ± 0.0041, which is 2.0σ above zero and 1.1σ above the Next-to-Leading Order Standard Model expectation of 0.00351 ± 0.00006. The agreement improves to 0.4σ with a higher order prediction. The inclusive leptonic asymmetry is 0.0058 ± 0.0014, which is 4.1σ above zero, showing strong evidence for charge asymmetry, and 2.8σ above the Next-to-Leading Order expectation of 0.00192 ± 0.00006. Again, the agreement improves with a higher order prediction to 1.3σ. The dilepton $t\bar{t}$ results are being combined with those in the lepton + jets channel and limits will be placed on an Effective Field Theory coupling coefficient that characterises effects beyond the Standard Model.

I would like to dedicate this thesis to my loving parents . . .

It doesn't matter how beautiful your theory is, it doesn't matter how smart you are. If it doesn't agree with experiment, it's wrong.

– Richard Feynman

Declaration

This work presented in this thesis could not have been possible without the efforts of thousands of experts in the design, construction and operation of the LHC and ATLAS detector.

The first chapter outlines the history and development of the Standard Model of particle physics. The second and third chapters describe the workings of the LHC and ATLAS detector, whilst the fourth chapter presents the ATLAS triggering system, in which I had a role in its optimisation of the data-taking rate for high-luminosity runs.

The subsequent chapters focus on the measurement of charge asymmetry in top quark pair production, with collaboration and guidance from a team at Kobe University in Japan, Comenius Univeristy in Slovakia, CERN in Switzerland, and colleagues from the University of Birmingham in the UK. Many of the codes used in the event selection and unfolding were shared and developed between the separate teams. The fifth chapter gives an introduction to the theory and previous measurements of charge asymmetry, for which I had no involvement. The sixth and seventh chapters cover charge asymmetry in the dilepton channel, of which I was a main analyser with the team from Kobe, and all the plots were produced by myself with great assistance from the aforementioned teams. The eighth chapter focuses on the lepton + jets channel and combination with the dilepton channel, in which I had a small role. I did not work on the plots shown and the Effective Field Theory interpretation.

Acknowledgements

There are numerous people I would like to thank who have supported me throughout my PhD. Firstly to my principal supervisor, Miriam Watson, whose expertise, approachability and knowledge throughout the four years were invaluable to my success. She was always on hand to help whenever I had questions no matter how silly on hindsight they were. My secondary supervisors, Stephen Hillier and Juraj Bracinik, gave excellent guidance throughout my work on the level-1 calorimeter triggering system, and I particularly enjoyed the yoga and squash sessions with Juraj outside of work. A huge thank you also to Paul Newman and the whole particle physics group at the University of Birmingham, who fostered a very friendly and welcoming environment. I was lucky to share offices with and get to know many students including Russell, Jack, Ryan and John from my year as well as Matt, Andy, James B, Alasdair, Dan B, James K, Elliot, Kristian, Robbie, Jon, Gov, Dan L, Nandish, Joel, Tom, Naomi, Rob, Antonio, Alexis and so on. I particularly gained insight from our regular top meetings with Miriam, Chris, Jacob and Alexis.

I was extremely fortunate to spend 14 months working at CERN, Switzerland. I lived across the border in St Genis, France, which was a great opportunity to practise my French, despite my best attempts often being replied to in English. Going regular hiking and exploring with a good friend, Tom, from my undergraduate days and skiing with my flatmate, Sam, with the CERN ski club were unforgettable experiences. It still amazes me how we managed to

Table of Contents

List of Figures

List of Tables

Chapter **1**

The Standard Model

1.1 Historical Prelude

For centuries, we have attempted to understand the fundamental constituents of the universe. From the basic elements of fire, earth, air and water postulated in Ancient Greece, our knowledge has progressed rapidly. The idea of matter being composed of fundamental particles called atoms was put forward by John Dalton [1] and developed by Dmitri Mendeleev [2] in the construction of the periodic table. The structure of the atom itself has also been of great debate. Joseph Thomson proposed the plum-pudding model in 1904 [3], whereby the atom is a positive mass with smaller, negative corpuscles called electrons distributed within to cancel out the charge. However, in 1911, Ernest Rutherford *et al* [4] composed an experiment to scatter alpha and beta radiation from a thin gold foil. They noticed some of the radiation scattered right back towards them, inconsistent with the plum-pudding model. It pointed to a very small, positive nucleus concentrated at the centre of the atom, rather than spread out, with electrons around the outside. With evidence that hydrogen nuclei are the building blocks of all other nuclei, he coined the name "proton" to describe these elementary hydrogen nuclei.

The number of protons is key to determining the element in the periodic table.

The Bohr model of the atom was later proposed in 1913 [5], with clouds of electrons in discrete, quantized orbitals around the nucleus of protons. In the 1920s, the theory of Quantum Mechanics was developed by the likes of Werner Heisenberg, Erwin Schrödinger and many others to improve the atomic model. The current consensus is that particles are also waves (and vice-versa) described by wavefunctions. The square of such a wavefunction gives the probability for finding a particle in a given state at a given time. Electrons in the orbitals are distributed in probability clouds around the nucleus rather than having defined positions. Moreover, the positions and momenta of the particles cannot be known at the same time due to the two quantities not commuting when acting on the wavefunction (Heisenberg's Uncertainty Principle [6]).

In 1932, James Chadwick observed that neutral particles (called neutrons) are also found in nuclei [7]. This accounted for why the masses of the atoms did not scale with their number of protons. But a question did remain regarding why the atom did not fly apart due to the electromagnetic repulsive force between the protons in such close proximity. Gravity is too weak to hold them together and so a new force, the strong force, was proposed that is both powerful ($\sim$100 times the strength of the electromagnetic force) and a has very short range (of order the size of the nucleus).

The same year yielded the discovery of the first antiparticle, the positron, by Carl Anderson [8]. This had identical properties to the electron but a positive rather than negative charge. Paul Dirac had earlier tried to combine special relativity and quantum mechanics, which predicted negative energy electron states, but physicists were unwilling to accept this. However, the Feynman-Stückelburg interpretation [9, 10] later showed that Dirac's equations

were equivalent to the existence of positive energy antiparticle states, which could describe the observed positron. At the time, nucleons (protons p, neutrons n and their antiparticle equivalents) were considered elementary particles, but this was to change with the discovery of mesons.

1.2 Onto the Quarks

The following two sections have been written with great assistance from the 2017 Lancaster summer school in High Energy Physics [11], the 2018 Fermilab-CERN summer school in Hadron Collider Physics [12], and the books of Modern Particle Physics by Thomson [13], Quarks and Leptons by Halzen and Martin [14], and Introduction to Elementary Particles by Griffiths [15].

The pion (π) was discovered in 1947 [16], setting the scene for a large number of new particle discoveries including the kaon (K), delta (Δ) and sigma (Σ). These new particles were unpredicted and were produced very quickly ($\sim 10^{-23}$ s) but decayed more slowly ($\sim 10^{-10}$ s). For instance, the Σ^- is produced by $\pi^- p \rightarrow K^+ \Sigma^-$ but the decay via $\Sigma^- \rightarrow n\pi^-$ is slower [17, 14]. However, a similar decay, $\Delta^- \rightarrow n\pi^-$ occurs much faster. Jumping to the present day, the Σ^- equations are attributed to strong force production and weak force decay, and the Δ^- decay via the strong force (owing to their internal structures - see Section 1.3.1). However, back in 1953, Murray Gell-Mann [18] along with Kazuhiko Nishijima and Tadao Nakano [19] proposed the idea of a strangeness quantum number, S, for the particles. Those decays that conserved strangeness could proceed faster than those that did not. With the Σ^- having $S = -1$, the K^+ having $S = +1$, and the neutron, proton and pion with $S = 0$, the fast Σ^- production conserves strangeness but the decay does not. The Δ^- has $S = 0$ so its fast decay is strangeness-conserving.

The plethora of new particles was split up into two families: the mesons and baryons, which Murray Gell-Mann and Yuval Ne'eman attempted to classify. They established the Eightfold Way [20] to group the mesons and baryons into geometrical patterns based on their charges, Q, and strangeness. In doing so, they were able to predict a missing particle, the Ω^-, in one of these multiplets, which was later discovered in 1964 [22] (see Figure 1.1). An underlying principle was proposed by Murray Gell-Mann and George Zweig in 1964 [23, 24] to explain these mathematical structures. They suggested the existence of smaller particles called quarks that make up the mesons and baryons. These come in three flavours: up (u), down (d) and strange (s), with charges $+2/3$, $+2/3$ and $-1/3$, respectively, and their corresponding antiquarks: anti-up ($\bar{u}$), anti-down ($\bar{d}$) and anti-strange ($\bar{s}$), with charges $-2/3$, $-2/3$ and $+1/3$, respectively. Mesons are made up of a quark-antiquark pair (such as $s\bar{s}$ in the ϕ particle), and baryons consist of three quarks or antiquarks (such as uud in the proton). Particles consisting of quarks are called hadrons. Particles not made from quarks such as the electron, muon, neutrinos and their antiparticles are called leptons. Quarks and leptons have spins of $\frac{1}{2}$ and are collectively referred to as fermions.
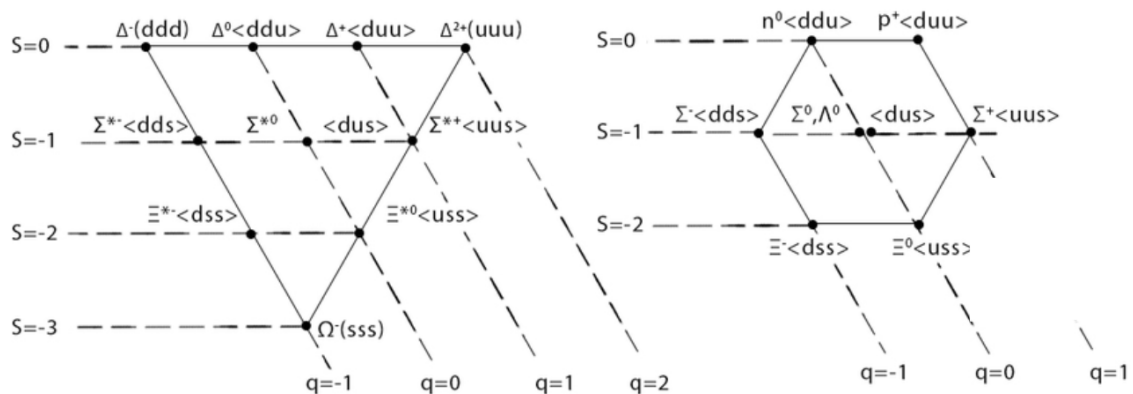
Fig. 1.1 Eightfold Way schematics arranged by charge and strangeness (with quark compositions also shown) in a baryon decuplet (left) and octet (right) [21]. The decuplet shows the predicted Ω^- at the lower point of the triangle.

One hadron that was identified was the Δ^{++} of charge $+2$, consisting of three up quarks (*uuu*) in a symmetric spin ground state. The Pauli Exclusion Principle [25] asserts that one or more fermions cannot occupy the same quantum state in a given time, so the Δ^{++} should be forbidden. However, quarks come with another property called colour charge. This comes in three forms: red (R), blue (B) and green (G), and antiquarks have equivalent anti-red ($\bar{R}$), anti-blue ($\bar{B}$) and anti-green ($\bar{G}$) forms. Combinations of quarks have to be constructed so the overall colour is white. To make white, we can combine one quark colour and its antiquark colour (such as $R\bar{R}$), as is the case for mesons, or a combination of three colours (such as RGB in the Δ^{++} baryon, which now obeys the Pauli Exclusion Principle). This concept explains why quarks had not been seen by themselves, referred to as "colour confinement".

The quark model at the time did well at categorising the particles, but there was a particular decay that did not seem to fit in. The K^0 meson decays to two muons but the probability of this occurring was greatly suppressed compared with the expectation. An answer to this was put forward by Sheldon Glashow, John Iliopoulos and Luciano Maiani in 1970 [26], by introducing a new, charm quark of charge $+2/3$. This enables an additional decay through the charm quark, which interferes destructively with the known decay through an up quark, and suppresses the overall decay. This process is known as the Glashow-Iliopoulos-Maiani (GIM) mechanism. In 1974, the charm quark was discovered in the bound charm-anticharm state of the J/ψ at both the Brookhaven National Laboratory (BNL) [27] and Stanford Linear Accelerator Center (SLAC) [28].

With the two generations of quarks – (up, down) and (charm, strange) – a third generation (top, bottom) was hypothesised by Makoto Kobayashi and Toshihide Maskawa [29] to explain Charge-Parity (CP) violation. It was already known that in exchanging a particle with an antiparticle or vice versa (C conjugation), the resulting physics could be different, as shown

in the decay of muons to electrons and anti-muons to positrons [30]. In exchanging the spatial coordinates of a system with their mirror image (P or parity), again the physics can manifest differently, such as in the decay of cobalt-60, which liberates an electron, a neutrino and two photons [31]. Furthermore, the combination of C and P conjugation was also found to be violated, which is needed to explain why there is more matter than antimatter in the universe. In 1964, it was observed that the K_L^0 particle (a combination of K^0 and $\bar{K}^0$) was found to decay to both two and three pions [32], where CP symmetry states it should just decay to three pions in the two quark generation model. With three generations of quarks, however, there are three rotation angles describing relative coupling strengths between quark vertices, in addition to one complex phase parameter which can account for CP violation. The bottom quark was subsequently discovered in 1977 at Fermilab in the USA through the observation of the bottom-antibottom, Υ, meson [33]. Later, in 1995, the top quark was discovered by the CDF (Collider Detector at Fermilab) [34, 35] and D0 [36, 37] experiments with the Tevatron collider [38] at Fermilab. The top quark is the main focus of this thesis. Alongside the quarks, we also have three generations of leptons: (electron e, electron neutrino ν_e), (muon μ, muon neutrino ν_μ) and (tau τ, tau neutrino ν_τ). A formal theory was needed to encompass the known quarks and leptons (and their respective antimatter equivalents) in addition to how they interact with the fundamental forces in nature. This ultimately led to the Standard Model.

1.3   Building the Standard Model

Within theoretical physics, great understanding of the universe has been made by considering symmetries: that is, a feature of the system which remains unchanged under transformations. Performing a translation of spatial coordinates of a moving system results in conservation of momentum, or a translation of time coordinates leads to conservation of energy. These can be formulated most effectively using Lagrangians, L. A Lagrangian is simply the kinetic

energy minus the potential energy of the system $(T - V)$. Or alternatively, as in particle physics, we use Lagrangian densities, $\mathscr{L}$ (where $L = \int \mathscr{L} d^3 x$), which are dependent on the wavefunctions, ψ. Using the Principle of Least Action, we obtain the equations of motion for a system in an analogous way to using Newton's well-known $F = ma$ relation. Quantum Field Theories (QFTs) such as the Standard Model involve taking the Lagrangian density and requiring it to be invariant under local gauge transformations: $\psi(x) \to U(x)\psi(x)$, with $U(x)$ a phase transformation in arbitrary space and time. From this, we obtain new conservation laws and associated fields.

1.3.1 Quantum Field Theories

Dirac's description of electrodynamics can be expressed in Lagrangian form and subjected to local gauge invariance, $\psi(x) \to e^{i\alpha(x)}\psi(x)$, with $\alpha(x)$ an arbitrary space-time function. This is a U(1) symmetry, where U(1) is a unitary matrix (of determinant $+1$ or -1), and simply of dimension 1×1. The invariance leads to a conserved quantity, the electric charge ($Q = -e$) in addition to a vector field (A) with an associated particle: the massless, spin-1 photon (γ, a boson). It is the fundamental force carrier responsible for electromagnetic interactions such as the attraction between oppositely-charged protons and electrons in the atom. This QFT for electromagnetism is called Quantum Electrodynamics (QED).

An SU(2) symmetry can describe the weak interaction that acts on quarks and leptons. SU(2) is a special unitary matrix (of determinant $+1$) and of dimension 2×2. The conserved quantity is the weak isospin, T, and it generates three fields. As introduced in Section 1.2, the Σ^- (sdd quark content) decays to a neutron (udd) and π^- ($\bar{u}d$), with a change in quark flavour of s to u through the weak interaction.

The weak and electromagnetic forces unify at high energy (around 200 GeV) to give the electroweak interaction (SU(2) × SU(1)) as described by Sheldon Glashow, Abdus Salam, and Steven Weinberg [39–41]. A new conserved quantity is established known as the weak hypercharge, Y:

$$Y = 2(Q - T^3), \tag{1.1}$$

where T^3 is the third component of the weak isospin. The unified force has four massless fields: W^1, W^2, W^3 (arising from SU(2)) and B (from U(1)). Linear combinations of these fields then yield the W^+, W^- and Z fields (with three associated spin-1 bosons) attributed to the weak force, as well as the A field of the electromagnetic force. Fermions can be left-handed (momentum vector in the opposite direction to the spin vector) or right-handed (momentum and spin vectors in the same direction). To conserve isospin, weak interactions involving charged W^+ or W^- currents can only take place on left-handed particles or right-handed antiparticles, explaining the C, P and CP violation experiments. The neutral current can work with both left- and right-handed particles and antiparticles, although their relative coupling strengths differ. The W bosons also enable quark flavour (but not lepton flavour) to change in interactions and the relative coupling strengths between the different quarks are described in the CKM (Cabibbo–Kobayashi–Maskawa) matrix [17]. In Equation 1.2, the relative magnitudes of the CKM coupling strengths, $|V_{xy}|$, are shown, where x and y are the interacting quarks:

$$\begin{pmatrix} |V_{ud}| & |V_{us}| & |V_{ub}| \\ |V_{cd}| & |V_{cs}| & |V_{cb}| \\ |V_{td}| & |V_{ts}| & |V_{tb}| \end{pmatrix} = \begin{pmatrix} 0.97446 \pm 0.00010 & 0.22452 \pm 0.00044 & 0.00365 \pm 0.00012 \\ 0.22438 \pm 0.00044 & 0.97359^{+0.00010}_{-0.00011} & 0.04214 \pm 0.00076 \\ 0.00896^{+0.00024}_{-0.00023} & 0.04133 \pm 0.00074 & 0.999105 \pm 0.000032 \end{pmatrix}. \tag{1.2}$$

The *W* and *Z* bosons were discovered in 1983 at the Super Proton Synchrotron (SPS) at CERN [42–45].

The strong nuclear force is characterised with an SU(3) symmetry: a special unitary matrix of dimension 3×3. It leads to conservation of colour charge and the presence of eight new fields, each giving a massless gluon. The quarks and gluons themselves carry colour; the latter having linear combinations of R, $\bar{R}$, B, $\bar{B}$, G and $\bar{G}$. The gluons are responsible for the strong force that binds the nucleons together in the nucleus. This QFT is called Quantum Chromodynamics (QCD). From Section 1.2, the Δ^- (*ddd* quark content) decays to a neutron (*udd*) and π^- ($\bar{u}d$) through a gluon emission in the strong interaction.

1.3.2   The Higgs Boson and Electroweak Symmetry Breaking

The above formalisms assume massless fermions and bosons, and whilst the photon and gluon are believed to be massless, experiments have shown the other particles are not. For instance, the *W* and *Z* bosons have masses of 80.379 ± 0.012 GeV and 91.1876 ± 0.0021 GeV, respectively [17].

Simply adding in mass terms for the fields of the Lagrangians violates local gauge invariance, so a more subtle method has to be employed. The concept of electroweak symmetry breaking was developed in the Brout-Englert-Higgs mechanism [46–48]. This introduces the Higgs field, ϕ, to describe the quantum vacuum:

$$\phi = \begin{pmatrix} \phi^+ \\ \phi^0 \end{pmatrix} = \frac{1}{\sqrt{2}} \begin{pmatrix} \phi_1 + i\phi_2 \\ \phi_3 + i\phi_4 \end{pmatrix}, \tag{1.3}$$

where the vacuum potential is:

$$V(\phi) = \mu^2(\phi^\dagger \phi) + \lambda(\phi^\dagger \phi)^2, \tag{1.4}$$

with μ^2 (< 0) a mass parameter and λ (> 0) the Higgs field self-coupling. The potential of the field is shaped like a Mexican hat (see Figure 1.2), such that the minimum is a circle of radius $\sqrt{-\mu^2/2\lambda}$. Any value on the circle could be chosen, which breaks the vacuum gauge invariance (since the minimum is not at the origin) but does not break the SU(2) × SU(1) Lagrangian gauge invariance. However, in order for the photon to remain massless after this symmetry breaking, the minimum must be chosen to yield a non-zero vacuum expectation for just the neutral scalar field, ϕ^0. The W^+, W^- and Z bosons do gain mass through this choice by coupling to the Higgs, where the Higgs coupling strength to the bosons is proportional to the square of their masses.
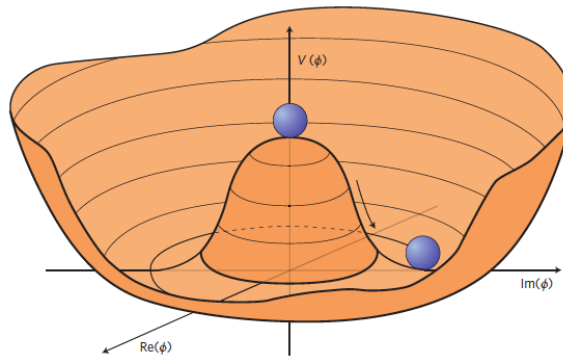
Fig. 1.2 The Higgs potential for $\mu^2 < 0$ and $\lambda > 0$. The minima do not fall at the origin, leading to a non-zero vacuum expectation value [49].

The Higgs also gives masses to the fermions through Yukawa couplings, where the Higgs coupling strength is proportional to the fermion mass. The Higgs field itself has an associated scalar particle, the Higgs boson, which was discovered at CERN in 2012 [50, 51], and has a mass of 125.10 ± 0.14 GeV [17].

1.3.3   The Standard Model

Our best interpretation of the fundamental forces and particles is encapsulated in the Standard Model of Particle Physics (SM). This is a combination of the aforementioned gauge groups, $SU(3) \times SU(2) \times SU(1)$, and encompasses all the known fermions (see Table 1.1) and forces (see Table 1.2) except for gravity. Interactions between bosons and fermions are shown in Feynman diagrams, with Table 1.2 showing some examples.

The strengths of the forces (running couplings) are a function of the energy scale, Q, which encodes the momentum transfer in the interaction taking place. For the electromagnetic and weak forces, the couplings increase with energy. For the strong force (under study through top quark pair production in this thesis), the coupling, α_s, decreases with energy. Gluons emitted from a given quark split into gluon pairs and act to spread out the effective colour charge of the quark as Q increases. This behaviour is useful for making precise perturbative QCD calculations, since Feynman diagrams of increasing orders in a given process (increasing powers of α_s) yield smaller and smaller corrections to the overall calculation when $\alpha_s < 1$. Indeed, as $Q \to \infty$, $\alpha_s \to 0$, which is known as asymptotic freedom, since the quarks behave as free particles when probed in experiments. Conversely, as $Q \to 0$, $\alpha_s \to \infty$, and quarks are confined inside hadrons. QCD corrections at higher orders become non-perturbative in this energy regime (increasing powers of α_s now give larger and larger corrections to the calculation), making processes difficult to calculate. The value of α_s is around unity at $Q = 1$ GeV.

Generation	Particle	Charge	Mass (GeV)
1st	Electron (e)	-1	5.11×10^{-4}
	Electron neutrino (ν_e)	0	$< 2.25 \times 10^{-7}$
	Up quark (u)	$+2/3$	2.2×10^{-3}
	Down quark (d)	$-1/3$	4.7×10^{-3}
2nd	Muon (μ)	-1	0.106
	Muon neutrino (ν_μ)	0	$< 1.9 \times 10^{-4}$
	Charm quark (c)	$+2/3$	1.28
	Strange quark (s)	$-1/3$	0.095
3rd	Tau lepton (τ)	-1	1.78
	Tau neutrino (ν_τ)	0	< 0.0182
	Top quark (t)	$+2/3$	173
	Bottom quark (b)	$-1/3$	4.18

Table 1.1 The three generations of spin-$1/2$ quarks and leptons with their charges and masses taken from Reference [17]. Anti-particle equivalents (of opposite charge) are not shown. In the Standard Model, neutrinos are massless, but in order to account for observed neutrino oscillations (see Section 1.4), they must have mass. Hence upper limits are placed on them.
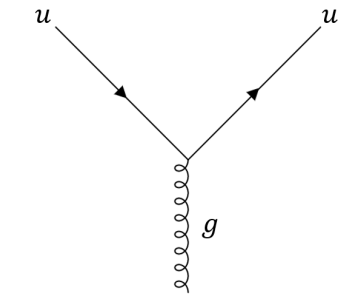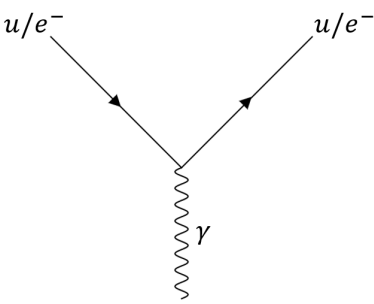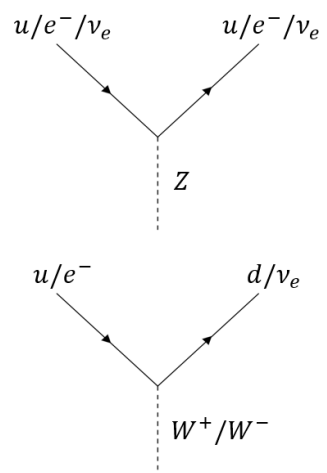
Force	Strength	Boson	Mass (GeV)	Vertex
Strong	~ 1	Gluon (g)	0	
Electro-magnetic	$\sim 10^{-3}$	Photon (γ)	0	
Weak	$\sim 10^{-6}$	W$^\pm$/Z boson	80.4/91.2	

Table 1.2 The fundamental forces along with their strengths, associated bosons and masses, and example Feynman vertices. Adapted from Table 1.3 of Reference [13]. The strong force only couples to quarks, whereas the electromagnetic and weak forces couple to both quarks and leptons. Diagrams created using the package in Reference [52].

1.4 Beyond the Standard Model

The Standard Model's predictions have been robustly tested and verified in particle physics experiments. However, it is not a complete theory. It does not account for gravity, and attempts to reconcile the Standard Model with Einstein's theory of gravity, General Relativity, have not been successful. The model also does not explain why the universe's expansion is accelerating (dark energy being the current theory), and also why galaxies are much more massive than can be described by visible matter (dark matter being a leading candidate). Figure 1.3 shows the relative proportions of mass-energy composition in the universe. Normal matter, which makes up the known particles that create our planets, stars, gas and radiation, account for only 5% [53]. Moreover, the Standard Model cannot explain fully why the universe is made up of matter rather than antimatter, and the small amounts of CP violation seen in weak interactions cannot explain the discrepancy. Neutrinos are also known to oscillate in flavour, which is only possible if they have mass, for which the theory does not allow. The weak force allows flavour changing in quarks (but not in leptons) and no other forces allow flavour change.

The Standard Model itself has 19 free parameters including the fermion masses (or fundamental force coupling strengths) and CKM matrix quantities. It is unknown why the top quark is so heavy with a mass of 172.9 ± 0.4 GeV [17]. This is 40 times greater than the mass of the bottom quark and 185 times greater than the mass of the proton. In conjunction with the Higgs mass and assuming the Standard Model, it would mean the quantum vacuum we are in now (introduced in Section 1.3.2) could be at a local rather than a global minimum of the Higgs potential [55]. In extrapolating the SM up to the Planck energy scale, $M_{\text{pl}} \sim 10^{19}$ GeV, the Higgs self-coupling, λ, decreases - the rate of which depends on the top mass. Should λ turn negative, the Higgs potential becomes deeper than the current electroweak vacuum, and

ENERGY DISTRIBUTION
OF THE UNIVERSE

69%

DARK
ENERGY

26%

DARK
MATTER

5%

NORMAL MATTER
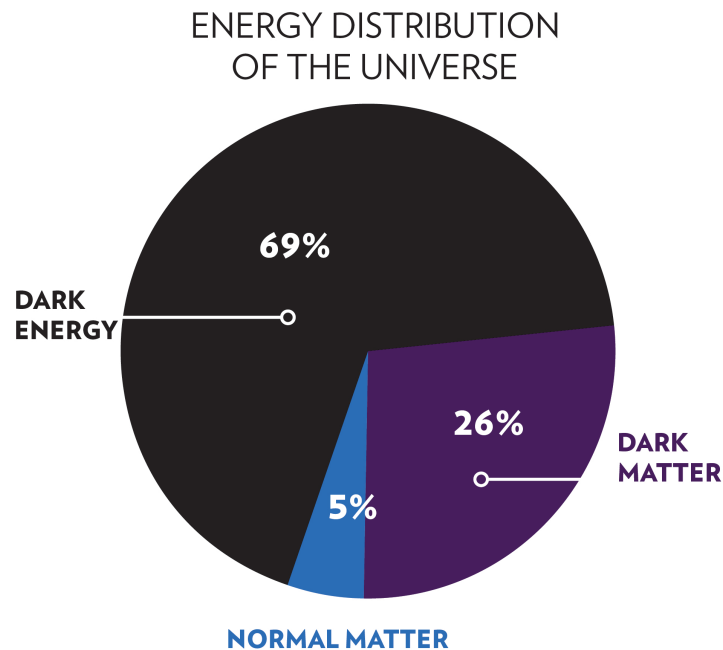
Fig. 1.3 The relative proportions of dark matter, dark energy and mass in the universe [54].

there is the possibility of quantum tunnelling to this global minimum in the future. Given the experimental measurements of the top mass, a deeper minimum should exist but the expected time for the tunnelling to occur is much greater than the age of the known universe. The universe is therefore described as being in a metastable state. However, this scenario may not occur given the SM is incomplete. Indeed, the top mass is similar to the energy of the electroweak scale, which could be a hint of new physics. An ultimate theory of the universe should be self-consistent with no free parameters.

In addition, the strong and electroweak forces do not unify into a single force within $SU(3) \times SU(2) \times SU(1)$, so grand unified theories are built in Beyond the Standard Model (BSM) interpretations. Supersymmetry (SUSY) [56] is one such example but it predicts each Standard Model fermion and boson to have a supersymmetric partner. These have not been

detected so far and SUSY introduces even more free parameters.

Particle physics experiments are designed to test our models of the universe. They can confirm predictions of the Standard Model, search for new physics processes predicted by BSM theories, or even hunt for new physics that has no theoretical description yet. The following section describes a particle accelerator known as the Large Hadron Collider.

The LHC and its Detectors

2.1   Introduction to the LHC

The Large Hadron Collider (LHC) [57] is the world's largest and most powerful particle accelerator based at CERN (Organisation - formerly Conseil - Européenne pour la Recherche Nucléaire) in Geneva, Switzerland. It is housed in a 26.7 km circumference circular tunnel between 45 m and 170 m underground, crossing the Franco-Swiss border. The tunnel originally contained the LEP (Large Electron-Positron) collider that took measurements between 1989 and 2000 [58]. This gave way to the LHC, which began data-taking in 2009 and still operates to this day. Rather than accelerating leptons, the LHC predominantly collides protons with protons: so-called *pp* collisions (the focus of this thesis), but also collides heavy ions. The LHC has the possibility to reach centre-of-mass energies, $\sqrt{s}$, of 14 TeV. The LHC has so far undergone two operational periods: Run 1 from 2009-2012, which had collisions at $\sqrt{s} = 7$ and 8 TeV, and then Run 2 from 2015-2018 at $\sqrt{s} = 13$ TeV. At 13 TeV, each proton (of 0.938 GeV mass) carries 6.5 TeV of energy corresponding to a speed of 0.9999999896 c, such that relativistic effects cannot be ignored.

2.2 Acceleration Stages

Before particles are introduced into the LHC, they undergo several stages of acceleration, as described in Reference [59]. A simple bottle of hydrogen gas acts as the source and an electric field strips off the electrons to give positively charged protons. A linear accelerator called Linac 2 then accelerates the protons up to 50 MeV. The particles then progress through three accelerating rings: the Proton Synchrotron Booster (PSB) to 1.4 GeV, the Proton Synchrotron (PS) to 25 GeV, and then the Super Proton Synchrotron (SPS) to 450 GeV. Finally, they are injected into the LHC ring. The system of acceleration stages and CERN experiments is shown in Figure 2.1.
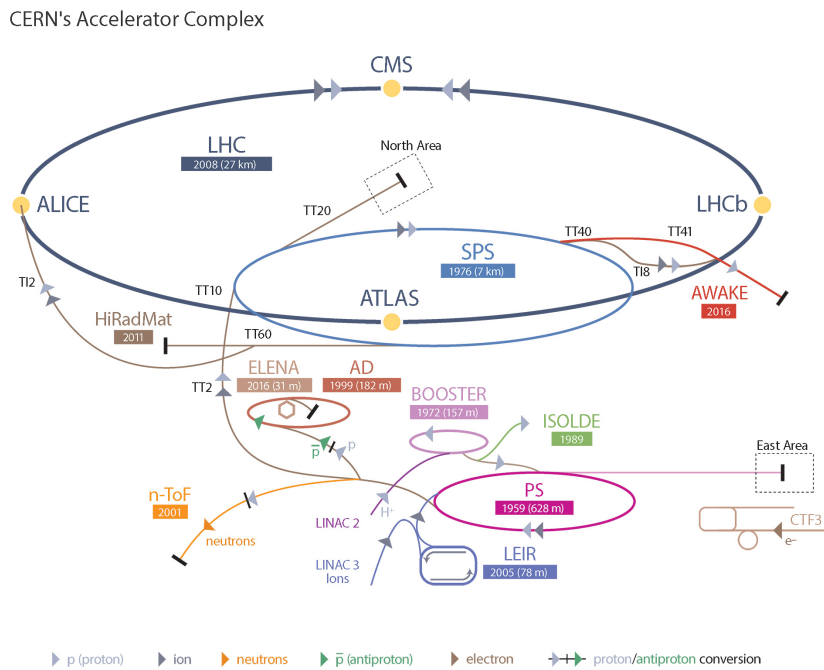
Fig. 2.1 A schematic showing the accelerator complex at CERN [60].

In order to accelerate the protons, Radio Frequency (RF) cavities are used. These are metallic chambers where oscillating electromagnetic fields are generated. In the LHC, there are 16 RF cavities for each proton beam, housed in a dedicated section of the ring. Each time the

protons circle the ring, they pass through the cavities. In order for a particle to be accelerated, it must be in the cavity when the electric field is pointing in the direction of travel. Thus, timing of the protons in the cavities is essential, with the radio frequency required to be an integer multiple of the proton revolution frequency around the ring. The RF oscillations of each cavity occur in the LHC at a rate of 400.8 MHz, or one oscillation per 2.495 ns. In theory, the protons could be spaced 2.495 ns apart, but 24.95 ns (commonly referred to as 25 ns) corresponding to 40.08 MHz is chosen due to the capabilities of the LHC detectors. At the desired energy, an ideal proton called a synchronous proton will arrive at the RF cavities when the electric field is zero and experience no acceleration or deceleration. However, there are a range of proton energies around this central value. If a proton is too energetic, it travels a shorter path around the detector and will arrive at the cavity too soon, when the electric field is in the opposite direction, and hence it is decelerated. Next time, it arrives at the cavity too late and will be accelerated again, hence always oscillating longitudinally around the synchronous particle. This leads to clumps of particles being spread around the synchronous one, where each clump is known as a bunch. Each bunch contains up to 1.15×10^{11} protons.
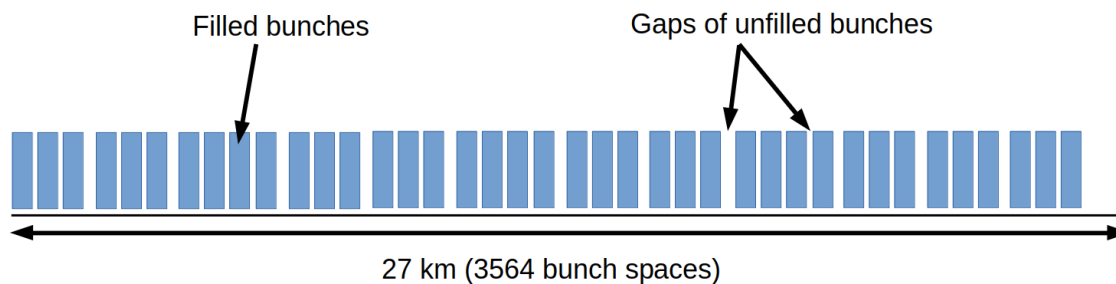
Fig. 2.2 An example bunch fill scheme across the 27 km length of the LHC. The blue rectangles show filled bunches and white gaps where there is no filling.

With a proton revolution frequency of 11.245 kHz and bunch crossings rates of 40.08 MHz, it is possible for there to be 3564 bunches in the ring. However, not all the bunches are filled, with gaps between some of the bunches (see Figure 2.2) to mitigate beam structure instability

and space for the beam dump kicker to use. A maximum of 2556 bunches are filled in the LHC. This means the average bunch crossing rate is 28.74 MHz.

2.3   Magnets

The bunches are subjected to two forms of magnet: lattice magnets distributed around the LHC and insertion magnets as they enter the detectors. The lattice magnets consist of 1232 powerful 8 T dipole magnets that are supercooled with liquid helium to 2 K to bend the protons around the accelerator. Since the colliding particles are the same charge and travel in opposite directions in adjacent pipes, it is necessary for the direction of the magnetic fields to be opposite in the two pipes. Figure 2.3 shows the magnetic field distributions in the pipes.
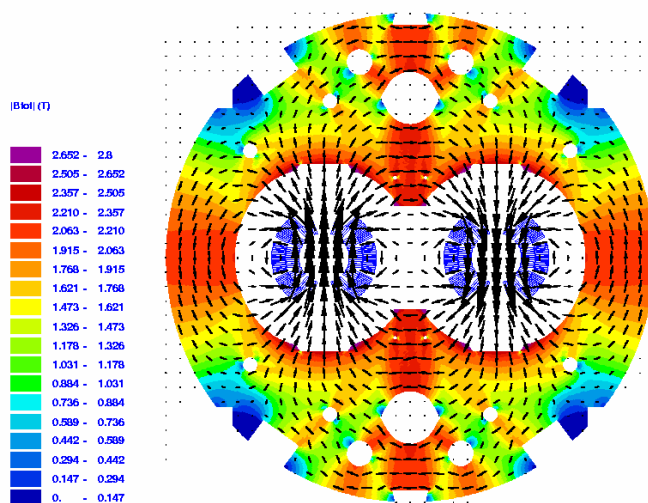
Fig. 2.3 A cross-section of the dipole magnetic field distribution for the two proton beampipes (left and right white central circles) [61]. The arrows show the strength and direction of the field, whereas the colours show the magnetic flux outside the beampipes.

Other lattice magnets include quadrupole, sextupole, octupole and decapole magnets that focus the bunches, counteracting forces such as gravity and the repulsive forces between the

protons. The principal lattice magnets are shown in Figure 2.4.
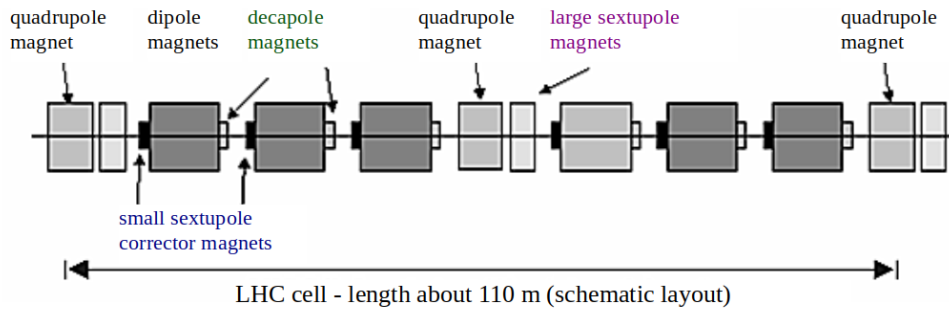
Fig. 2.4 The arrangement of lattice magnets along the LHC, which is repeated along the 27 km ring [62].

The insertion magnets consist of quadrupole magnets placed just before the detectors where the protons collide. These squeeze the protons into tightly-focussed beams to maximise the probability of particle collisions, although it does increase pile-up (see Section 3.3). There are four main detectors as shown in Figure 2.5.
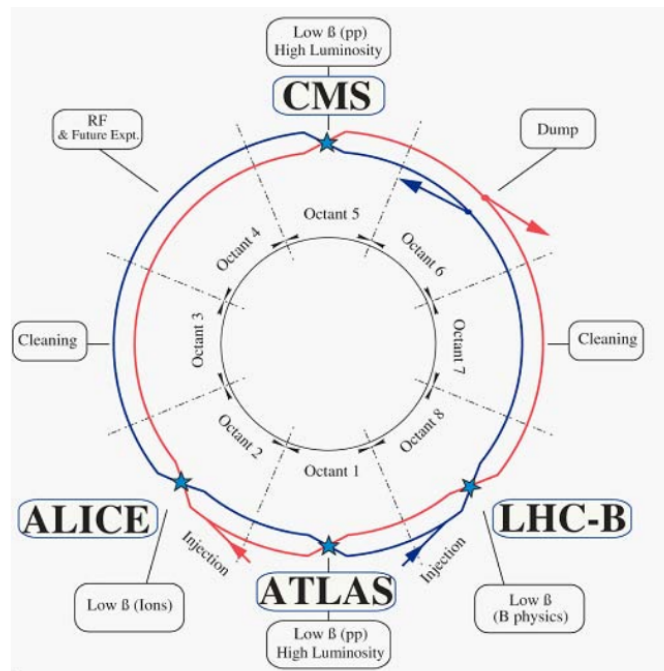
Fig. 2.5 The bunches of protons are made to collide at four points along the LHC: Point 1 (ATLAS), Point 2 (ALICE), Point 5 (CMS) and Point 8 (LHCb) [57].

2.4 The Detectors

The four main detectors in the LHC are described below. Three smaller detectors also exist that focus on forward physics (when protons or ions deflect off each other rather than directly collide) or in the hunt for theoretical particles called magnetic monopoles, but are not described here.

2.4.1 ALICE

The detector called A Large Ion Collider Experiment (ALICE) [63] concentrates on heavy ion collisions such as lead-lead and xenon-xenon, as well as proton-proton. Its main aim is to understand strong interactions encoded in QCD. Quarks bind together through gluon interactions to form hadrons in the process of colour confinement. However, with the high effective temperatures at the LHC, the quarks can overcome the force, existing as free particles in a quark-gluon plasma. The properties of the quark-gluon plasma are observed in ALICE, such as how it cools and expands to produce bound particle states.

2.4.2 LHCb

LHC beauty (LHCb) [64] is a combination of subdetectors optimised for highly boosted particles along the beamline. As the name suggests, its main focus is on beauty (or bottom) quarks. It measures rare decays of B hadrons to look for BSM enhancements in their production, as well as CP violation in particle decays. The detector has excellent vertex (collision or decay position) detection and mass measurements, being able to differentiate between similarly massive pions and kaons from B decays. It is also asymmetrical: the subdetectors range from the collision point centre to 20 m beyond in only one direction (due to construction costs). This is not a problem for symmetric pp collisions, since the

emitted particles have an equal probability of travelling in either direction and so can still be measured half of the time.

2.4.3 CMS and ATLAS

The Compact Muon Solenoid (CMS) [65] and A Toroidal LHC ApparatuS (ATLAS) [66] experiments are general-purpose detectors that perform precise measurements of Standard Model predictions and hunt for new particles and BSM phenomena such as dark matter and SUSY. They jointly discovered the Higgs boson in 2012 [50, 51]. Despite having the same goals, the two detectors have different structures. CMS is characterised by a huge 4 T solenoid magnet, whereas ATLAS has a 2 T central solenoid and a series of 1 T outer toroid magnets, all of which bend charged particles so their momenta can be determined. The ATLAS solenoid wraps around the inner detector while the CMS solenoid envelops the inner detector, electromagnetic and hadronic calorimeters, causing additional bending in the calorimeters. For the electromagnetic calorimeter, ATLAS uses liquid argon as the scintillating material, whereas CMS uses a lead tungstate crystal. In the inner detector, ATLAS uses silicon pixel and strip sensors in the central section and transition radiation trackers in the outer section, whereas CMS uses silicon pixel and strip sensors throughout. The ATLAS experiment, described in more detail in the following chapter, is used for the charge asymmetry measurement in this thesis.

The ATLAS Detector

3.1 Introduction to ATLAS
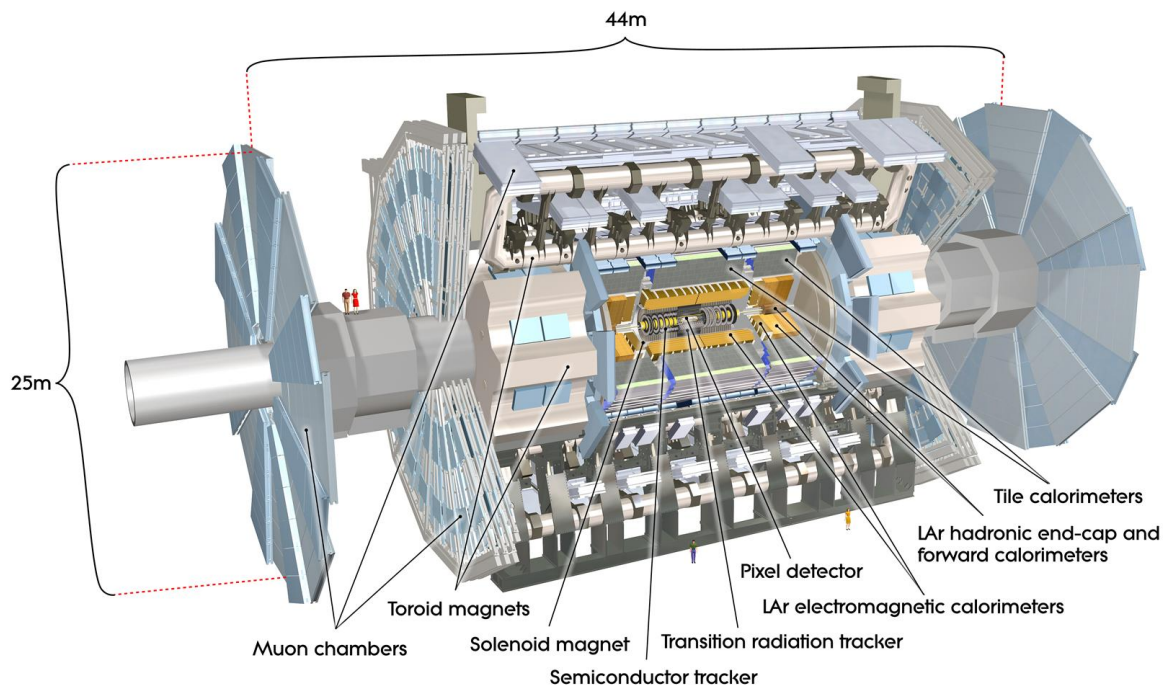
Fig. 3.1 The ATLAS detector with its major components labelled [66].

Despite measuring the properties of such small particles ($< 10^{-15}$ m), ATLAS is a huge detector: 7,000 tonnes in weight, 44 m in length and 25 m in width and height. A schematic is shown in Figure 3.1.

3.2   ATLAS Geometry
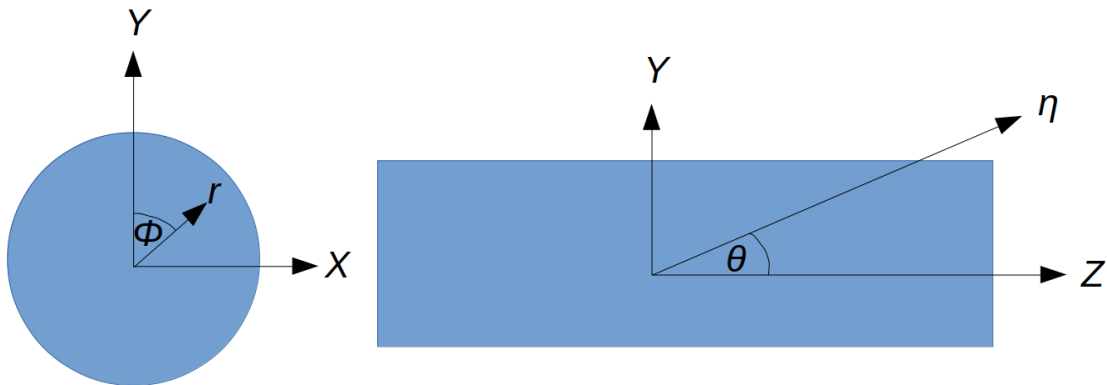
Fig. 3.2 The geometry at ATLAS with the origins defined by the collision interaction points. Left: end-on view of the beampipe with the Z direction out of the plane of the paper. Right: side view, with X into the plane of the paper.

To describe the positions of particles in the detector, a co-ordinate system complementing the detector geometry and the LHC beampipe is used. The origin is defined as the interaction point, with the Z-axis along the beam direction (left to right in the side view of Figure 3.2), the X-axis pointing from the interaction point to the LHC ring centre and the Y-axis pointing upwards. Furthermore, r is the radial distance from the beam axis, θ is the angle from the beam axis and ϕ the azimuthal angle around the beam axis. Momentum is often put into its transverse X- and Y-components, where the quadrature sum is the transverse momentum, $p_T = \sqrt{p_X^2 + p_Y^2}$. The longitudinal component, p_Z, is less important because, although the colliding protons have well-defined longitudinal momenta, the individual quarks and gluons (partons) within them do not. They rather follow probability distributions called Parton Distribution Functions (PDFs) and so it is not possible to know the exact parton longitudinal

parameters and infer much information from the p_Z of the collision products. However, since the pp collisions are head-on, the total sum of the transverse momenta components of the partons is approximately zero before the collision and therefore the sum should be zero after the collision. If it is not measured to be zero after the collision, it tells us that undetectable particles such as neutrinos or possibly BSM particles were produced. This missing transverse momentum (often called missing transverse energy, MET or E_T^{miss}) is given by:

$$
\begin{aligned}
p_X^{\mathrm{miss}} &= -\sum p_X \\
p_Y^{\mathrm{miss}} &= -\sum p_Y \\
E_T^{\mathrm{miss}} &= \sqrt{p_X^{\mathrm{miss}\,2} + p_Y^{\mathrm{miss}\,2}}.
\end{aligned}
\tag{3.1}
$$

Another parameter used in ATLAS is the rapidity, y. The parameter is useful as rapidity differences are Lorentz invariant, meaning they will be the same regardless of the longitudinal boost of the system with respect to the lab frame. The rapidity is given by:

$$
y = \frac{1}{2} \ln\left(\frac{E + p_Z}{E - p_Z} \right),
\tag{3.2}
$$

where E is the total energy of the particle.

This equation tends to the pseudorapidity, η, in the high-energy or massless limit:

$$
\eta = -\ln\tan\left(\frac{\theta}{2} \right).
\tag{3.3}
$$

The pseudorapidity ranges from $\eta = 0$ (particles travelling perpendicular to the beampipe at $\theta = 90°$) to $\eta = \infty$ (parallel to the beampipe at $\theta = 0°$).

Distances between objects or spatial points in the detector are regularly described with the ΔR variable:

$$
\Delta R = \sqrt{(\Delta\eta)^2 + (\Delta\phi)^2},
\tag{3.4}
$$

where $\Delta\eta$ and $\Delta\phi$ are the differences in pseudorapidity and azimuthal angle between the objects, respectively.

3.3   Luminosity and Pile-Up

Proton interactions are focussed in the very centre of the detector: in some cases passing by one another with or without being deflected and other times one or both protons being broken apart, with the energy released converted into mass and kinetic energy of new particles. There are of order 1 billion collisions per second in ATLAS [67]. An important measure of the number of interactions is the instantaneous luminosity, $\mathcal{L}$. This gives the number of collisions occurring per second over an area of 1 cm^2. Assuming head-on collisions of two identical beams with Gaussian density profiles, and each having cross-sectional area, $A = 4\pi\sigma_X\sigma_Y$, where σ_X and σ_Y are the transverse widths of the beams in the X and Y directions, the luminosity is given by:

$$\mathcal{L} = \frac{N^2 f n_b}{4\pi\sigma_x\sigma_y}F, \tag{3.5}$$

where N is the number of protons per bunch (1.15×10^{11}), f is the revolution frequency of protons around the LHC (11.245 kHz), n_b the number of bunches in the LHC (up to 2556) and F the geometric factor that encompasses additional information about the colliding beams. Example contributions to F are the relative offset of the two beams, their crossing angle and non-Gaussian features in their transverse profiles. These mean that not all particles in a beam will have the opportunity to overlap with the colliding beam, decreasing $\mathcal{L}$. The instantaneous luminosity also decreases exponentially with time as the number of protons available to interact decreases. In Run 2, the maximum recorded luminosity at ATLAS was 2.1×10^{34} cm^{-2} s^{-1} [68].

A related quantity is the integrated luminosity, L, which describes the the total amount of data collected per unit area in time $t_2 - t_1$:

$$L = \int_{t_1}^{t_2} \mathcal{L} dt. \tag{3.6}$$

The total integrated luminosity for Run 2 was around 1.39×10^{41} cm^{-2}. Units of barns (1 barn $= 10^{-24}$ cm^2) or rather femtobarns (1 fb $= 10^{-39}$ cm^2) are often used in particle collisions, such that the quoted number is 139 fb^{-1}. The integrated luminosity throughout Run 2 is shown in Figure 3.3.
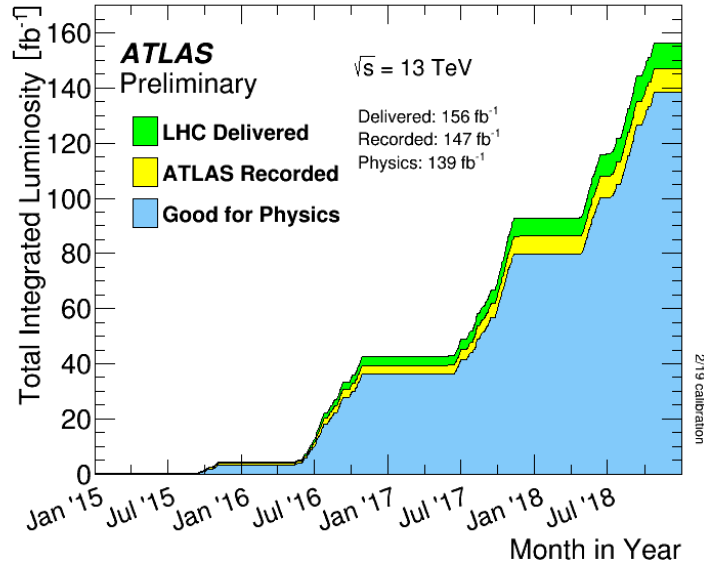
Fig. 3.3 The integrated luminosity for the full Run 2 period of 2015-2018 [68]. The ATLAS recorded luminosity (yellow) is always below the LHC luminosity (green) due to detector adjustments being made when stable beams are declared, and since the detector is not 100% efficient at saving particle collisions. Poor quality data due to abnormalities in the detector components are also discarded leading to the final (blue) histogram of 139 fb^{-1}.

Given the integrated luminosity, it is possible to determine the expected number of events, $N_{process}$, from various processes:

$$N_{process} = L\sigma_{process}, \tag{3.7}$$

where σ_{process} is the cross-section for the process that can be calculated from the Standard Model. The incoming, outgoing and exchange particles of Feynman diagrams are combined into mathematical constructs using Quantum Field Theory, and the diagrams of a particular final state are summed together to form a matrix element. The square of the matrix element is integrated over all available phase space, taking into account conservation of momentum and energy and divided by the flux of incoming particles to give a cross-section. The rarer the process, the smaller its cross-section.

During data-taking, it is possible for multiple proton-proton interactions to occur in the time it takes for the detector to record an interaction. This is known as pile-up, and has two main forms: in-time and out-of-time pile-up [69]:

- In-time pile-up involves additional interactions within the same bunch crossing as the collision of interest. This became as high as 37.8 per crossing for 2017 data-taking [68].

- Out-of-time pile-up involves interactions occurring in neighbouring bunch crossings to the collision of interest. Since the electronics can take more than 25 ns to record an event, it is possible for particle tracks in this form of pile-up to be saved in the main event.

Figure 3.4 shows an example recorded event at ATLAS with multiple pile-up interactions as well as the distribution of pile-up throughout the years of Run 2.
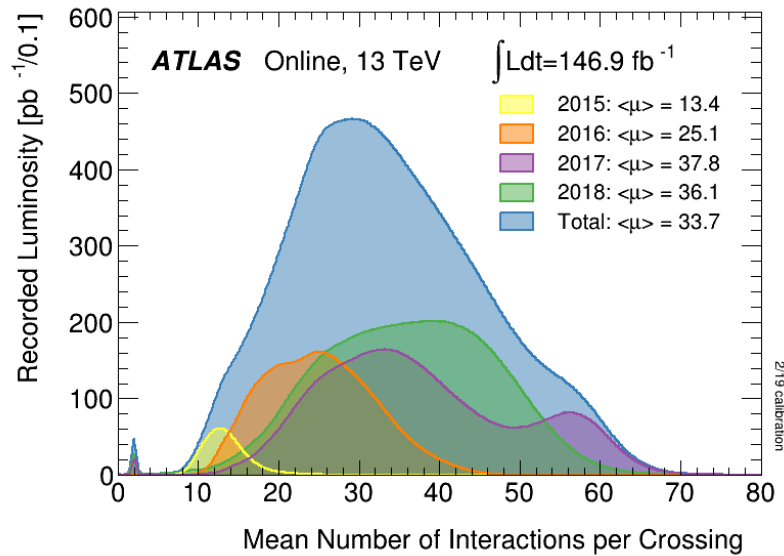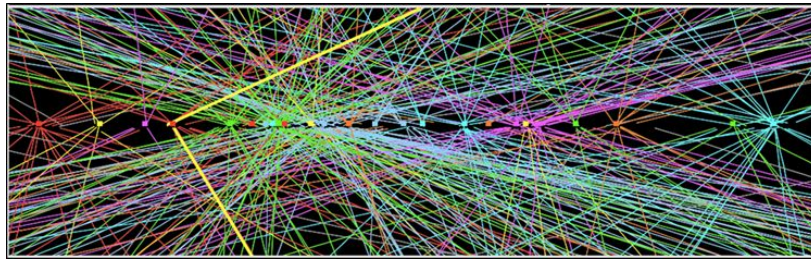
Fig. 3.4 Upper figure: an example event with in-time pile-up at ATLAS [70]. A candidate *Z* boson decays to two muons (yellow lines) but 25 reconstructed vertices are present in total. Lower figure: the pile-up distributions for Run 2 in ATLAS, showing individual annual and combined plots [68]. The average number of pile-up interactions per bunch crossing per year, $\langle\mu\rangle$, are shown in the legend.

3.4   The Subdetectors

The particles produced in collisions first pass through the inner detector, then through to the two calorimeters (the electromagnetic and hadronic calorimeters), before reaching the muon system on the outside of the detector. These components are described in more detail below, summarised from Reference [66] and other sources where stated.

3.4.1   The Inner Detector and Solenoid Magnet

The inner detector (ID) is the section of the detector closest to the interaction point. It is composed of three trackers: the pixel detector, which includes the new Insertable B-Layer (IBL) introduced in Run 2 [71], the Semiconductor Tracker (SCT) and the Transition Radiation Tracker (TRT). The ID records the paths of charged particles (above a p_T threshold of typically 0.5 GeV) within $|\eta| < 2.5$, by using a large 2 T solenoid magnet surrounding the subdetector. The magnetic field points along the Z direction of the detector and bends the charged particles; the direction of which identifies the particle charge, and the degree of curvature the particle momentum, since the smaller the curvature the greater the momentum. The ID also reconstructs primary vertices (the proton-proton collision points) and secondary vertices (the position at which a produced particle decays). The distances between the primary and secondary vertices can give us information about the intermediate particle, such as whether it is a B hadron, which has a long enough lifetime ($\sim 10^{-12}$s [17]) for its distance travelled to be measurable.
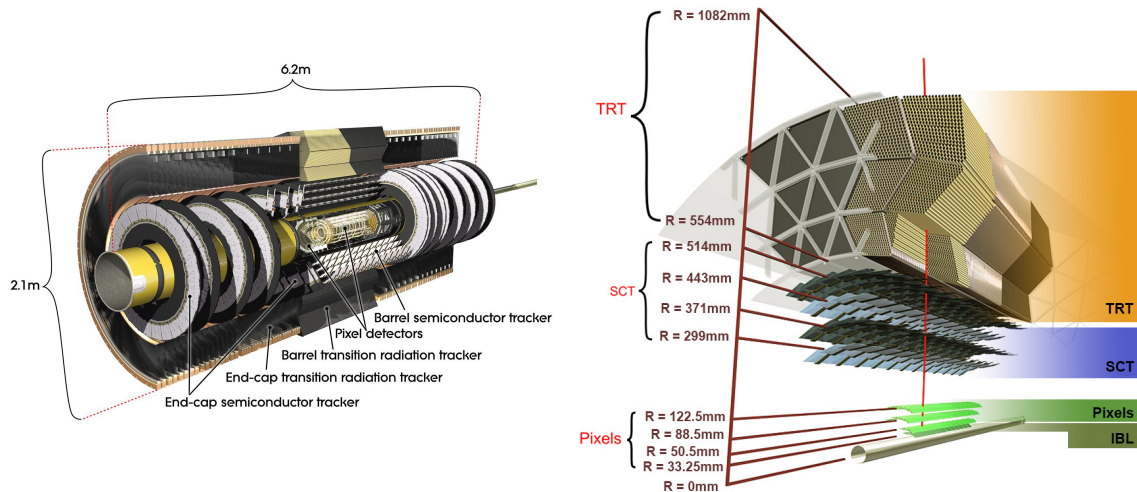
Fig. 3.5 Left: the ATLAS inner detector, showing the pixel, semiconductor and transition trackers [72]. Right: the cross-section through the centre of the ID [73].

The pixel detector consists of four barrel layers of pixels (centred around the beam axis) at $r = 33.25$ mm (the IBL), 50.5 mm, 88.5 mm and 122.5 mm, as well as two end-caps, each with three disc layers [73]. There are a total of 92 million pixels, each of typical size 50 μm $\times$ 400 μm (in $r\phi \times Z$) and the positions of the particles can be recorded to a resolution of 10 μm $\times$ 115 μm, giving accurate two-dimensional information. This high granularity is needed to be able to distinguish between the huge number of tracks. The pixels are made from silicon, a semiconductor material. When the charged particles pass through the silicon, electron-hole pairs are produced with minimal reduction of the particle energy (given the low thickness of the material). These are then separated due to an electric field and the charges build up on electrodes, producing a measurable current. This enables single points in space to be identified. With many pixel hits, multiple points are constructed, enabling the trajectories of the particles to be determined.

Further out from the beam is the SCT, with four concentric barrel layers at $r = 299$ mm, 371 mm, 443 mm and 514 mm, as well as two end-caps that each comprise nine discs [74]. At these distances, very fine granularity is not required as the track density is lower, but more area needs to be covered. As such, the tracker consists of 6.3 million semiconductor strips of dimension 80 μm $\times$ 12 cm (in $r\phi \times Z$) giving a spatial resolution of 17 μm $\times$ 580 μm.

The outer section of the ID is the TRT, which covers the range 554 mm to 1082 mm in r for the barrel region, and also has two end-caps [75]. It consists of around 300,000 tubes called straws, which are 4 mm in width and up to 144 cm in length in the barrel. The straws are filled predominantly with xenon gas. In between the straws is a radiator material of multiple fibres, whereby charged particles crossing the material boundaries emit X-ray photons known as transition radiation. The probability of radiation is related to the relativistic γ factor, which can be expressed as $\gamma = E/m$. For a given energy, lower mass particles have a higher γ and

emit more X-rays, which enables pions and electrons to be distinguished. The X-rays travel into the straws and ionise the xenon gas. A potential difference applied across the straws leads to ions drifting towards the straw walls and electrons towards anodes placed at the straw centres. The current is measured (the magnitude related to the particle mass) and since each track can have up to 30 hits in the TRT, the particle trajectories can be recorded to a precision of 0.17 mm.

A Run 2 event showing the combination of pixel, SCT and TRT hits is shown in Figure 3.6.
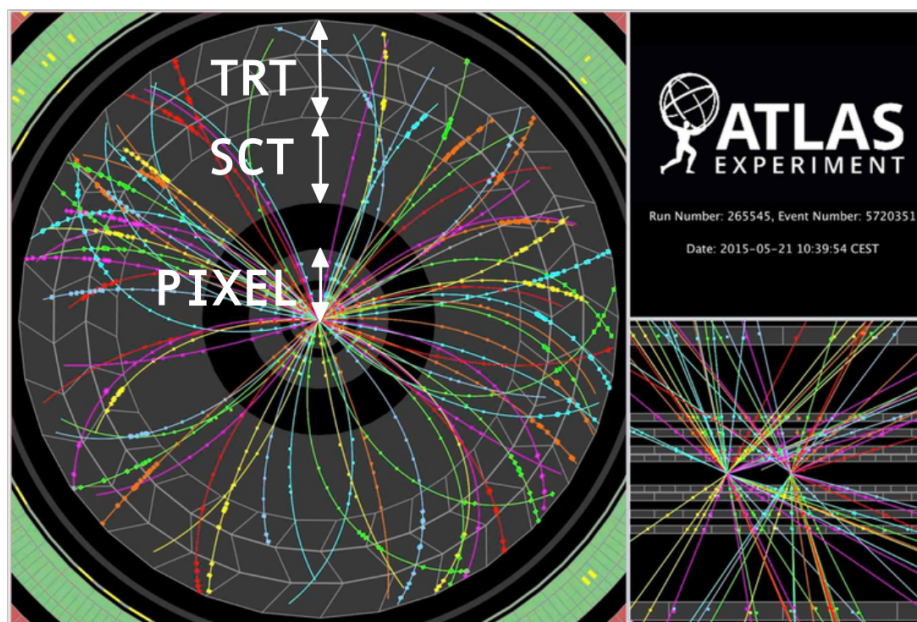
Fig. 3.6 Tracks of charged particles through the ID for a Run 2 event [76]. There are up to four hits in both the pixel and SCT, and multiple hits in the TRT.

3.4.2   The Electromagnetic and Hadronic Calorimeters

Wrapping around the ID are the electromagnetic and hadronic calorimeters. These subdetectors are used to determine the energies of charged and neutral particles. The electromagnetic calorimeter makes use of the electromagnetic interaction to measure electrons and photons, and the hadronic calorimeter uses both the strong and electromagnetic interaction to mea-

sure particles such as pions, protons and neutrons. The calorimeters are constructed from high-density absorber materials to cause the particles to emit radiation in a runaway manner (showering), as well as active materials that convert the showers into electrical signals, which are translated into particle energy. They also indirectly measure the missing transverse energy by summing the transverse momentum components of the known particles (see Equation 3.1).
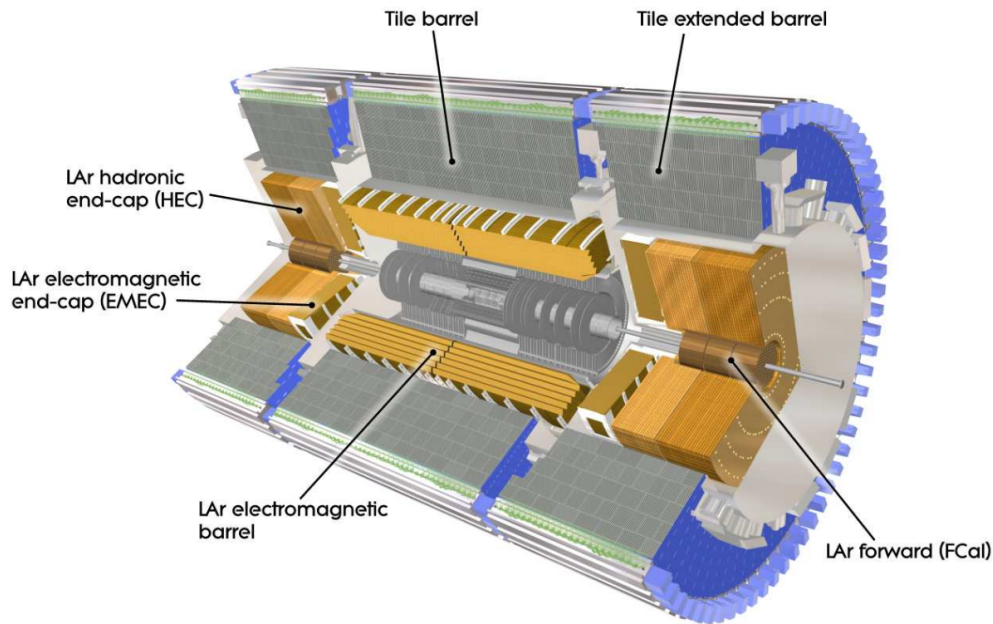
Fig. 3.7 The ATLAS calorimeter system [66]. The major components of the electromagnetic calorimeter and hadronic calorimeter are labelled.

The electromagnetic calorimeter comprises the barrel region ($|\eta| < 1.475$) and end-cap discs ($1.375 < |\eta| < 2.5$). It contains alternating layers of the absorber material, lead (Pb), and the active scintillating material, liquid argon (LAr). As a high-energy (> 1 GeV) electron passes through the calorimeter, it will undergo two main showering processes in the electromagnetic interaction: bremsstrahlung and pair production. Bremsstrahlung involves a change in speed or direction of the electron as it passes through the Pb (and LAr to an extent) due to the positive nuclei in the materials. This acceleration then causes photon emission. The emitted photons undergo pair production, spontaneously decaying into an

electron and positron, which then ionise the LAr and Pb. The LAr ionisation is converted into an electrical signal for the energy measurement. The electrons and positrons continue to shower by bremsstrahlung and pair production, leading to a runaway chain reaction as shown in Figure 3.8. The measure of distance used is the radiation length, X_0, where one radiation length corresponds to both the mean distance over which an electron loses all but $1/e$ of its energy by bremsstrahlung, and 7/9 of the mean free path for a photon undergoing pair production [17]. The total thickness of the EM calorimeter is greater than 22 X_0 in the barrel and greater than 24 X_0 in the end-caps. While all particles except neutrinos and neutral hadrons will interact with the electromagnetic calorimeter, electrons and photons will be completely absorbed and so their total energies can be determined from the sum of their electrical signals. Hadrons, muons, neutrinos and possibly BSM particles will escape further into the hadronic calorimeter.
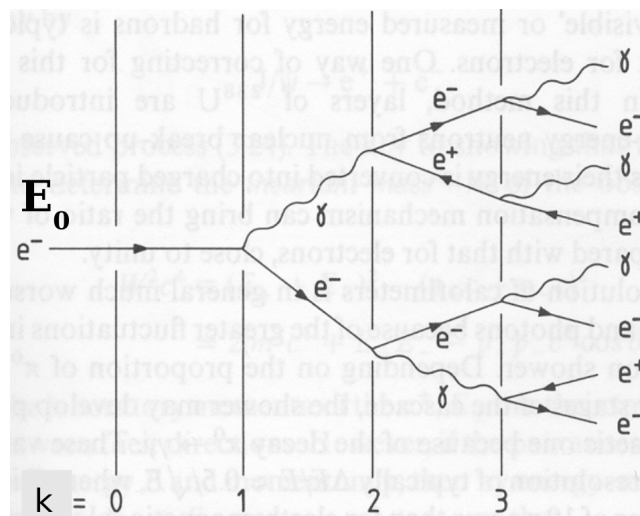
Fig. 3.8 A simplified schematic of the showering of an electron in a calorimeter [77]. The k value refers to the mean distance at which a doubling of the number of particles occurs and subsequently a halving of each particle's energy, E_0, the total energy of the electron. After a certain number of splits, the energies of the particles fall below a certain critical energy at which bremsstrahlung and pair production can no longer occur. The energy is then dissipated by ionisation and excitation.

The hadronic calorimeter surrounds the electromagnetic calorimeter and consists of three parts: the tile calorimeter, the LAr hadronic end-caps and the LAr forward calorimeters. The tile calorimeter has a central barrel ($|\eta| < 1.0$) and two extended barrels ($0.8 < |\eta| < 1.7$) that use steel as the absorber and plastic scintillator as the active material. The end-caps ($1.5 < |\eta| < 3.2$) each consist of two wheels of copper absorber and are located directly behind the electromagnetic calorimeter end-caps with which they share the same LAr cryostats. The forward calorimeters ($3.1 < |\eta| < 4.9$) are made from copper and tungsten absorbers, also sharing the same LAr system. The process of hadronic showering is more complicated than electromagnetic showering. An incoming hadron will hit a target nucleus in an inelastic collision through the strong interaction, generating a shower of secondary hadrons such as pions and kaons. π^0 hadrons that are generated decay to two photons, which themselves produce electromagnetic showers in the electromagnetic interaction. The other secondary hadrons cause further inelastic collisions and the chain reaction continues. Hadronic showers will tend to be much wider than electromagnetic showers owing to the large transverse momentum transfers in the nuclear interactions, whereas the electromagnetic shower width comes mainly from multiple scattering. Figure 3.9 shows an example of a hadronic shower. As opposed to radiation lengths for electromagnetic showers, nuclear interaction lengths, λ_I, are used to describe hadronic showers, which show the mean distance travelled by a hadron before undergoing an inelastic nuclear interaction. These are much longer than radiation lengths. For example, in lead an electron has a radiation length of 0.6 cm but a hadron has a typical interaction length of 17.6 cm [17]. The hadronic calorimeter stretches to lengths of greater than 11 λ_I at $\eta = 0$ to ensure almost all hadrons are absorbed in the material. In the LHC experiments, hadrons are identified through topological clustering of electromagnetic and hadronic calorimeter shower deposits (see Section 6.3.3), and are referred to as jets.
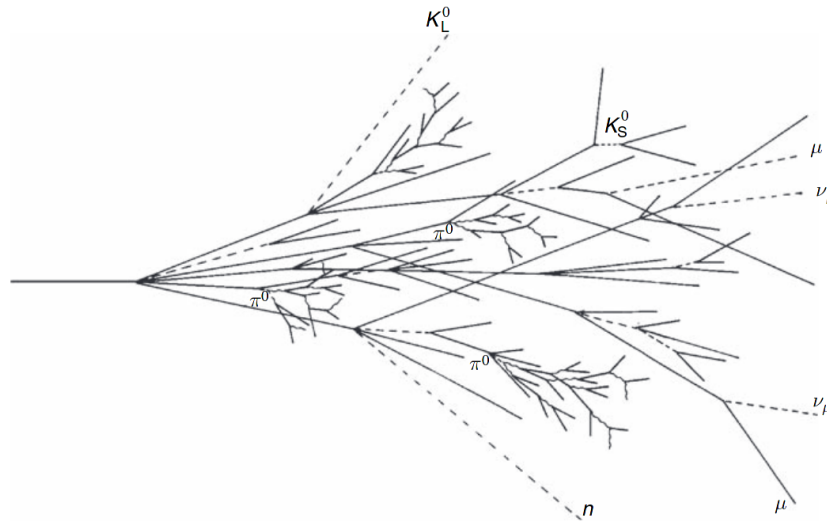
Fig. 3.9 The showering of a hadron in a calorimeter [78]. Secondary pions and kaons are produced in inelastic scattering, and neutral pions (such as towards the bottom of the image) initiate electromagnetic showers.

3.4.3 The Muon System and Toroid Magnets

The outer section of the ATLAS detector is composed of the muon system (MS) and toroid magnets (of strength around 1 T), both shown in Figure 3.10. In the barrel region ($|\eta| < 1.4$), muons are deflected by a large eight-coil central toroid surrounding the hadronic calorimeter, whereas in the end-cap regions ($1.6 < |\eta| < 2.7$) two smaller toroid magnets inserted into each end of the barrel toroid are used. For the intermediate region ($1.4 < |\eta| < 1.6$), a combination of the barrel and end-cap magnets provide the magnetic field. The toroid magnetic field lines wrap around the ϕ direction, unlike the Z direction of the solenoid magnet. This causes bending perpendicular to that from the solenoid. The amount of bending is used to determine the muon momentum. Tracks in the MS are matched with those in the ID to assist the identification.
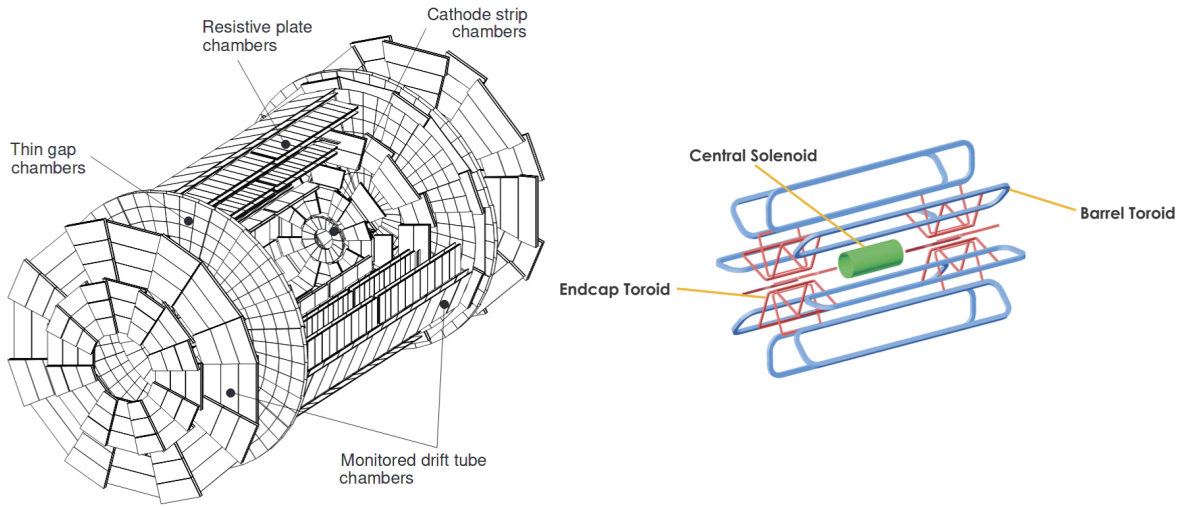
Fig. 3.10 Left: the ATLAS muon system showing its four component parts [79]. Right: the toroid magnets that bend the muons are shown in blue (barrel region) and red (end-caps) [67]. For comparison, the green magnet shows the central solenoid used by the inner detector.

The MS itself consists of four components: Monitored Drift Tubes (MDTs), Cathode Strip Chambers (CSCs), Resistive Plate Chambers (RPCs) and Thin Gap Chambers (TGCs).

The MDTs are arranged in three layers concentrically around the barrel ($r = 5$ m, 7.5 m and 10 m) and four layers vertically in the end-cap regions ($|Z| \simeq 7.4$ m, 10.8 m, 14 m and 21.5 m from the interaction point). They cover the majority of the $|\eta| < 2.7$ range, except for the innermost layer, where the coverage is $|\eta| < 2.0$. Each layer contains two pairs of three tubes mounted on each side of a support structure. There are a total of 354,000 tubes, each 3 cm in diameter and 0.85-6.5 m in length. The layout enables high-precision determinations of the Z and r coordinates in the barrel and end-caps, respectively, to resolutions of 80 μm averaged across the tubes. The tubes contain predominantly argon gas, which is ionised as the muons pass through it. The electrons drift to positive anode wires in the centres of the tubes, and the time taken for the drift in each tube is used to determine the position of the muon in the tube as it passed through, demonstrated in Figure 3.11.
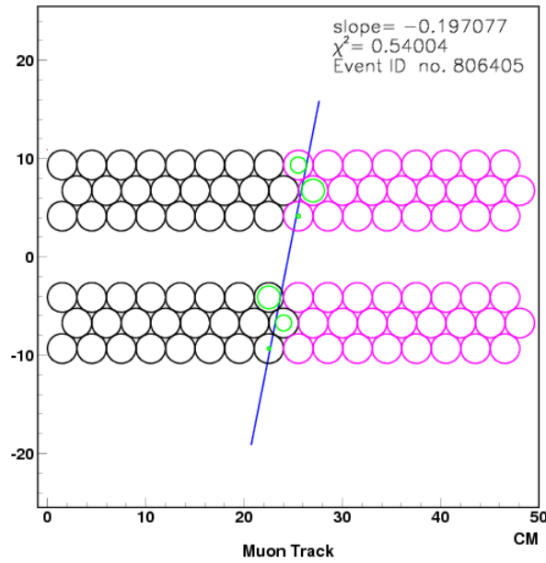
Fig. 3.11 A muon passing through the six tubes of an MDT layer [80]. The green circles show the points of ionisation in the tubes (gathered from the timing information), that together are used to build the muon track.

At $2.0 < |\eta| < 2.7$ in the innermost layer, the CSCs make up the second MS component. They again measure Z and r, whereby the cathode strips gather avalanche charges from the anode wires. There are 70,000 of these channels, each giving a resolution of 60 μm. These have greater granularity than the MDTs and are needed due to a higher rate of events close to the beam and to achieve good time resolution.

The other two components make up a dedicated triggering system for the MS: the RPCs in the $|\eta| < 1.05$ region making up 380,000 channels and the TGCs in the $1.05 < |\eta| < 2.7$ region comprising 440,000 channels. These ensure muons only above given p_T thresholds are selected. They also identify the bunch crossing from which a muon originated, and the coordinate orthogonal to that from the MDTs and CSCs (the ϕ direction, which is approximately parallel to the magnetic field lines). The two systems work with the same concept of gas ionisation and charge collection to find signals.

3.5   Particles Trajectories in the Detector

The ATLAS detector is designed to measure directly or indirectly particles above given thresholds. Figure 3.12 shows examples of particle paths through a cross-section segment of the detector, travelling radially outward from the centre, which are described below.
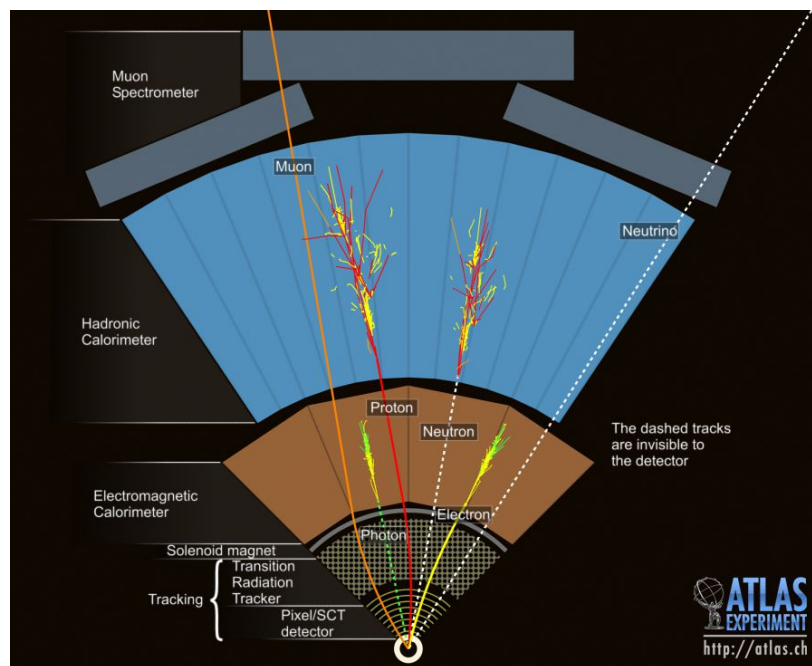
Fig. 3.12 A cross-section of the ATLAS detector, showing typical paths of particles produced in the collisions [81].

- Electrons and positrons travel through the ID with multiple hits, being bent by the solenoid magnet. They pass into the electromagnetic calorimeter, where all their energy is deposited.

- Photons do not leave any trace in the ID (unless they pair produce) and are not bent by the solenoid. However, they deposit all their energy in the electromagnetic calorimeter.

- Protons and other charged hadrons give hits in the ID (being bent by the solenoid as they do so), pass through into the electromagnetic calorimeter (with some showering)

and go on into the hadronic calorimeter, where the remaining and majority of the energy is deposited.

- Neutrons and other neutral hadrons pass straight through the ID without hits and without being bent by the solenoid. They also will not shower in the electromagnetic calorimeter since the positive nuclei in the detector will not accelerate the neutral hadrons and cause bremsstrahlung emission. However, they will cause showering in the hadronic calorimeter, depositing all of their energy.

- Muons and antimuons give hits in the ID (being bent by the solenoid), pass through the electromagnetic and hadronic calorimeters with little interaction (since they are minimally ionising) and on into the muon system, where they give hits and are bent by the toroid magnets.

- Tau and antitau leptons decay in the beampipe (35% of the time to leptons, 65% of the time to hadrons, of which most are pions [17]). The decay products then pass through the subdetectors. Leptonic tau decay products cannot be distinguished from leptons produced directly in collisions, but hadronic tau decays can be distinguished from directly produced hadrons, allowing tau reconstruction.

- Neutrinos and some BSM particles will not interact with the subdetectors, passing straight through the experiment. However, the E_T^{miss} measured from other decay products as in Equation 3.1 can be used to identify their presence.

Triggering and Optimisation of the Level-1 Calorimeter Trigger

4.1 Motivation for Triggering

During Run 2, the LHC instantaneous luminosity, $\mathcal{L}$, was expected to increase beyond 2×10^{34} cm^{-2} s^{-1}. As described in Section 2.2, the average bunch crossing rate was nearly 30 MHz, and the average pile-up of Run 2 was 33.7 interactions per crossing (see Figure 3.4). This means there were around 1 billion collisions per second (1 GHz) leading to roughly 1 petabyte of data flow per second [82]. It is not possible to store such vast quantities of data to disk, and so a trigger system is used in ATLAS that brings the average recording rate to 1 kHz whilst keeping the most important events. It is made up of the Level-1 Trigger (L1 Trigger) and High-Level Trigger (HLT). Figure 4.1 shows the data flow from the detector, through the individual parts of the triggering systems and onto Tier 0, the CERN data centre, where it is distributed to computers for storage around the globe.

Fig. 4.1 The Run 2 triggering system at ATLAS [83]. The top left section encompasses the L1 trigger, which is made up of L1Calo, L1Muon, L1Topo and the CTP, which takes information from the other systems to make decisions on whether to keep the event. These are then passed onto the HLT.

4.2   The Level-1 and High-Level Triggers

The L1 Trigger consists of custom-made electronics and gathers reduced-granularity data from both the electromagnetic and hadronic calorimeters, as well as the muon system. It takes the 30 MHz bunch crossing rate down to an equivalent of around 100 kHz, making decisions in less than 2.5 μs. The following description summarises the information in References [66, 83, 84].

One section of the trigger is the Level-1 Calorimeter Trigger (L1Calo) [85], which aims to select out high transverse energy (E_T) electrons, photons, tau leptons decaying to hadrons,

jets, and events with large total E_T or E_T^{miss}. L1Calo is described in more detail in Section 4.3. Another section is the Level-1 Muon Trigger (L1Muon) [86], which searches for high p_T muons from the RPCs and TGCs of the muon system. The data from the two trigger subcomponents is then passed on to the Central Trigger Processor (CTP). The CTP is programmed with a series of selection requirements (known as the trigger menu [87]), where if the data pass the menu thresholds, the Level-1 accept criteria is met, and the event is passed on to the HLT. A fourth component in the system is the Level-1 Topological Trigger (L1Topo) [88], which performs selections based on the associations of kinematic and geometric variables of trigger objects received from L1Calo and L1Muon. However, this was used minimally during Run 2, and served mostly for testing.

The HLT is a software-based system, made up of a large farm of 40,000 processing cores, taking the L1 Trigger rate of 100 kHz down to around 1 kHz, with decisions taken in 300 ms. It uses the full granularity and precision of the calorimeter and muon system measurements, as well as data from the inner detector. Therefore, particle identification can be achieved (such as distinguishing electrons from photons), event building is initiated, and more stringent threshold requirements can be set. The thresholds are augmented into selection algorithms called chains. There are around 2,500 separate chains in the HLT, some of which have very specific requirements on the events and others have more general conditions that can be used in numerous analyses. The desired chains are specified in the trigger menu in combination with the Level-1 requirements. The events that pass any of the chains are saved and distributed to Tier 0.

4.3   The Level-1 Calorimeter Trigger

As described in Reference [85], L1Calo combines calorimeter cells into approximately 7,200 coarse granularity structures called trigger towers. There are separate sets of towers for the

electromagnetic and hadronic calorimeters. These cover typically 0.1×0.1 in $\Delta\eta \times \Delta\phi$ (the spatial area in the pseudorapidity and azimuthal angle coordinates). However, at larger $|\eta|$ such as the end-caps and forward calorimeters, the towers become even more coarse, as shown in Figure 4.2.
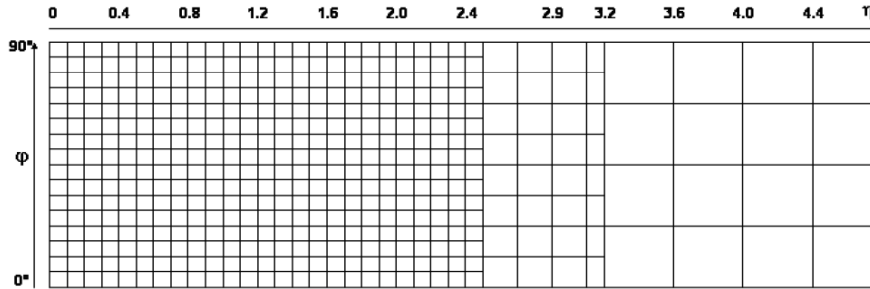
Fig. 4.2 Trigger tower granularity across η (*x*-axis) and ϕ (*y*-axis) for $\eta > 0$ in one ϕ quadrant [85]. At extreme η, each tower covers a much larger area. The setup is identical for the electromagnetic and hadronic calorimeters.

Figure 4.3 shows a zoomed in schematic of the data flow through L1Calo. Analogue information from the trigger towers is passed on to the L1Calo pre-processor, which digitises it and determines the bunch crossing from which any high E_T deposits came. A look-up table is also used for tasks such as E_T calibration and noise suppression. The signals are then sent in parallel to the Cluster Processor (CP) and Jet Energy Processor (JEP), which contain algorithms to determine whether the event is of interest. The CP searches for electron/photon candidates and tau leptons decaying to hadrons, while the JEP identifies jets and sums of total and missing E_T. Both processors use a sliding-window method to search for the objects. For the CP, the method generates a 4×4 window of trigger towers in each calorimeter, covering the same $\Delta\eta \times \Delta\phi$ area in both. The window is moved in steps of one trigger tower in both η and ϕ and searches for objects. An explanation of how the CP searches for regions of interest in the windows is described in the following sections together with optimisation of the selection thresholds.
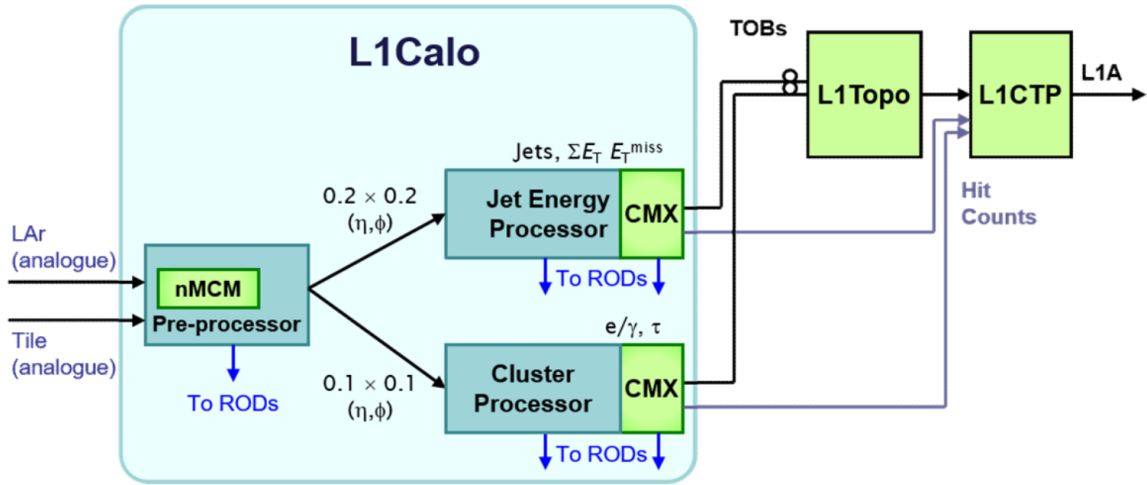
Fig. 4.3 A schematic of L1Calo showing data transfer between the pre-processor, the CP and JEP algorithmic processors, before being sent to the decision-making CTP [89].

4.4 The Cluster Processor Algorithms

Figure 4.4 shows a 4×4 window of trigger towers in the two calorimeters used by the CP, where two algorithms determine whether threshold criteria are met. The electron/photon (e/γ) and tau (τ) algorithm components are described in detail below, summarised from Reference [90].

- The four central towers in the electromagnetic calorimeter window (green squares in Figure 4.4) make up the electromagnetic (EM) inner core. There are four possible 1×2 or 2×1 configurations in the core called EM clusters. The E_T values of the two towers making up each cluster are summed. The largest sum is defined as the EM cluster energy.

- The twelve towers (yellow squares) around the EM core make up the EM isolation ring. The total E_T in these is summed to give the EM isolation energy. Since electromagnetic showers are narrower than hadron showers (see Section 3.4), most of their energy will be deposited in the central EM cluster, with little isolation energy. This allows good
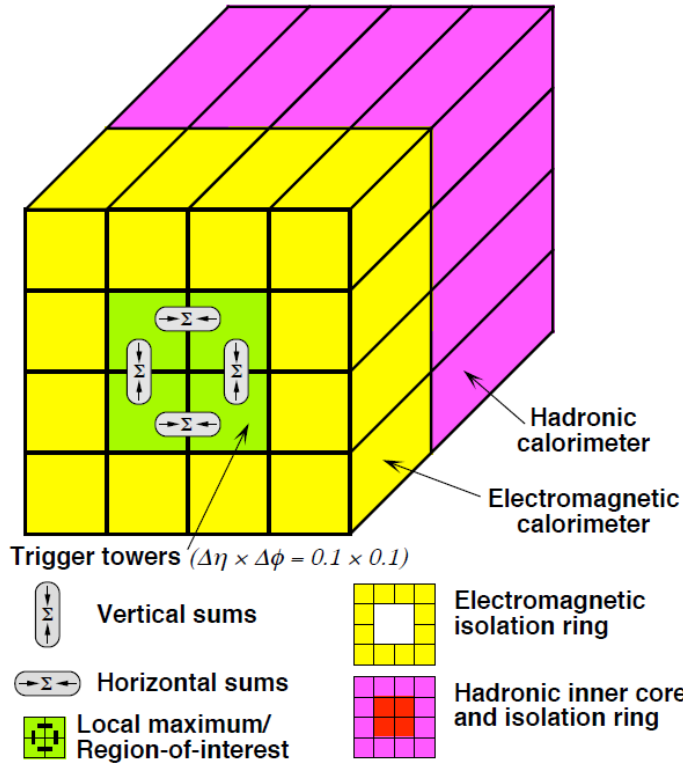
Fig. 4.4 A single 4×4 window of electromagnetic (front) and hadronic (back) trigger towers from the sliding-window method in the CP, where energies are compared with threshold criteria for event selection [90].

discrimination from tau leptons and jets, which have more energy deposited in the isolation zone.

- The four central towers of the hadronic calorimeter window (red squares) are the hadronic inner core. The 2×2 trigger tower sum of E_T is summed up to give the hadronic core energy (used in the e/γ algorithm). Electron/photon candidates will not pass into the hadronic calorimeter, so the core energy deposition should be zero apart from a small degree of irreducible noise, whereas jet/tau candidates will deposit energy. This allows further discrimination between the two types of candidates. The hadronic inner core E_T is added to the E_T of each of the four EM clusters to give four hadronic clusters. The largest of the four is referred to as the hadronic cluster energy (used in the τ algorithm).

- The twelve towers (pink squares) around the hadronic core make up the hadronic isolation ring, where again the E_T in these is summed to give the hadronic isolation energy. However, this is not used for trigger decisions as it has little discriminating power.

- The largest EM cluster and hadronic inner core E_T are summed together to make a cluster Region of Interest (RoI). As the window slides across η and ϕ, only the cluster RoI with the largest local maximum in E_T is considered. This avoids multiple counting of the same object that would satisfy threshold requirements in one or more adjacent windows.

For the e/γ algorithm (studied in this thesis), thresholds in the EM isolation energy against EM cluster energy space and the hadronic core energy against EM cluster energy space must be satisfied. The hadronic thresholds are tight to minimise tau and jet selection. There are two preset isolation criteria used in triggering: 22VHI and 24VHI. The number refers to the nominal cluster energy cut-off in GeV (24VHI being a tighter cut for higher luminosity), the "V" the fact that the cut-off has a pseudorapidity dependence (between 19.0 and 24.0 GeV for 22VHI, and 21.0 and 26.0 GeV for 24VHI), the "H" meaning that the hadronic core energy is required to be less than or equal to a variable threshold (around 1 GeV), and the "I" that isolation cuts have been applied. The 22VHI and 24VHI thresholds used in 2016 Run 2 data-taking (henceforth labelled "original cuts") are shown in Figure 4.5.

The flat lines (EMCutMin and HadCutMin) can be modified in the y direction, and the vertical line, CutMax (common to both isolation criteria) in the x direction. The sloped lines have the form:

$$y = \text{EMCutSlope} \times x + \text{EMCutOff} \quad \text{(electromagnetic isolation)}$$

$$y = \text{HadCutSlope} \times x + \text{HadCutOff} \quad \text{(hadronic isolation)}$$

$$(4.1)$$
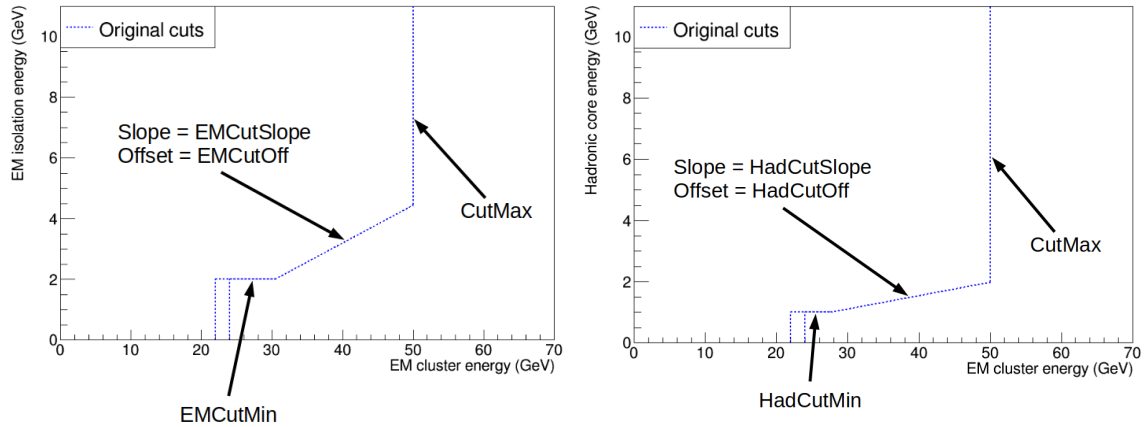
Fig. 4.5 The parameters of the e/γ algorithm (labelled), corresponding to the original cuts. Left: EM isolation energy against EM cluster energy. Right: hadronic core energy against EM cluster energy. The two blue vertical lines on the bottom left of each plot refer to the 22VHI and 24VHI cluster energy thresholds.

with the gradients and y-intercepts free parameters. The values of the original cut parameters are shown in Table 4.1. The algorithm works by selecting RoIs falling below and to the right of the lines in Figure 4.5, where the acceptance is proportional to the L1Calo rate. The CutMax parameter is present since any high-energy RoI is of interest regardless of the isolation energy.

EMCutMin (GeV)	EMCutSlope	EMCutOff (GeV)	CutMax (GeV)
2.0	1.0/8.0	-1.8	50.0

HadCutMin (GeV)	HadCutSlope	HadCutOff (GeV)	CutMax (GeV)
1.0	1.0/23.0	-0.2	50.0

Table 4.1 Summary of the original cuts for the electromagnetic (top) and hadronic (bottom) isolation criteria. These are common to both 22VHI and 24VHI.

The setup is similar for the τ algorithm (not studied here) but the hadronic cluster energy is used instead of the hadronic core energy for the hadronic calorimeter thresholds.

4.5 Optimising the e/γ Thresholds for Higher Luminosity

For 2017-2018 data-taking in Run 2, new e/γ algorithm backup thresholds were determined to replace the original 22VHI and 24VHI configurations, should $\mathcal{L}$ increase much beyond 2×10^{34} cm^{-2} s^{-1} and give a L1 acceptance rate greater than 100 kHz. The aim was to reduce the rate whilst maintaining similar efficiency. The values of the four parameters in the electromagnetic calorimeter were investigated, leaving the parameters in the hadronic calorimeter constant as in Table 4.1. Three sets of new parameters (working points) for both 22VHI and 24VHI were established of varying stringency: loose, medium and tight cuts. These correspond to increasing background rejection and hence decreasing recording rates of the trigger compared with the original cuts. Efficiency tests were undertaken on the working points to determine their effect on signal events. The working point with the best balance between background rejection and signal extraction was kept. The ROOT [91] framework was used to perform the analysis.

4.5.1 Rate Reduction from Background Events

Background events to the e/γ algorithm are predominantly jets that are reconstructed as electron/photon objects. To see the effect of thresholds on background rejection, an enhanced bias (EB) dataset was used. EB data are taken in LHC runs where events passing loose L1 thresholds are written out without requiring the HLT to accept them, which would otherwise bias the study. They act as a good background set since most of the saved events are jets. The EB data used for the study are shown as a function of EM isolation against EM cluster energy in Figure 4.6. The original 2016 cuts are overlaid on the figure as black lines. The data show all RoIs in the events, where one event can have more than one RoI. RoI energies come in discrete digital values to a precision of 0.5 GeV. Zero RoIs are seen in the 0.5-1.0 GeV bins

of the *x*- and *y*-axes due to noise cuts. Any trigger tower with an E_T less than 1.0 GeV is set to 0.0 GeV and so the E_T sum in the EM cluster or isolation ring can never be 0.5-1.0 GeV.
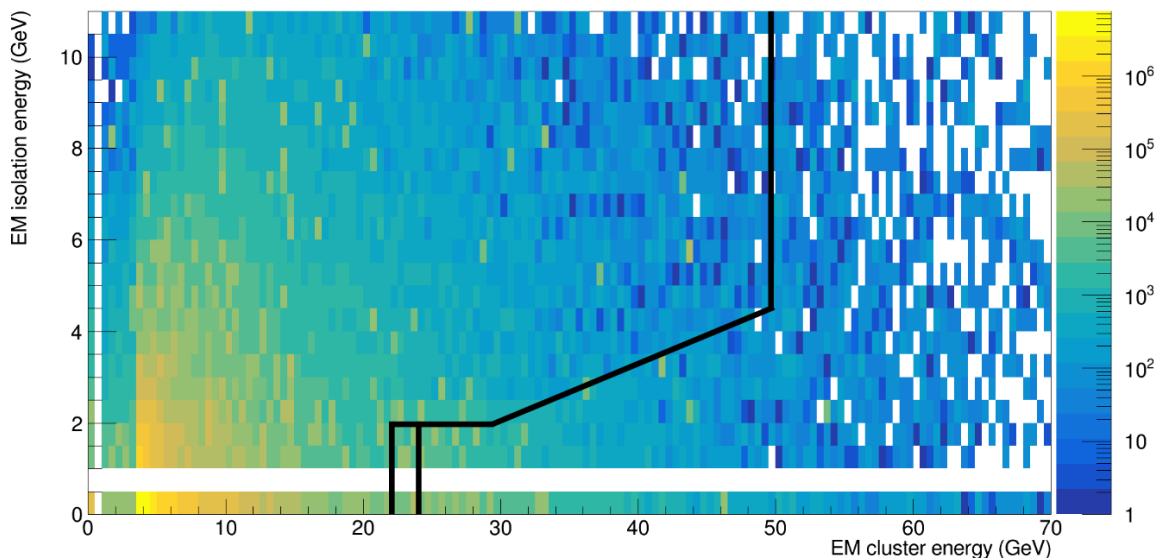
Fig. 4.6 The EM isolation energy against EM cluster energy for the RoIs in EB data, with the original 22VHI and 24VHI cuts shown by the black lines. RoIs falling below and to the right of the lines are kept by the trigger. The number of RoIs per bin is given in the colour scale.

Preliminary tests were undertaken with a smaller subset of the EB data. As a first pass to see the maximum possible rate reduction, the sloped EM line of Figure 4.5 was removed and the *x* extent of EMCutMin extended up to CutMax, where CutMax was kept constant at 50.0 GeV. Since the trigger tower energies have a precision of 0.5 GeV, EMCutMin was tested at 2.0, 1.5 and 1.0 GeV. The effect on the rate is shown in Figure 4.7. The maximum rate reduction possible is almost 25% for 22VHI and 24VHI. Since this does not include the sloped line (needed to improve the efficiency), the rate will go up again with this addition.
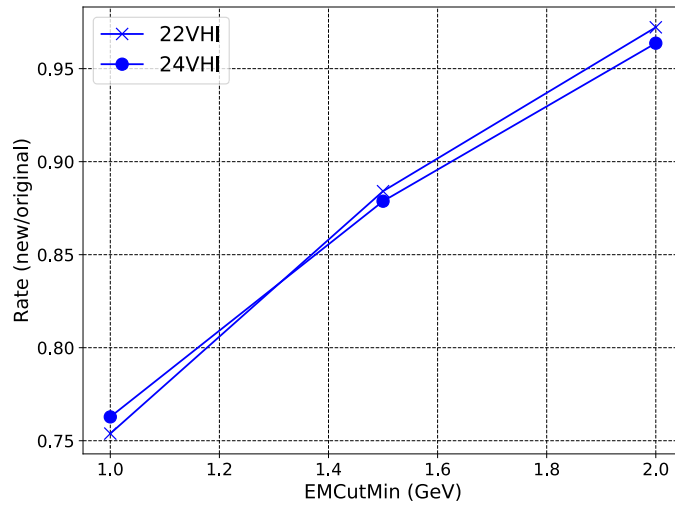
Fig. 4.7 The relative rate of new cuts to original cuts as a function of EMCutMin for both 22VHI and 24VHI.

With the sloped line added back in, EMCutSlope and EMCutOff were varied individually (keeping the other constant at the original cut value). EMCutMin was lowered to 1.0 GeV and CutMax was kept constant at 50.0 GeV. Figure 4.8 shows how the rate changes with these parameters.
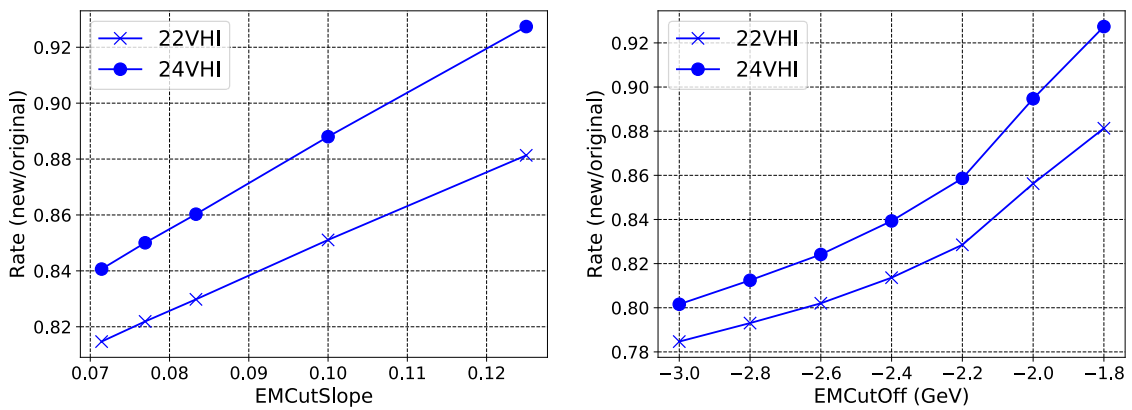
Fig. 4.8 The relative rate of new cuts to original cuts as a function of EMCutSlope (left) and EMCutOff (right) for both 22VHI and 24VHI.

As expected, the rate reduction increases as EMCutSlope and EMCutOff are both decreased. The rate change is linear for EMCutSlope and curved for EMCutOff. Below -2.6 GeV

the rate change for EMCutOff is small. It was decided to keep EMCutSlope constant at 1.0/8.0 (0.125) for the three working points. The CutMax variable was also kept the same at 50.0 GeV to ensure high-energy signal events were saved. The working points were therefore defined by different EMCutMin and EMCutOff values where the rate was reduced by 5-7% (loose), 10-15% (medium) and 18-20% (tight) – the ranges arising from 22VHI and 24VHI thresholds. The full EB dataset was subsequently used to verify the rates, and the cut values and rates compared with the original cuts are shown in Table 4.2. Efficiency tests were later performed on the working points.

Working point	EMCutMin (GeV)	EMCutOff (GeV)	Rate ratio (new/original)	
			22VHI	24VHI
Original	2.0	-1.8	1.000	1.000
Loose	1.5	-1.8	0.937	0.951
Medium	1.0	-2.0	0.853	0.892
Tight	1.0	-2.6	0.799	0.821

Table 4.2 The original cut and three working point relative rates for the full EB dataset. Binomial errors of order 10^{-5} are not shown. EMCutSlope and CutMax are the same for all cases at 1.0/8.0 and 50.0 GeV, respectively.

4.5.2 Efficiency Determination from Signal Events

To see the effect of the working point parameters on signal events in an efficiency estimate, an Electron-Gamma Z (EGZ) dataset was used. EGZ data contain pre-selected events: predominantly $Z \rightarrow e^+ e^-$ decays, to provide a good selection of typical electrons that are important in many analyses. The EM isolation against cluster energies of the RoIs from the events are shown in Figure 4.9. For the particles to be identified and reconstructed, they needed to pass the HLT. Typically one (but possibly both) of the two electrons in the dataset will have triggered the event. An efficiency measurement needs to establish whether an RoI

would pass just the L1Calo e/γ thresholds without a HLT requirement. Therefore, seeing whether the RoIs in the figure pass the parameter cuts (as for the rate determination) would give a biased estimate.
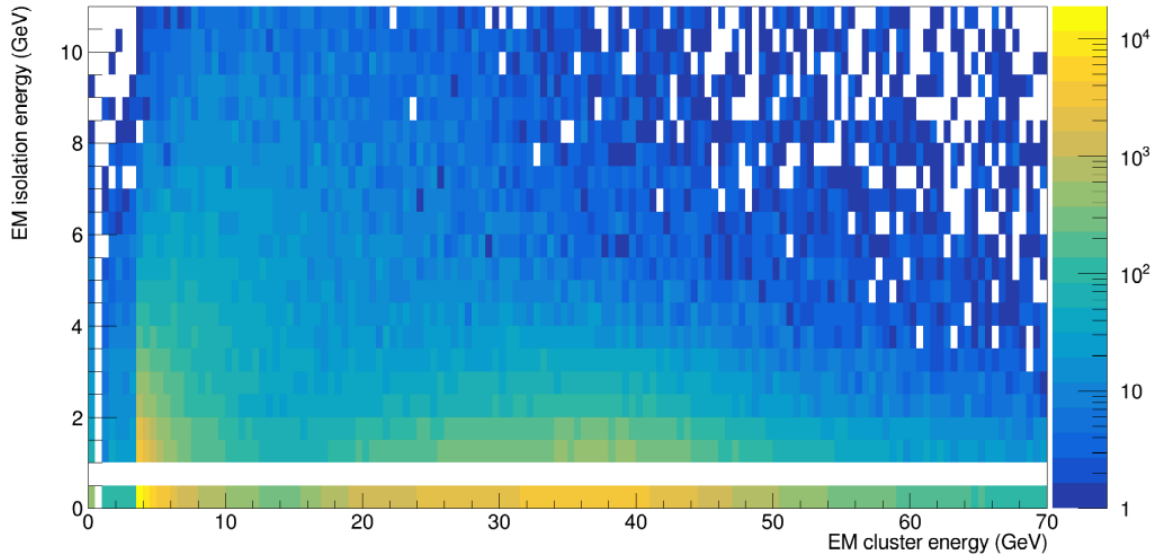
Fig. 4.9 The EM isolation energy against EM cluster energy for the RoIs in EGZ data.

To remove the bias, a tag-and-probe method was employed. This looks for an electron or positron in the Z decay that triggered the event (known as the tag), having passed both the L1 trigger and the HLT. It then determines if the other lepton (known as the probe) would have passed the L1Calo e/γ algorithm, which goes into the efficiency calculation. The reconstructed events were required to meet the following criteria to be used in the efficiency measurement:

- Two oppositely charged electrons of tight identification quality [92].
- Electron $p_T \geq 20$ GeV to further improve the quality.
- Exclude the region between the electromagnetic calorimeter barrel and end-caps $(1.37 < |\eta| < 1.52)$ where reconstruction is poor.
- An invariant mass, M_{inv}, in the Z window of $80 \leq M_{\mathrm{inv}} \leq 100$ GeV.

Having selected the electron pairs, the tag-and-probe method worked as follows:

1. Check if the first reconstructed electron in the pair matches an RoI in L1Calo. A match requires $\Delta R = \sqrt{(\Delta\eta)^2 + (\Delta\phi)^2} \leq 0.15$, where $\Delta\eta$ and $\Delta\phi$ are the differences in pseudorapidity and azimuthal angle between the electron and RoI.

2. Check if this electron passes the HLT.

3. If both of these criteria are met, then this electron is a tag and would have triggered the event. The other reconstructed electron is a candidate probe.

4. Check if the second reconstructed electron is a tag and if so, the first electron in the pair is a candidate probe.

5. If both the first and second electron in a pair pass the tag criteria, use a random number generator to select one electron as the tag and the other as the probe.

6. See if the probe matches an RoI and also passes the e/γ thresholds. If so, count the electron as a passed probe.

7. The ratio of passed probes to all probes is the efficiency.

The efficiencies were determined in differential bins of E_T, average pile-up (average number of interactions per bunch crossing, $\langle\mu\rangle$), and inclusively across all the data. The 22VHI and 24VHI E_T distributions, known as turn-on curves, for the original cuts and working points are shown in Figure 4.10. Far below the cluster energy cut-offs, no electrons will be flagged due to the trigger requirement (giving efficiencies of 0), and far above, electrons should pass the thresholds (giving efficiencies of 1). At around 22 and 24 GeV, there is a sharp rise in efficiency. The rise is not a vertical line due to the more precise reconstructed electron energies being smeared about their cluster cut-off energies from the trigger energy resolution, and the pseudorapidity dependence of the cut-off energies. Tighter e/γ algorithm thresholds also affect the convergence to 1.
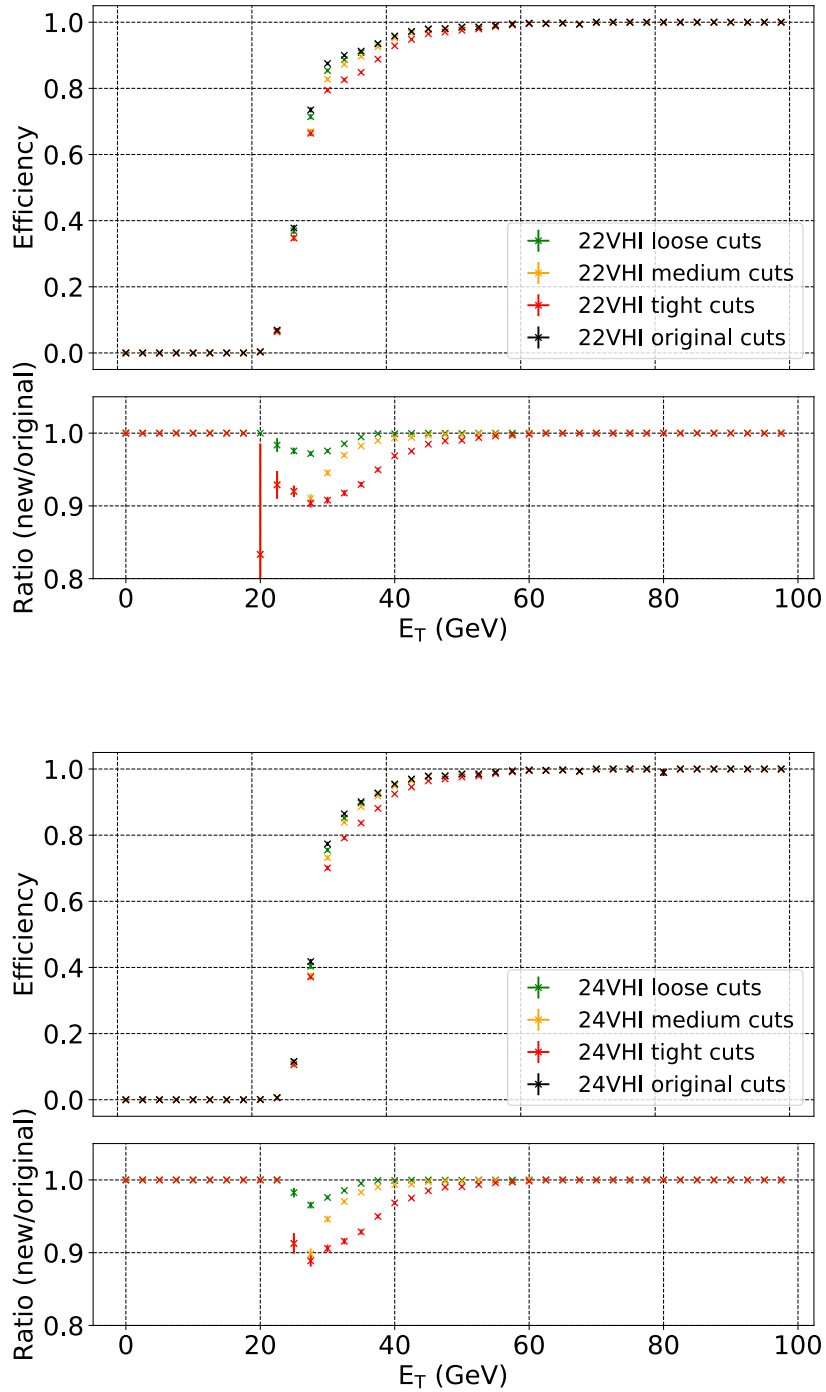
Fig. 4.10 Efficiency as a function of reconstructed electron E_T (turn-on curves) for the original cuts and three working points. Upper plot: 22VHI trigger cuts. Lower plot: 24VHI trigger cuts. The errors in efficiency are binomial, $\sigma_{\text{eff}} = \sqrt{\varepsilon(1-\varepsilon)/n}$, where ε is the efficiency and n is the number of probes passing the original cuts.

From the figures, it can be seen that the red points (tight thresholds) lie quite far below the black points (original cuts). However, the yellow points (for medium thresholds) are much closer so there is not much loss in efficiency. Small undulations such as at 81.25 GeV for 24VHI are present. These are due to rare cases where the ΔR matching between a reconstructed electron and RoI is ≤ 0.15 but the measured E_T of the RoI is small (so does not pass the isolation cuts) and the reconstructed electron E_T is large.

The efficiencies as a function of $\langle \mu \rangle$ are shown in Figure 4.11. The E_T of the reconstructed electron was required to be greater than 27 GeV (29 GeV) for 22VHI (24VHI) to ensure only the plateau of the turn-on curves was considered, which is the usual case for physics analyses.
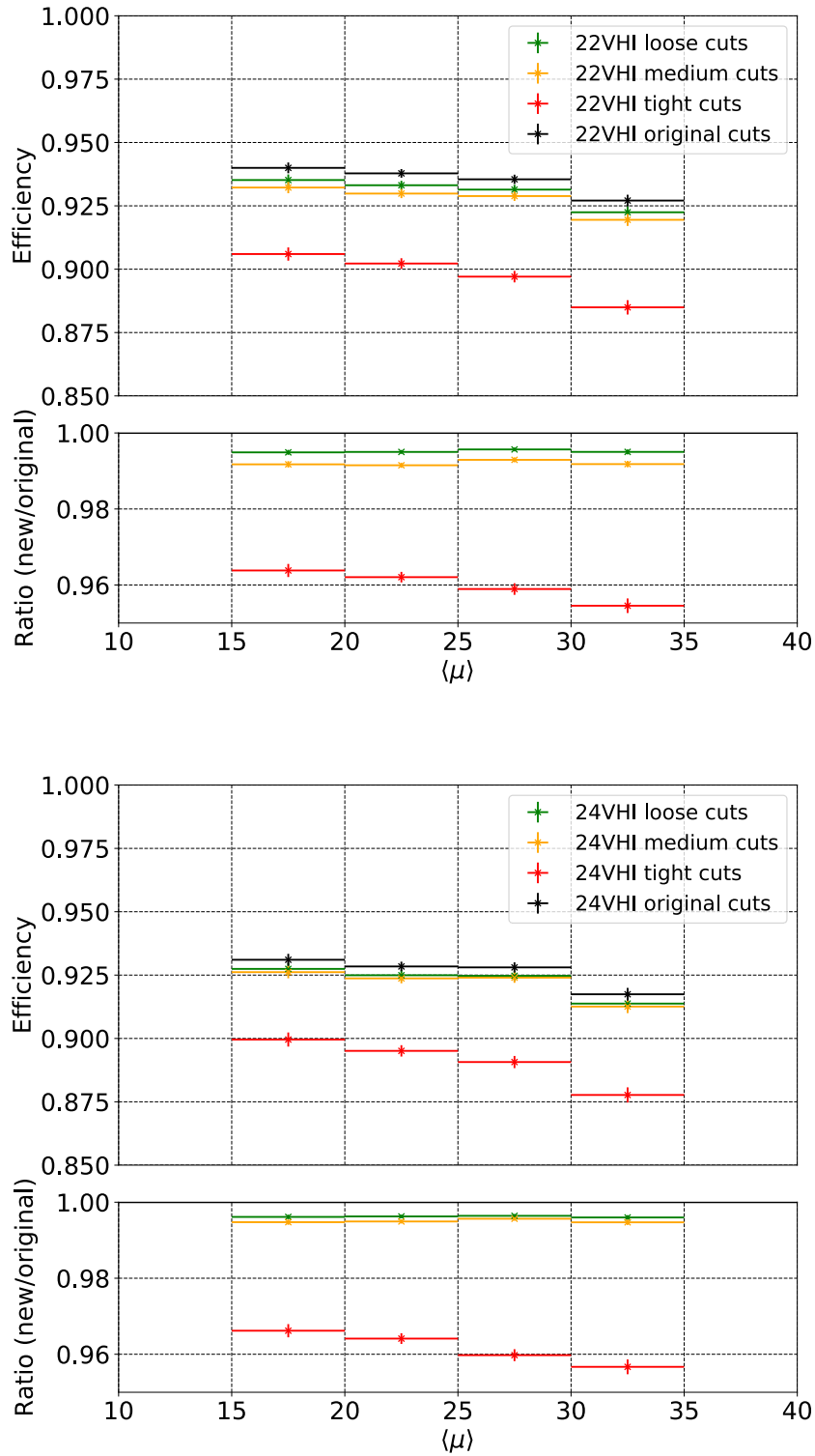
Fig. 4.11 Efficiency as a function of $\langle\mu\rangle$ for the original cuts and three working points. Upper plot: 22VHI ($E_T > 27$ GeV). Lower plot: 24VHI ($E_T > 29$ GeV). The errors are binomial.

As pile-up increases, the efficiency decreases for all cases, which could have an impact on higher luminosity data taking. This is worst for the tight cuts (red), where the efficiency drops by 2.1% (2.2%) between the 15-20 and 30-35 $\langle \mu \rangle$ bin for 22VHI (24VHI). This is better for the medium cuts with a drop of 1.3% (1.4%) for 22VHI (24VHI). Looking at the ratios of the working points to the original cuts, the loose and medium cuts stay rather flat, though the tight cuts show a downward trend.

Inclusive efficiencies compared with the original cuts are shown in Table 4.3 for both 22VHI ($E_T > 27$ GeV) and 24VHI ($E_T > 29$ GeV). The tight cuts have the most profound effect in the efficiency whereas the loose and medium cuts have a modest effect.

Working point	EMCutMin (GeV)	EMCutOff (GeV)	Efficiency ratio (new/original)	
			22VHI	24VHI
Original	2.0	-1.8	1.000	1.000
Loose	1.5	-1.8	0.995	0.996
Medium	1.0	-2.0	0.985	0.988
Tight	1.0	-2.6	0.960	0.962

Table 4.3 The original cut and three working point relative efficiencies for the EGZ dataset. Binomial errors of order 10^{-4} are not shown. EMCutSlope and CutMax are the same for all cases at 1.0/8.0 and 50.0 GeV, respectively. For 22VHI (24VHI), a cut of $E_T > 27$ GeV ($E_T > 29$ GeV) is present.

4.6   Results and Conclusions

From the three working points, it was established that the medium cuts gave a good rate reduction compared with the original cuts (14.7% for 22VHI and 10.8% for 24VHI). With tag-and-probe measurements, the efficiency was affected by only a small amount (1.5% for

22VHI and 1.2% for 24VHI) and the distributions with E_T and $\langle\mu\rangle$ are similar to those of the original cuts. A summary of the medium cuts is shown in Table 4.4 with their distributions for the isolation and cluster energies in Figure 4.12. The CutMax, EMCutSlope and hadronic parameters were kept the same as for the original cuts.

EMCutMin (GeV)	EMCutSlope	EMCutOff (GeV)	CutMax (GeV)
1.0	1.0/8.0	-2.0	50.0

HadCutMin (GeV)	HadCutSlope	HadCutOff (GeV)	CutMax (GeV)
1.0	1.0/23.0	-0.2	50.0

Table 4.4 Summary of the medium working point cuts that give the best balance between rate reduction and signal loss. The EM cuts (top) were modified but the hadronic cuts (bottom) kept the same. The cuts are common to both 22VHI and 24VHI.
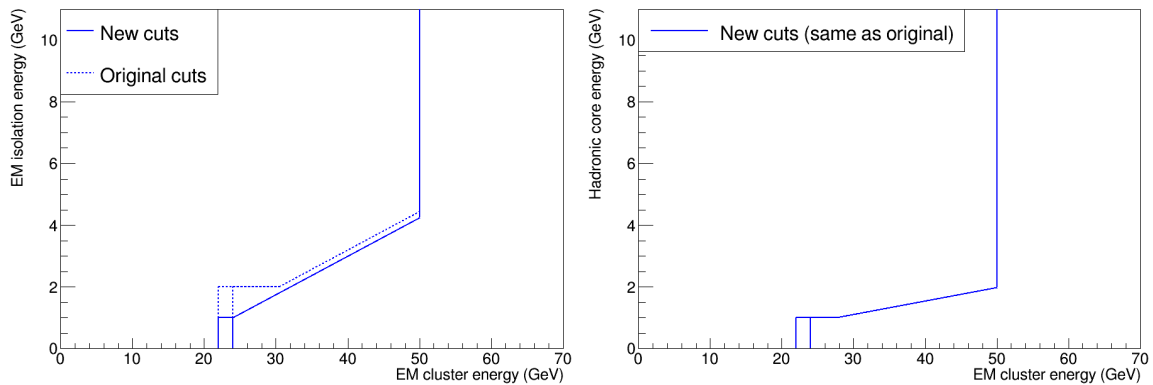
Fig. 4.12 The new (solid lines) and original (dotted lines) cuts of the e/γ algorithm. Left: EM isolation energy against EM cluster energy. Right: hadronic core energy against EM cluster energy. The format is the same as in Figure 4.5.

The new 24VHI thresholds were placed in the trigger menu, referred to as 24VHIM, where the "M" stands for medium cuts. 22VHIM was not invoked since the original 22VHI and 24VHI cuts together with the 24VHIM cuts were sufficient to cover the expected luminosity.

The 24VHIM efficiency measurements were repeated by the L1Calo collaboration with the full 2016 ATLAS dataset used for analyses [93]. The E_T and $\langle \mu \rangle$ distributions are shown in Figure 4.13. Even with larger pile-up, the medium cuts still perform well compared with the original cuts. For the remainder of Run 2 data-taking, the LHC luminosity did not reach high enough values to require 24VHIM, but it was available as a backup in case circumstances changed. It could also be required in Run 3.
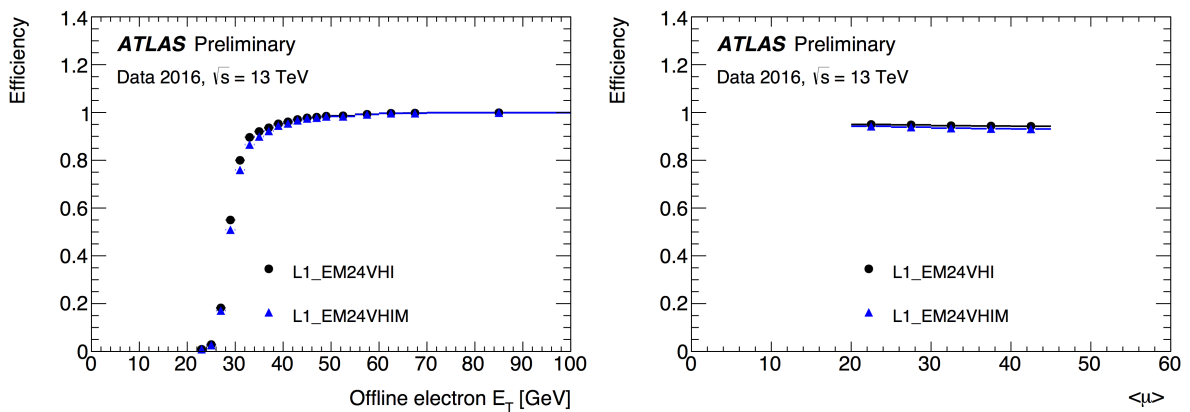
Fig. 4.13 Efficiency distributions for the full 2016 ATLAS dataset produced by the L1Calo collaboration comparing the new 24VHIM cuts (blue) with the original 24VHI cuts (black) [93]. Left: efficiency turn-on curve as a function of E_T. Right: efficiency as a function of $\langle \mu \rangle$.

Charge Asymmetry in Top Quark Pair Production

5.1 The Top Quark

Numerous measurements of top quark properties have been and are currently being determined in accelerator experiments. Good theoretical descriptions of the production and decay processes of the top quark (introduced in Sections 5.2 and 5.3) are important to understand and make comparisons with the collision data. The top quark has a very short lifetime, τ, of order 10^{-25} s due to its large width, Γ, of $1.42^{+0.19}_{-0.15}$ GeV [17][1]. This means it does not have time to bind with other quarks (it does not hadronise, which takes of order 10^{-23} s [94]) and so quantum mechanical information will be propagated to its decay products. It is therefore possible to study the top quark's fundamental properties.

---

[1]Here the conversion $\tau = \hbar/\Gamma$ is used, where $\hbar$ is the reduced Planck constant.

5.2 $t\bar{t}$ Production

Top quarks can be produced in association with an antitop quark[2] (known as $t\bar{t}$ production) or with other particles (single top production). In this thesis, $t\bar{t}$ production is the process under study. It occurs through quark-antiquark ($q\bar{q}$) annihilation, gluon-gluon (gg) fusion, as well as qg and $\bar{q}g$ mechanisms. The Leading Order (LO) Feynman diagrams are shown in Figure 5.1. LO diagrams are those with the smallest power in the coupling constants that make a non-zero contribution to the calculation of the process.
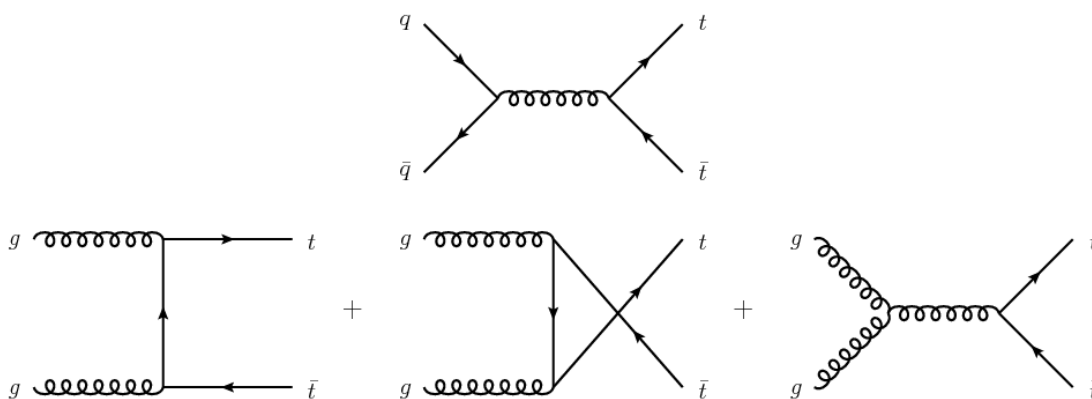
Fig. 5.1 LO diagrams for $t\bar{t}$ production [95]. The upper diagram is for $q\bar{q}$ annihilation and the lower three for gg fusion. At Next-to-Leading Order (NLO) and higher orders, more production methods are possible through $q\bar{q}$, gg, as well as qg and $\bar{q}g$ diagrams.

The diagrams contribute different relative amounts to the $t\bar{t}$ production cross-section owing to the Parton Distribution Functions (PDFs) of the interacting partons. PDFs give the probability of a type of parton in the proton to carry a fraction, x, of the total proton momentum. The three *uud* quarks (known as valence quarks) carry the majority of the proton momentum at low energy scales, Q (the momentum transfer in the interaction). However, there are also gluons in the proton, which can split into $q\bar{q}$ pairs (known as sea quarks), emitting further gluons, and so on. At high Q, the proton is seen to a higher resolution and the density of gluons and sea quarks becomes greater, with each individual parton carrying a smaller

---

[2]The top antiquark is referred to as an antitop quark in this thesis.

fraction of the proton's total momentum. The PDFs therefore depend on x and Q, as shown

in Figure 5.2.
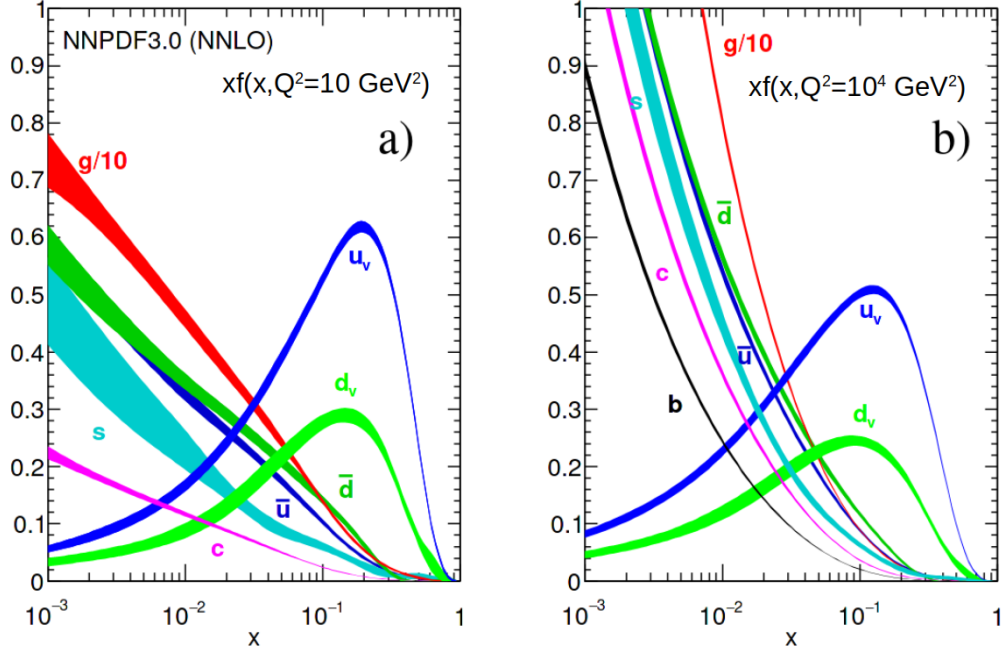
Fig. 5.2 PDFs (here denoted $f(x, Q^2)$ and multiplied by x), for partons in the proton at two different energy scales [17]: a) $Q^2 = 10$ GeV^2; b) $Q^2 = 10^4$ GeV^2. The PDFs are modelled with the NNPDF3.0 NLO [96] set. The gluon PDFs (shown in red) are scaled down by a factor of 10.

For collisions of partons, the effective centre of mass energy is given by $\hat{s} = x_1 x_2 s$, where x_1

and x_2 are the momentum fractions of the two partons. In order to produce a $t\bar{t}$ pair with a

top mass of $m_t = Q$ (the approximate energy scale of Figure 5.2b), the threshold is:

$$\sqrt{x_1 x_2 s} \geq 2m_t, \tag{5.1}$$

If $x_1 \simeq x_2 = x$, this approximates to:

$$x \gtrsim \frac{2m_t}{\sqrt{s}}. \tag{5.2}$$

Using this formula, $t\bar{t}$ production at the Tevatron ($\sqrt{s} = 1.96$ TeV) required $x \gtrsim 0.2$. From Figure 5.2b, at this high value of x, the gluon PDF is very small but the quark PDFs are higher. Therefore, quarks are more likely to have the required threshold for $t\bar{t}$ production. Furthermore, since the collisions are $p\bar{p}$ at the Tevatron, the incoming quark and antiquark can come from valence quarks in the proton and antiproton, respectively. The valence quarks have higher PDF probabilities than sea quarks. Due to these effects, around 85% of the $t\bar{t}$ production cross-section came from $q\bar{q}$ annihilation at the Tevatron [97]. However, for Run 2 at the LHC ($\sqrt{s} = 13$ TeV), $x \gtrsim 0.03$ for $t\bar{t}$ production. At this lower value of x, the gluon PDF is much greater than the quark PDFs. Also, since LHC collisions are pp, the antiquark for $q\bar{q}$ annihilation must come from a low PDF probability sea quark, further reducing the $q\bar{q}$ production mechanism. Therefore, at 13 TeV, 90% of $t\bar{t}$ production comes from gg fusion [97].

The $t\bar{t}$ production cross-sections are calculated by factorising out the PDFs, $\phi_{i,A}$ and $\phi_{j,B}$ (the long distance interaction), and the parton scattering cross-sections, $\hat{\sigma}_{ij \to t\bar{t}}$ (short distance interaction):

$$\sigma(s, m_t) = \sum_{i,j=q,\bar{q},g} \int_0^1 dx_1 \int_0^1 dx_2 \phi_{i,A}(x_1, \mu_F^2) \phi_{j,B}(x_2, \mu_F^2) \hat{\sigma}_{ij \to t\bar{t}}(\frac{m_t^2}{\hat{s}}, \mu_R^2, \mu_F^2, \alpha_s(\mu_R^2)).$$

(5.3)

A and B refer to the hadrons, and i and j the partons within them. The sum is performed over all pairs of colliding partons and the integrals over all possible parton fractional momenta, x_1 and x_2. The long distance interaction is non-perturbative, whereas the short distance interaction is perturbative at high energy scales (when the strong coupling, α_s, is smaller than one, as discussed in Section 1.3.3). μ_F is the factorisation scale, which separates out partons participating in the main interaction and those in the PDFs. μ_R is the renormalisation scale that accounts for divergences in higher order corrections. It is usual to set $\mu_F^2 = \mu_R^2 = Q^2 \simeq m_t^2$ in the calculations.

5.3 $t\bar{t}$ **Decay**

From Equation 1.2, $|V_{tb}|$ is approximately one, meaning that the top quark almost always decays into a bottom quark and W boson: $t \rightarrow bW^+$. The W^+ then either decays hadronically to two quarks with a branching ratio of approximately ⅔ or leptonically to a lepton and neutrino with a branching ratio of ⅓ [17]. The lepton can be a positron, antimuon or antitau lepton, each with similar probabilities of being produced. The above also applies to the $\bar{t} \rightarrow \bar{b}W^-$ decay with the signs of the particles flipped.

For $t\bar{t}$ decay, both W bosons can decay hadronically (all-jets channel), one can decay hadronically and the other leptonically (lepton + jets channel), or both can decay leptonically (dilepton channel). A Feynman diagram of all decay possibilities and a pie chart of branching ratios are shown in Figures 5.3 and 5.4.
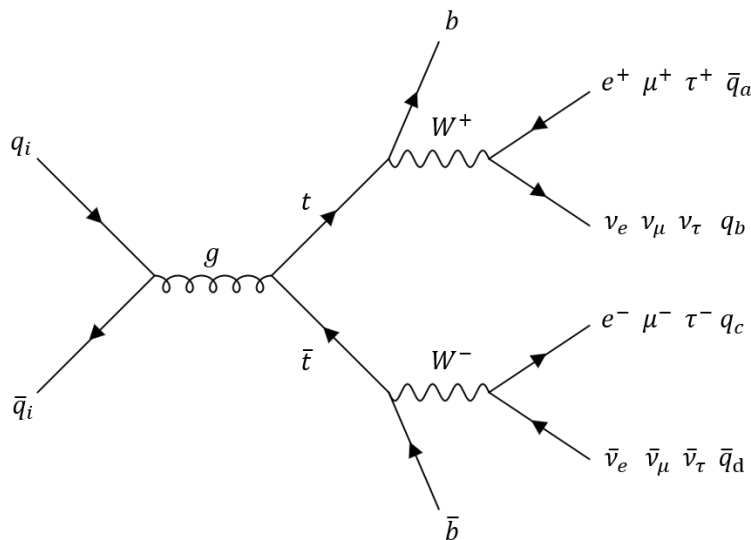
Fig. 5.3 The possible decay modes of $t\bar{t} \rightarrow W^+bW^-\bar{b}$. Each W boson can decay hadronically or leptonically. Diagram created using the package in Reference [52].

Top Pair Branching Fractions
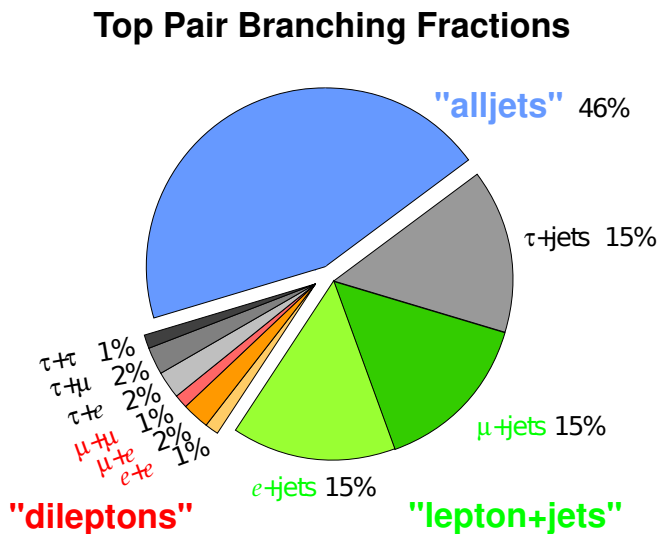
Fig. 5.4 The branching ratios of the $t\bar{t} \rightarrow W^+ b W^- \bar{b}$ decay modes [98].

5.4   Top Properties Measurements

Through measuring the decay products in experiments and reconstructing the top quarks, many properties have been precisely determined. The top mass has been measured at ATLAS and CMS using Run 1 data at $\sqrt{s} = 7$ and 8 TeV. The ATLAS integrated luminosities are 4.6 fb^{-1} at 7 TeV and 20.3 fb^{-1} at 8 TeV. For CMS, these are 5.0 fb^{-1} and 19.6 fb^{-1}, respectively. In combining the all-jets, lepton + jets and dilepton channels, ATLAS measured a top mass, $m_t = 172.69 \pm 0.25 \pm 0.41$ GeV [99], where the first uncertainty is the statistical uncertainty and the second the systematic uncertainty. CMS equivalently measured a mass, $m_t = 172.44 \pm 0.13 \pm 0.47$ GeV [100] in the combination of channels. Ongoing analyses at 13 TeV will reduce the uncertainties further and help to underpin our understanding of the quantum vacuum minimum (see Section 1.4).

Given the top quark mass, predictions of the total $t\bar{t}$ cross-section have been compared with measurements at ATLAS and CMS. The results at $\sqrt{s} = 13$ TeV are summarised in

Figure 5.5. Any deviations from the expectations could indicate BSM physics, such as heavy particles decaying to $t\bar{t}$ pairs, which themselves decay through the usual three channels and enhance the cross-section. However, the theoretical predictions and data agree well within the uncertainties.
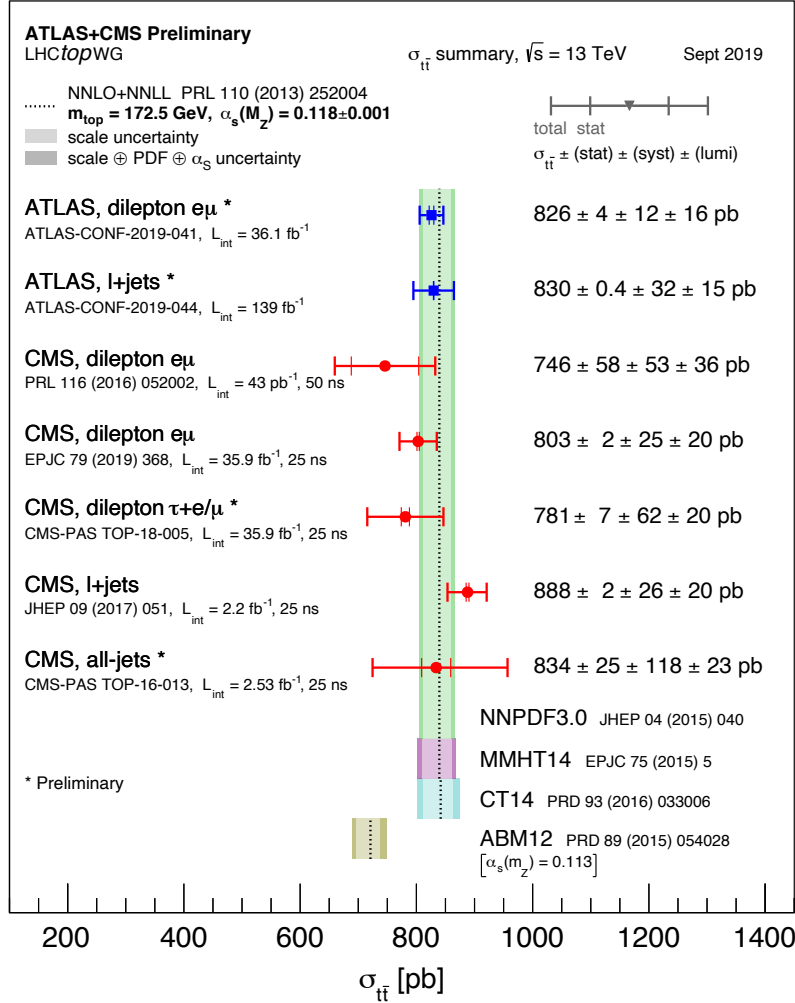
Fig. 5.5 A summary of ATLAS and CMS measurements [101] for the total $t\bar{t}$ production cross-section at $\sqrt{s} = 13$ TeV (points with error bars) compared with the theoretical calculations (filled bands) such as a Next-to-Next-to-Leading Order (NNLO) QCD calculation with the resummation of soft-gluon terms at Next-to-Next-to-Leading Logarithm (NNLL) [102]. The measurements and the theory calculations are determined assuming $m_t = 172.5$ GeV.

The cross-sections can be also determined in bins of differential quantities. For instance, the spin direction is correlated between the top and antitop quark, which propagates to the dilepton decay products and can be accessed through angular variables between the leptons. At $\sqrt{s} = 13$ TeV, the cross-section against the azimuthal opening angle, $\Delta\phi$, and the absolute difference in pseudorapidity, $|\Delta\eta|$, between the two leptons was measured using the ATLAS data recorded in 2015 and 2016 at an integrated luminosity of 36.1 fb^{-1} [103]. The data were corrected for detector effects and mapped back to the full truth-level phase space using a technique known as unfolding, described in Chapter 7. The data suggest an enhancement in spin correlation over the Next-to-Leading Order (NLO) theory prediction by 2.2σ, particularly noticeable in the $\Delta\phi$ plot of Figure 5.6, where the gradient is smaller in data than the prediction.
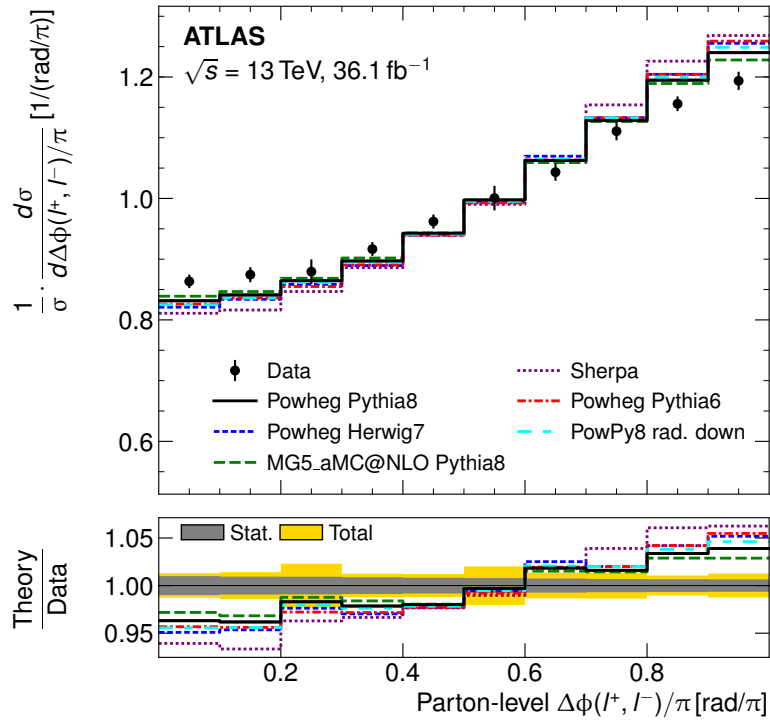
Fig. 5.6 The differential cross-section against $\Delta\phi$ between the two leptons in the dilepton channel using $\sqrt{s} = 13$ TeV ATLAS data with an integrated luminosity of 36.1 fb^{-1} [103]. The data were unfolded to truth-level (here labelled parton-level).

However, the agreement improves with Next-to-Next-to-Leading Order (NNLO) corrections, and the 13 TeV CMS measurement with their 2015-2016 dataset of 35.9 fb^{-1} showed a less pronounced difference between data and predictions [104].

In a similar fashion to spin correlation, the charge asymmetry in $t\bar{t}$ production (discussed in the next section) is propagated to the decay products.

5.5 Introduction to Charge Asymmetry

The LO $t\bar{t}$ production processes in Figure 5.1 are symmetric under charge conjugation, meaning there is no preferred direction for the emitted top or antitop quark to travel. In $t\bar{t}$ production via gg fusion, this is also true at NLO and beyond, where more branches (and hence additional orders of the coupling constants) are added to the Feynman diagrams. However, the $q\bar{q}$ annihilation (and to a smaller extent $qg \to t\bar{t}q$ and $\bar{q}g \to t\bar{t}\bar{q}$) production mechanisms are not symmetric at NLO [105]. This is due to interference occurring particularly between the $q\bar{q}$ initial- and final-state gluon radiation (ISR and FSR) processes in addition to the box and Born processes, as shown in Figure 5.7. In the $t\bar{t}$ rest frame, this leads to the top quark being emitted more often in the incoming quark direction and the antitop in the incoming antiquark direction. This effect is known as charge asymmetry.

Charge asymmetry can be determined across all the data (inclusively) or differentially across kinematic variables. One differential choice is the $t\bar{t}$ transverse momentum, $p_{T,t\bar{t}}$. At low $p_{T,t\bar{t}}$, the number of $t\bar{t}$ events generated by the Born and box processes is greater, with their interference giving a positive contribution to the asymmetry. However, at high $p_{T,t\bar{t}}$, events with an associated jet are more common (likely coming from the ISR and FSR production processes), with their interference giving a negative contribution to the asymmetry [106]. Charge asymmetry is expected to increase with the $t\bar{t}$ invariant mass, $m_{t\bar{t}}$, since there is an
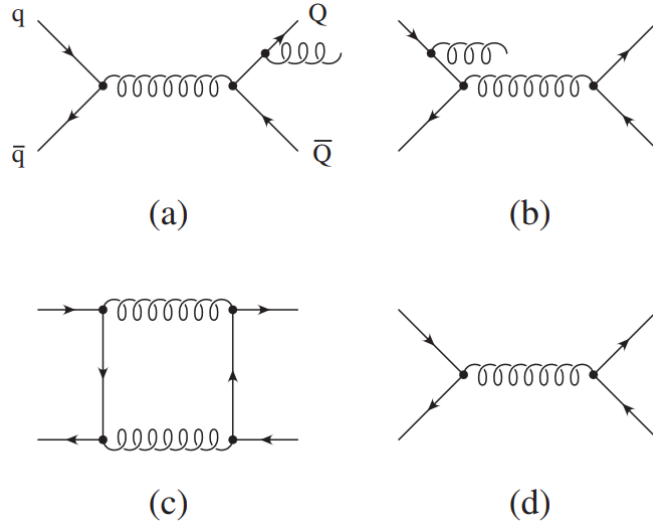
Fig. 5.7 The lowest order $q\bar{q}$ annihilation $\rightarrow t\bar{t}$ production processes that give rise to charge asymmetry [105]. (a) and (b) show the final- and initial-state gluon bremsstrahlung Feynman diagrams and (c) and (d) the double virtual gluon exchange (box) and Born diagrams. Interference between (a) and (b) leads to a decreasing charge asymmetry and interference between (c) and (d) leads to an increasing charge asymmetry.

enhancement in the production from $q\bar{q}$ annihilation, particularly relevant for the LHC. This is also the case for the boost of the $t\bar{t}$ system, which can be described by the velocity in the Z direction, $\beta_{Z,t\bar{t}}$, given by:

$$\beta_{Z,t\bar{t}} = \frac{|p_{Z,t} + p_{Z,\bar{t}}|}{E_t + E_{\bar{t}}}, \tag{5.4}$$

where $p_{Z,t}$ and $p_{Z,\bar{t}}$ refer to the longitudinal momenta of the top and antitop quarks, and E_t and $E_{\bar{t}}$ their total energies.

BSM Physics could lead to deviations in expected charge asymmetries. The exchange of new, heavy bosons between the incoming quark and antiquark such as axigluons [105], Z' bosons [107] and coloured octet Kaluza-Klein couplings [108], or more generally through Standard Model extensions in the form of Effective Field Theories (EFTs) [109] are possible candidates. Charge asymmetry has been measured at both the Tevatron (involving $p\bar{p}$ collisions) and the LHC (pp collisions).

5.5.1 Charge Asymmetry at the Tevatron

For $p\bar{p}$ collisions, the direction of the proton and antiproton are known. The incoming quark is most likely to come from the proton and the antiquark from the antiproton in the $q\bar{q}$ annihilation process. Therefore, due to the Feynman diagram interference (and to an extent momentum conservation), the outgoing top quark is more likely to be produced in the incoming proton direction and the outgoing antitop quark in the incoming antiproton direction (see Figure 5.8).
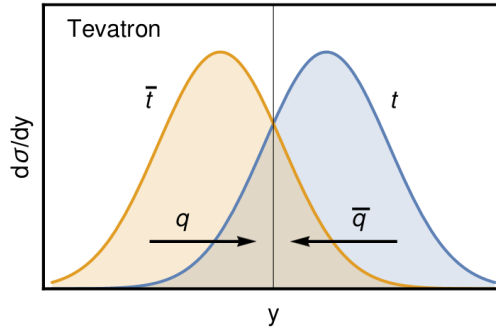
Fig. 5.8 The top and antitop rapidity distributions at the Tevatron, where Feynman diagram interference leads to the two being offset from one another [110].

This asymmetry can be measured in the laboratory frame by either comparing the polar angles, $\cos\theta$, between the top and antitop quarks, or, more usually, their rapidities in a forward-backward asymmetry, $A_{\text{FB, lab}}^{t\bar{t}}$:

$$A_{\text{FB, lab}}^{t\bar{t}} = \frac{N(y_t > 0) - N(y_{\bar{t}} > 0)}{N(y_t > 0) + N(y_{\bar{t}} > 0)} \tag{5.5}$$

where $N(y_t)$ and $N(y_{\bar{t}})$ are the number of events as a function of the top and antitop rapidities, respectively. The asymmetry is calculated as a ratio with the total number of events on the denominator since it cancels normalisation uncertainties that are correlated between the first and second terms of the numerator. The expected asymmetry is greater than zero in the

Standard Model. It can be measured in all $t\bar{t}$ decay channels.

Since differences in rapidity are Lorentz independent, a frame-independent (therefore applying to the $t\bar{t}$ rest frame) asymmetry, $A_{\text{FB}}^{t\bar{t}}$, can also be established by using the variable, $\Delta y = y_t - y_{\bar{t}}$:

$$A_{\text{FB}}^{t\bar{t}} = \frac{N(\Delta y > 0) - N(\Delta y < 0)}{N(\Delta y > 0) + N(\Delta y < 0)}. \qquad (5.6)$$

As Δy is expected to be on average greater than zero, $A_{\text{FB}}^{t\bar{t}}$ should therefore be positive.

In reconstructing the $t\bar{t}$ systems to calculate the asymmetry, large uncertainties are involved in the top and antitop rapidities due to uncertainties in the jet energies and in associating jets to the top or antitop decay. However, in the dilepton channel, the asymmetry propagates to the two leptons, which do not have such large modelling uncertainties. The leptons will approximately follow (but not strictly) the direction of their top quark parents, leading to a smaller, but more precise, asymmetry measurement. Since the leptons have a much smaller mass than their energies, their pseudorapidities can be used in the leptonic asymmetry, A_{FB}^{ll}:

$$A_{\text{FB}}^{ll} = \frac{N(\Delta\eta > 0) - N(\Delta\eta < 0)}{N(\Delta\eta > 0) + N(\Delta\eta < 0)}, \qquad (5.7)$$

where $\Delta\eta = \eta_{l^+} - \eta_{l^-}$. Pseudorapidity is easier to measure in detectors, since only the angle from the beam axis, θ, needs to be measured. For rapidity, the required energy and momentum measurements suffer from larger uncertainties (see Section 6.8.1).

The CDF and D0 collaborations at the Tevatron measured the values of $A_{\text{FB}}^{t\bar{t}}$ and A_{FB}^{ll} using their full datasets of 9.4 fb^{-1} and 9.7 fb^{-1}, respectively. The data were unfolded back to the full truth-level phase space. The individual and combined inclusive results and references are

shown in Figure 5.9. The asymmetries are typically of order 10% and are slightly larger than the theory expectations. Furthermore, an earlier CDF measurement with 5.3 fb^{-1} of data showed that at high $t\bar{t}$ invariant mass, $m_{t\bar{t}} > 450$ GeV, the data asymmetry was above that of the NLO prediction by 3.4σ [112]. In the combination of the full CDF and D0 datasets, with the theoretical asymmetries calculated at NNLO, fits of $A_{\mathrm{FB}}^{t\bar{t}}$ against $m_{t\bar{t}}$ were compared in data and theory, as shown in Figure 5.10 [111]. The agreement was better although the slope of the data fit was greater than the theory fit by 1.3σ. With the results from the Tevatron, there was high motivation to investigate charge asymmetry further at the LHC.
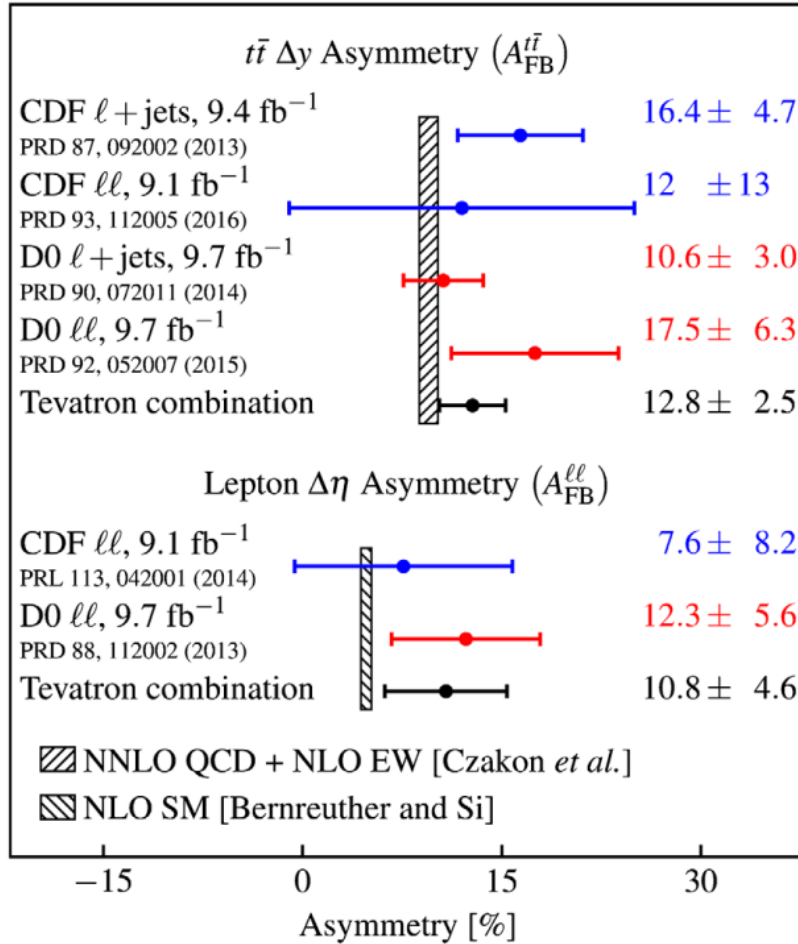
Fig. 5.9 $A_{\mathrm{FB}}^{t\bar{t}}$ and A_{FB}^{ll} measurements for the CDF and D0 detectors (and the combination of their results) for their full datasets unfolded back to truth-level [111]. The data are shown by the points and the theory by the grey hatched bands.
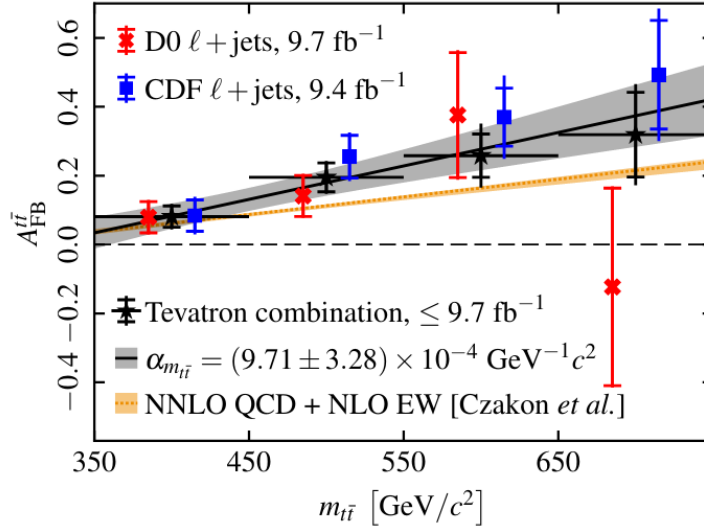
Fig. 5.10 $A_{\mathrm{FB}}^{t\bar{t}}$ vs $m_{t\bar{t}}$ measurements for the CDF and D0 detectors (and the combination of their results) for their full unfolded datasets [111]. The data slope (black line) is greater than the theory slope (orange line) by 1.3σ. At D0, the highest $m_{t\bar{t}}$ point has a large uncertainty due to limited events recorded in the detector at this scale.

5.5.2   Charge Asymmetry at the LHC

With pp collisions, it is impossible to determine the initial quark and antiquark directions. The top and antitop quarks can be emitted in either direction along the beampipe with equal probability. As such, the forward-backward asymmetries of Equations 5.6 and 5.7 would be zero. However, a charge asymmetry can still be determined at the LHC, owing to the quark configuration of the protons. In the $q\bar{q}$ annihilation process, the incoming quark can be either a valence or sea quark, whereas the antiquark must be a sea quark. Since the momentum fraction of the valence quarks is usually greater than the sea quarks, the incoming quark, and hence the top, will typically be more boosted along the beampipe than the antitop (see Figure 5.11).

Considering the absolute rapidities, $|y|$, of the top and antitop quarks, the difference in their values, $\Delta|y| = |y_t| - |y_{\bar{t}}|$, should be greater than zero on average, due to the broader shape
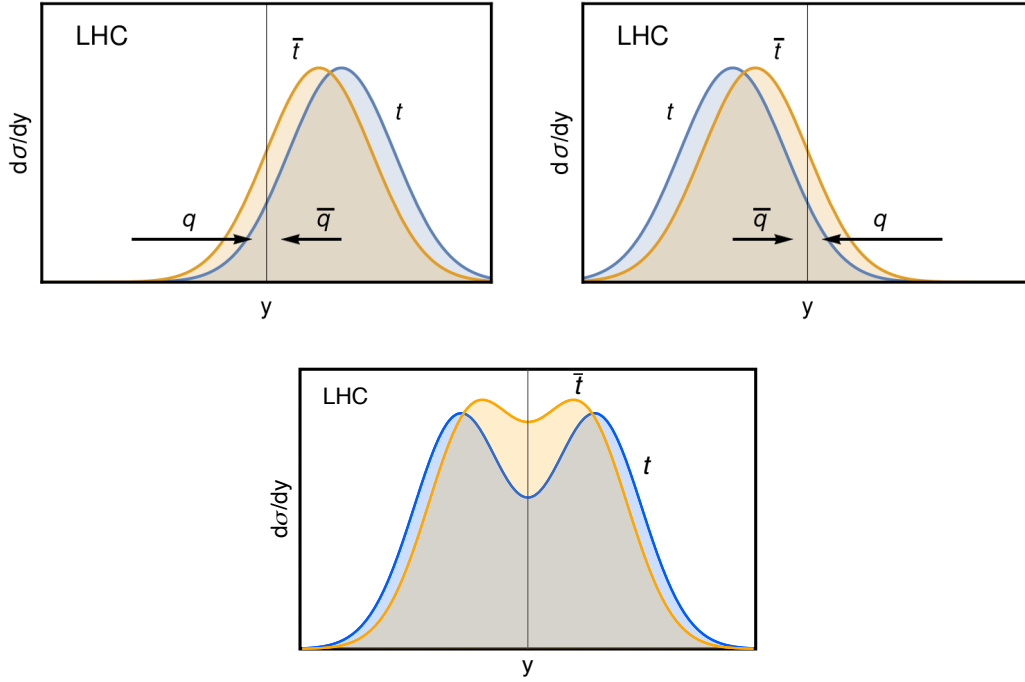
Fig. 5.11 Upper plots: the top and antitop rapidity distributions at the LHC, with the $t\bar{t}$ system produced in either direction along the beampipe, depending on the relative magnitudes of the initial $q\bar{q}$ momenta [110]. Lower plot: the sum of the above two as seen experimentally.

from the top quark. One defines a new, central charge asymmetry, $A_C^{t\bar{t}}$, which can be measured in all $t\bar{t}$ decay channels:

$$A_C^{t\bar{t}} = \frac{N(\Delta|y| > 0) - N(\Delta|y| < 0)}{N(\Delta|y| > 0) + N(\Delta|y| < 0)}. \tag{5.8}$$

Again, the equation compares the number of events with absolute rapidity difference greater than zero, $N(\Delta|y| > 0)$ with those less than zero, $N(\Delta|y| < 0)$, for which the overall $A_C^{t\bar{t}}$ value should be positive. However, $\Delta|y|$ is no longer Lorentz invariant, and since the rapidities are measured in the laboratory frame, the asymmetry is that in the laboratory frame. The equivalent leptonic asymmetry, only measurable in the dilepton channel, A_C^{ll}, is given by:

$$A_C^{ll} = \frac{N(\Delta|\eta| > 0) - N(\Delta|\eta| < 0)}{N(\Delta|\eta| > 0) + N(\Delta|\eta| < 0)}, \tag{5.9}$$

where $\Delta|\eta| = |\eta_{l^+}| - |\eta_{l^-}|$.

Both ATLAS and CMS have determined the charge asymmetries unfolded to truth-level at $\sqrt{s} = 7$ and 8 TeV with their full datasets [113–123]. The inclusive results are summarised in Figure 5.12. Differential measurements in bins of $p_{T,t\bar{t}}$, $m_{t\bar{t}}$ and $\beta_{Z,t\bar{t}}$ in the dilepton channel at 8 TeV in ATLAS are also shown in Figure 5.13. The asymmetries typically lie around a few percent and are smaller than those calculated at the Tevatron. This is expected due to the higher energies at the LHC yielding more gg fusion, the collisions being pp rather than $p\bar{p}$, and that A_{C} rather than A_{FB} values are being calculated. No significant deviations were found from the Standard Model expectation in either the inclusive or differential cases but they suffer from large statistical uncertainties. This was particularly the case for the differential measurements and so no sensitivity to asymmetry was observed or indeed an enhancement seen across the $m_{t\bar{t}}$ bins like at the Tevatron.
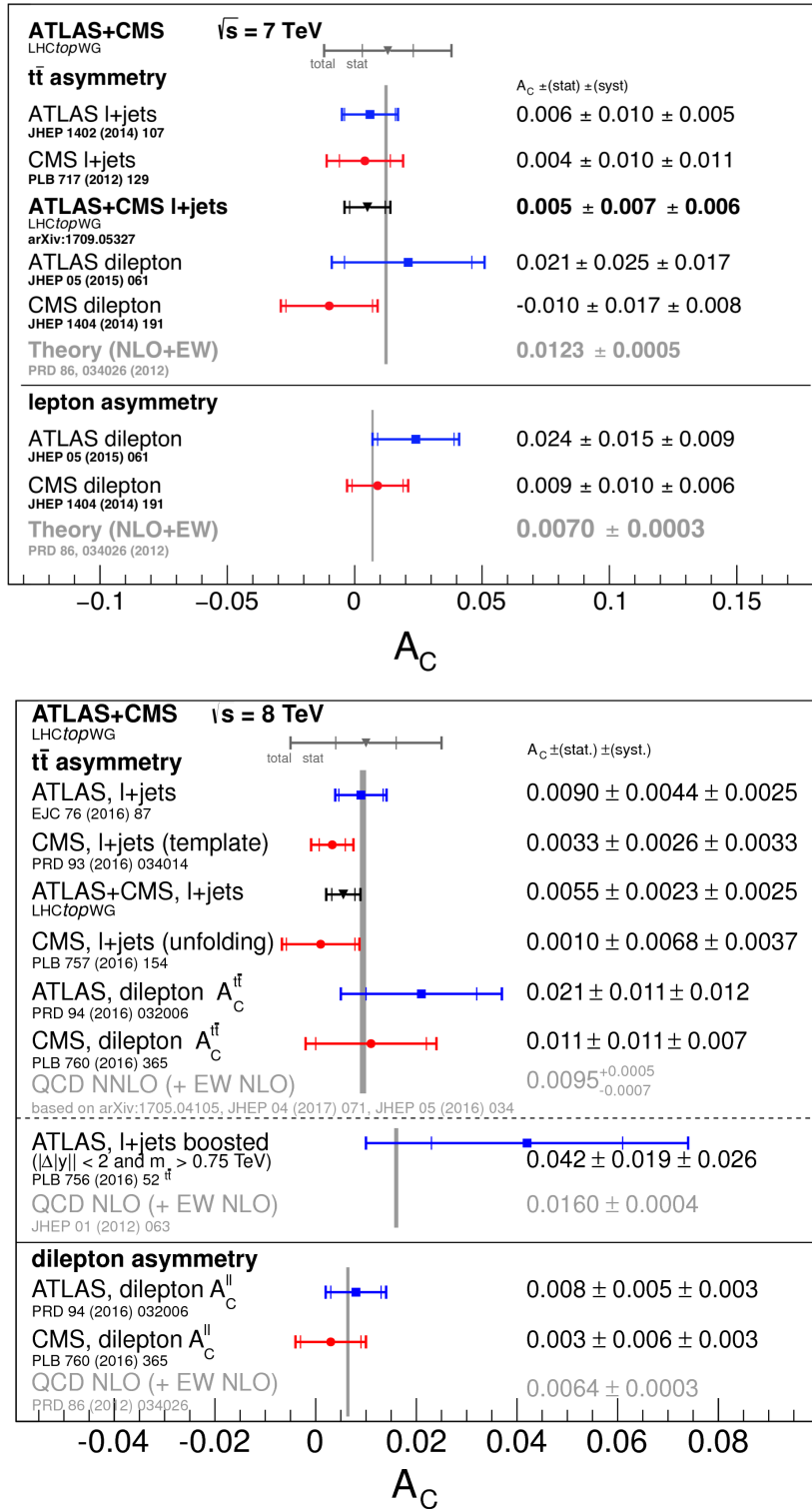
Fig. 5.12 $A_{FB}^{t\bar{t}}$ and A_{FB}^{ll} measurements at the LHC for $\sqrt{s}$ = 7 TeV (upper plot) and 8 TeV (lower plot) for CMS and ATLAS (and their combination) unfolded back to the full truth-level phase space [101]. The data are shown by the points and the theory by the grey hatched bands.
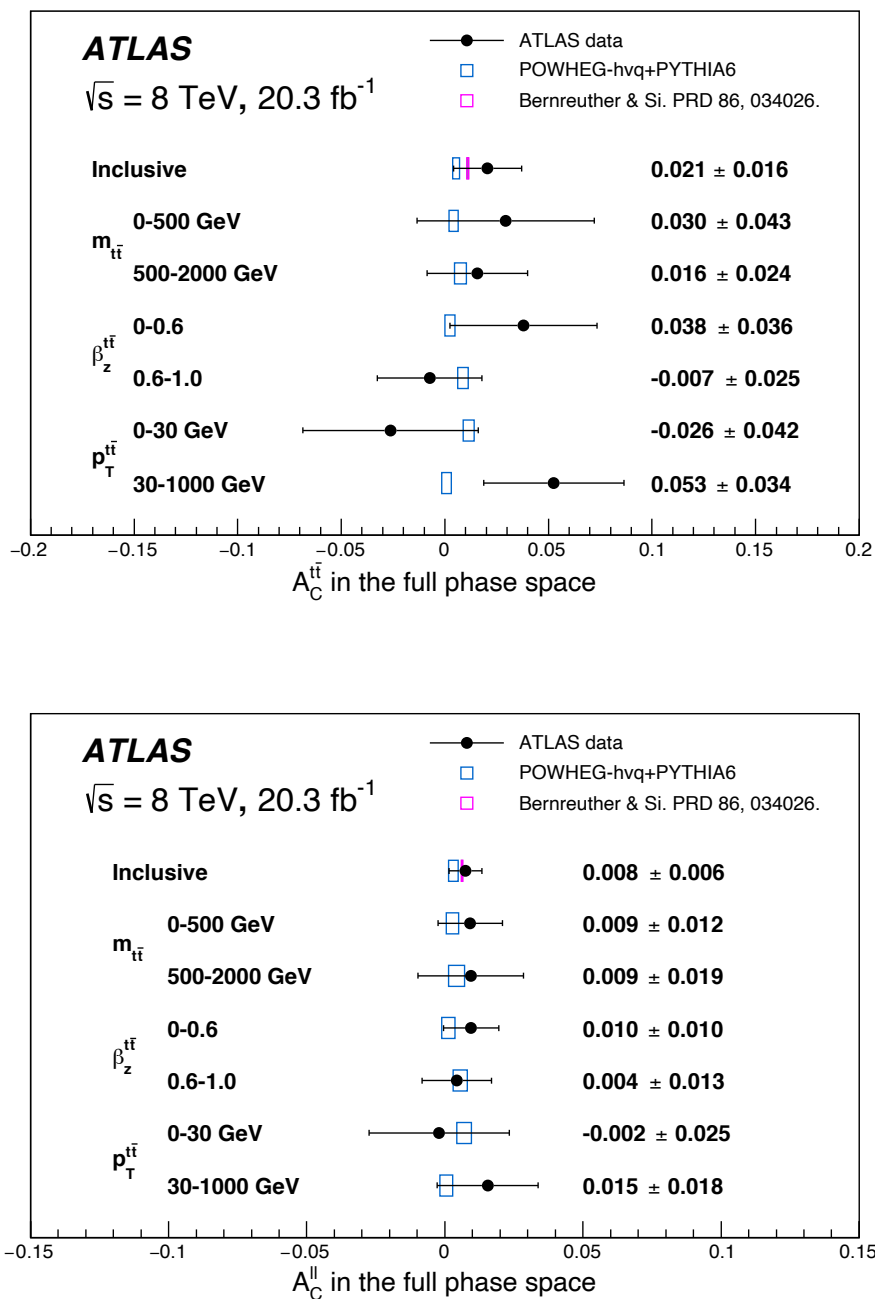
Fig. 5.13 Inclusive and differential unfolded charge asymmetries ($A_C^{t\bar{t}}$ in upper plot, A_C^{ll} in lower plot) in the dilepton channel for the ATLAS experiment at $\sqrt{s} = 8$ TeV [121]. The data are shown by the points and the theory by the bands with blue or magenta outlines.

This thesis details charge asymmetry measurements at $\sqrt{s} = 13$ TeV with the ATLAS detector using the full Run 2 (2015-2018) dataset of 139 fb^{-1}. The main focus is on the dilepton channel, in which I had a significant role. $A_C^{t\bar{t}}$ was calculated for the inclusive case and differentially across $p_{T,t\bar{t}}$, $m_{t\bar{t}}$ and $\beta_{Z,t\bar{t}}$ for both the dilepton and lepton + jets channels (and their combination). The higher energy and statistics in the dataset allowed more events to be reconstructed and additional differential bins to be investigated, especially important for the asymmetry as a function of $m_{t\bar{t}}$. The differential bins considered were:

- $p_{T,t\bar{t}}$ - 3 bins: $[0, 30, 120, \infty]$ GeV
- $m_{t\bar{t}}$ - 5 bins: $[0, 500, 750, 1000, 1500, \infty]$ GeV
- $\beta_{Z,t\bar{t}}$ - 4 bins: $[0, 0.3, 0.6, 0.8, 1]$.

For the dilepton channel, A_C^{ll} was also calculated for the inclusive case and differentially across the dilepton transverse momentum ($p_{T,l\bar{l}}$), mass ($m_{l\bar{l}}$) and velocity in the Z direction ($\beta_{Z,l\bar{l}}$). These were determined as a function of dilepton rather than $t\bar{t}$ observables (as shown in the 8 TeV results of Figure 5.13) to further reduce systematic uncertainties associated with $t\bar{t}$ reconstruction. The following bins were used:

- $p_{T,l\bar{l}}$ - 3 bins: $[0, 20, 70, \infty]$ GeV
- $m_{l\bar{l}}$ - 4 bins: $[0, 200, 300, 400, \infty]$ GeV
- $\beta_{Z,l\bar{l}}$ - 4 bins: $[0, 0.3, 0.6, 0.8, 1]$.

Chapter **6**

Event Selection in the Dilepton Channel

6.1 Data and Simulation

Theoretical processes that should model collision data are simulated using Monte-Carlo (MC) generators, which handle the following stages:

1. Generation of the main parton-parton interaction in the pp collision, known as the hard scatter.

2. Simulation of other parton pair interactions in the collision, which are of lower energy than the hard scatter, known as soft QCD processes.

3. Parton showering: one-to-two interactions of quarks radiating gluons, and gluons splitting into quark-antiquark pairs.

4. Hadronisation: since bare quarks cannot exist (other than the top and antitop), they are combined with other quarks to form bound, colourless states of baryons and mesons.

5. Resonance decays of unstable particles such as the top quark and B hadrons into leptons and partons, which themselves shower and hadronise.

In ATLAS, the MC events are finally passed through a model of the detector constructed with the GEANT4 toolkit [124]. This simulates the limited phase space coverage of the detector and the passage of particles through the detector material. To reduce the statistical uncertainties in the simulation, many MC events are generated. Each event is then normalised by the total number of events and multiplied by the integrated luminosity of 139 fb^{-1} from the ATLAS data, the cross-section for the process, and the k-factor (a scale factor which accounts for higher order corrections to the Feynman diagrams). Multiple primary vertices in pile-up are also accounted for by reweighting the MC to match the pile-up in data. MC $t\bar{t}$ signal as well as background processes in the dilepton channel are generated. The backgrounds can produce very similar signatures to the signal, especially taking into account detector reconstruction effects. For instance, jets may be misidentified as leptons, or leptons may fall outside the detector acceptance or not be reconstructed due to cracks or dead channels, leading to an incorrect missing transverse energy determination.

The resultant signal plus background MC simulation (described in the next sections) should map onto the data if the Standard Model is correct and fully described by the simulation, and if the detector response is well-modelled. The MC samples used are shown in Appendix A.

6.1.1   Signal $t\bar{t}$ Modelling

MC events that yield $t\bar{t}$ pairs from theoretical matrix elements were produced at NLO in α_s with the POWHEG BOX v2 generator [125] assuming a top mass, m_t, of 172.5 GeV. The renormalisation and factorisation scales, μ_R and μ_F, were set to $\sqrt{m_t^2 + p_{T,t}^2}$, where $p_{T,t}$ is the transverse momentum of the top quark. A parameter known as h_{damp}, which gives the cut-off scale for the first gluon radiation emission was set to 1.5 m_t. The PDFs were modelled with the NNPDF3.0 NLO [96] set. The matrix element calculations were interfaced with the parton showering and hadronisation generator, Pythia8.230 [126], which uses the NNPDF2.3

LO [127] PDF set and the ATLAS 2014 (A14) set of tuned parameters [128]. The parameters adjust the QCD calculations to account for higher order non-perturbative effects, leading to better modelling of physical observables. The combined generators are henceforth referred to as Powheg + Pythia8. The MC was normalised through a k-factor to the inclusive production cross-section, $\sigma(t\bar{t}) = 832 \pm 51$ pb, calculated at NNLO in QCD with the resummation of soft-gluon terms at NNLL using Top++2.0 [129].

6.1.2 Single Top
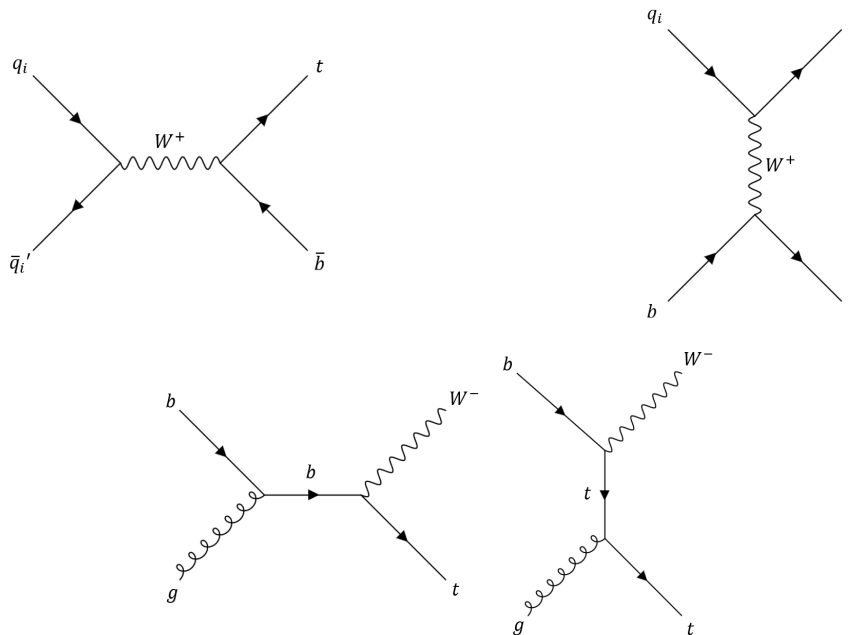
Fig. 6.1 Main Feynman diagrams for single top production. Upper left: *s*-channel process. Upper right: *t*-channel processes. Lower diagrams: *tW* associated production processes.

An important background is from single top production, which comes in three forms: the *s*-channel, *t*-channel and *tW* associated production process, as shown in Figure 6.1. The MC for all three channels were produced using the same tools as the $t\bar{t}$ signal: POWHEG BOX v2 (with the NNPDF3.0 NLO PDF set) interfaced to Pythia8.230 (with the NNPDF2.3 LO set) using the A14 tune. The *tW* process can result in two leptons through the decay of the *W* boson and top, whereas selection of the *s*- and *t*-channels will usually require an object to be

misidentified as a lepton, and thus they were placed into the fake lepton background category (see Section 6.1.6). At NLO, the *tW* process gives rise to an identical configuration (through a gluon emission, followed by splitting into $b\bar{b}$) as for the LO $t\bar{t}$ signal. As such, a Diagram Removal (DR) technique was used [130, 131], which sets the matrix element amplitude of the single top NLO diagram to zero and removes the interference between this diagram and the LO $t\bar{t}$ diagram.

6.1.3   *V* + **Jets**
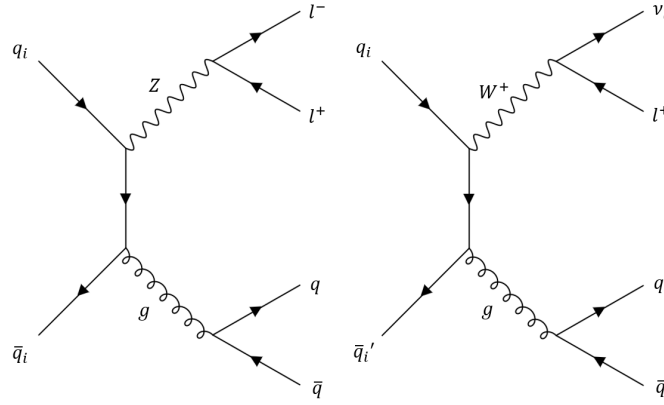
Fig. 6.2 Example Feynman diagrams for the *V* + jets background. In this case, two jets are emitted. Left: *Z* + jets. Right: *W* + jets with just the W^+ case shown.

Backgrounds from events yielding a *Z* or *W* boson in association with jets are collectively known as *V* + jets. The matrix elements were simulated with the Comix [132] and OpenLoops [133] generators, which calculate NLO matrix elements for up to two jets and LO matrix elements for up to four jets. They were interfaced with the parton shower and hadronisation generator, Sherpa2.2.1 [134] using a dedicated set of tuning parameters within Sherpa based on the NNPDF3.0 NNLO PDF set. For the *Z* + jets background, the leptonic decay of the *Z* boson closely resembles the $t\bar{t}$ dilepton signal. MC samples were used for decays to e^+e^-, $\mu^+\mu^-$ and $\tau^+\tau^-$. These were further split into low mass (10 GeV $< m_{l\bar{l}} <$ 40 GeV) and high mass ($m_{l\bar{l}} >$ 40 GeV) samples, and also for light (*u*, *d* or *s* quark), medium (*c* quark) and

heavy (b quark) flavour jets. Data-driven control regions were used to aid the simulation (see Section 6.9). The W + jets samples included the W boson leptonic decays to $e^+\nu_e$, $\mu^+\nu_\mu$ and $\tau^+\nu_\tau$ (and the negative lepton equivalents). However, since their diagrams involve one charged lepton, their contribution to the total background is much smaller than for Z +jets. They require an additional lepton to mimic the $t\bar{t}$ signature, and so were placed in the fake lepton background category.

6.1.4 Diboson
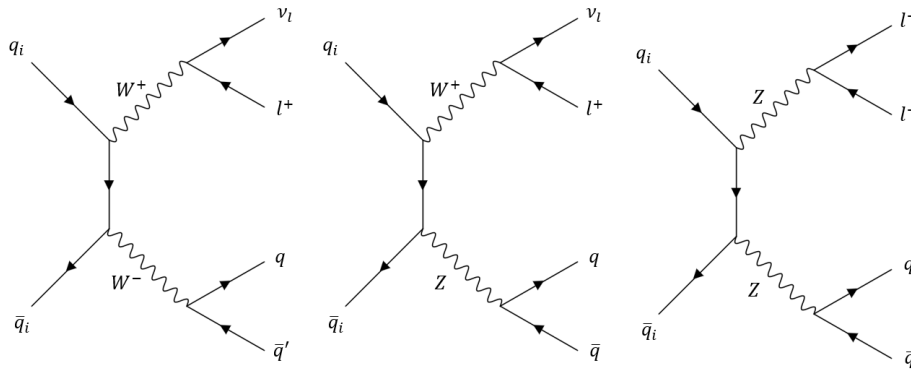
Fig. 6.3 Example Feynman diagrams for the diboson background. WW, WZ (just the W^+ case) and ZZ are shown as examples from left to right.

Feynman diagrams giving rise to WW, WZ and ZZ production (collectively known as VV or diboson backgrounds) can also resemble the signal. The processes were simulated with the Comix and OpenLoops matrix element generators for up to one parton at NLO and up to three partons at LO. They were interfaced with Sherpa2.2.1 (for one-lepton samples) and Sherpa2.2.2 (for two- and three-lepton samples) using the Sherpa tuning parameters based on the NNPDF3.0 NNLO PDF set. Example diagrams are shown in Figure 6.3, where the W and Z bosons can decay leptonically or hadronically.

6.1.5 Rare SM
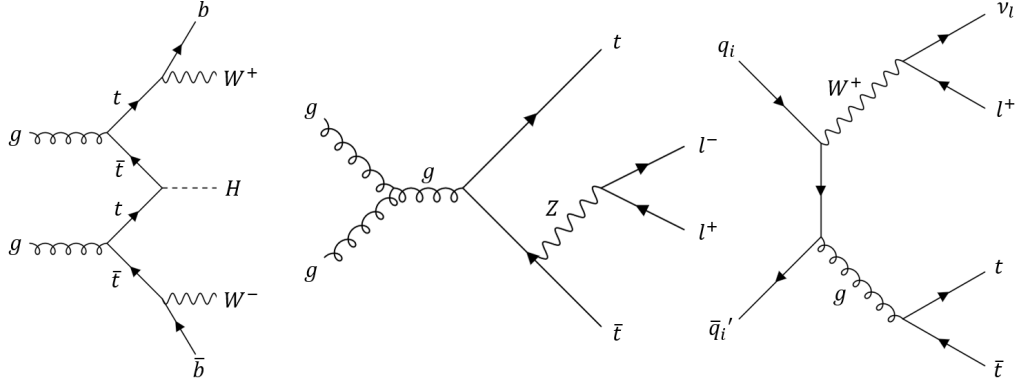
Fig. 6.4 Example Feynman diagrams for the rare SM background. The $t\bar{t}H$, $t\bar{t}Z$ and $t\bar{t}W$ processes are shown from left to right.

The background $t\bar{t}W$ and $t\bar{t}Z$ processes were simulated with MadGraph 5 (MG5_aMC) v2.3.3 [135], which generates matrix elements at NLO with the NNPDF3.0 NLO PDF set. They were interfaced with Pythia8.210, which uses the A14 tune and the NNPDF2.3 LO PDF set. In addition, $t\bar{t}H$ events were produced with the POWHEG BOX v2 matrix element generator interfaced with Pythia8.230, again using the A14 tune and NNPDF2.3 LO PDF set. Processes yielding tWZ and tZ events are important in control regions of same-sign leptons, which were used to estimate the fake lepton backgrounds, as discussed in Section 6.9. These were both simulated with the MG5_aMC2.3.3 matrix element generator at NLO with the NNPDF3.0 NLO PDF set and interfaced with Pythia8.212 using the A14 tune and the NNPDF2.3 LO PDF set.

6.1.6 Fake Leptons

It is possible for leptons not coming from the main $t\bar{t}$ event (non-prompt leptons) to be incorrectly assigned to the dilepton decay channel, and for other particles to be misidentified
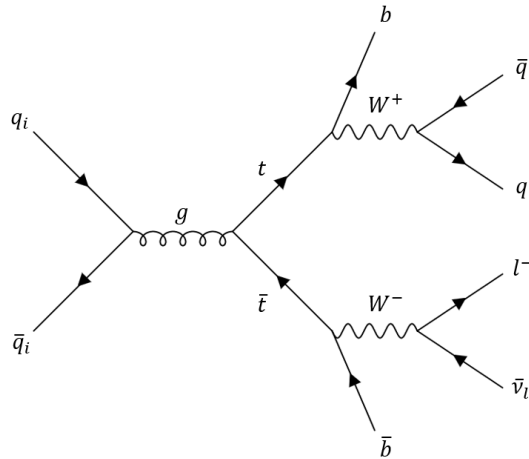
Fig. 6.5 Example Feynman diagram for the main source of the fake lepton background: lepton + jets production.

as leptons. These are collectively known as the fake lepton background. The main processes which lead to fake leptons include:

- Semileptonic decays of heavy hadrons containing b or c quarks.

- In-flight decays of pions and kaons.

- π^0 decays to two photons.

- Photons or photon conversions to leptons that are matched to inner detector tracks.

- High energy hadrons making their way into the muon system (punch-through).

The main source is from $t\bar{t}$ decays to lepton + jets (see Figure 6.5) with an extra reconstructed lepton, but all the other backgrounds can contribute fake leptons. Data-driven control regions were used to help with the simulation (see Section 6.9).

6.2   Truth-Level Object Definitions

A truth-level (also known as parton-level) description of the $t\bar{t}$ signal MC was also employed in Powheg + Pythia8, in which the particles are not subjected to detector effects. In this description, the top and antitop quarks are defined after final-state radiation. The W bosons must originate from $t\bar{t}$ decays and are defined after final-state radiation. The leptons from the

W boson decays are taken prior to soft (low energy) emissions and required to be electrons, muons or τ leptons, where the τ leptons decay to electrons or muons. The full possible phase-space at $\sqrt{s} = 13$ TeV was considered with no kinematic cuts on the particles except for the A_C^{ll} measurements, discussed in Section 7.5.

6.3 Reconstructed-Level Object Definitions

The data and MC simulated events (except for the truth-level signal MC) were subjected to selection requirements (cuts) and reconstruction algorithms to choose good quality events with a high probability of coming from $t\bar{t}$ dilepton decays and not backgrounds. These events are referred to as detector-level, reconstructed-level, or simply reco-level events. Requirements were made on the measurable physics signatures (objects) in the events: electrons, muons, jets and E_T^{miss} associated with the two neutrinos, which are detailed below and were combined to reproduce the $t\bar{t}$ systems. Tau leptons which decay hadronically were not included, but those decaying leptonically to electrons and muons were, as discussed in Section 7.3.

6.3.1 Electrons

Electrons are reconstructed based on clusters in the electromagnetic calorimeter matched with tracks in the ID. Requirements on parameters such as the electromagnetic shower shape and number of hits in the ID (which are passed into a likelihood fitting method) lead to different efficiencies for electron reconstruction, identification, isolation and trigger performance, as well as background rejection [92, 136, 137]. The efficiencies are determined with $Z \rightarrow e^+e^-$ and $J/\psi \rightarrow e^+e^-$ tag-and-probe methods. Operating points are then defined based on the efficiencies and background rejections.

For this analysis, the "tight" identification operating point was chosen, corresponding to an 80% identification efficiency at $E_T \simeq 40$ GeV, but with high background rejection of misidentified electrons (above 99%) [136]. The operating point requires seven hits over the pixel and silicon strip detectors, with at least two in the pixel detector; one of which in the Insertable B-Layer.

The energy and momentum deposits around the electron candidates can be used to separate prompt electrons in $t\bar{t}$ decays from background processes such as electrons arising from photon conversions and heavy flavour hadron decays, as well as light hadrons misidentified as electrons. A gradient isolation scheme was used, which removes events with certain p_T deposits in cones of $\Delta R = \min(0.2, 10 \text{ GeV}/p_T)$ around the electron ID tracks and E_T deposits in cones of $\Delta R = 0.2$ around the electron calorimeter clusters [92]. This yields isolation efficiencies of $\geq 90\%$ (99%) at $p_T = 25$ GeV (60 GeV).

Electron clusters were selected within the detector acceptance ($|\eta| < 2.47$), except for the transition region between the barrel and the end-caps of the liquid argon calorimeter ($1.37 < |\eta| < 1.52$), which contains a large amount of inactive material.

A close matching between the collision point (primary vertex) and ID track is required to ensure the reconstructed electron is from the prompt interaction and not from a pile-up interaction or a secondary electron such as bremsstrahlung emission and photon conversion. The matching agreement is determined by two impact parameters: d_0 (the transverse parameter defined by the distance of closest approach of the track to the primary vertex in the $r - \phi$ plane) and $z_0 \sin\theta$ (the equivalent longitudinal parameter). The impact parameter cuts applied were $|d_0|/\sigma(d_0) < 5$, where $\sigma(d_0)$ is the uncertainty on d_0, and $|z_0 \sin\theta| < 0.5$ mm.

6.3.2 Muons

Selection cuts for muons are based on the combination of information from the muon system and the ID. An outside-in pattern recognition is employed, in which the muons are first reconstructed in the muon system and then matched with an ID track by extrapolating inwards. Similar to electrons, efficiencies in muon reconstruction, identification, isolation and trigger performance are determined through techniques such as $Z \rightarrow \mu^+\mu^-$ and $J/\psi \rightarrow \mu^+\mu^-$ tag-and-probe methods [138].

The "medium" identification operating point was required in the analysis, leading to identification efficiencies above 95% and background rejections above 99.5% [138]. This selection requires at least three hits in two or more MDT layers of the muon system, apart from at $|\eta| < 0.1$, where this reduces to one or more layers.

A gradient isolation scheme was used again, which removes background events such as those producing muons in semileptonic decays, which are embedded in jets. It considers the p_T deposits in cones of $\Delta R = \min(0.3, 10\,\text{GeV}/p_T)$ around the muon ID track and E_T deposits in cones of $\Delta R = 0.2$ around the muon calorimeter cluster [138]. As for electrons, this yields isolation efficiencies of $\geq 90\%$ (99%) at $p_T = 25$ GeV (60 GeV).

Muons falling within $|\eta| < 2.5$ were selected and the impact parameters required were $|d_0|/\sigma(d_0) < 3$ and $|z_0 \sin\theta| < 0.5$ mm. This leads to good track-to-vertex association (TTVA) and reduces the background from decays of secondary hadrons (rather than $t\bar{t}$ decays) to muons.

6.3.3 Jets

Hadronic jets are measured by first grouping neighbouring electromagnetic and hadronic calorimeter cells that have energy deposits above noise thresholds [139]. The clusters are then passed to the anti-k_T algorithm [140]. Distance measures (functions of transverse momentum) between pairs of clusters (d_{ij}) and clusters with respect to the beam direction (d_{iB}) are calculated:

$$d_{ij} = \min(k_{T,i}^{-2}, k_{T,j}^{-2}) \frac{\Delta_{ij}^2}{R^2}$$
$$d_{iB} = k_{T,i}^{-2},$$

(6.1)

where R is the radius parameter (set to 0.4), $\Delta_{ij}^2 = (y_i - y_j)^2 + (\phi_i - \phi_j)^2$, and y_i, ϕ_i and $k_{T,i}$ are respectively the rapidity, azimuthal angle and transverse momentum of cluster i. All possible values of d_{ij} and d_{iB} are calculated for the clusters and are placed in a list. If the smallest distance in the list is a d_{ij}, then clusters i and j are combined. If it is a d_{iB}, cluster i is called a jet and removed from the list of clusters. The process repeats (updating the list after each iteration) until no clusters remain in the list and they are all grouped into jets.

Pile-up corrections are applied to the p_T values of the jets. The contribution of pile-up in a jet is proportional to its area in $\eta - \phi$ space, $A_i = \pi R^2$, so is subtracted away [141]:

$$p_{T,i}^{\text{corr.}} = p_{T,i} - A_i \rho,$$

(6.2)

where $p_{T,i}^{\text{corr.}}$ is the corrected transverse momentum of jet i, $p_{T,i}$ the jet's transverse momentum and ρ the mean amount of transverse momentum per unit area added to the event by pile-up. Further residual corrections to the subtraction are also made based on calibrations from simulation and data [142]. Some pile-up jets will still remain in the event and so a

discriminant known as the Jet Vertex Tagger (JVT) [143] is used, which uses information from the tracks matched to the jets in the jet phase space of $p_T < 60$ GeV and $|\eta| < 2.4$. The higher the value of the discriminant (falling between 0 and 1), the larger the probability the jet is associated with the primary vertex of the hard scatter. The discriminant was required to be greater than 0.59. This leads to an efficiency of 92% and a pile-up rejection of 99%.

6.3.4 b-Tagging

The MV2c10 algorithm [144–146] was employed to identify jets coming from b quarks. It uses a Boosted Decision Tree (BDT) implemented in the Toolkit for Multivariate Data Analysis (TMVA) package [147]. b quarks form B hadrons, which have relatively long lifetimes, so the secondary vertices from the B decays are displaced from the primary vertex. Impact parameter information, jet kinematics and decay products of the jet help to determine whether a b quark was present. A BDT discriminant score between -1 and $+1$ is determined, where the higher the value, the higher the probability the jet came from a b quark. However, a more stringent cut also leads to more true b jets not passing the selection, reducing the efficiency. Here, an MV2c10 score of greater than 0.63 was chosen, leading to high rejection factors of 114, 5 and 19 for light quarks, c quarks and jets originating from hadronic τ decays, respectively. The identification efficiency for b quarks in $t\bar{t}$ decays is 77%. This therefore kept a high proportion of the events, which was important for the differential measurements of charge asymmetry that suffer from large statistical uncertainties.

6.3.5   Missing Transverse Energy

E_T^{miss} is calculated from the vectorial p_T sum of the reconstructed objects as in Equation 3.1. Calibrated electrons, muons, photons, hadronically-decaying τ leptons, and reconstructed jets from calorimeter energy deposits, all known as hard objects, go into the calculation, as well as soft hadronic deposits not associated with reconstructed objects. Since there are two

neutrinos in the dilepton channel, the E_T^{miss} is shared between them, being determined by $t\bar{t}$ reconstruction algorithms.

6.3.6 Overlap Removal

It is possible for a single object in the detector to pass the identification requirements of more than one object type, leading to double-counting. As such, an overlap removal method was employed:

- A candidate electron is removed if it shares a track with a candidate muon.
- A jet is removed if its angular distance from a candidate electron is $\Delta R < 0.2$. However, if more than one jet meets this condition, only the closest jet to the electron is dropped.
- A candidate electron is removed if its angular distance from a jet is $0.2 < \Delta R < 0.4$.
- If the angular distance between a candidate muon and jet is $\Delta R < 0.4$, the muon is removed if the jet has more than two associated tracks. Otherwise the jet is dropped.

6.4 Data Quality

The analysis used pp collision data at $\sqrt{s} = 13$ TeV, which were collected between 2015 and 2018 to give an integrated luminosity of 139 fb^{-1}. The events were recorded under stable beam conditions with all the LHC and ATLAS subdetector components operating well. The data are placed into Good Run Lists (GRLs) [148] for use in physics analyses.

6.5 Trigger Requirements

At reconstructed-level, at least one lepton was required to pass either an electron or a muon trigger. Low threshold triggers were used with $E_T > 24$ GeV for electrons and $p_T > 20$ GeV for muons in the 2015 data, and $E_T > 26$ GeV for electrons and $p_T > 26$ GeV for muons

in the 2016-2018 data. These were accompanied by high E_T and p_T threshold triggers with looser identification and isolation requirements to increase the event acceptance. The full list of triggers is detailed in Table 6.1:

Year	Lepton	Trigger
2015	Electron	HLT_e24_lhmedium (L1EM20VH)
		HLT_e60_lhmedium (L1EM22VHI)
		HLT_e120_lhloose (L1EM22VHI)
	Muon	HLT_mu20_iloose (L1MU15)
		HLT_mu50 (L1MU20)
2016-2018	Electron	HLT_e26_lhtight_nod0_ivarloose (L1EM22VHI)
		HLT_e60_lhmedium_nod0 (L1EM22VHI)
		HLT_e140_lhloose_nod0 (L1EM22VHI)
	Muon	HLT_mu26_ivarmedium (L1MU20)
		HLT_mu50 (L1MU20)

Table 6.1 The single-lepton triggers for the 2015 and 2016-2018 Run 2 datasets. The HLTs are shown outside of brackets and the Level-1 electromagnetic calorimeter and muon triggers (L1EM and L1MU) are shown inside brackets.

For the High-Level Triggers (HLTs), the "e" ("mu") followed by a number specifies that the electron (muon) candidate must have an E_T (p_T) greater than that number in GeV. The "lhtight", "lhmedium" and "lhloose" notation refers to the lepton satisfying a likelihood-based tight, medium or loose identification, and the "ivarmedium" and "ivarloose" that medium and loose p_T-dependent isolation criteria are required around the lepton [149, 150]. The "nod0" states that no requirements are made on the transverse impact parameter, d_0. For the Level-1 triggers, the number again refers to the electron E_T and muon p_T threshold, and the "V", "H" and "I" that L1Calo pseudorapidity, hadronic core energy and isolation requirements are applied (see Section 4.4).

6.6   Event Selection

To select $t\bar{t}$ dilepton events of good quality, the following criteria were required to be met for the objects in Section 6.3:

- The primary vertex to have two or more outgoing tracks, and chosen according to which vertex has the largest $\sum p_{T,\text{track}}^2$, where $p_{T,\text{track}}$ is the transverse momentum of a track associated with the vertex.

- Exactly one charged lepton with $p_T > 28$ GeV and a second charged lepton with $p_T > 25$ GeV. The leptons to be oppositely charged and of electron or muon flavour. Three channels were subsequently defined corresponding to the final-state leptons: ee, $e\mu$ and $\mu\mu$.

- At least two jets with $p_T > 25$ GeV.

- At least one b-tagged jet. Each of the three channels were further divided into two sub-channels of exactly 1 b-tag and ≥ 2 b-tag events. 1 b-tag events were accepted since it is possible for true b jets to not be identified by the MV2c10 algorithm. The 1 b-tag and ≥ 2 b-tag events were not merged since the background contributions and systematic uncertainties on background normalisation and b-jet efficiencies (see Section 6.8.1) for the two channels differ.

- For the ee and $\mu\mu$ channels, the reconstructed invariant mass of the dilepton system, $m_{l\bar{l}}$, to fall outside the Z mass window: $|m_{l\bar{l}} - m_Z| > 10$ GeV, where $m_Z = 91.2$ GeV. This reduces the background from Z + jets events.

- An additional mass cut, $m_{l\bar{l}} > 15$ GeV, in the ee (1 b-tag) and $\mu\mu$ (1 b-tag) channels to remove low mass resonances such as the J/ψ and Drell-Yan processes.

- Cuts on E_T^{miss} to further reduce the Z + jets background: $E_T^{\text{miss}} > 60$ GeV (30 GeV) in the 1 b-tag (≥ 2 b-tag) events for the ee and $\mu\mu$ channels. See Section 7.4 for detailed studies.

- Reconstruction of the $t\bar{t}$ system with the Neutrino Weighting algorithm, with a weight greater than one. See Section 6.7 for details.

Tables that show how each of the cuts affect the number of data, MC signal and MC background events in each channel are shown in Appendix B.

6.7 $t\bar{t}$ Event Reconstruction

In order to reconstruct the $t\bar{t}$ system, the four-momentum of each of the six decay products must be known, giving twenty-four degrees of freedom. The momenta of the jets and leptons, as well as the masses of all the decay products (assuming zero mass for the neutrinos) are known. The two neutrinos are not directly detected so there remain six degrees of freedom and hence an under-constrained system. Two methods that solve this problem are the Neutrino Weighter (NW) [151] and Kinematic Likelihood Fitter (KLFitter) [152].

The NW works with additional kinematic constraints. The known masses of the top quark (and hence antitop quark), and the W^+ and W^- bosons are used, removing four more degrees of freedom:

$$
(l_{1,2} + \nu_{1,2})^2 = m_W^2 = (80.4 \text{ GeV})^2
$$
$$
(l_{1,2} + \nu_{1,2} + b_{1,2})^2 = m_t^2 = (172.5 \text{ GeV})^2,
$$

(6.3)

where $l_{1,2}$, $\nu_{1,2}$, and $b_{1,2}$ are the four-momenta of the charged leptons, neutrinos and b-jets, respectively. The two final degrees of freedom are included by assuming values of the neutrino pseudorapidities ($\eta(\nu)$, $\eta(\bar{\nu}) = \eta_1$, η_2), trialling values of η_1 and η_2 between -5 and $+5$ in steps of 0.2. Equation 6.3 can now be solved, leading to solutions for each assumption of $\eta(\nu)$ and $\eta(\bar{\nu})$. Solutions leading to imaginary components, negative top or antitop energies, and $t\bar{t}$ invariant masses less than 300 GeV are discarded.

A complication is the possible presence of more than two jets per event, and the number of b-tagged jets. For 1 b-tag events, the b-tagged jet and the non-tagged jet with the highest p_T are used in the reconstruction. In the case of ≥ 2 b-tag events, the two b-tagged jets with the highest weight from the MV2c10 algorithm are used. Also, while the leptons can be matched to the top or antitop according to their charges, this is less easy with the jets. Therefore, the two

selected jets are tested in both the top and the antitop reconstruction, giving two permutations.

Sometimes, no solutions are found for Equation 6.3 for the given inputs. This may be due to incorrect object assignments from background events but also poor measurements of the four-momenta of the decay products for real signal events. To improve the signal efficiency, smearing is allowed on the kinematic quantities. The p_T values of the jets are smeared five times according to Gaussian distributions (of width 8-14% depending on the p_T value itself), and the value of m_t is varied from 171 to 174 GeV in steps of 0.5 GeV.

The measured p_X^{miss} and p_Y^{miss} values in the detector give the sum of the two neutrinos' p_X and p_Y values, respectively. These two additional degrees of freedom can be used to determine which of the solutions coming from the 51×51 neutrino η trials, 2 jet position permutations, 5×5 jet p_T smearings and 7×7 top mass scannings (giving a total of 6,372,450 possible arrangements per event) is the best. The measured p_X^{miss} and p_Y^{miss} values in the event are compared with the reconstructed values inferred from Equation 6.3, using a weight, w:

$$w = \exp\left(\frac{-(\Delta p_X^{\text{miss}})^2}{2\sigma_X^2}\right) \cdot \exp\left(\frac{-(\Delta p_Y^{\text{miss}})^2}{2\sigma_Y^2}\right), \qquad (6.4)$$

where $\Delta p_{X,Y}^{\text{miss}}$ is the difference between the measured and reconstructed missing momentum, and $\sigma_{X,Y}$ is the resolution of the measured missing momentum in the X and Y directions. The solution giving the highest weight is matched to the $t\bar{t}$ event. Cuts can be placed on w to select higher quality events.

The KLFitter first uses the NW to select values for the neutrino pseudorapidities and calculate weights according to Equation 6.4. The W mass is kept constant at 80.4 GeV and the top mass of 172.5 GeV is allowed to be smeared within its decay width of 1.4 GeV [17]. As opposed to choosing the highest value of w for the $t\bar{t}$ reconstruction, the KLFitter combines the weight

with other functions to calculate a likelihood for each jet permutation. For instance, Gaussian functions are used to determine probabilities for the neutrino pseudorapidities given the top mass. Transfer functions additionally give the probability of measuring certain kinematics for an observable (such as lepton and jet energies) given their true values. These are derived from MC, and depend on the detector geometry and resolution. The permutation and parameters giving the highest likelihood are used for the $t\bar{t}$ reconstruction.

The NW and KLFitter techniques were compared and the one giving the best performance was used for the analysis. MC for $t\bar{t}$ decays to $e\mu$ pairs was used, requiring one lepton of $p_T > 28$ GeV and the other of $p_T > 25$ GeV, and at least one b-tagged jet. For the NW, cases with no $t\bar{t}$ pair reconstruction (weight < 0) were discarded (a loss of 5.8% of the events). For the KLFitter, a candidate $t\bar{t}$ pair was always reconstructed but could be of very low likelihood. To compare the two algorithms, mean values of the reconstructed-level (reco-level) minus truth-level $\Delta|y|$, which should centre on zero, were plotted across bins of reconstructed variables (see Figures 6.6 – 6.12). The error bars show the standard errors on the means, $\sigma_m = \frac{\sigma}{\sqrt{N}}$, with σ and N the standard deviation and number of events per bin, respectively.
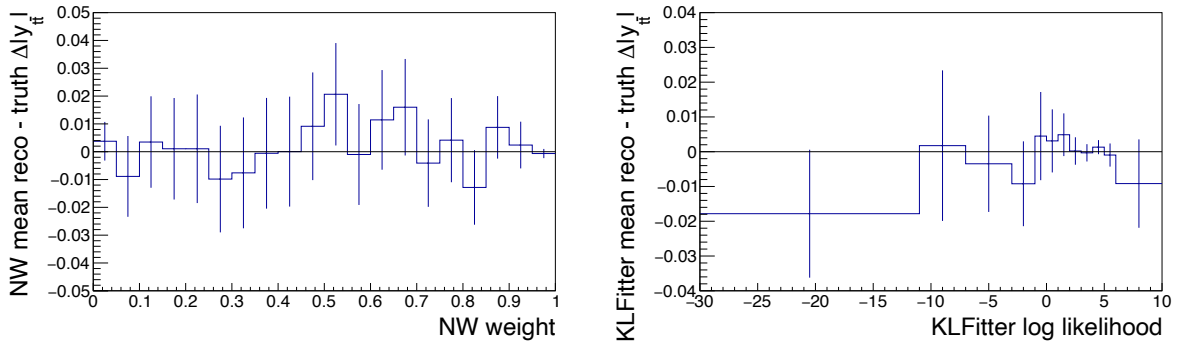
Fig. 6.6 Mean reconstructed $-$ truth $\Delta|y|$ against NW weight (left) and KLFitter log likelihood (right), the discriminants used in reconstruction quality.
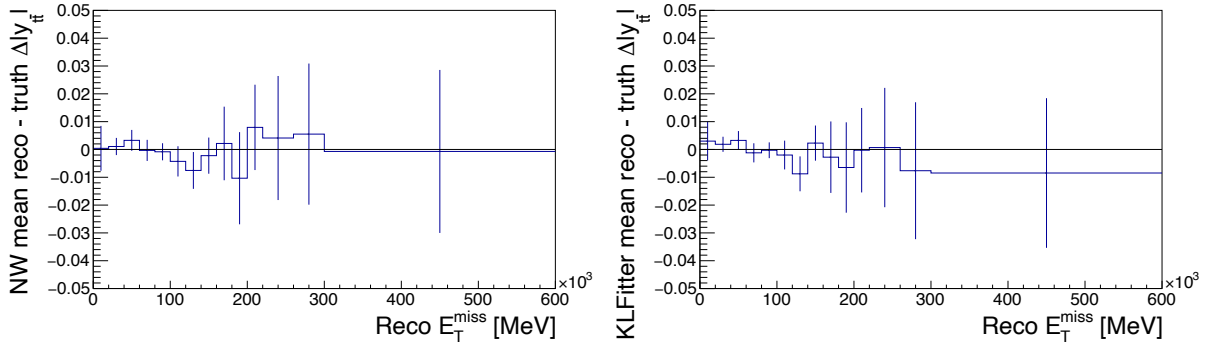
Fig. 6.7 Mean reconstructed − truth $\Delta|y|$ against reconstructed E_T^{miss} for the NW (left) and KLFitter (right).
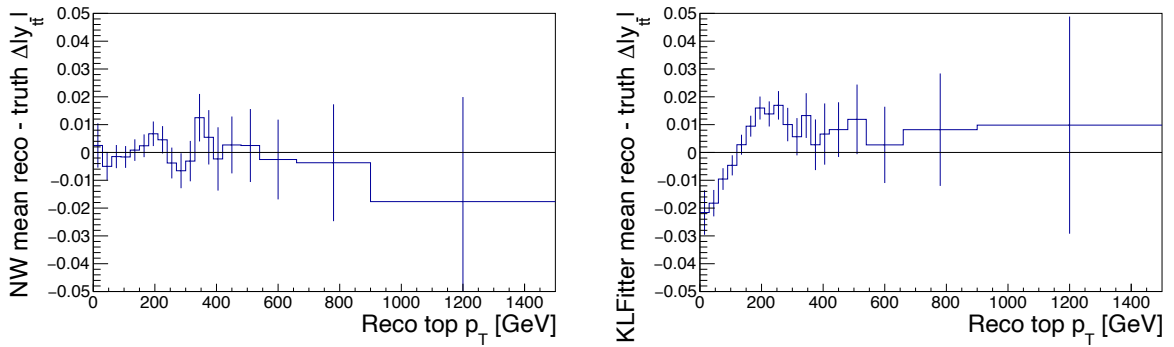
Fig. 6.8 Mean reconstructed − truth $\Delta|y|$ against reconstructed top p_T for the NW (left) and KLFitter (right).
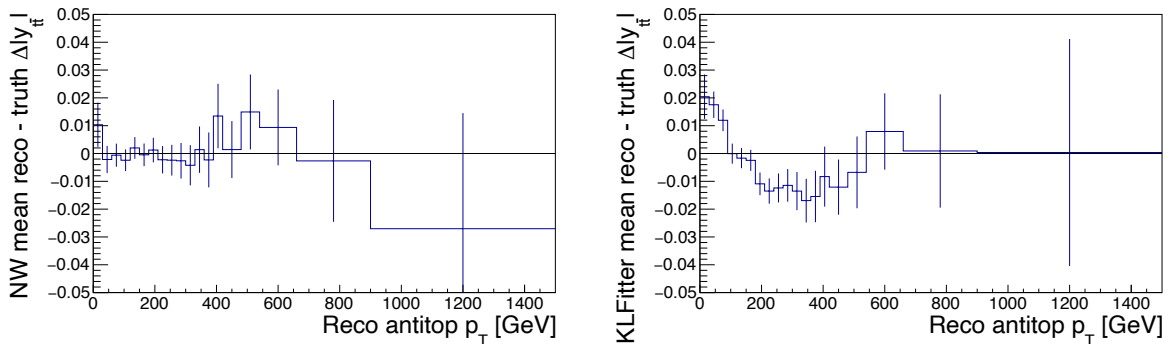
Fig. 6.9 Mean reconstructed − truth $\Delta|y|$ against reconstructed antitop p_T for the NW (left) and KLFitter (right).
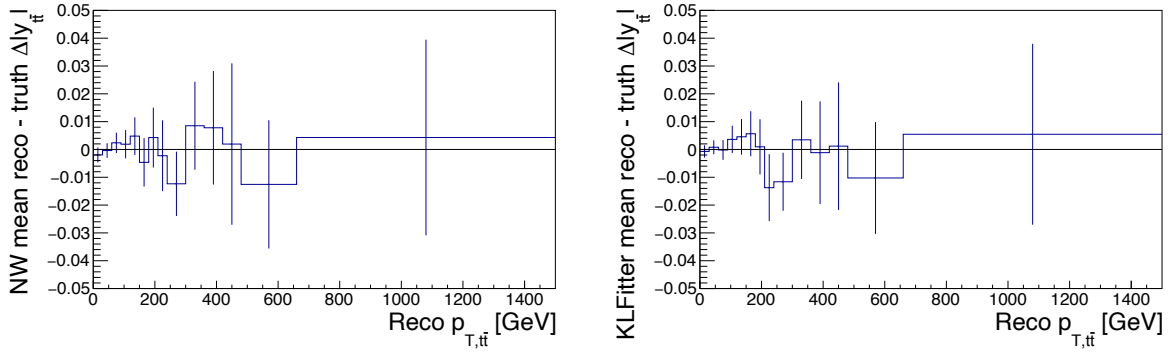
Fig. 6.10 Mean reconstructed − truth $\Delta|y|$ against reconstructed $p_{T,t\bar{t}}$ for the NW (left) and KLFitter (right).
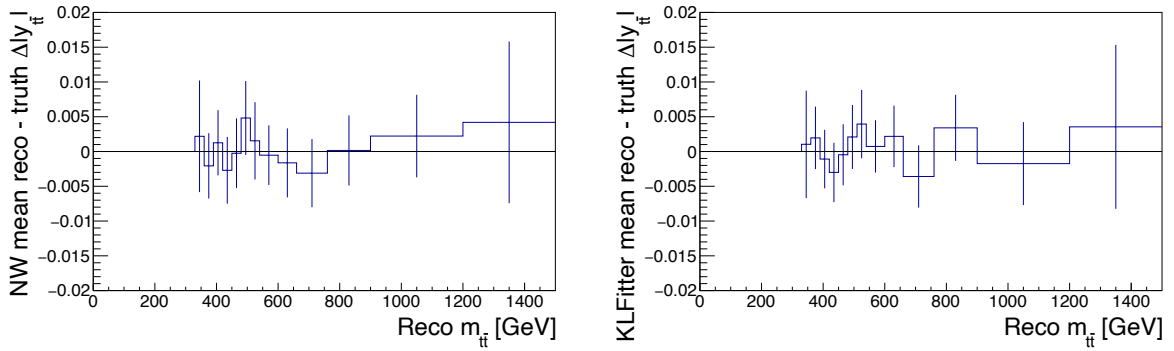
Fig. 6.11 Mean reconstructed − truth $\Delta|y|$ against reconstructed $m_{t\bar{t}}$ for the NW (left) and KLFitter (right). Invariant masses less than 300 GeV are discarded.
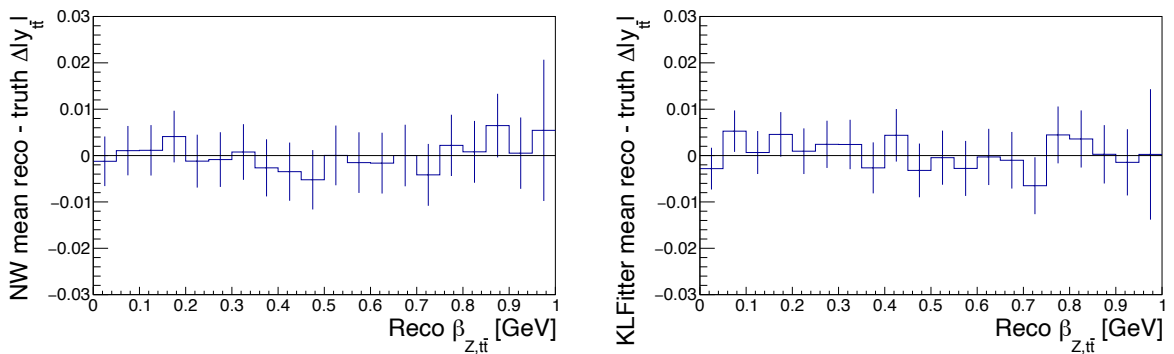
Fig. 6.12 Mean reconstructed − truth $\Delta|y|$ against reconstructed $\beta_{Z,t\bar{t}}$ for the NW (left) and KLFitter (right).

Across most of the variables, there is little difference between the two algorithms, except for the top and antitop p_T, which shows a poor reconstruction in the KLFitter. To help improve the KLFitter selection quality, events of log likelihood < 0 were discarded (a loss of 7.8% of the events). This improves the p_T dependence to a small degree, as shown in Figure 6.13.
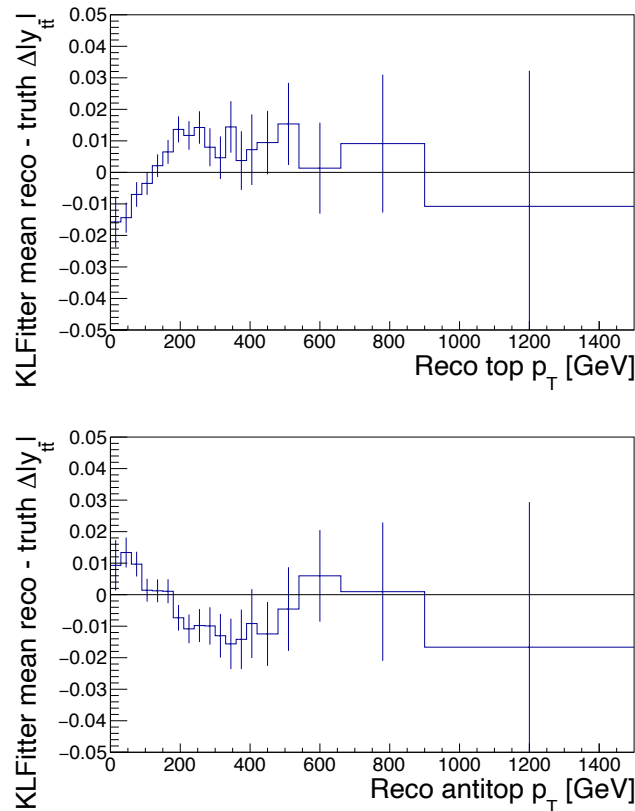
Fig. 6.13 Mean reconstructed $-$ truth $\Delta|y|$ against reconstructed top p_T (upper plot) and antitop p_T (lower plot) for the KLFitter. Here, events of log likelihood < 0 are removed. The reconstruction is slightly improved with respect to the right-hand side plots of Figures 6.8 and 6.9.

A further test was to look at the performance of mean reconstructed-level minus truth-level values for variables other than $\Delta|y|$ plotted against their truth-level values. These in general should centre on zero, but are subject to edge effects. For example, for large positive and negative values in truth top and antitop y, the lack of detector acceptance for leptons at $|\eta| > 2.5$ disallows extreme reconstructed-level values for the top and antitop. This causes

non-zero behaviour in the outer regions of Figures 6.14 and 6.15. A similar effect is seen for $m_{t\bar{t}}$, where the cut of 300 GeV causes a positive bias in the lower mass bins. However, the response matrices described later in Section 7.1 can model this approximately. For the tests, the NW weight > 0 and KLFitter log likelihood > 0 requirements were used. The error bars show the standard errors on the means.
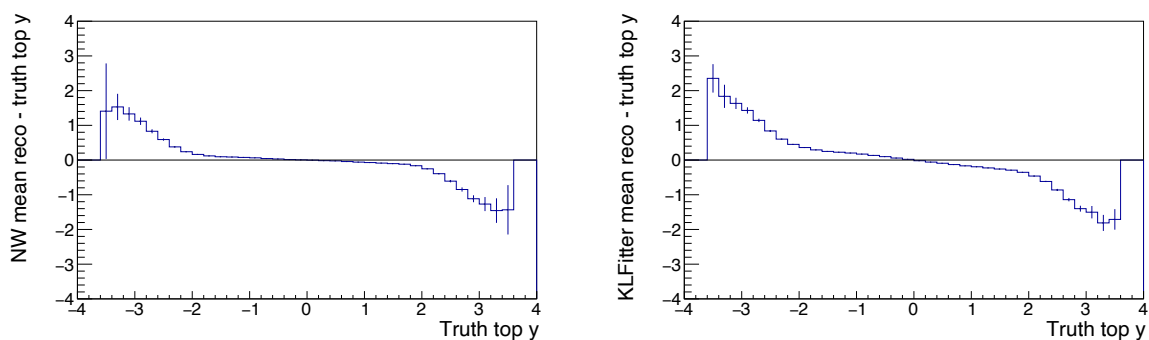
Fig. 6.14 Mean reconstructed $-$ truth top y against truth top y for the NW (left) and KLFitter (right).
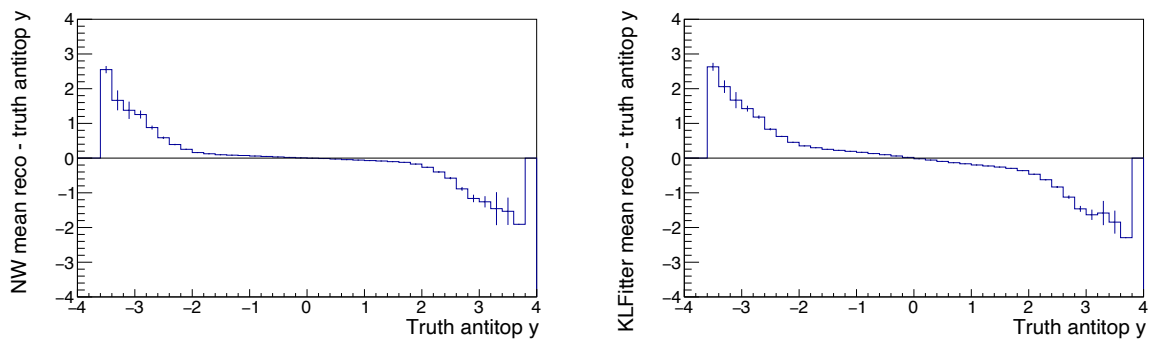
Fig. 6.15 Mean reconstructed $-$ truth antitop y against truth antitop y for the NW (left) and KLFitter (right).
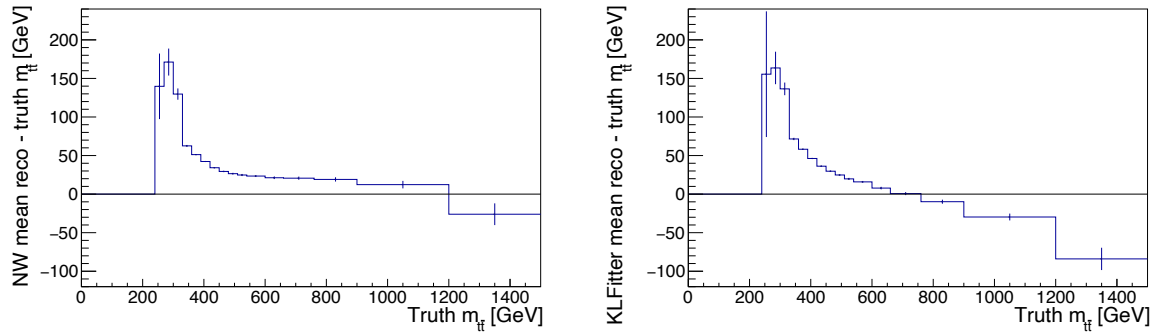
Fig. 6.16 Mean reconstructed − truth $m_{t\bar{t}}$ against truth $m_{t\bar{t}}$ for the NW (left) and KLFitter (right).

The NW and KLFitter show similar performance across the truth-level variables, but with slightly flatter distributions for y and $m_{t\bar{t}}$ in the NW plots. From these results, and with a smaller loss in signal events with NW weight > 0 compared with KLFitter log likelihood > 0, and due to the faster processing time of the NW, it was decided to use the NW for $t\bar{t}$ reconstruction.

6.8   Systematic Uncertainties

In addition to Poisson statistical fluctuations, systematic uncertainties (known also as nuisance parameters, NPs, within the unfolding framework discussed in Chapter 7) affect the number of selected events and kinematic distributions at reconstructed-level and therefore the charge asymmetry values. The uncertainties fall into two broad groups: experimental and modelling uncertainties, which can affect either or both the signal and background MC. For the modelling uncertainties, the MC was sometimes generated with ATLAS fast simulation software, ATLFAST 2.0 (AFII) [153] to reduce the MC processing time. This uses a faster calorimeter simulation than the default in GEANT4, but does reduce the reconstruction accuracy. To show the true effect of the systematic uncertainty, AFII samples that are not shifted by the uncertainty were also generated. The systematically-shifted and non-shifted

AFII samples were compared and the difference used as an uncertainty on the full simulation sample. These cases are specified in the text.

6.8.1 Experimental Uncertainties

6.8.1.1 Luminosity

The uncertainty on the full Run 2 integrated luminosity is 1.7% [154]. This was determined from beam separation scans (van der Meer scans [155, 156]) in dedicated low luminosity runs and calibrated to the high luminosity data-taking runs.

6.8.1.2 Pile-Up

The PileupReweighting tool [157] was used to correct the MC pile-up distributions to match those in data. A systematic uncertainty arises through variations of the scale factors in the tool by $\pm 1\sigma$.

6.8.1.3 Jet Vertex Tagger Efficiency

Scale factors to correct for differences in the JVT efficiency between MC and data are extracted from $Z \rightarrow \mu^+\mu^-$ and $t\bar{t}$ events [158]. Uncertainties on the factors come from statistical errors, different choices of MC generator and varying the event selection to increase the contribution from pile-up jets. These are incorporated into a single uncertainty.

6.8.1.4 Jet Energy Scale

Jets clustered with the anti-k_T algorithm have their energies calibrated to account for kinematic dependencies, the calorimeter materials, energy losses due to dead cells, leakage outside the calorimeter acceptance and deposits below noise thresholds, as well as excess energy due to pile-up [159, 160]. This correction is known as the jet energy scale (JES). The sources of uncertainty on the JES used in the analysis are listed below:

- Pile-up:

  - The average jet energy density in the $\eta - \phi$ plane, ρ, used in the area subtraction method [141].

  - The number of additional pp collisions per bunch crossing, μ.

  - The number of reconstructed primary vertices in an event, N_{PV}.

  - The p_T dependence of the N_{PV} and μ pile-up terms as a residual uncertainty.

- Jet response in the central calorimeter regions (low $|\eta|$) across p_T. Events producing well-calibrated Z/γ bosons with a low p_T jet recoiling against the boson, and multijet topologies with a high p_T jet recoiling against well calibrated low p_T jets are used to calibrate central jets. A large range of uncertainties such as the lepton and photon energy scales and resolutions of the boson decay products, JVT, MC generator choice, jet angular measurements and statistical uncertainties are present. Many of these are combined and reduced in number with an eigenvector decomposition method [160] to give:

  - Physics modelling effects (4 NPs).

  - Detector effects (2 NPs).

  - Effects which which cannot be fully attributed to either a detector or a modelling uncertainty - hence labelled "mixed" (3 NPs).

  - Statistical fluctuations (6 NPs).

- η-intercalibration. The response of the calorimeter is less well understood in the forward regions (high $|\eta|$). As such, dijet events with one jet in the well-calibrated central region and one jet in the forward region are studied. The p_T of the jets should be balanced at NLO in QCD and so the forward jets are corrected. Uncertainties include:

  - Mismodelling of physics effects in MC generator choice, pile-up and event topologies.

– Data-MC disagreement in $\eta < 0$, $\eta > 0$, and high energy regions.

– Statistical fluctuations.

• Very high p_T jets of > 2 TeV that are beyond the reach of the above methods.

• Data-MC differences in the degree of punch-through of jets from the hadronic calorimeter to the muon system.

• Jets originating from light quarks, b quarks and gluons have different responses in the calorimeter:

– Relative proportion of quarks to gluon jets.

– Detector response from different jet flavours (split into light jets and b-jets).

6.8.1.5 Jet Energy Resolution

The precision of the jet energy about its central value is termed the Jet Energy Resolution (JER):

$$\frac{\sigma(p_T)}{p_T} = \frac{N}{p_T} \oplus \frac{S}{\sqrt{p_T}} \oplus C, \tag{6.5}$$

where N is the noise from electronics and pile-up, S a stochastic term from sampling in the calorimeter and C a p_T-independent constant term. Contributions to these terms are determined in data through measurements of dijet and Z/γ + jets events across jet p_T and η, taking into account pile-up, and are also established in MC [159]. An eigenvector decomposition combines and decorrelates the contributions resulting in seven overall nuisance parameters. An eighth uncertainty comes from the data-MC difference, in which the JER is smeared further if the JER from data measurements is greater than that in the MC simulation, but no additional smearing is made if the MC JER is greater than the data JER.

6.8.1.6 Jet Flavour Tagging

Scale factors adjust for data-MC efficiency differences in correctly tagging jets as b-jets and incorrectly tagging c- and light jets as b-jets with the MV2c10 algorithm [145, 161, 162].

These are derived in samples containing a high purity of the different jet flavours. The numerous sources of uncertainty on the factors are combined using eigenvector decomposition into a smaller set. Two additional uncertainties are assigned on the extrapolation of b-jet and c-jet efficiencies to high p_T.

- b-jet efficiencies (9 NPs and extrapolation uncertainty).
- c-jet efficiencies (4 NPs and extrapolation uncertainty).
- Light jet efficiencies (5 NPs).

6.8.1.7 Lepton Efficiency Scale Factors and Track Uncertainties

As described in 6.3.1 and 6.3.2, efficiencies in lepton reconstruction, identification, isolation and trigger performance are obtained with tag-and-probe methods using Z and J/ψ decays. These are calculated in both data and MC and the data-MC ratios used as scale factors (usually close to one) to correct the simulation yields [136, 138]. Uncertainties on these factors are established by varying selection requirements on the tag-and-probe leptons as well as fit models of the signal and background, for example. For muons, the uncertainties are split further into their statistical and systematic components. The uncertainties used in the analysis are shown below:

- Reconstruction - a single uncertainty for electrons.
- Identification - one electron and two muon (statistical and systematic) uncertainties.
- Isolation - one electron and two muon (statistical and systematic) uncertainties.
- Trigger - one electron and two muon (statistical and systematic) uncertainties.
- Track-to-vertex association of muons to the hard-scatter vertex.

Alignment imperfections and deformities in the detector cause asymmetric track curvature measurements in positive and negative muons, known as sagitta variations. Corrections are applied from $Z \rightarrow \mu^+\mu^-$ events. An uncertainty comes from this calibration as well as a residual uncertainty after the correction [163].

6.8.1.8 Lepton Energy Scales and Resolutions

Additional data-MC corrections are made on the electron and muon energy scales (the calibration of energy deposits in the EM or muon calorimeters to candidate lepton energies) and their resolutions (sizes of the energy uncertainties compared with their energies) using $Z \rightarrow l^+l^-$ and $J/\psi \rightarrow l^+l^-$ decays (and $W \rightarrow e\nu$ decays for electrons) [164, 138]. Uncertainties on the lepton scales and resolutions are determined by varying the signal and background fits and sizes of the invariant mass windows for the decays, as well as in modelling the detector materials. The electron and muon energy scales each have one associated uncertainty. The electron resolution has one uncertainty and the muon resolution has one uncertainty component from the inner detector and another from the muon system.

6.8.1.9 Missing Transverse Energy Scale and Resolution

The E_T^{miss} estimation includes signals associated with reconstructed objects, coined the hard term, as well as detector signals not associated with objects, known as the soft term, as described in Section 6.3.5. Uncertainties on the hard term are accounted for in the objects themselves but separate systematic uncertainties are applied to the soft term. $Z \rightarrow \mu^+\mu^-$ and $Z \rightarrow e^+e^-$ events are used where the soft term transverse momentum, p_T^{soft}, should be balanced against the hard term transverse momentum, p_T^{hard} [165, 166]. Differences between data and different MC generators are used to determine three uncertainties:

- Energy scale - the mean value of the parallel projection of p_T^{soft} against p_T^{hard}, $p_{\parallel}^{\mathrm{soft}}$.
- Parallel energy resolution - the root-mean-square of $p_{\parallel}^{\mathrm{soft}}$.
- Perpendicular energy resolution - the root-mean-square of the perpendicular projection of p_T^{soft} against p_T^{hard}, $p_{\perp}^{\mathrm{soft}}$.

6.8.2 $t\bar{t}$ Signal Modelling

6.8.2.1 $t\bar{t}$ Parton Shower and Hadronisation Modelling

The MC generator choice can yield differences in the output distributions of simulated events and so the parton shower and hadronisation generator was investigated[1]. The POWHEG BOX v2 generator was interfaced with Herwig7.04 [167, 168] using a set of default tuning parameters in Herwig known as the H7-UE tune [168] based on the MMHT14 LO PDF set [169]. This was run through the AFII ATLAS simulation and so compared with the AFII Powheg + Pythia8 MC.

6.8.2.2 $t\bar{t}$ Radiation Modelling

Since ISR and FSR strongly affect the degree of charge asymmetry, uncertainties in their emission were accounted for in the analysis:

- Variation of ISR μ_R factor by a multiple of 0.5 and 2 in the matrix element generators.
- Variation of ISR μ_F factor by a multiple of 0.5 and 2 in the matrix element generators.
- Up and down variation of α_s in the showering parameter, Var3c of the A14 tune [128], for ISR.
- Changing the h_{damp} parameter from 1.5 m_t to 3 m_t.
- Variation of α_s for FSR QCD emission by shifting the μ_R factor by a multiple of 0.5 and 2 in the parton shower generators.

6.8.2.3 $t\bar{t}$ Parton Distribution Functions

The uncertainties on the quark and gluon PDFs are described in the PDF4LHC framework [170]. Uncertainties from the NNPDF3.0 [96], MMHT14 [169] and CT14 [171] PDF sets are

---

[1]A further systematic uncertainty can be accounted for by varying the matrix element generator and keeping the parton shower and hadronisation generator the same. A MG5_aMC sample interfaced with Pythia8 does exist, although the differences in matching between the two generators yields an unfair comparison with Powheg + Pythia8. At the time of writing, the ATLAS recommendation was to neglect this uncertainty.

combined into 30 eigenvector nuisance parameters. These variations were stored as weights in the $t\bar{t}$ Powheg + Pythia8 sample and the systematic uncertainties obtained by comparing the 30 variations with the baseline PDF4LHC15 prediction.

6.8.2.4 $t\bar{t}$ Mass

To account for a possible variation in charge asymmetry with top mass, four samples of $m_t = 171, 172, 173$ and 174 GeV were produced. These were generated in AFII through POWHEG BOX v2 interfaced with Pythia8.230 using the same PDF sets and tuning parameters as for the 172.5 GeV sample. The mass sample giving the largest variation across $\Delta|y|$ and $\Delta|\eta|$ compared with the AFII 172.5 GeV sample (in this case 173 GeV) was used to evaluate the uncertainty.

6.8.3 Background Uncertainties

6.8.3.1 Single Top tW Process Diagram Removal vs Diagram Subtraction

In addition to Diagram Removal (DR) (see Section 6.1.2), Diagram Subtraction (DS) [131] can be used to prevent double-counting of events from the LO $t\bar{t}$ and NLO single top tW processes. In DS, the NLO tW cross-section (rather than the amplitude as for DR) is modified to include a subtraction term to cancel the $t\bar{t}$ contribution. The difference between the DR and DS methods on the distribution of single top events across $\Delta|y|$ and $\Delta|\eta|$ was included as a systematic uncertainty.

6.8.3.2 Single Top Parton Shower and Hadronisation Modelling

As for $t\bar{t}$ modelling, the effect from a different parton shower and hadronisation generator was evaluated for single top events. The POWHEG BOX v2 generator was interfaced with Herwig7.04 using the H7-UE tune and MMHT14 LO PDF set. This was run through AFII and so compared with the AFII Powheg + Pythia8 single top MC.

6.8.3.3   Single Top Radiation Modelling

Variation of μ_R and μ_F, both by factors of 0.5 and 2, in the single top matrix element generator give uncertainties on the magnitude of ISR emission. Adjusting the value of μ_R by a factor of 0.5 and 2 in the parton shower generator changes the extent of QCD emission and yields an uncertainty on FSR.

6.8.3.4 Z + Jets Scale Variations

Variation of the μ_R and μ_F scales by factors of 0.5 and 2 on the Z + jets samples leads to an additional uncertainty.

6.8.3.5   Cross-Section and Normalisation

For the single top, diboson and rare SM background processes, calculations adjusting the μ_R and μ_F scales and varying the PDFs within their uncertainties are performed leading to uncertainties on their cross-sections. The values used in the analysis were 5.3% for single top [172, 173], 6% for diboson [174] and 13% for the rare SM backgrounds [175]. The Z + jets and fake lepton background uncertainties were determined in control regions (see Section 6.9). Normalisation uncertainties of 30% were applied to the Z + jets events, 30% for the fake lepton ee and $e\mu$ events, and 50% for the fake lepton $\mu\mu$ events.

6.9 Z + Jets and Fake Lepton Normalisation Factors

6.9.1 Z + Jets

For the ee and $\mu\mu$ channels, scaling factors were applied to the Z + jets backgrounds due to the difficulty of modelling the heavy flavour contributions in MC. For the $e\mu$ channels, Z + jets events are produced where the Z decays to $\tau^+\tau^-$ with one τ weakly decaying to an

electron and the other to a muon. This mechanism yields far fewer events so no scale factors were determined in the $e\mu$ channels. To increase the statistics and given the processes are similar, the ee (1 b-tag) and $\mu\mu$ (1 b-tag) channels were merged, as well as the ee (≥ 2 b-tag) and $\mu\mu$ (≥ 2 b-tag) channels and labelled the $ee + \mu\mu$ (1 b-tag) and $ee + \mu\mu$ (≥ 2 b-tag) channels, respectively. The proportion of light, c and b jets differs significantly between the 1 b-tag and ≥ 2 b-tag events so these events were not merged. The Z boson mass window ($|m_{l\bar{l}} - m_Z| < 10$ GeV) of opposite-sign (OS) leptons was used as a control region to scale the Z + jets MC (labelled the "OSZ" region). The E_T^{miss} cuts were not applied in order to increase the number of Z + jets events in the control region. However, factors with E_T^{miss} cuts were also calculated as a comparison. The scale factors, μ_Z, were then calculated according to the following formula:

$$\mu_Z = \frac{N_{\mathrm{Data}} - (N_{\mathrm{predicted} - Z + \mathrm{jets}})}{N_{Z + \mathrm{jets}}},\tag{6.6}$$

where N_{Data} is the number of data events in the channel, $N_{\mathrm{predicted} - Z + \mathrm{jets}}$ is the number of predicted MC events excluding the Z + jets events and $N_{Z + \mathrm{jets}}$ the number of Z + jets events in the MC. The event yields for the 1 b-tag and ≥ 2 b-tag channels are shown in Table 6.2. The extracted μ_Z scale factors are shown below the data field in each channel. The uncertainties on the event numbers and μ_Z scale factors include the statistical and systematic uncertainties. The factors evaluated with the E_T^{miss} cuts are also shown in the table with their statistical uncertainties.

The OSZ control region events before and after application of the μ_Z factors for the 1 b-tag and ≥ 2 b-tag cases are shown in Figure 6.17 as a function of the $t\bar{t}$ signal variable, $\Delta|y|$.

Conservative 30% uncertainties on the factors were applied to cover the differences with and without the E_T^{miss} cuts, as well as shape dependencies on the factors across the inclusive

Sample	$ee + \mu\mu$ (1 b-tag)			$ee + \mu\mu$ (≥ 2 b-tags)		
$t\bar{t}$	28530	$\pm$	550	32400	$\pm$	1100
Single top	1900	$\pm$	100	773	$\pm$	42
Diboson	3600	$\pm$	230	788	$\pm$	55
Z + jets	392800	$\pm$	8200	50300	$\pm$	1100
Rare SM	757	$\pm$	99	608	$\pm$	79
Fake lepton	5550	$\pm$	170	1260	$\pm$	44
Prediction	433200	$\pm$	8200	86200	$\pm$	1600
Data		515182			105558	
μ_Z	1.21	$\pm$	0.03	1.39	$\pm$	0.04
μ_Z (with E_T^{miss} cut)	1.23	$\pm$	0.02	1.47	$\pm$	0.02

Table 6.2 Event yields and Z + jets scale factors in the OSZ control region for the merged $ee + \mu\mu$ channels. The uncertainties include the statistical and systematic uncertainties summed in quadrature except on the μ_Z values with the E_T^{miss} cuts, which only include statistical uncertainties.

and differential variables. The plots in Figure 6.18 show the residual μ_Z factors across bins of $p_{T,l\bar{l}}$ for the $ee + \mu\mu$ 1 b-tag and ≥ 2 b-tag channels after the global factors have been applied. For low p_T, the global factor is too large but at high p_T, it is too small. However, the 30% normalisation uncertainties cover this trend. The other differential variables were shown to have much smaller shape dependencies.

A 30% background normalisation uncertainty was also applied to the Z + jets events in the $e\mu$ 1 b-tag and ≥ 2 b-tag channels, which have no derived scaling factor. The final global Z + jets scale factors and uncertainties for all channels are summarised in Table 6.3. These were then applied to the Z + jets events in the signal regions where the uncertainties have negligible impact on the overall charge asymmetry uncertainties.
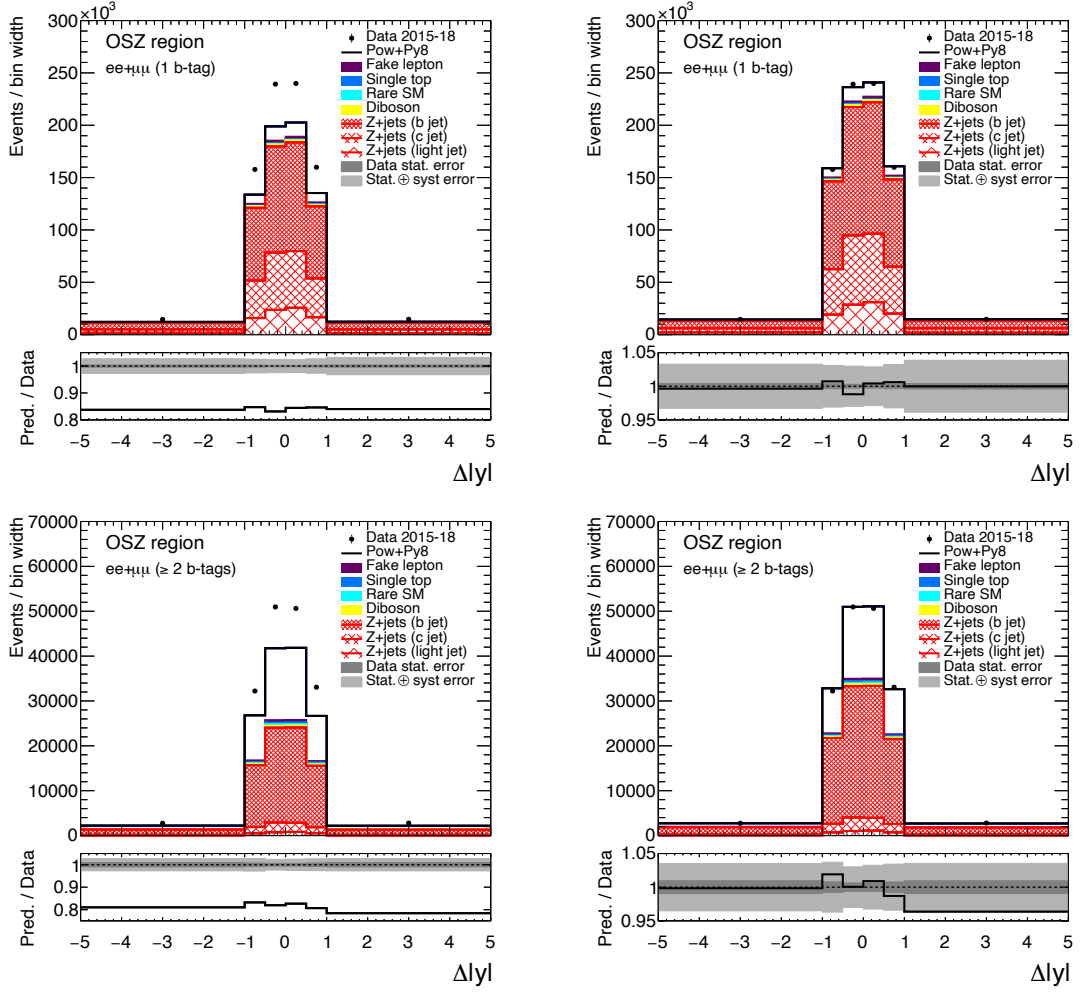
Fig. 6.17 The events in the $ee + \mu\mu$ 1 b-tag (upper plots) and ≥ 2 b-tag (lower plots) OSZ regions across the $t\bar{t}$ $\Delta|y|$ variable before (left) and after (right) the μ_Z factors are applied. The breakdown of light, c and b quark Z + jets events is shown, which differs for the two regions. Uncertainties on the data points are plotted but are too small to see.

Channel	μ_Z
$ee + \mu\mu$ (1 b-tag)	1.21 ± 0.36
$ee + \mu\mu$ (≥ 2 b-tags)	1.39 ± 0.42
$e\mu$ (1 b-tag)	1.00 ± 0.30
$e\mu$ (≥ 2 b-tags)	1.00 ± 0.30

Table 6.3 Final Z + jets scaling factors for the four channels with their overall background normalisation uncertainties.
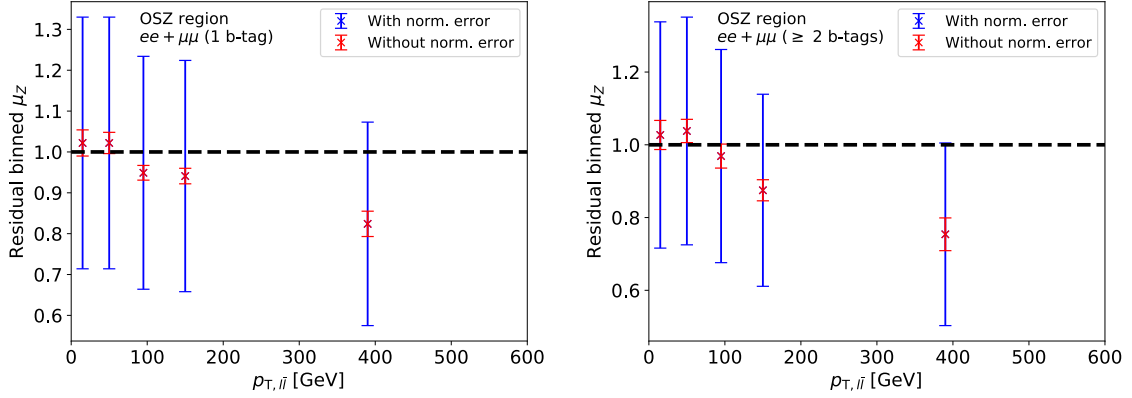
Fig. 6.18 The residual binned μ_Z factors in the $ee + \mu\mu$ 1 b-tag (left) and ≥ 2 b-tag (right) OSZ regions across the $p_{T,l\bar{l}}$ variable after the global μ_Z factors are applied. The uncertainties before (red error bars) and after (blue error bars) the 30% Z + jets background uncertainties are included are shown.

6.9.2 Fake Leptons

As for Z + jets, data-MC agreement for fake leptons can be poor due to inaccurate modelling of their individual sources. A same-sign lepton control region (denoted "SS"), where the events are dominated by those containing fake leptons, was used to scale the MC prediction. Misidentification of muons is less likely than for electrons owing to good momentum matching between the muon system and inner detector. Therefore, the ee and $e\mu$ channels were merged (labelled $ee + e\mu$) since the electron is most likely to be the fake lepton candidate, and the $\mu\mu$ channels were treated separately. The scale factors, μ_{Fake}, were determined for the $ee + e\mu$ and $\mu\mu$ channels in both the 1 b-tag and ≥ 2 b-tag cases:

$$\mu_{\text{Fake}} = \frac{N_{\text{Data}} - (N_{\text{predicted – fake}})}{N_{\text{fake}}}, \tag{6.7}$$

where N_{Data} is the number of data events, $N_{\text{predicted – fake}}$ is the number of predicted MC events excluding the fake lepton events and N_{fake} the number of MC fake lepton events. Tables 6.4 and 6.5 show the event yields in the SS region for the $ee + e\mu$ and $\mu\mu$ channels for both the 1 b-tag and ≥ 2 b-tag events. The numbers from the tables were then substituted into

Equation 6.7 to obtain the fake lepton scale factors, which are shown below the data field in each channel. The uncertainties on the event numbers and μ_{Fake} scale factors include the statistical and systematic uncertainties.

A possible data-MC mismatch in the fraction of events where an electron is incorrectly identified with the wrong charge (charge-flipped) was investigated. Events in the SS region that come from dilepton $t\bar{t}$, single top and Z + jets processes will certainly have an electron candidate with the wrong charge. To investigate the mismatch, two regions were considered: the Z mass window of same-sign events (denoted "SSZ" region) that contains predominantly charge-flipped leptons, and the Z mass window of OS events (labelled "OSZ" region, the same used in the μ_Z estimation) that will usually have correctly assigned lepton charges. The ratio of SSZ to OSZ events in data was compared with that in MC. Only the $ee + e\mu$ channels were considered since a muon in the $\mu\mu$ channels is very unlikely to be assigned the wrong charge, again due to the good matching of inner detector and muon system tracks. The MC fake leptons were scaled by both the μ_Z and μ_{Fake} factors first in these two regions to ensure any data-MC discrepancies were really due to charge misidentification and not the background normalisation. The disagreement can be seen across the electron η variable, with the charge-flip probability slightly overestimated in MC relative to data (see Figure 6.19). To account for this, the $t\bar{t}$, single top and Z + jets MC contributions in the SS region (outside the Z window) were reweighted for the discrepancy across electron η and the μ_{Fake} scale factors were recalculated. These new scale factors are also shown at the bottom of Table 6.4 with their statistical uncertainties. Their differences with the non-weighted scale factors were incorporated into the fake lepton normalisation uncertainty.
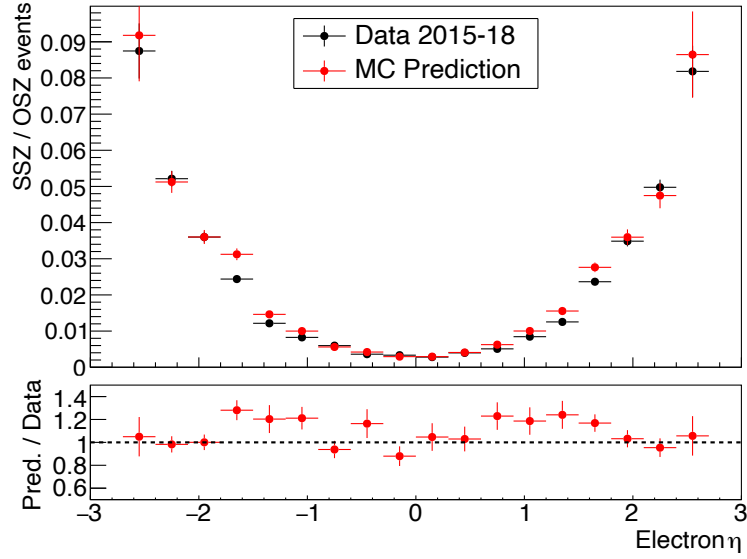
Fig. 6.19 Ratio of SSZ to OSZ events across electron η for data (black) and MC (red). The error bars show the statistical uncertainties.

Sample	$ee + e\mu$ (1 b-tag)			$ee + e\mu$ (≥ 2 b-tags)		
$t\bar{t}$	751	$\pm$	22	701	$\pm$	30
Single top	55.0	$\pm$	4.0	29.7	$\pm$	2.6
Diboson	278	$\pm$	21	22.6	$\pm$	1.8
Z + jets	16.1	$\pm$	4.6	10.2	$\pm$	3.2
Rare SM	586	$\pm$	76	519	$\pm$	68
Fake lepton	2649	$\pm$	48	1875	$\pm$	47
Prediction	4335	$\pm$	95	3158	$\pm$	88
Data	4230			3049		
μ_{Fake}	0.96	$\pm$	0.04	0.94	$\pm$	0.06
μ_{Fake} (charge-flip reweight)	0.98	$\pm$	0.02	0.98	$\pm$	0.02

Table 6.4 Event yields and fake lepton scale factors in the SS control region for the merged $ee + e\mu$ channels. The uncertainties include the statistical and systematic uncertainties summed in quadrature except on the μ_{Fake} values with the charge-flip corrections, which only include statistical uncertainties.

The SS control region events before and after application of the non-weighted μ_{Fake} factors for the 1 b-tag and ≥ 2 b-tag cases are shown for the $ee + e\mu$ and $\mu\mu$ channels in Figures 6.20 and 6.21, respectively. The variable shown is dilepton $\Delta|\eta|$ since $t\bar{t}$ events from SS leptons cannot be reconstructed in the NW.

Sample	$\mu\mu$ (1 b-tag)	$\mu\mu$ (≥ 2 b-tags)
$t\bar{t}$	0.15 ± 0.10	0 ± 0
Single top	0 ± 0	0 ± 0
Diboson	40.8 ± 3.3	5.85 ± 0.53
Z + jets	0.02 ± 0.03	0.04 ± 0.04
Rare SM	129 ± 17	154 ± 20
Fake lepton	63.3 ± 4.3	24.1 ± 2.5
Prediction	234 ± 18	184 ± 20
Data	319	261
μ_{Fake}	2.3 ± 0.4	4.2 ± 1.2

Table 6.5 Event yields and fake lepton scale factors in the SS control region for the $\mu\mu$ channels. The uncertainties include the statistical and systematic uncertainties summed in quadrature.
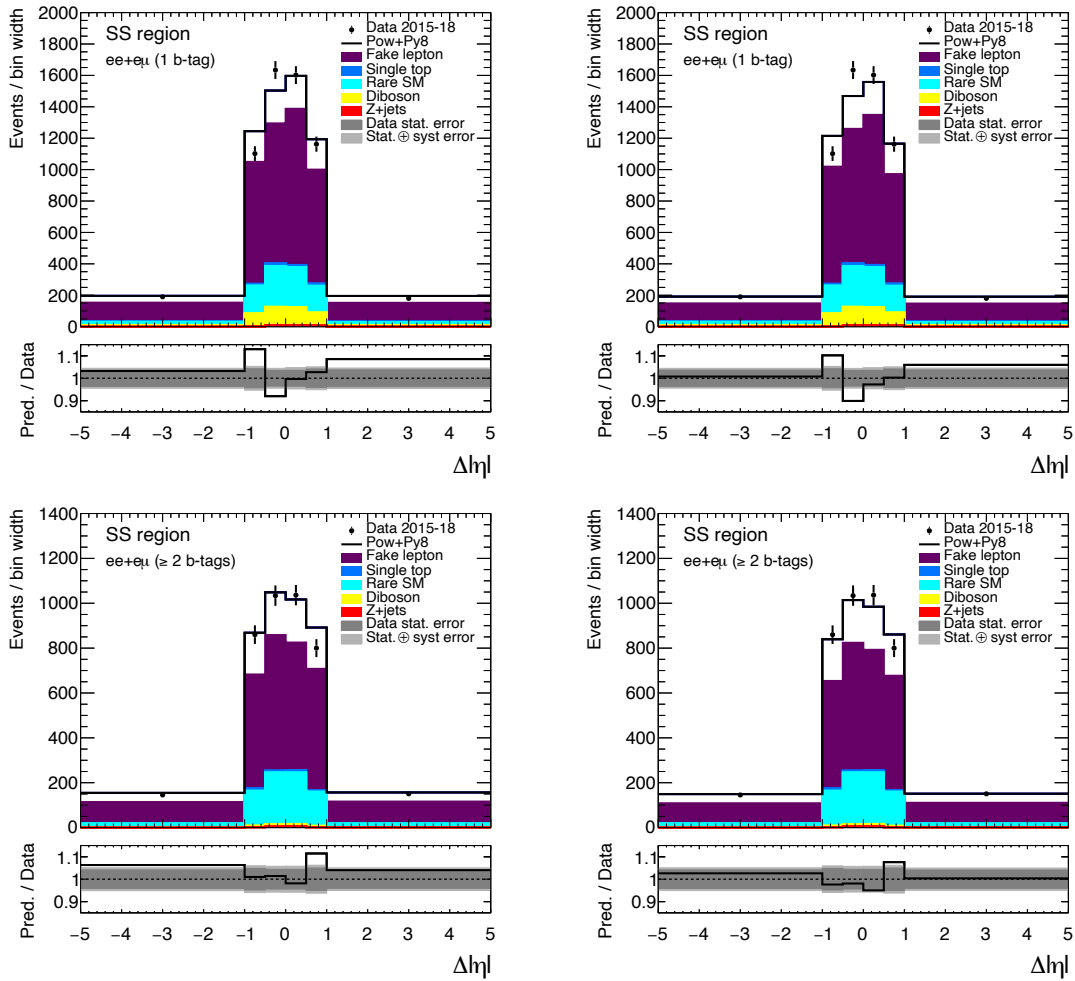
Fig. 6.20 The events in the $ee + e\mu$ 1 b-tag (upper plots) and ≥ 2 b-tag (lower plots) SS regions across the dilepton $\Delta|\eta|$ variable before (left) and after (right) the μ_{Fake} factors are applied.
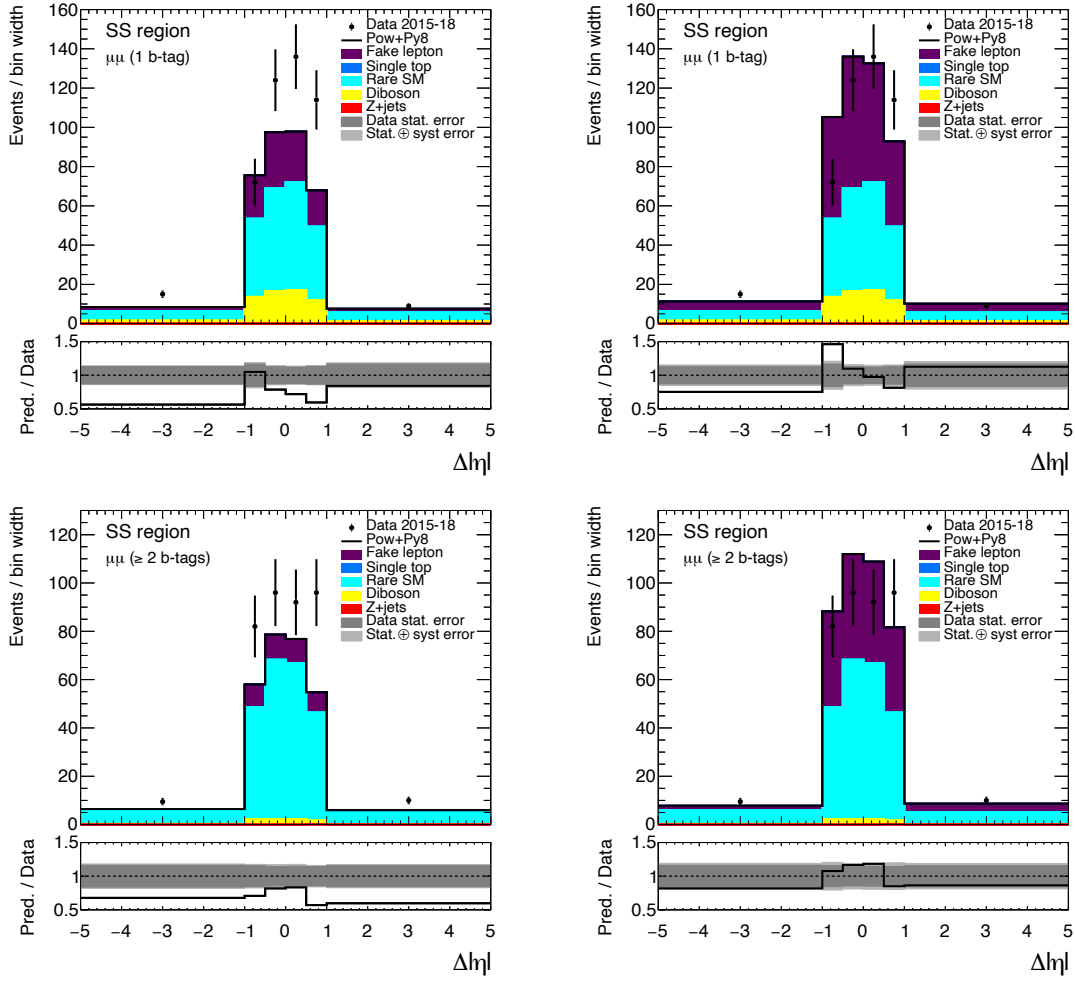
Fig. 6.21 The events in the $\mu\mu$ 1 b-tag (upper plots) and ≥ 2 b-tag (lower plots) SS regions across the dilepton $\Delta|\eta|$ variable before (left) and after (right) the μ_{Fake} factors are applied.

For the $ee + e\mu$ channels, Table 6.4 shows the overall integral of data and MC is in good agreement and so the fake lepton factors are close to one. However, the uncertainties do not account for the charge-flip differences or fully cover the shape differences across the inclusive and differential variables, such as in Figure 6.20. Therefore, 30% uncertainties were applied to the factors. The plots in Figure 6.22 show the residual μ_{Fake} factors for the $ee + e\mu$ 1 b-tag and ≥ 2 b-tag channels after the global factors have been applied. The 30% fake lepton normalisation uncertainties fully cover any shape dependencies.
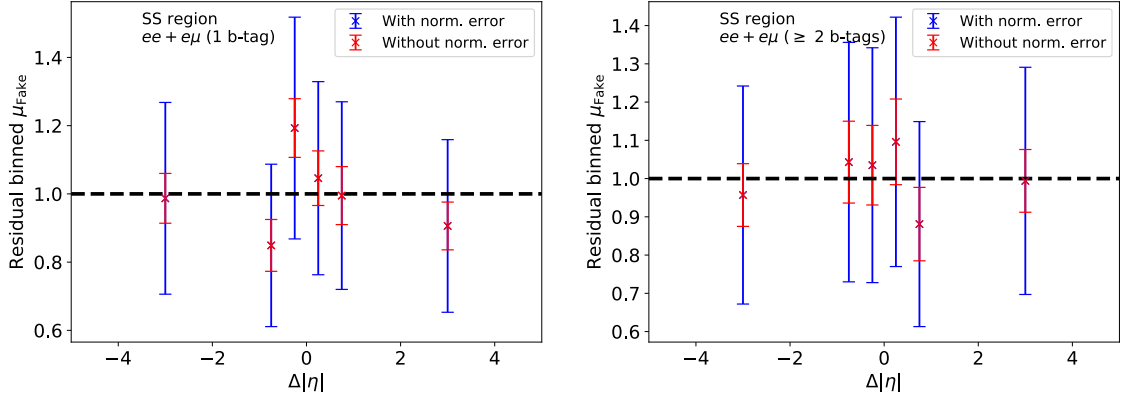
Fig. 6.22 The residual binned μ_{Fake} factors in the $ee + e\mu$ 1 b-tag (left) and ≥ 2 b-tag (right) SS regions across the $\Delta|\eta|$ variable after the global μ_{Fake} factors are applied. The uncertainties before (red error bars) and after (blue error bars) the 30% fake lepton background uncertainties are included are shown.

For the $\mu\mu$ channels, there are very few events in the SS regions, the data-MC agreement is poor, and the regions are dominated by rare SM events. Due to this high contamination, highly conservative uncertainties of 50% were applied to the $\mu\mu$ fake lepton factors. Confidence is gained in that the μ_{Fake} factors and uncertainties are consistent with those in other public results [121, 176]. Since the $\mu\mu$ fake leptons make up less than 1% of the signal events, the 50% uncertainties have negligible effect on the overall charge asymmetry uncertainty. The final fake lepton factors are shown in Table 6.6 and were applied to the signal region fake lepton events.

Channel	μ_{Fake}
$ee + e\mu$ (1 b-tag)	0.96 ± 0.29
$ee + e\mu$ (≥ 2 b-tags)	0.94 ± 0.28
$\mu\mu$ (1 b-tag)	2.3 ± 1.2
$\mu\mu$ (≥ 2 b-tags)	4.2 ± 2.1

Table 6.6 Final fake lepton scale factors for the four channels with their overall uncertainties.

6.10   Event Yields and Control Plots

To verify the agreement between the MC and data after the scaling factors have been applied, event yields in the signal regions are shown in Tables 6.7 and 6.8. There is excellent data-MC agreement within the uncertainties. Control plots of the yields binned by several variables are shown in Figures 6.23 – 6.29.

Sample	*ee* channel		$\mu\mu$ channel	
	1 *b*-tag	$\geq$ 2 *b*-tags	1 *b*-tag	$\geq$ 2 *b*-tags
$t\bar{t}$ Pow+Py8 (no τ)	42300 ± 1800	77300 ± 5700	52700 ± 1900	96700 ± 7300
$t\bar{t}$ Pow+Py8 (τ)	5220 ± 240	8910 ± 680	5320 ± 220	9190 ± 660
Single top	2760 ± 280	1820 ± 320	3330 ± 330	2230 ± 390
Diboson	133 ± 15	23.4 ± 2.7	162 ± 19	31.1 ± 3.7
Z + jets	1490 ± 580	1620 ± 560	2000 ± 880	2180 ± 710
Rare SM	182 ± 24	394 ± 53	207 ± 28	451 ± 61
Fake lepton	940 ± 290	1380 ± 480	240 ± 140	520 ± 280
Prediction	53000 ± 1900	91400 ± 5800	64000 ± 2200	111300 ± 7400
Data	52505	91888	63591	111079
$t\bar{t}$ Pow+Hw7 (no τ)	41740 ± 87	75930 ± 120	52320 ± 92	94830 ± 130
$t\bar{t}$ Pow+Hw7 (τ)	5132 ± 31	8655 ± 41	5353 ± 29	9025 ± 39

Table 6.7 Event yields in the *ee* and $\mu\mu$ channels split by *b*-tag multiplicity. The uncertainties include statistical and systematic uncertainties, and the μ_Z and μ_{Fake} factors have been applied. The $t\bar{t}$ Powheg + Pythia8 (Pow+Py8) signal is split whereby the *W* bosons decay directly into electrons or muons (no τ case), and where one or both *W* bosons decay through a τ lepton into an electron or muon (τ case). The alternative Powheg+Herwig7 $t\bar{t}$ samples (Pow+Hw7) are also shown with their statistical uncertainties.

Sample	$e\mu$ channel	
	1 *b*-tag	$\geq$ 2 *b*-tags
$t\bar{t}$ Pow+Py8 (no τ)	203000 ± 7200	237000 ± 17000
$t\bar{t}$ Pow+Py8 (τ)	22320 ± 780	25100 ± 1800
Single top	13800 ± 1200	5590 ± 900
Diboson	653 ± 71	45.1 ± 5.8
Z + jets	610 ± 200	77 ± 25
Rare SM	690 ± 91	1040 ± 140
Fake lepton	2460 ± 790	2120 ± 670
Prediction	243500 ± 7400	271000 ± 17000
Data	244258	273856
$t\bar{t}$ Pow+Hw7 (no τ)	203060 ± 190	232820 ± 200
$t\bar{t}$ Pow+Hw7 (τ)	22256 ± 62	24507 ± 66

Table 6.8 Event yields in the *e*μ channels with the same format as in Table 6.7.
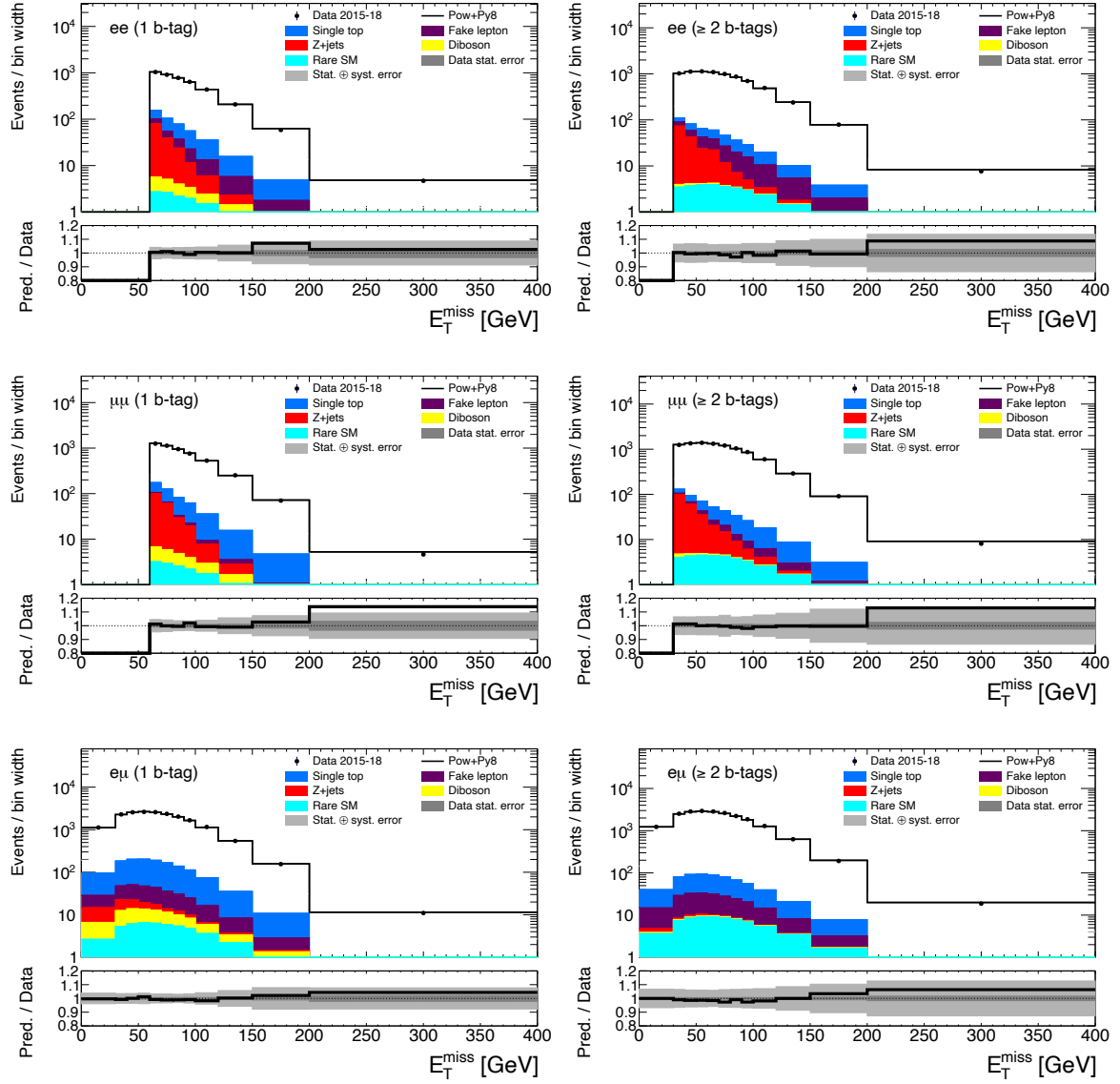
Fig. 6.23 The events in the *ee* (upper plots), $\mu\mu$ (middle plots) and *eμ* (lower plots) channels for the 1 *b*-tag (left) and ≥ 2 *b*-tag (right) cases across the E_T^{miss} variable.
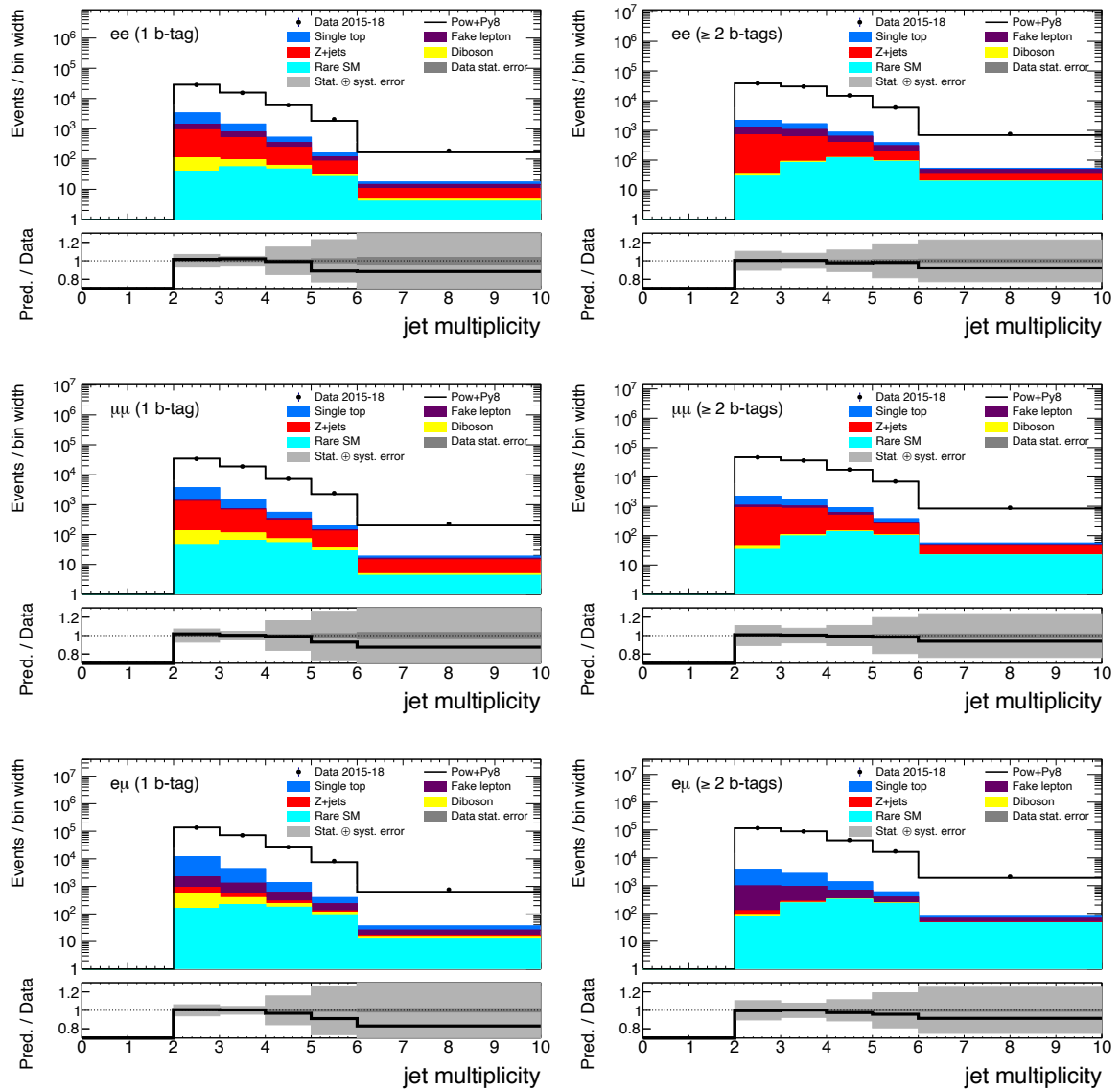
Fig. 6.24 The events in the *ee* (upper plots), $\mu\mu$ (middle plots) and *eμ* (lower plots) channels for the 1 *b*-tag (left) and ≥ 2 *b*-tag (right) cases as a function of the number of jets.
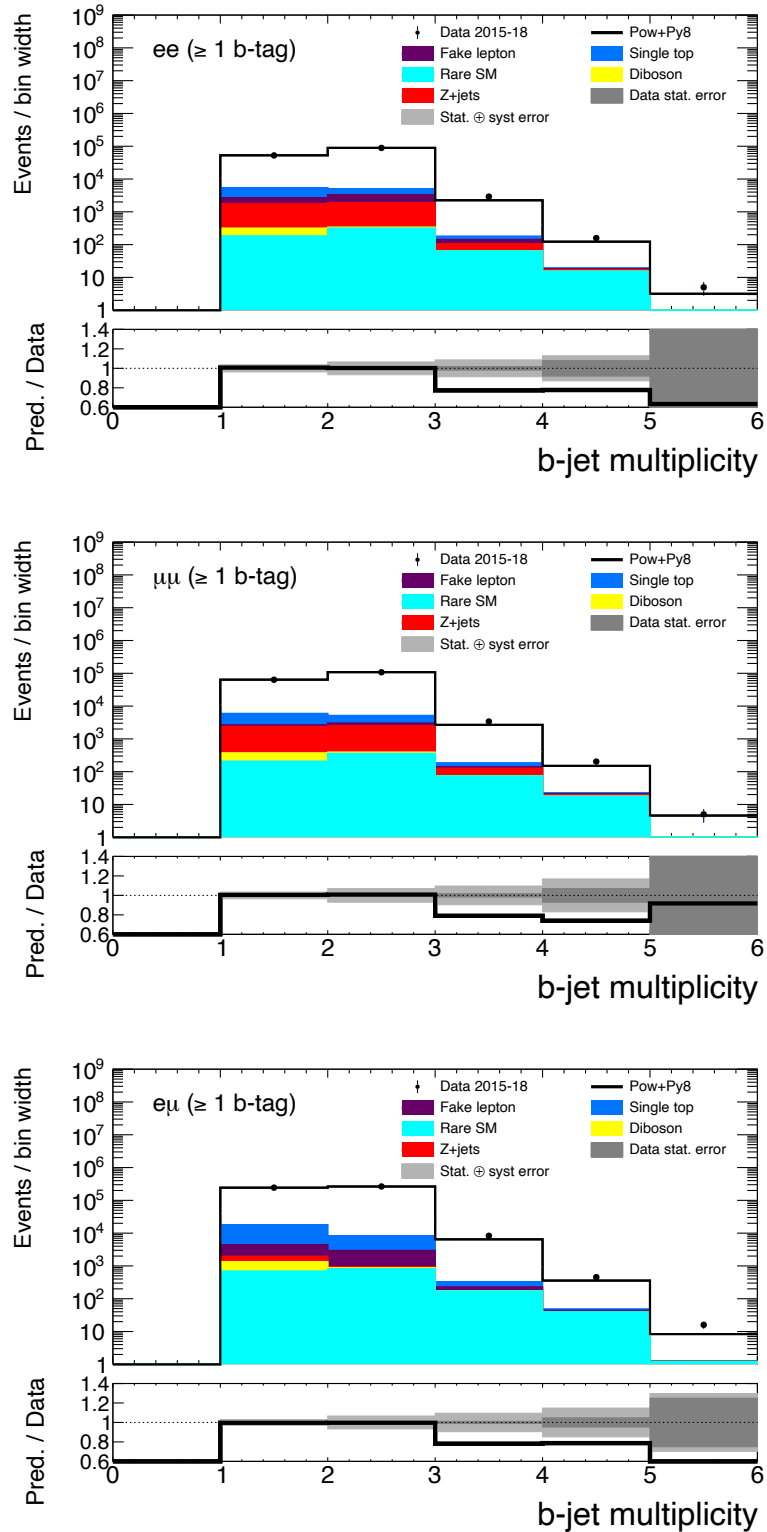
Fig. 6.25 The events in the *ee* (upper plots), $\mu\mu$ (middle plots) and *eμ* (lower plots) channels across as a function of the number of *b*-tagged jets. The 1 *b*-tag and ≥ 2 *b*-tag events are combined.
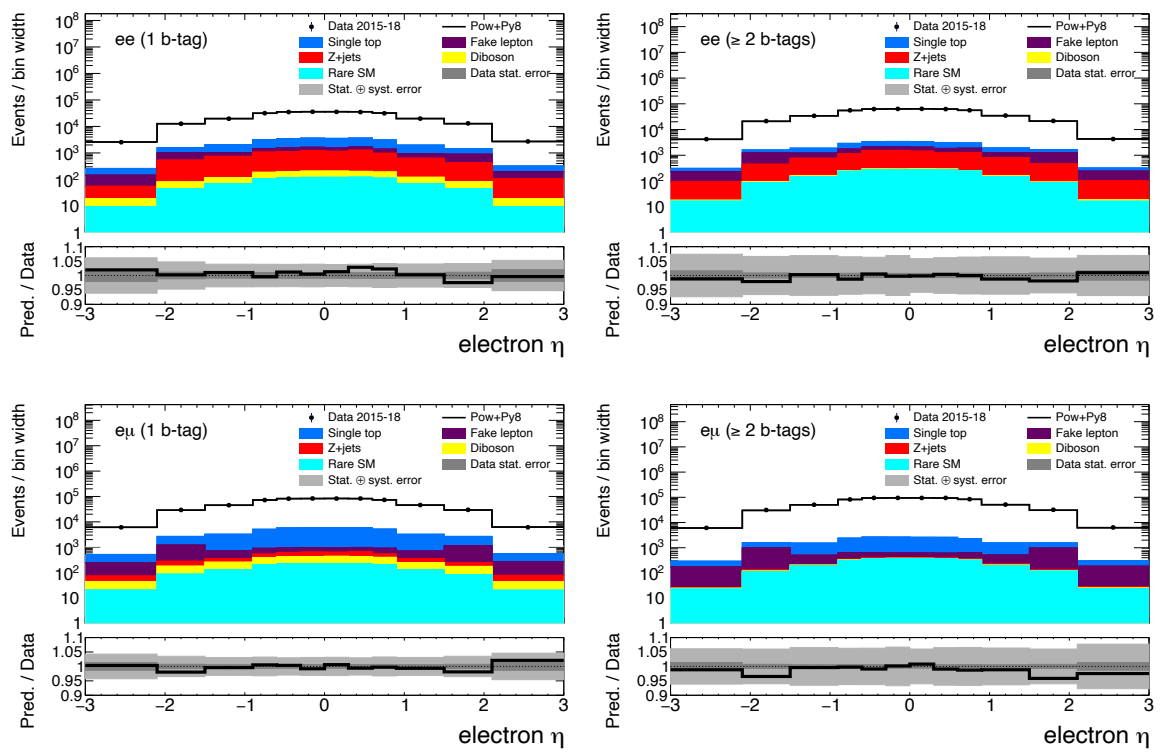
Fig. 6.26 The events in the *ee* (upper plots) and *eμ* (lower plots) channels for the 1 *b*-tag (left) and ≥ 2 *b*-tag (right) cases across the electron η variable.
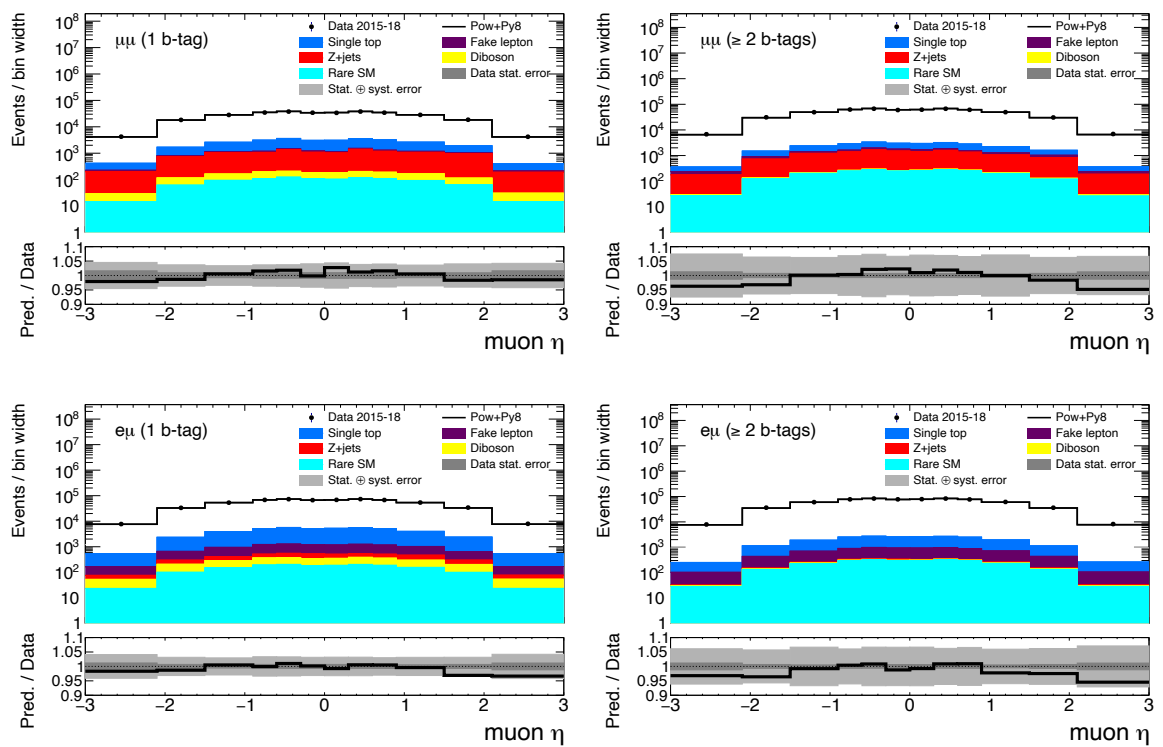
Fig. 6.27 The events in the $\mu\mu$ (upper plots) and $e\mu$ (lower plots) channels for the 1 b-tag (left) and ≥ 2 b-tag (right) cases across the muon η variable.
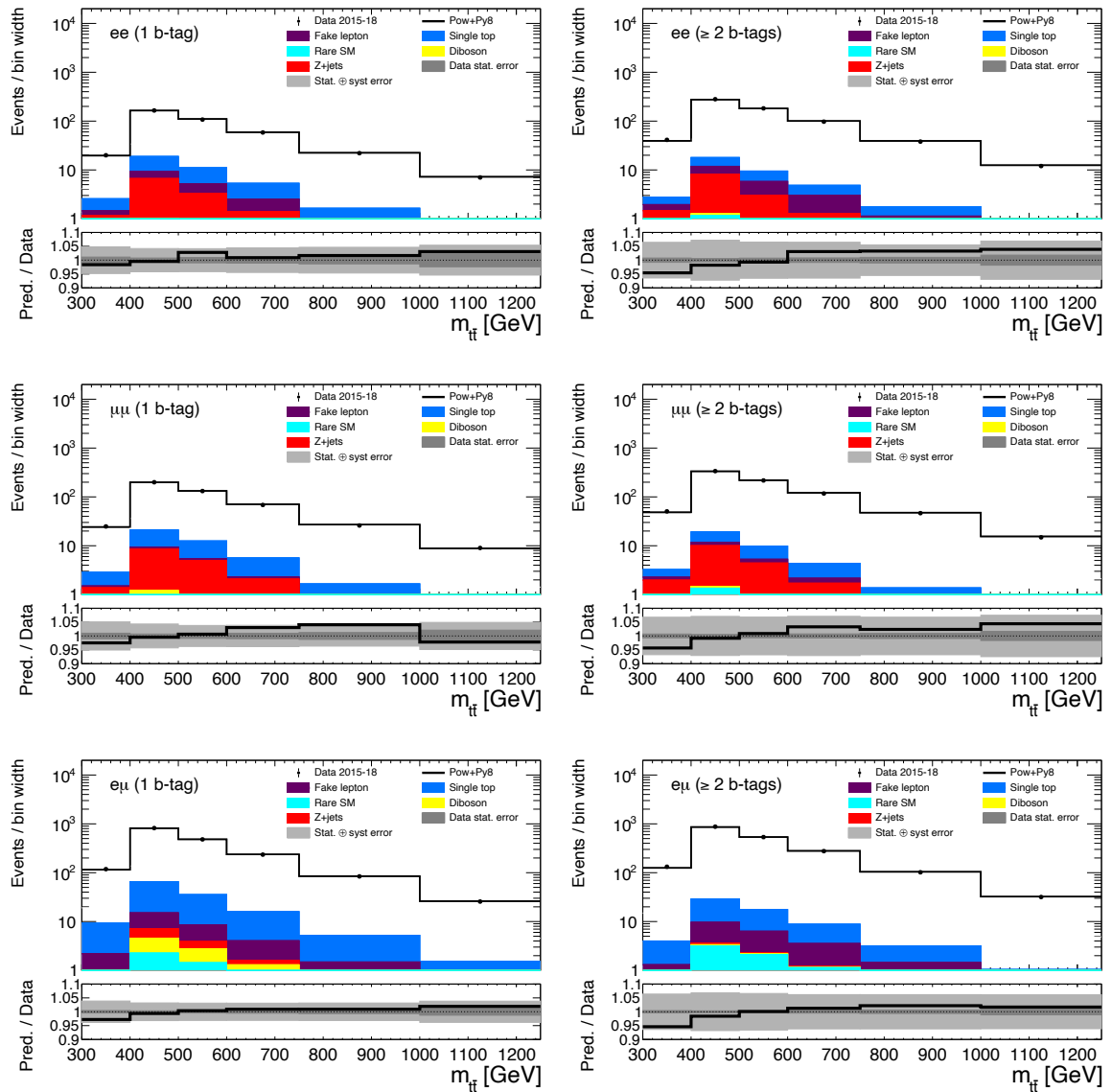
Fig. 6.28 The events in the *ee* (upper plots), $\mu\mu$ (middle plots) and $e\mu$ (lower plots) channels for the 1 *b*-tag (left) and ≥ 2 *b*-tag (right) cases across the $m_{t\bar{t}}$ variable.
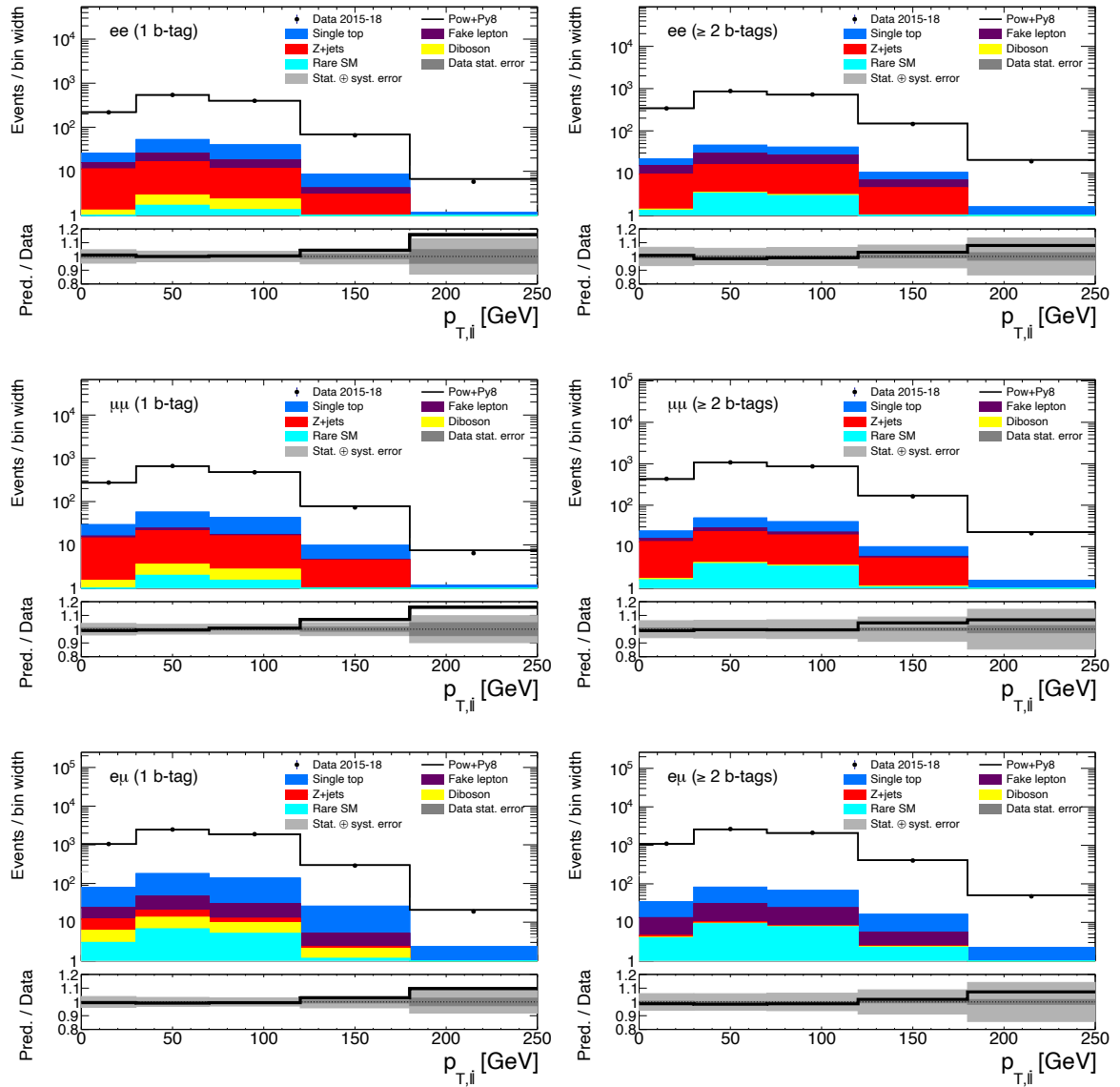
Fig. 6.29 The events in the *ee* (upper plots), $\mu\mu$ (middle plots) and *eμ* (lower plots) channels for the 1 *b*-tag (left) and ≥ 2 *b*-tag (right) cases across the $p_{T,l\bar{l}}$ variable.

Consistent data-MC agreement is seen across E_T^{miss}, jet multiplicity and $p_{T,l\bar{l}}$ except for the highest bins, which suffer from limited statistical precision. For the b-tagged jet multiplicity, there is a slight excess in data events above the expectation for ≥ 3 b-tags, since b-tagging is difficult to model. These make up around 2.5% of the total events in each of the ≥ 2 b-tag channels, so the discrepancies have a negligible impact on the total number of expected events. The agreement between data and MC across electron η is good for the ee and $e\mu$ channels. For muon η in the $e\mu$ and $\mu\mu$ channels, there is a small shape dependency with an excess of data at high $|\eta|$ and an excess of MC at low $|\eta|$. The dependency is fully covered in the uncertainty bands. Across the $m_{t\bar{t}}$ variable, there is also a trend of excess data at low $m_{t\bar{t}}$ and excess MC at high $m_{t\bar{t}}$. This will also be evident in the pre-marginal signal region plots of Figure 7.30 where $\Delta|y|$ is plotted for the differential $m_{t\bar{t}}$ bins. However, the unfolding technique described in the following chapter was able to rectify this effect (as seen in the post-marginal plots) without introducing significant bias into the asymmetry measurements.

For the signal regions, as in the OSZ control regions, the ee (1 b-tag) and $\mu\mu$ (1 b-tag) events were merged together, as were the ee (≥ 2 b-tag) and $\mu\mu$ (≥ 2 b-tag) events. The processes that yield ee and $\mu\mu$ events are very similar and it is sensible to correlate the systematic uncertainties between them. However, the ee and $\mu\mu$ fake lepton normalisation uncertainties were kept decorrelated within the channels. The mergers help to reduce the statistical uncertainties in the channels, which suffer from reduced signals owing to the E_T^{miss} cuts.

Given the ATLAS data and MC simulation at reconstructed-level, the events in the channels were unfolded and charge asymmetries were determined, as described in Chapter 7. The unfolded asymmetries were compared with the asymmetries of the truth-level events defined in Section 6.2.

Unfolding and Results in the Dilepton Channel

7.1 Introduction

Measured quantities such as charge asymmetry can be determined at reconstructed-level. However, the results will depend on the detector capabilities, making it difficult to compare them across different experiments. Furthermore, MC that can be passed through detector simulations may not exist for theory calculations, making direct comparisons with the experimental data impossible. In light of this, a technique known as unfolding is applied, which maps the reconstructed-level events on to truth-level events that are independent of the experimental setup. The unfolding procedure corrects for the following processes:

- Limited detector acceptance: due to detector geometry, inefficiencies and trigger requirements, the full phase space of event production cannot be covered and recorded at reconstructed-level.

- Migrations: the finite detector resolution and fluctuations in measured observables cause reconstructed-level quantities to be smeared about or shifted from the truth-level quantities.

A Fredholm convolution equation of the first kind can be used for the reconstructed-truth mapping [177]:

$$r(x) = \int A(x,y)t(y)dy, \qquad (7.1)$$

where $r(x)$ is the reconstructed-level distribution of a measured variable, x, and $t(y)$ the truth-level distribution of the variable, y. $A(x,y)$ is the kernel function used to describe the detector response. With an infinite amount of data, $A(x,y)$ could be established and Equation 7.1 used directly. Since there are only finite data, a solution is to bin the reconstructed- and truth-level distributions so there are sufficient events per bin, and to determine the average response in those bins. In discrete form, Equation 7.1 becomes:

$$r_i = \sum_{j=0}^{N_t} \mathcal{M}_{ij}t_j, \qquad (7.2)$$

where r_i and t_j are the entries per i and j bin of the reconstructed- and truth-level distributions, respectively, and N_t the number of truth-level bins. $\mathcal{M}_{ij}$ are the elements of the response matrix that are probability factors for a truth-level event in bin j to be reconstructed in bin i:

$$\mathcal{M}_{ij} = \text{P(reconstructed in bin } i \mid \text{truth value in bin } j). \qquad (7.3)$$

In matrix form, over the N_r reconstructed-level bins, Equation 7.2 can be written as:

$$\mathbf{R} = \mathcal{M}\mathbf{T}, \qquad (7.4)$$

where $\mathbf{R} = (r_1, r_2, ..., r_{N_r})$ and $\mathbf{T} = (t_1, t_2, ..., t_{N_t})$. For physics analyses, the response matrices are typically generated with MC simulation using the expected truth- and reconstructed-level distributions. They are then used to unfold the raw data from the detector back to truth-level. Figures 7.1 – 7.5 show the response matrices for the inclusive and differential bins of the $t\bar{t}$ $\Delta|y|$ and dilepton $\Delta|\eta|$ variables with the Powheg + Pythia8 simulation. Eight $\Delta|y|$ and $\Delta|\eta|$ bins are shown, whose edges are identical in the reconstructed-level and truth-level bins. These are presented for display purposes before binning optimisation, discussed in Section 7.5. The four channels are separated with thick black lines and the differential bins with thinner black lines. Each square shows the percentage probability for an event to be reconstructed in bin i (x-axis) of channel n given there is a truth-level dilepton event in bin j (y-axis). The limited detector acceptance means the row values do not sum to 100% over all channels, and the off-diagonal elements show migrations. Migrations can be seen across the $\Delta|y|$ bins and the $\Delta|\eta|$ bins. They are much greater for $\Delta|y|$ than $\Delta|\eta|$ due to uncertainties in the top and antitop y reconstruction, where the leptons, jets and E_T^{miss} are combined. Leptonic η values are well-defined from the inner detector and electromagnetic calorimeter or muon system deposits. Migrations also occur between the differential bins, particularly for the $t\bar{t}$ quantities. For instance, there are important migrations between a given truth-level $m_{t\bar{t}}$ bin and the next highest reconstructed-level $m_{t\bar{t}}$ bin. This can be also been seen in Figure 6.16 where the NW has a bias for reconstructing higher $t\bar{t}$ mass.

Given the response matrices, an obvious step would be to invert the matrices and apply them to the distributions of data events to return the unfolded distributions. However, the matrices can sometimes not be inverted numerically and the results are highly sensitive to statistical fluctuations. The true unfolded spectrum may have very fine structure that is smeared out at reconstructed-level. Slightly different reconstructed-level distributions, such as a data spectrum in comparison with a simulated spectrum that encodes the same underlying physics

but differs only in Poisson statistics, can lead to vastly different unfolded results [178].

A more stable approach is to sample different distributions of truth-level events and fold these to reconstructed-level. This involves calculating Equation 7.4 directly, by applying the response matrix to the truth-level events. One can then determine how well the folded distributions agree with the actual reconstructed-level distributions and select the truth distribution giving the best match. This is the principle employed in Fully Bayesian Unfolding.
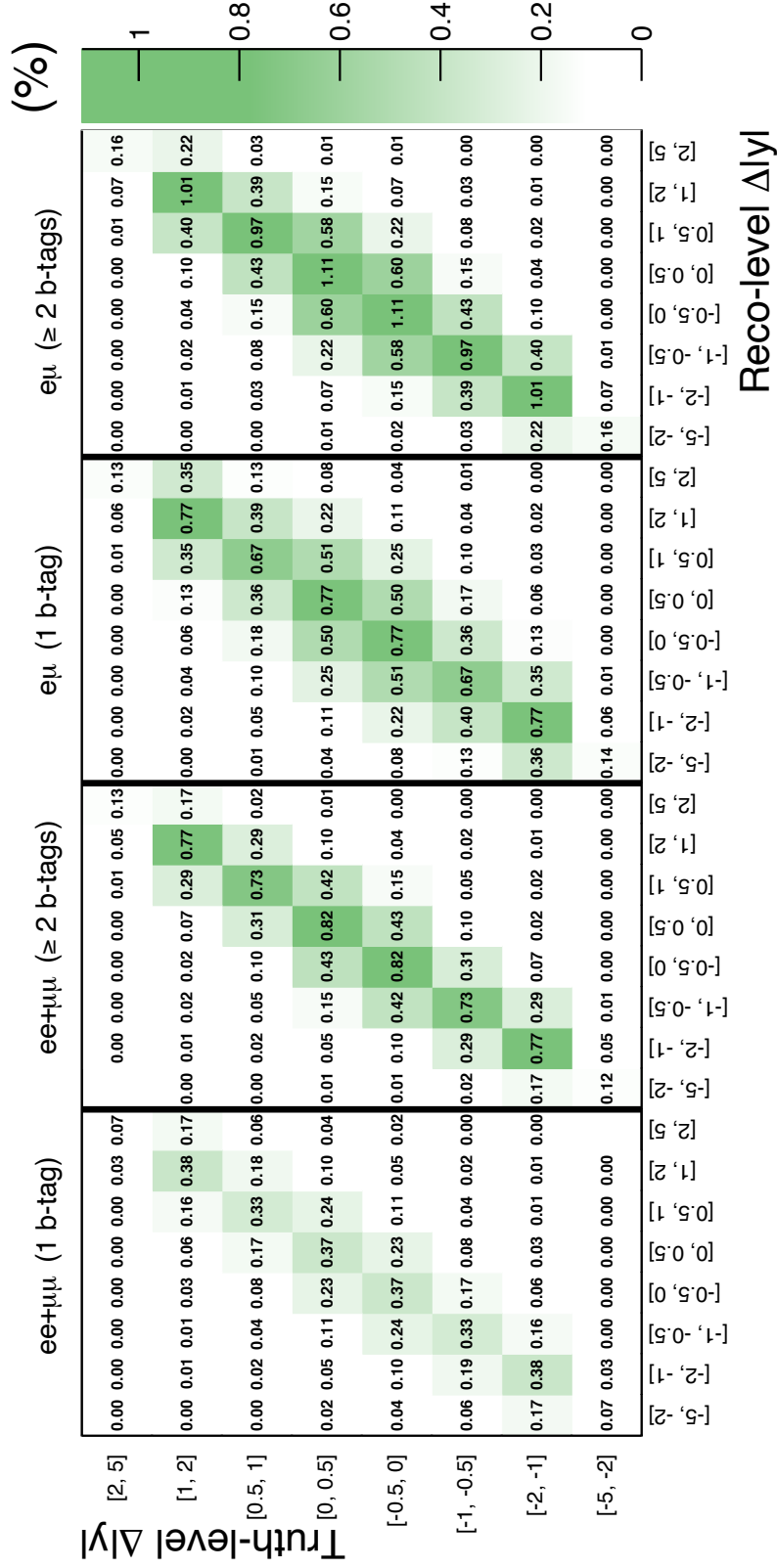
Fig. 7.1 Response matrix for $t\bar{t}$ $\Delta|y|$ (inclusive case) determined with the Powheg + Pythia8 MC. The numbers in the squares show the percentage probability for a truth-level event to fall into a particular reconstructed-level bin and channel. Blank white squares mean there is zero probability of reconstruction.
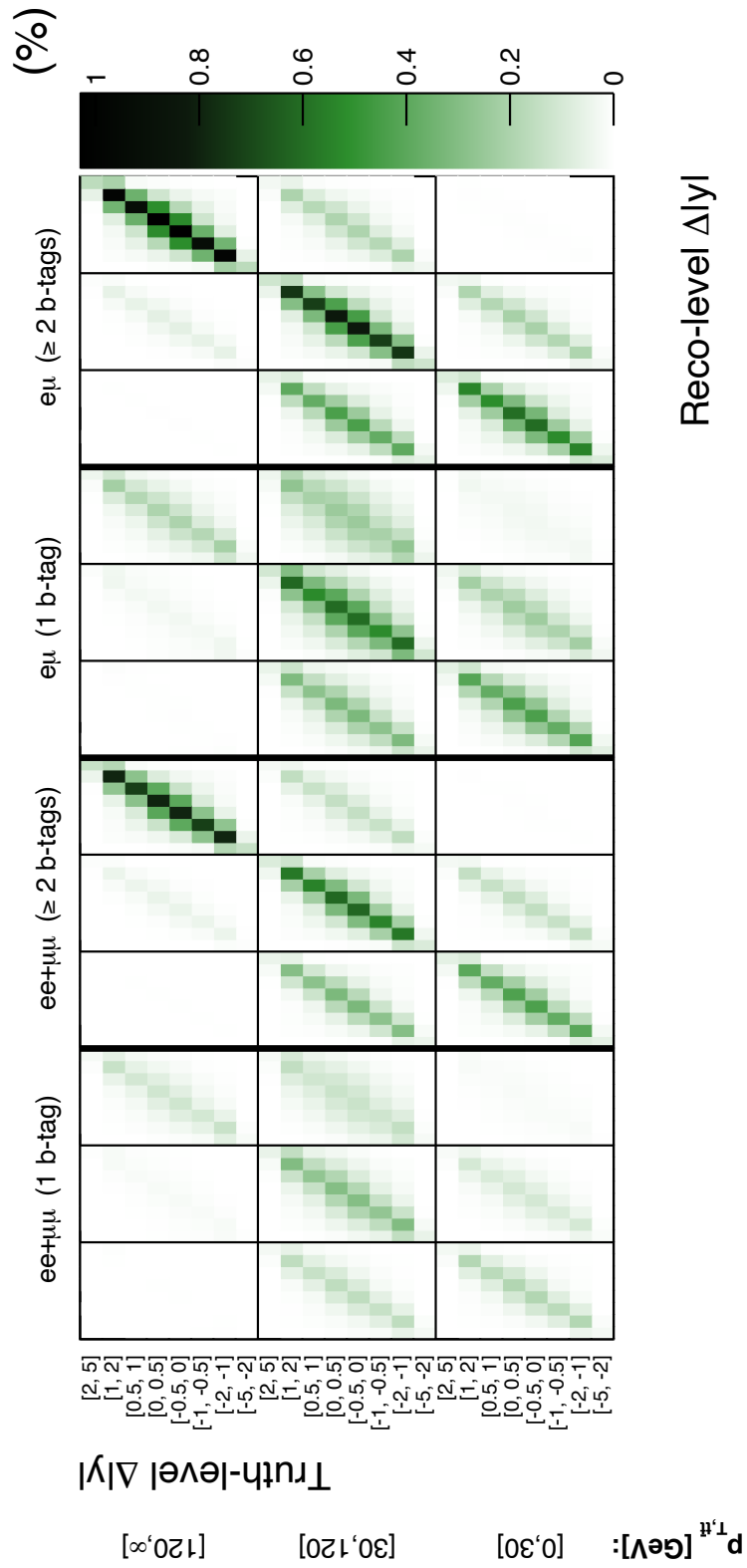
Fig. 7.2 Response matrix for $t\bar{t}$ $\Delta|y|$ across the three differential $p_{T,t\bar{t}}$ bins. The binning in $\Delta|y|$ and $p_{T,t\bar{t}}$ on the y-axis is the same for all channels on the x-axis.
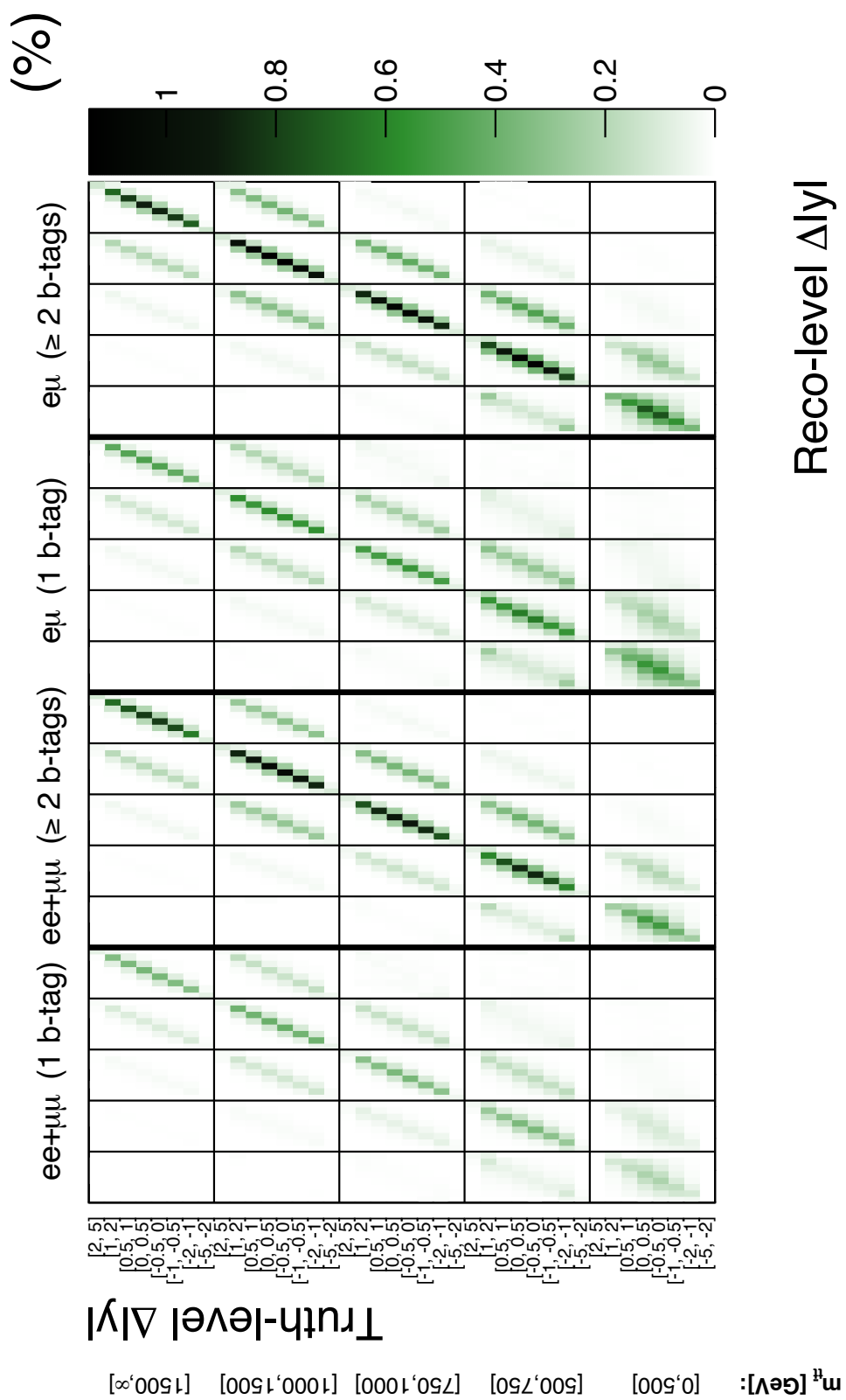
Fig. 7.3 Response matrix for $t\bar{t}$ $\Delta|y|$ across the five differential $m_{t\bar{t}}$ bins. The binning in $\Delta|y|$ and $m_{t\bar{t}}$ on the y-axis is the same for all channels on the x-axis.
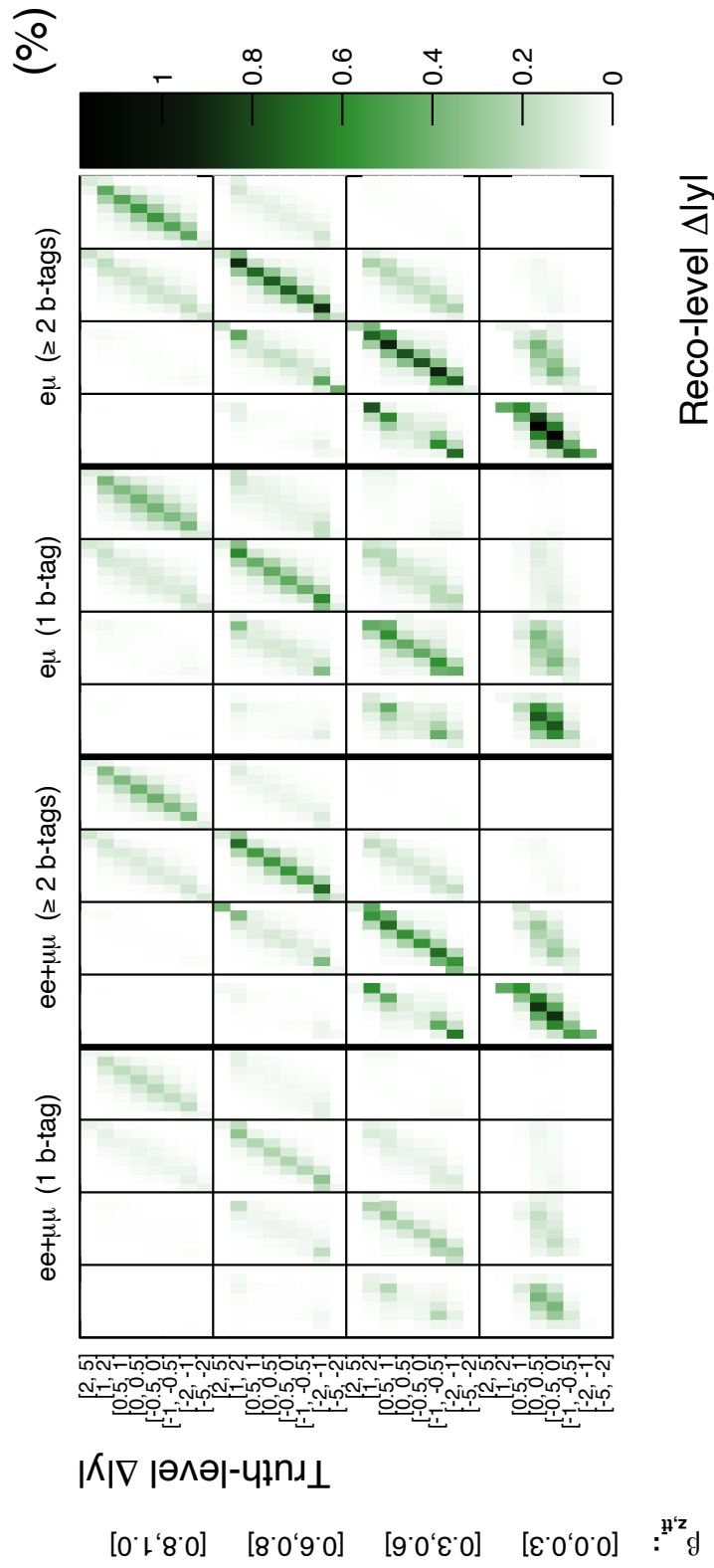
Fig. 7.4 Response matrix for $t\bar{t}$ $\Delta|y|$ across the four differential $\beta_{Z,t\bar{t}}$ bins. The binning in $\Delta|y|$ and $\beta_{Z,t\bar{t}}$ on the y-axis is the same for all channels on the x-axis.
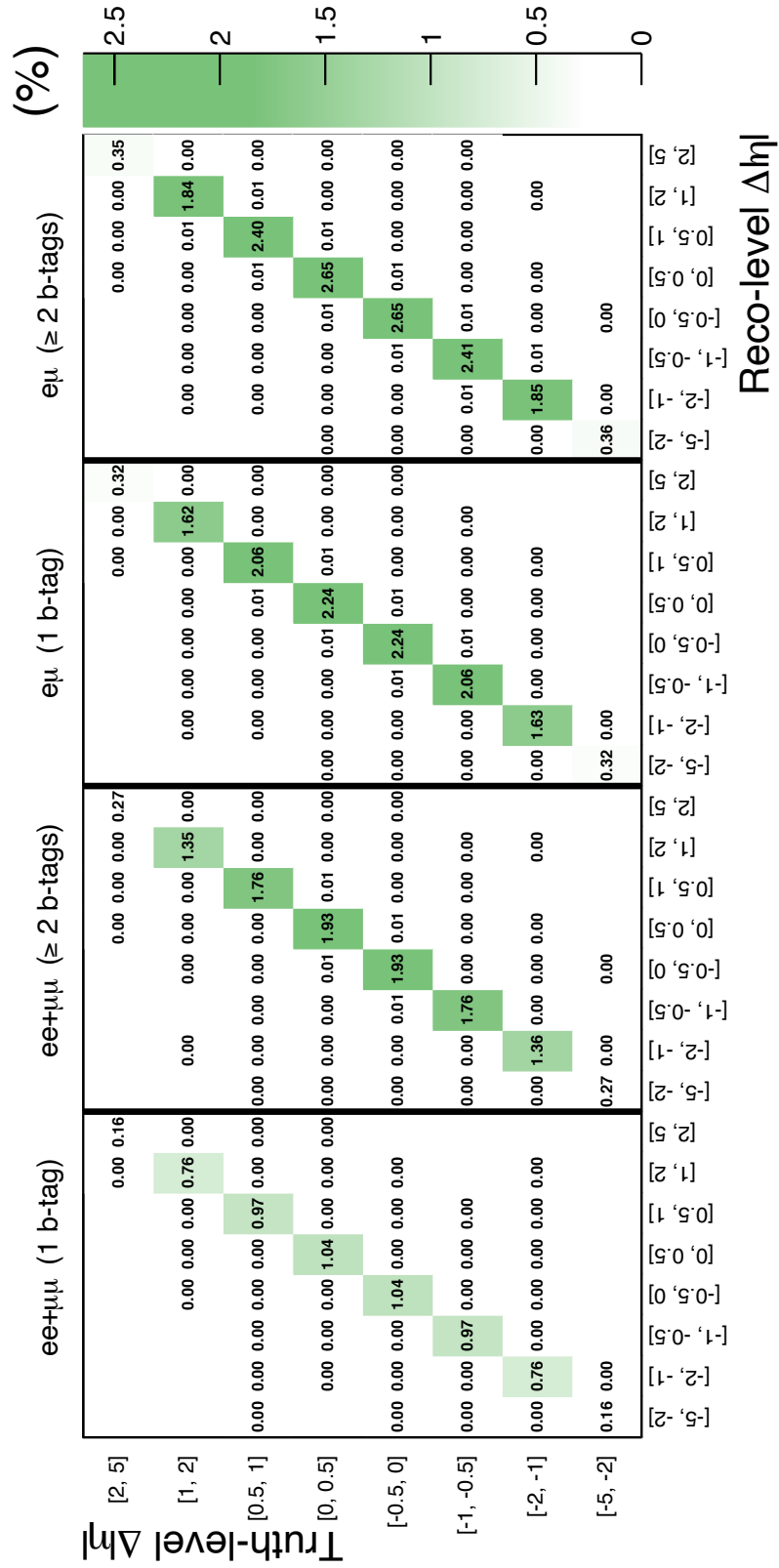
Fig. 7.5 Response matrix for dilepton $\Delta|\eta|$ (inclusive case).
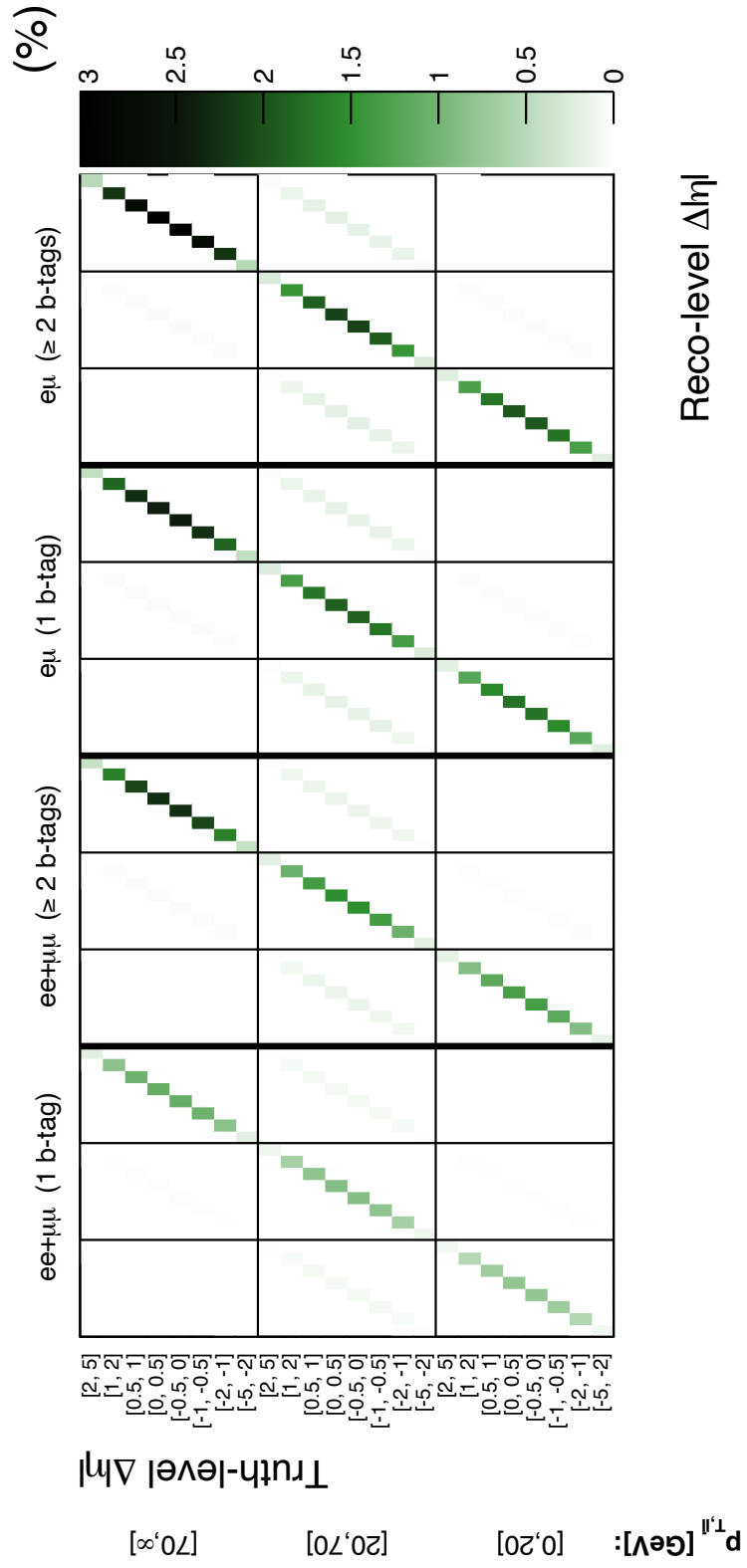
Fig. 7.6 Response matrix for dilepton $\Delta|\eta|$ across the three differential $p_{T,l\bar{l}}$ bins. The binning in $\Delta|\eta|$ and $p_{T,l\bar{l}}$ on the y-axis is the same for all channels on the x-axis.
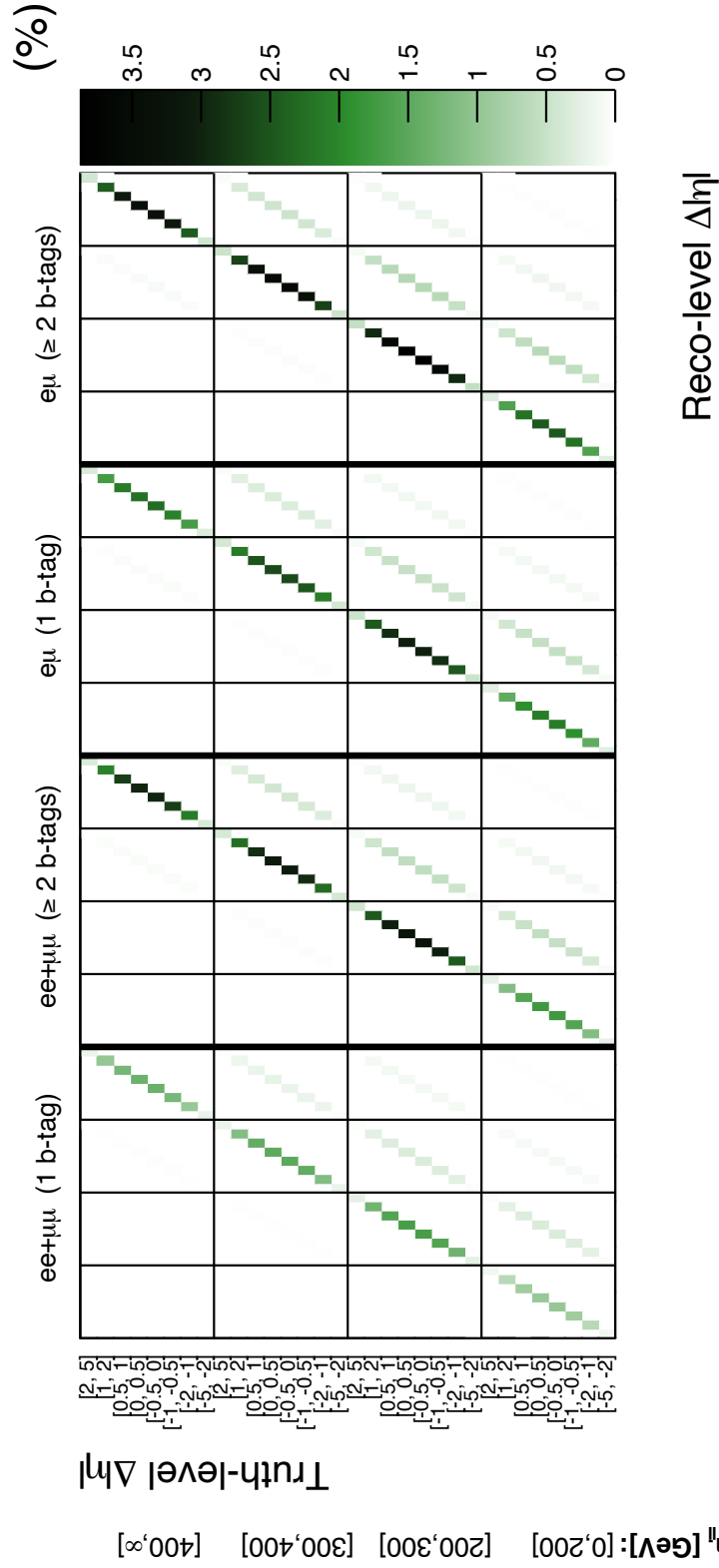
Fig. 7.7 Response matrix for dilepton $\Delta|\eta|$ across the four differential $m_{l\bar{l}}$ bins. The binning in $\Delta|\eta|$ and $m_{l\bar{l}}$ on the y-axis is the same for all channels on the x-axis.
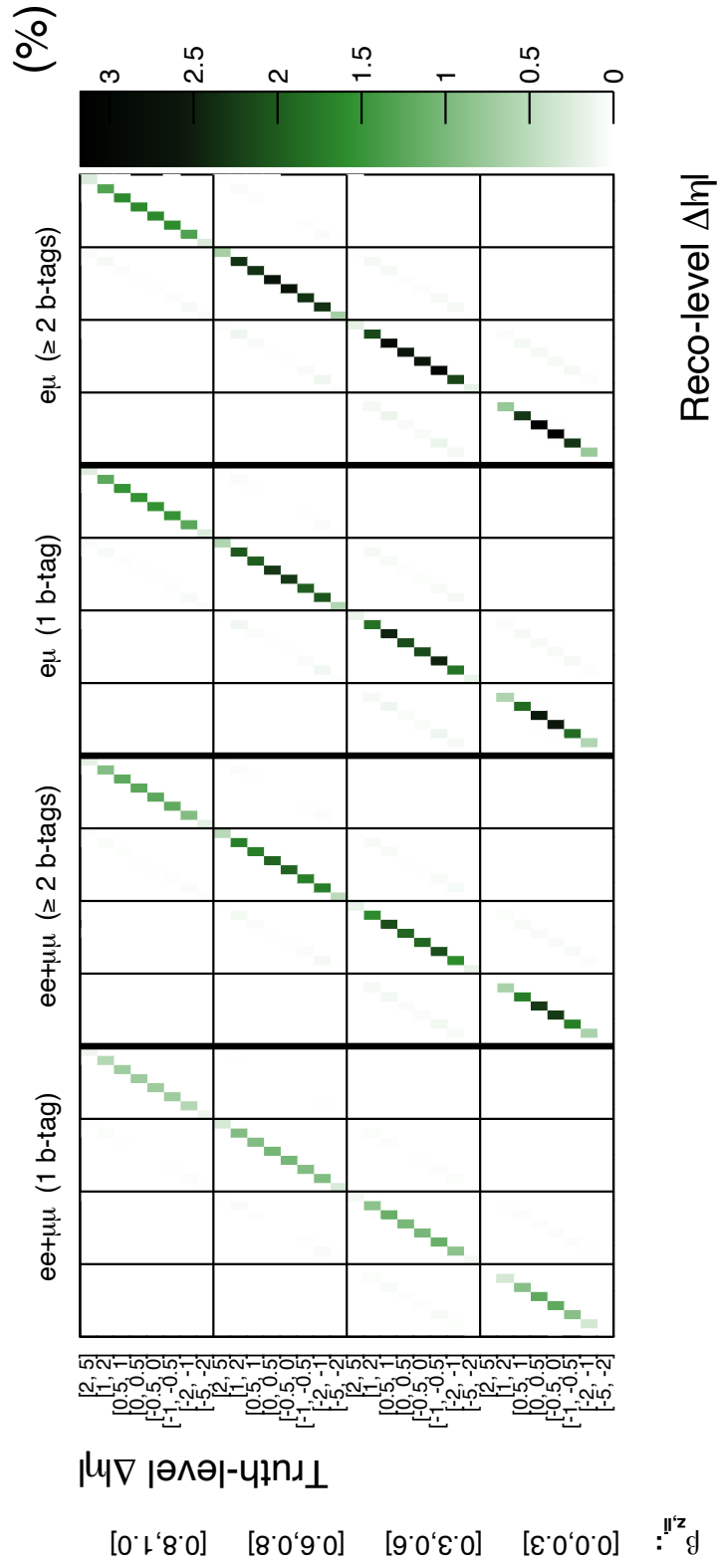
Fig. 7.8 Response matrix for dilepton $\Delta|\eta|$ across the four differential $\beta_{Z,l\bar{l}}$ bins. The binning in $\Delta|\eta|$ and $\beta_{Z,l\bar{l}}$ on the y-axis is the same for all channels on the x-axis.

141

7.2 Fully Bayesian Unfolding

The foundations of Fully Bayesian Unfolding (FBU) [179] lie in the application of Bayes' Theorem [180]. A posterior distribution, $P(\mathbf{T}|\mathbf{D}, \mathcal{M})$, for the truth spectrum given the data spectrum, $\mathbf{D} = (d_1, d_2, ..., d_{N_r})$, is given by:

$$P(\mathbf{T}|\mathbf{D}, \mathcal{M}) \propto \mathcal{L}(\mathbf{D}|\mathbf{T}, \mathcal{M})\pi(\mathbf{T}), \tag{7.5}$$

where $\mathcal{L}(\mathbf{D}|\mathbf{T}, \mathcal{M})$ is the likelihood function of data given truth and $\pi(\mathbf{T})$ is a prior probability distribution assigned to the truth bin entries. These are described in more detail below.

7.2.1 Likelihood

The likelihood is calculated assuming that the data follow Poisson statistics. Signal values, r_i, are calculated by sampling truth values, t_j, (see Section 7.2.4) and substituting into Equation 7.2. These are are added to the background b_i values from the MC spectrum, $\mathbf{B} = (b_1, b_2, ..., b_{N_r})$, to give expected yields, $r_i + b_i$, per bin. These yields are compared with the data values, d_i, in the likelihood equation:

$$\mathcal{L}(\mathbf{D}|\mathbf{T}, \mathcal{M}) = \prod_{i=1}^{N_r} \frac{(r_i + b_i)^{d_i}}{d_i!} e^{-(r_i + b_i)}. \tag{7.6}$$

7.2.2 Prior

The truth prior probability distribution, $\pi(\mathbf{T})$, is a user-defined initial spectrum of the truth-level events in $\Delta|y|$ or $\Delta|\eta|$ used by the Bayesian framework. Lower and upper limits (denoted $t_j^{\llcorner}$ and $t_j^{\urcorner}$, respectively) can be set on the bin entries in the spectrum based on expected behaviour and to reduce the computing time. The shape of the prior distribution for each bin can be a uniform distribution over a range of values or have a functional form

with lower probability for certain truth values to disfavour their choice. However, this can introduce bias into the overall measurement, so the uniform, bounded prior distribution was chosen:

$$\pi(\mathbf{T}) \propto \begin{cases} 1, & \text{if } t_j \in [t_j^{\ulcorner}, t_j^{\urcorner}], \forall j \in [1, N_t] \\ 0, & \text{otherwise} \end{cases} \quad . \tag{7.7}$$

The bounded range was chosen to be very large: $[t_j^{\ulcorner}, t_j^{\urcorner}] = [0, 2\tilde{t}_j]$, where $\tilde{t}_j$ is the Powheg + Pythia8 MC truth prediction for bin j. This ensures there is no truncation in the posterior distribution even if there are large discrepancies from the SM expectation. Figure 7.9 shows the bounded prior ranges for the inclusive $\Delta|y|$ case.
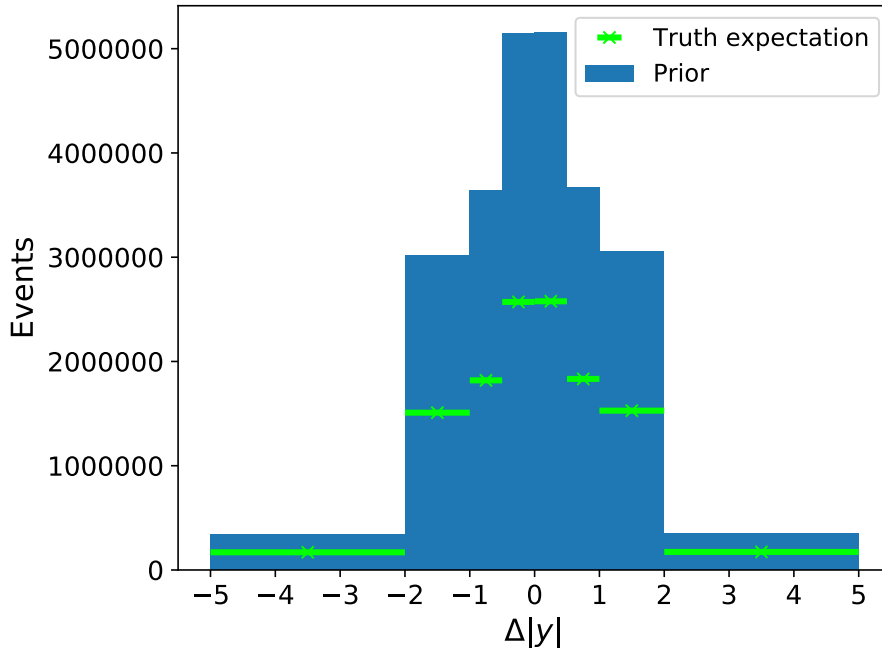
Fig. 7.9 The prior probability ranges (blue regions covering $[0, 2\tilde{t}_j]$) on the truth expectations (green lines of $\tilde{t}_j$) for eight $\Delta|y|$ bins in the inclusive case. For each bin, the prior probability distribution is uniform across the range.

7.2.3   Inclusion of Systematic Uncertainties

Systematic uncertainties can be included in FBU by extending the likelihood with nuisance parameters (NPs), $\boldsymbol{\theta} = (\theta_1, \theta_2, ..., \theta_{N_{\mathrm{NP}}})$, where θ_k refers to a particular NP in $\boldsymbol{\theta}$ and N_{NP} is the total number of NPs:

$$\mathcal{L}(\mathbf{D}|\mathbf{T}, \mathcal{M}) = \int \mathcal{L}(\mathbf{D}|\mathbf{T}, \mathcal{M}; \boldsymbol{\theta}) \pi(\boldsymbol{\theta}) \mathrm{d}\boldsymbol{\theta}. \tag{7.8}$$

The NPs are split into two categories:

- Experimental and modelling uncertainties, $\boldsymbol{\theta}_o$, affecting both signal and background, as detailed in Sections 6.8.1, 6.8.2 and Section 6.8.3 (except Section 6.8.3.5).
- Background normalisation uncertainties, $\boldsymbol{\theta}_{bn}$, as detailed in Section 6.8.3.5.

The signal and background distributions are therefore denoted as $\mathbf{R}(\mathbf{T}, \mathcal{M}; \boldsymbol{\theta}_o)$ and $\mathbf{B}(\boldsymbol{\theta}_o, \boldsymbol{\theta}_{bn})$, respectively. The $\pi(\boldsymbol{\theta})$ are Gaussian prior distributions, G, on the NPs. These prior distributions are centred on zero and given standard deviations of one. The full signal prediction in bin i is now given by:

$$r_i(\mathbf{T}, \mathcal{M}; \boldsymbol{\theta}_o) = r_i(\mathbf{T}, \mathcal{M}; 0) \left(1 + \sum_k \theta_o^k \Delta r_i^k\right), \tag{7.9}$$

where $r_i(\mathbf{T}, \mathcal{M}; 0)$ is that calculated from Equation 7.2 and Δr_i^k is the relative systematic uncertainty variation from nuisance parameter k on the signal yield in reconstructed-level bin i, which is multiplied by its prior distribution, θ_o^k.

The background prediction in bin i is:

$$b_i(\boldsymbol{\theta}_o, \boldsymbol{\theta}_{bn}) = b_i(0)(1 + \theta_{bn}\Delta b) \left(1 + \sum_k \theta_o^k \Delta b_i^k\right), \tag{7.10}$$

where $b_i(0)$ is the MC background yield in that bin, Δb the relative uncertainty on the background normalisation, which is multiplied by its prior distribution, θ_{bn}, and Δb_i^k is the relative systematic uncertainty variation from nuisance parameter k on the background yield in bin i, which is multiplied by its prior distribution, θ_o^k.

In full, Equation 7.8 becomes:

$$\mathcal{L}(\mathbf{D}|\mathbf{T}, \mathcal{M}) = \int \mathcal{L}(\mathbf{D}|\mathbf{R}(\mathbf{T}, \mathcal{M}; \boldsymbol{\theta}_o), \mathbf{B}(\boldsymbol{\theta}_o, \boldsymbol{\theta}_{bn})) G(\boldsymbol{\theta}_o) G(\boldsymbol{\theta}_{bn}) \mathrm{d}\boldsymbol{\theta}_o \mathrm{d}\boldsymbol{\theta}_{bn}. \tag{7.11}$$

7.2.4 Sampling

$P(\mathbf{T}|\mathbf{D}, \mathcal{M})$ is determined in practise by sampling the probability space. For each truth bin, a value, t_j, is tested (within the prior distribution bounds) and similarly, for each NP, a value θ_k. This means a hyperspace of $N_t + N_{\mathrm{NP}}$ dimensions is investigated. With such a large volume to test, it is unfeasible to calculate $\mathcal{L}(\mathbf{D}|\mathbf{T}, \mathcal{M})\pi(\mathbf{T})$ in a grid-like fashion across the whole space. For most points, $\mathcal{L}(\mathbf{D}|\mathbf{T}, \mathcal{M})\pi(\mathbf{T})$ will be zero or close to zero. Instead, Markov Chain Monte-Carlo (MCMC) methods [181] are used, which are much faster. These produce sequences of sampling points, where the choice of location for a particular sampling point depends on information obtained from the previous sampling point. For this analysis, the No-U-Turn Sampler (NUTS) MCMC algorithm [182] was employed.

To understand the NUTS algorithm, consider the 2D gravitational potential of Figure 7.10. A position is chosen in the 2D space and a kick of random velocity (grey arrow) is given to a fictitious ball placed at the point, so it follows the turquoise trajectory. At the same time, a second ball placed at the same point is given a kick of the same magnitude but in the opposite direction and follows the dark blue trajectory. From the two trajectories, the algorithm determines when the paths start to turn around (perform a U-turn). The balls are
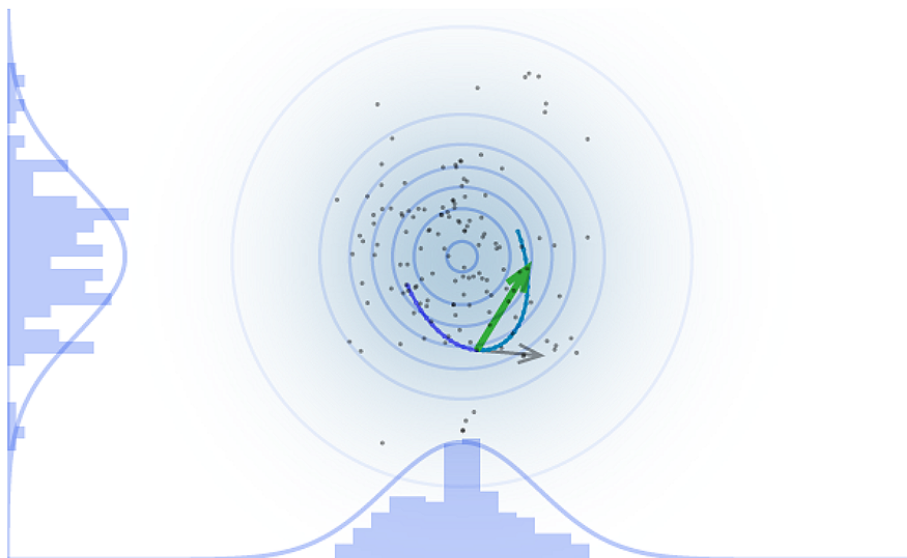
Fig. 7.10 The NUTS algorithm in a 2D circular potential well [183]. The grey arrow shows the initial kick momentum (starting at the previous sampling point), the turquoise and dark blue lines the path of the ball (from the kick in both directions) and the green arrow the position of the new sampling point along the path with respect to the previous point. The grey sampling points map out the potential.

then stopped and a sampling point is chosen at a random position on either the turquoise or dark blue paths and saved (here on the turquoise path). The tip of the green arrow shows the position of the new sampling point from the kick position. Once saved, the balls are then kicked from the position of the new sampling point and the process is repeated. With many sampling points saved, the distribution of points maps out the potential with more points clustering at lower values of the potential. This technique is applied to the $N_t + N_{NP}$ dimensions for this analysis, with the gravitational potential replaced by the negative log of the posterior distribution. Four Markov chains using separate CPU cores are run in parallel. For each chain, 2,500 initial tuning samples are run so the parameters of the sampler are adapted for the setup. Then, 10,000 actual samples are run per chain giving a total of 40,000 points of $\mathcal{L}(\mathbf{D}|\mathbf{T}, \mathcal{M})\pi(\mathbf{T})$. The NUTS sampling is implemented through the open-source PYMC3 package [184], which itself takes input from the FBU framework.

7.2.5   Combination of Channels

For the dilepton events, the four channels ($e\mu$ and $ee + \mu\mu$, each divided into 1 b-tag and ≥ 2 b-tag events) are merged at truth-level. This is since there is no expected dependence on channel for the underlying asymmetry. In FBU, it is possible to combine N_{ch} reconstructed-level channels and obtain a merged result by adjusting the posterior probability distribution:

$$
P(\mathbf{T}|\{\mathbf{D}_1 \cdots \mathbf{D}_{N_{\text{ch}}}\}) = \int \prod_{n=1}^{N_{\text{ch}}} \mathcal{L}\left(\mathbf{D}_n | \mathbf{R}_n(\mathbf{T}, \mathcal{M}; \boldsymbol{\theta}_o), \mathbf{B}_n(\boldsymbol{\theta}_o, \boldsymbol{\theta}_{bn})\right)
$$
$$
G(\boldsymbol{\theta}_o)G(\boldsymbol{\theta}_{bn})\pi(\mathbf{T})\mathrm{d}\boldsymbol{\theta}_o\mathrm{d}\boldsymbol{\theta}_{bn}.
\tag{7.12}
$$

In practise, the reconstructed, background, truth, response matrix and systematic uncertainty events are put into arrays, which are concatenated for the four channels (except in truth where they are already merged) and a joint fitting of all channels for the likelihood is performed. Some NPs, such as fake background normalisation uncertainties, are decorrelated across the channels by having channel-specific names for the NPs and setting their contributions to zero in the channels that they should not affect. It is possible for the resultant posterior distributions of the NPs to be different from the prior distributions due to information gained in the channel combination and correlations between the NPs. This is detailed in Section 7.6.6. To see how each NP is affected, the full multi-dimensional posterior distribution of Equation 7.12 is integrated out over all the truth bins and systematic uncertainties, except the one being investigated, to show a one-dimensional posterior distribution for that NP. This is known as marginalisation.

For each posterior sampling point, an A_{C} value is calculated from the number of events in the positive and negative unfolded $\Delta|y|$ (or $\Delta|\eta|$) bins as in Equations 5.8 and 5.9. The distribution of values for all sampling points gives the A_{C} posterior distribution. The mean is taken as the central A_{C} value and the standard deviation the A_{C} uncertainty, which reflects

the statistics of the data and the constrained systematic uncertainties. An example posterior distribution is shown in Figure 7.11, where the mean of the Gaussian fit to the unfolded blue posterior distribution coincides with the expected truth asymmetry, since this is performed in simulated MC. For the following sections, the unfolding tests are undertaken with simulation (rather than the raw ATLAS data) unless otherwise stated.
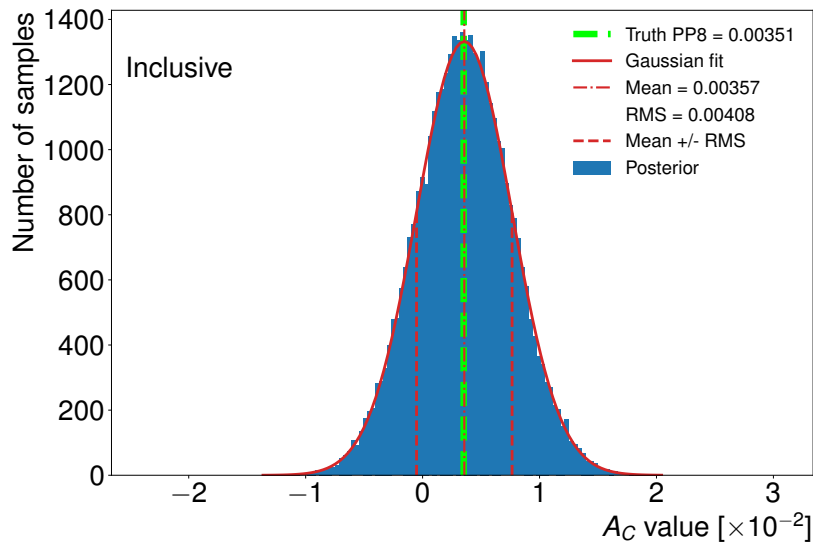
Fig. 7.11 Unfolded $A_C^{t\bar{t}}$ posterior distribution (blue histogram) for the inclusive case in simulated Powheg + Pythia8 (PP8) MC. All four channels are combined in the results. A Gaussian fit to the posterior distribution is plotted with a red curve. The mean and standard deviation (RMS) of the fit are shown with red vertical lines. The PP8 truth expectation is given by a green vertical line.

7.3 Inclusion of Leptonically-Decaying Taus

Tests were undertaken to determine whether $t\bar{t}$ decays yielding tau leptons that themselves decay into electrons and muons should be included in the signal or treated as a background at reconstructed-level. Matrices showing the number of reconstructed-level events that fall in the different reconstructed-level against truth-level bins in $\Delta|y|$ and $\Delta|\eta|$ are shown in Figures 7.12 and 7.13. The matrices are split into events where $t\bar{t}$ decays must include τ leptons, $t\bar{t}$ decays without τ leptons, and $t\bar{t}$ decays with both possibilities. All channels are merged in

the plots and the inclusive cases are considered for simplicity. The τ leptons account for 10.7% of the total $t\bar{t}$ events. On the diagonal elements, efficiencies are plotted, which show the ratio of events where the reconstructed- and truth-level bin is the same to all events in that reconstructed-level bin column. With no migrations, this ratio would be one. Despite the NW sharing the E_T^{miss} between two neutrinos and each τ lepton yielding two additional neutrinos, the $t\bar{t}$ reconstruction remains good. The upper matrix of Figure 7.12 shows only slightly reduced efficiencies compared with the middle plot. Indeed, when these events are added to the signal (as in the lower plot) the overall matrix diagonality is decreased by a very small amount. This is even better for the dilepton $\Delta|\eta|$ bins of Figure 7.13 since the lepton quantities are well measured in the detector.

A further test was to see how the tau inclusion as signal or background affected the unfolded A_{C} values and uncertainties. The unfolding was performed without systematic uncertainties to see purely the statistical difference. Tables 7.1 and 7.2 show the inclusive and differential results for the $A_{\mathrm{C}}^{t\bar{t}}$ and A_{C}^{ll} values, respectively. In all cases, the uncertainty is reduced by several percent when they are in the signal. Owing to the good reconstruction and reduced uncertainties, it was decided to include the τ lepton contribution in the signal.
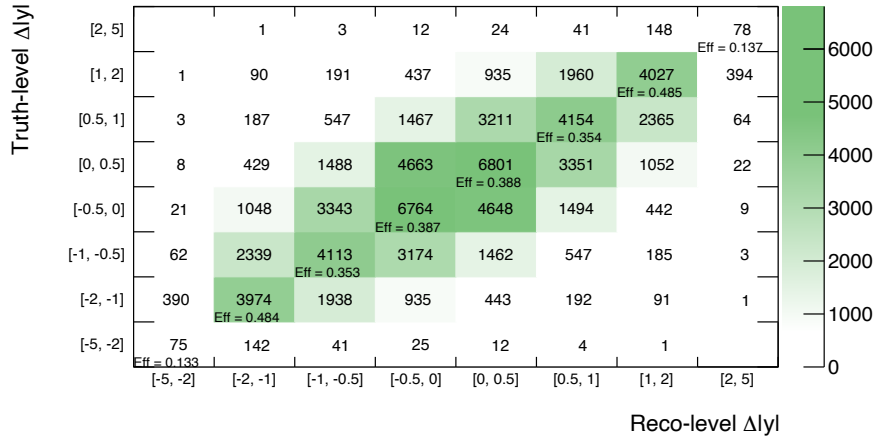
(a) $t\bar{t}$ decays yielding τ leptons.
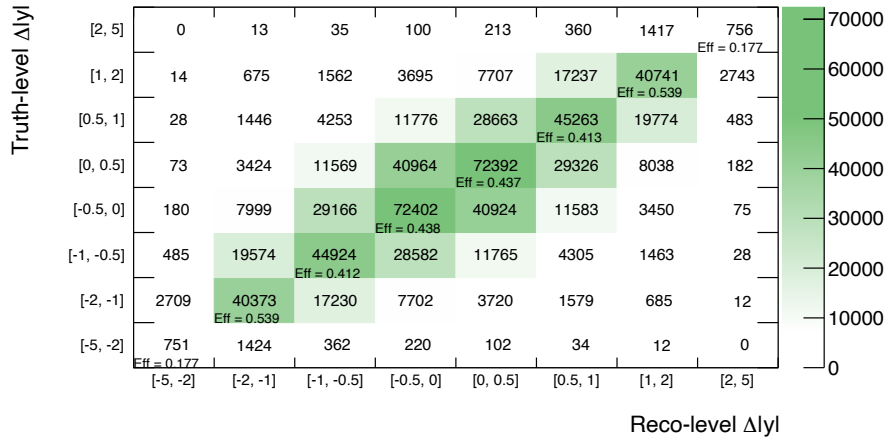
(b) $t\bar{t}$ decays without τ leptons.
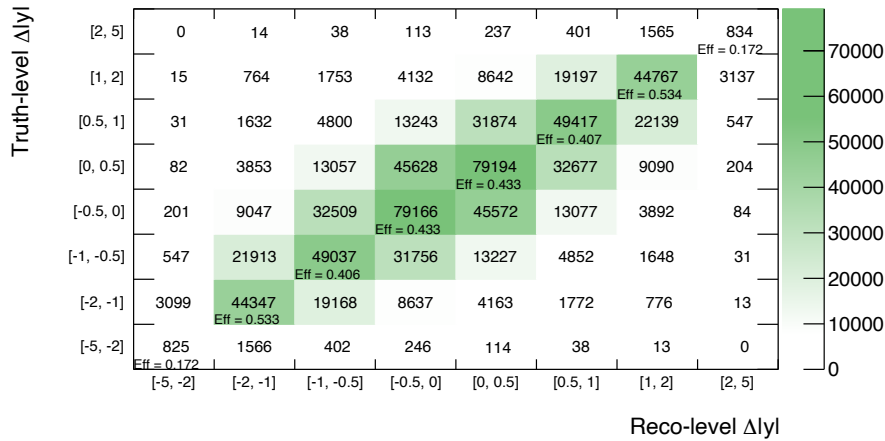
(c) $t\bar{t}$ decays yielding any lepton flavour.

Fig. 7.12 Matrices showing the number of reconstructed-level events in eight reconstructed-level and truth-level $t\bar{t}$ $\Delta|y|$ bins. Plots (a) and (b) are matrices where $t\bar{t}$ decays yield and do not yield τ leptons, respectively, and (c) is the sum of matrices (a) and (b).
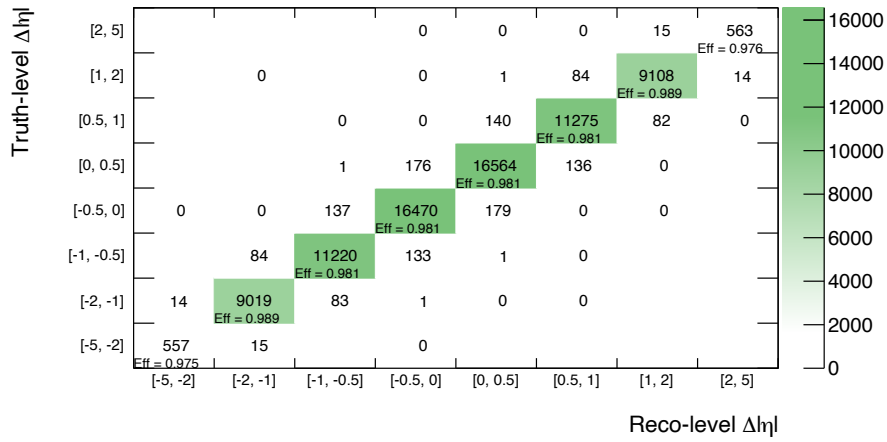
(a) $t\bar{t}$ decays yielding τ leptons.
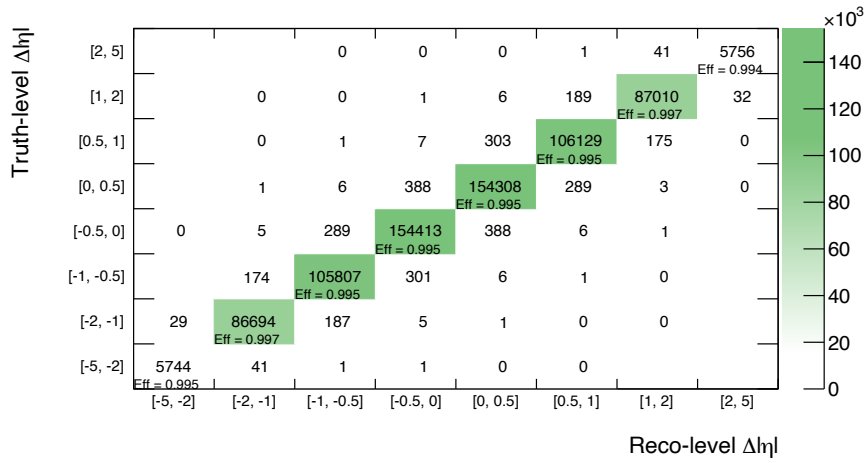
(b) $t\bar{t}$ decays without τ leptons.
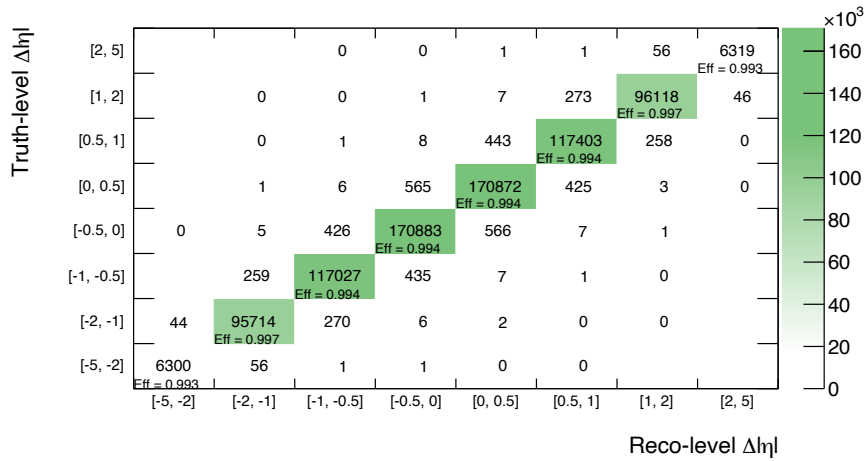
(c) $t\bar{t}$ decays yielding any lepton flavour.

Fig. 7.13 Matrices showing the number of reconstructed-level events in eight reconstructed-level and truth-level dilepton $\Delta|\eta|$ bins. The format is the same as in Figure 7.12.

	τ in background Unfolded $A_C^{t\bar{t}}$	τ in signal Unfolded $A_C^{t\bar{t}}$	$\Delta(A_C^{t\bar{t}}$ stat. unc.)
Inclusive	0.0035 ± 0.0036	0.0036 ± 0.0033	0.0003 (7.0%)
$p_{T,t\bar{t}} \in [0, 30]$ GeV	0.0085 ± 0.0115	0.0089 ± 0.0108	0.0007 (6.1%)
$p_{T,t\bar{t}} \in [30, 120]$ GeV	0.0007 ± 0.0101	0.0004 ± 0.0095	0.0006 (6.3%)
$p_{T,t\bar{t}} \in [120, \infty]$ GeV	0.0007 ± 0.0132	0.0009 ± 0.0124	0.0008 (6.0%)
$m_{t\bar{t}} \in [0, 500]$ GeV	0.0030 ± 0.0119	0.0036 ± 0.0117	0.0002 (2.1%)
$m_{t\bar{t}} \in [500, 750]$ GeV	0.0041 ± 0.0064	0.0038 ± 0.0060	0.0004 (6.4%)
$m_{t\bar{t}} \in [750, 1000]$ GeV	0.0047 ± 0.0199	0.0049 ± 0.0185	0.0014 (7.1%)
$m_{t\bar{t}} \in [1000, 1500]$ GeV	0.0052 ± 0.0379	0.0044 ± 0.0354	0.0025 (6.6%)
$m_{t\bar{t}} \in [1500, \infty]$ GeV	0.0099 ± 0.1424	0.0089 ± 0.1311	0.0113 (7.9%)
$\beta_{Z,t\bar{t}} \in [0.0, 0.3]$	<0.0001 ± 0.0186	0.0001 ± 0.0179	0.0007 (3.7%)
$\beta_{Z,t\bar{t}} \in [0.3, 0.6]$	0.0012 ± 0.0121	0.0017 ± 0.0116	0.0005 (4.3%)
$\beta_{Z,t\bar{t}} \in [0.6, 0.8]$	0.0029 ± 0.0097	0.0029 ± 0.0092	0.0005 (5.3%)
$\beta_{Z,t\bar{t}} \in [0.8, 1.0]$	0.0085 ± 0.0075	0.0081 ± 0.0069	0.0006 (7.9%)

Table 7.1 Comparison of the expected unfolded $A_C^{t\bar{t}}$ values and statistical uncertainties, where $t\bar{t}$ decays yielding τ leptons that themselves decay into electrons or muons are included as either background or signal. The comparison is done for an older setup, where the $\Delta|y|$ binning is not yet optimised. The last column shows the changes in the $A_C^{t\bar{t}}$ statistical uncertainties when the τ lepton events are included as signal or background, with the percentage differences, accounting for rounding errors, in brackets.

	τ in background Unfolded A_C^{ll}	τ in signal Unfolded A_C^{ll}	$\Delta(A_C^{ll}$ stat. unc.)
Inclusive	0.0019 ± 0.0014	0.0019 ± 0.0012	0.0001 (11%)
$p_{T,l\bar{l}} \in [0, 20]$ GeV	0.0016 ± 0.0065	0.0017 ± 0.0064	0.0002 (2.3%)
$p_{T,l\bar{l}} \in [20,70]$ GeV	0.0017 ± 0.0021	0.0017 ± 0.0020	0.0001 (6.6%)
$p_{T,l\bar{l}} \in [70, \infty]$ GeV	0.0022 ± 0.0019	0.0022 ± 0.0018	0.0001 (7.1%)
$m_{l\bar{l}} \in [0, 200]$ GeV	0.0017 ± 0.0015	0.0017 ± 0.0014	0.0001 (8.3%)
$m_{l\bar{l}} \in [200, 300]$ GeV	0.0036 ± 0.0041	0.0036 ± 0.0040	0.0001 (2.7%)
$m_{l\bar{l}} \in [300, 400]$ GeV	0.0049 ± 0.0086	0.0049 ± 0.0083	0.0002 (2.5%)
$m_{l\bar{l}} \in [400, \infty]$ GeV	0.0058 ± 0.0126	0.0056 ± 0.0120	0.0006 (4.8%)
$\beta_{Z,l\bar{l}} \in [0.0, 0.3]$	0.0001 ± 0.0029	0.0001 ± 0.0028	0.0002 (6.3%)
$\beta_{Z,l\bar{l}} \in [0.3, 0.6]$	0.0007 ± 0.0026	0.0008 ± 0.0024	0.0002 (6.6%)
$\beta_{Z,l\bar{l}} \in [0.6, 0.8]$	0.0018 ± 0.0028	0.0018 ± 0.0026	0.0002 (7.2%)
$\beta_{Z,l\bar{l}} \in [0.8, 1.0]$	0.0040 ± 0.0030	0.0040 ± 0.0028	0.0002 (7.6%)

Table 7.2 Comparison of the expected unfolded A_C^{ll} values and statistical uncertainties, where $t\bar{t}$ decays yielding τ leptons that themselves decay into electrons or muons are included as either background or signal. The format is the same as in Table 7.1.

7.4   Optimisation of the E_T^{miss} Cut

As discussed in Section 6.1.3, a large source of background in the $ee + \mu\mu$ channels origi-nates from Z + jets events. Since these do not have neutrinos in their final states, placing a cut on E_T^{miss} will reduce the background. Figure 7.14 shows the percentage of Z + jets events that make up the total MC prediction against increasing E_T^{miss} cuts. Figure 7.15 shows how the cuts affect the number of $t\bar{t}$ signal events and the signal statistical significance, $S/\sqrt{S+B}$, where S is the number of signal $t\bar{t}$ events and B the total number of background events. Two working points were investigated: a loose and tight setup. The loose setup used E_T^{miss} cuts of 20 GeV (0 GeV) in the ee and $\mu\mu$ 1 b-tag ($\geq$ 2 b-tag) channels, where the significance was highest. The tight setup used E_T^{miss} cuts of 60 GeV (30 GeV) in the ee and $\mu\mu$ 1 b-tag ($\geq$ 2 b-tag) channels, where the Z + jets background is reduced to only 2-3% of the MC expectation. The tight setup was tested as a maximum threshold since E_T^{miss} cuts greater than these have minimal reduction in the background and reduce the $t\bar{t}$ signal events substantially.

Unfolding of the inclusive and differential bins for the loose and tight working points was undertaken including the systematic uncertainties. The $A_C^{t\bar{t}}$ and A_C^{ll} values are shown in Tables 7.3 and 7.4, respectively. The last columns show the changes in the A_C uncertainties between the loose and tight working points.

From the results, the tight setup generally gives the smallest uncertainties on $A_C^{t\bar{t}}$ and A_C^{ll}, particularly for the inclusive cases. This arises due to large Z + jets MC statistical uncertain-ties and scale variation systematic uncertainties becoming less important. Whilst the tight working point does halve the number of $t\bar{t}$ events in the 1 b-tag channels, the significance is not strongly affected. Minimising the background is also preferable to ensure the charge asymmetry measurement is as pure as possible for the $t\bar{t}$ signal.
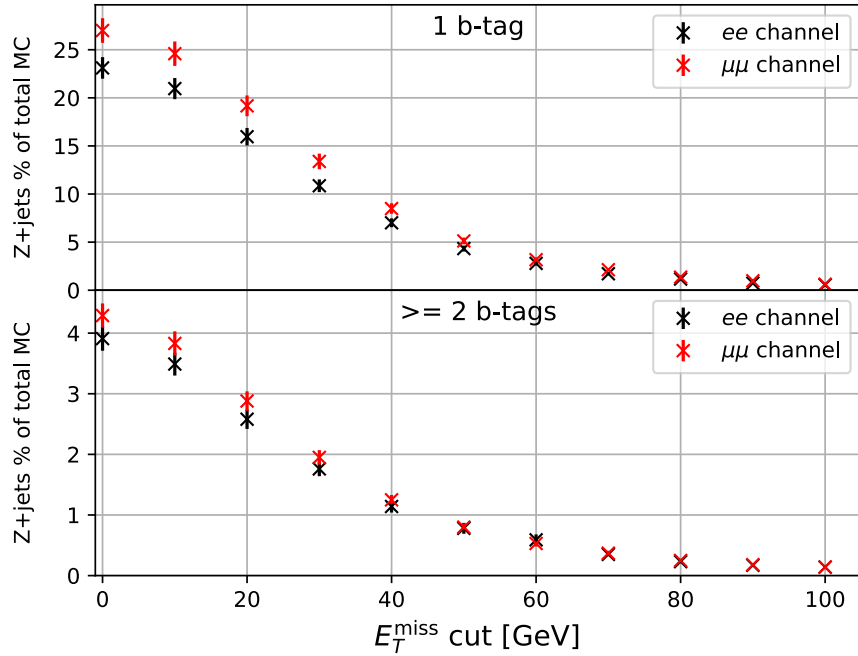
Fig. 7.14 The percentage of Z + jets events to total predicted MC events as a function of the E_T^{miss} cut. The error bars show the MC statistical uncertainties.
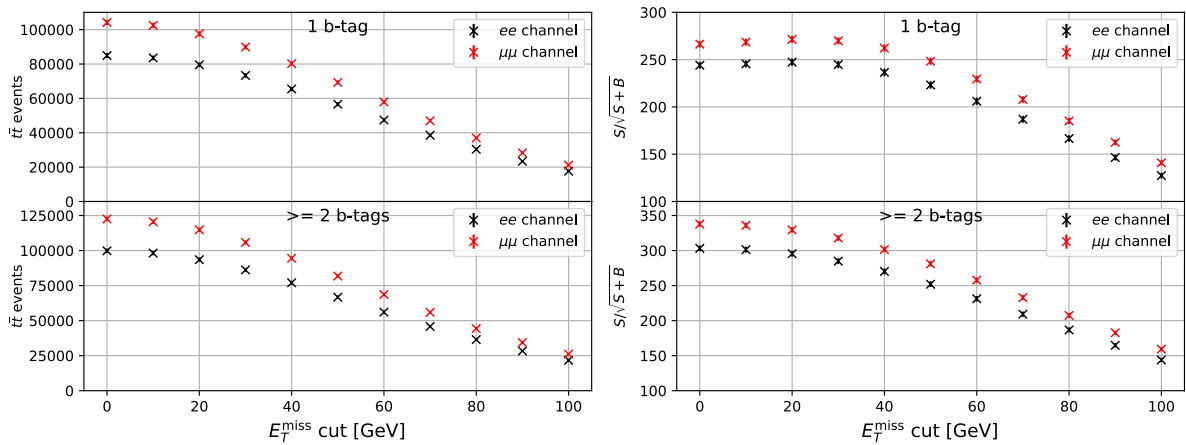
Fig. 7.15 The number of $t\bar{t}$ events (left) and the signal statistical significance (right) as a function of the E_T^{miss} cut. The error bars show the MC statistical uncertainties.

154

	Loose working point Unfolded $A_C^{t\bar{t}}$		Tight working point Unfolded $A_C^{t\bar{t}}$		$\Delta(A_C^{t\bar{t}}$ stat. + syst. unc.)
Inclusive	0.0036 $\pm$	0.0054	0.0035 $\pm$	0.0045	0.0009 (16%)
$p_{T,t\bar{t}} \in [0, 30]$ GeV	0.0088 $\pm$	0.0157	0.0084 $\pm$	0.0136	0.0021 (13%)
$p_{T,t\bar{t}} \in [30, 120]$ GeV	0.0004 $\pm$	0.0126	0.0006 $\pm$	0.0111	0.0015 (12%)
$p_{T,t\bar{t}} \in [120, \infty]$ GeV	0.0013 $\pm$	0.0153	0.0010 $\pm$	0.0149	0.0004 (2.8%)
$m_{t\bar{t}} \in [0, 500]$ GeV	0.0031 $\pm$	0.0147	0.0030 $\pm$	0.0150	-0.0003 (-2.3%)
$m_{t\bar{t}} \in [500, 750]$ GeV	0.0041 $\pm$	0.0074	0.0040 $\pm$	0.0073	0.0001 (1.0%)
$m_{t\bar{t}} \in [750, 1000]$ GeV	0.0046 $\pm$	0.0207	0.0048 $\pm$	0.0202	0.0005 (2.2%)
$m_{t\bar{t}} \in [1000, \infty]$ GeV	0.0061 $\pm$	0.0270	0.0059 $\pm$	0.0264	0.0006 (2.1%)
$\beta_{Z,t\bar{t}} \in [0.0, 0.3]$	<0.0001 $\pm$	0.0224	0.0001 $\pm$	0.0209	0.0015 (6.9%)
$\beta_{Z,t\bar{t}} \in [0.3, 0.6]$	0.0012 $\pm$	0.0134	0.0010 $\pm$	0.0130	0.0004 (2.7%)
$\beta_{Z,t\bar{t}} \in [0.6, 0.8]$	0.0023 $\pm$	0.0108	0.0028 $\pm$	0.0104	0.0004 (3.7%)
$\beta_{Z,t\bar{t}} \in [0.8, 1.0]$	0.0088 $\pm$	0.0084	0.0086 $\pm$	0.0081	0.0003 (3.7%)

Table 7.3 Comparison of the expected unfolded $A_C^{t\bar{t}}$ values and uncertainties (joint statistical and systematic) for the loose and tight E_T^{miss} cut working points. An older arrangement is used in the comparison, with non-merger of the *ee* and $\mu\mu$ channels and the fourth and fifth $m_{t\bar{t}}$ bins merged together. The last column shows the changes in the $A_C^{t\bar{t}}$ uncertainties between the two working points, with the percentage differences, accounting for rounding errors, in brackets.

	Loose working point Unfolded A_C^{ll}		Tight working point Unfolded A_C^{ll}		$\Delta(A_C^{ll}$ stat. + syst. unc.)
Inclusive	0.0021 $\pm$	0.0023	0.0021 $\pm$	0.0014	0.0009 (40%)
$p_{T,l\bar{l}} \in [0, 20]$ GeV	0.0017 $\pm$	0.0070	0.0020 $\pm$	0.0069	0.0001 (1.1%)
$p_{T,l\bar{l}} \in [20,70]$ GeV	0.0021 $\pm$	0.0023	0.0020 $\pm$	0.0022	0.0001 (2.7%)
$p_{T,l\bar{l}} \in [70, \infty]$ GeV	0.0023 $\pm$	0.0020	0.0022 $\pm$	0.0018	0.0002 (8.8%)
$m_{l\bar{l}} \in [0, 200]$ GeV	0.0019 $\pm$	0.0016	0.0019 $\pm$	0.0015	0.0001 (6.3%)
$m_{l\bar{l}} \in [200, 300]$ GeV	0.0042 $\pm$	0.0046	0.0043 $\pm$	0.0044	0.0002 (4.4%)
$m_{l\bar{l}} \in [300, 400]$ GeV	0.0050 $\pm$	0.0093	0.0050 $\pm$	0.0090	0.0003 (3.2%)
$m_{l\bar{l}} \in [400, \infty]$ GeV	0.0058 $\pm$	0.0128	0.0055 $\pm$	0.0124	0.0004 (3.5%)
$\beta_{Z,l\bar{l}} \in [0.0, 0.3]$	0.0001 $\pm$	0.0030	0.0001 $\pm$	0.0029	0.0001 (4.5%)
$\beta_{Z,l\bar{l}} \in [0.3, 0.6]$	0.0005 $\pm$	0.0028	0.0006 $\pm$	0.0025	0.0003 (9.3%)
$\beta_{Z,l\bar{l}} \in [0.6, 0.8]$	0.0018 $\pm$	0.0028	0.0018 $\pm$	0.0030	-0.0002 (-5.8%)
$\beta_{Z,l\bar{l}} \in [0.8, 1.0]$	0.0046 $\pm$	0.0033	0.0045 $\pm$	0.0031	0.0002 (4.8%)

Table 7.4 Comparison of the expected unfolded A_C^{ll} values and uncertainties (joint statistical and systematic) for the loose and tight E_T^{miss} cut working points. In this older arrangement, unfolding is undertaken to the full $\Delta|\eta|$ phase-space, which is later modified (see Section 7.5.2). The format is the same as in Table 7.3.

7.5 Binning Choice and Bias

Since the data will be unfolded with the Powheg + Pythia8 response matrix, it is essential that deviations in data from the MC expectation do not lead to biases in the A_C measurements. The number of bins and positioning of bin edges in $\Delta|y|$ and $\Delta|\eta|$ can affect the migrations and lead to different unfolded results. More bins allows better tracking of the migrations and hence smaller biases in the measurement. Fewer bins reduce the relative statistical uncertainties in each bin. In the analysis, two positive and two negative bins were tested in $\Delta|y|$ and $\Delta|\eta|$ for the inclusive and differential cases. Migrations which change the sign of $\Delta|y|$ and $\Delta|\eta|$ are most important for the A_C values so four bins should suffice. The binning was therefore $[-5, \ -x, \ 0, \ x, \ 5]$ for the distributions, where x was to be determined. For this evaluation, the truth- and reconstructed-level $\Delta|y|$ and $\Delta|\eta|$ MC events were scaled using two methods that modify the asymmetry:

- Protos reweighting: a 250 GeV BSM axigluon that yields $t\bar{t}$ in pair-production was modelled with the PROTOS generator [185]. Different coupling strengths of the axigluon to the top and light quarks yield different asymmetries. The reweighting functions, $w_p(\text{true}(\Delta|y|))$ and $w_p(\text{true}(\Delta|\eta|))$, are functional scale factors that depend on the truth-level $\Delta|y|$ and $\Delta|\eta|$ values. The truth-level events and reconstructed-level events were multiplied by these factors. The Protos reweighting function for an injected $+4\%$ asymmetry is shown in Figure 7.16. Since there is no form beyond ± 3 on the x-axis, any values of $\Delta|y|$ and $\Delta|\eta|$ outside this range were reweighted with the value at $w_p(\pm 3)$.

- Linear reweighting: the truth- and reconstructed-level distributions were reweighted according to $w_l = 1 + k \times \text{true}(\Delta|y|)$ or $w_l = 1 + k \times \text{true}(\Delta|\eta|)$, where k is a constant to vary the asymmetry.
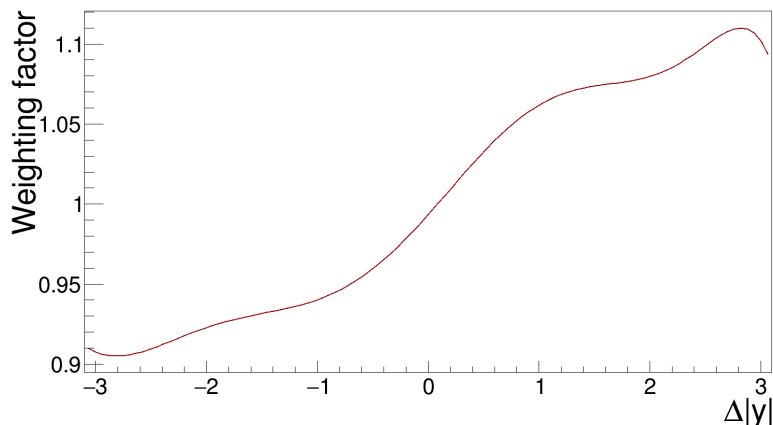
Fig. 7.16 The Protos reweighting function corresponding to a $+4\%$ asymmetry above the SM expectation.

For each method, eight functions were produced that vary the asymmetry between -4% and $+4\%$ at the truth-level in 1% steps, giving eight working points. For the inclusive case and each differential bin, the x values were determined separately. In FBU, x can be different for the truth- and reconstructed-level bins but the initial tests kept them identical for simplicity.

For a chosen value of x, the reconstructed-level events for each Protos working point were smeared according to Poisson statistics in 100 separate pseudo-experiments. Each pseudo-experiment was then unfolded (without including systematic uncertainties first of all) with the SM response matrix. The mean and standard deviation of the set of unfolded asymmetries from the pseudo-experiments were taken as the overall asymmetry value and its uncertainty, respectively, for each working point. A plot of the unfolded asymmetries against the actual truth-level asymmetries from MC for each working point was produced and a straight line fit to the points. The line should have a gradient of 1 and offset of 0. Any deviations were incorporated as a bias:

$$
\begin{aligned}
\text{bias} &= \text{unfolded } A_{\text{C}} - \text{truth } A_{\text{C}} \\
&= \text{unfolded } A_{\text{C}} - \frac{\text{unfolded } A_{\text{C}} - \text{offset}}{\text{slope}}.
\end{aligned}
\tag{7.13}
$$

The bias on the slope scales with the magnitude of the unfolded A_C, whereas the bias on the offset is independent of the value. An example linearity plot is shown in Figure 7.17. Here, the offset is close to 0 but there is a significant bias in the slope. This is therefore not a good bin edge to use. The best bin edges were determined by scanning different values of x and
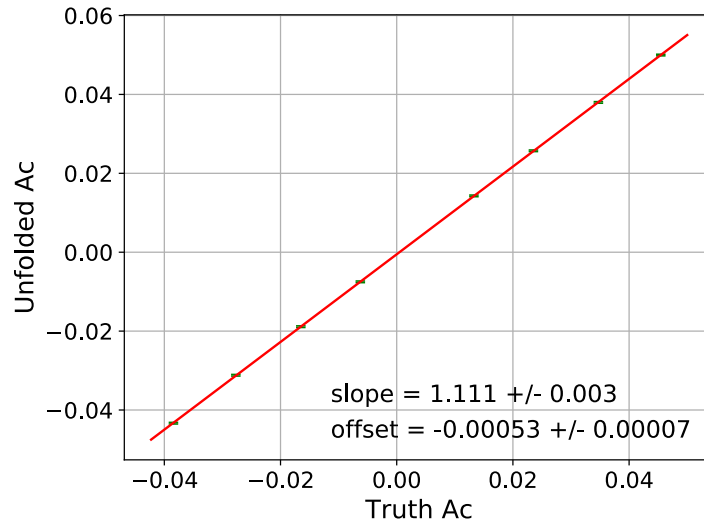
Fig. 7.17 An example linearity test for the eight Protos points (shown as green points with statistical error bars) for the inclusive $t\bar{t}$ asymmetry. A bin edge of $x = 1.0$ is used here for the truth- and reconstructed-level bins.

producing the linearity plots. The edges leading to the smallest biases were chosen. These were then verified by running 300 pseudo-experiments with full-systematic uncertainties on each Protos point, and 300 statistical-only pseudo-experiments on each linearly reweighted point for the binning configurations as a cross-check. The systematic uncertainties only have a small effect on the slope and offset uncertainties and negligible effect on their central values. The biases were then compared between Protos and linear reweighting.

7.5.1 Binning Optimisation for $t\bar{t}$ $\Delta|y|$

For the inclusive $A_C^{t\bar{t}}$, x values between 0.3 and 1.1 were tried for the initial 100 pseudo-experiment scan with the Protos points. Their slopes and offsets are shown in Figure 7.18.

At $x = 0.5$, these are very close to 1 and 0, respectively.
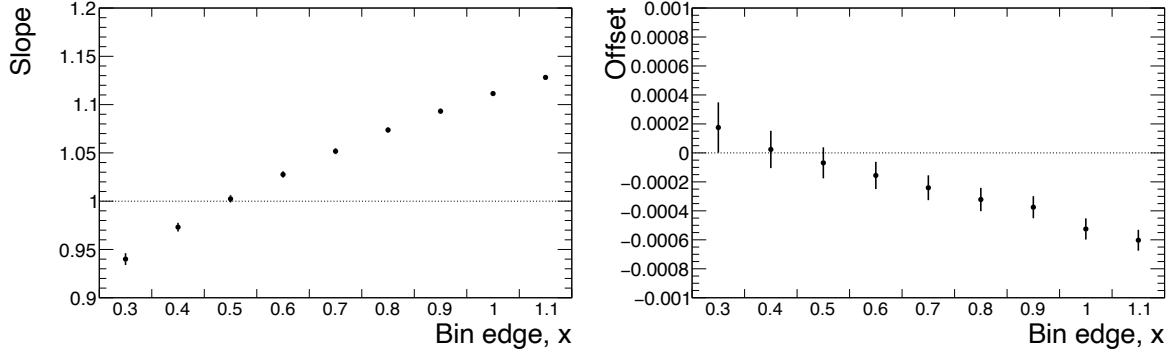
Fig. 7.18 The slopes (left) and offsets (right) against x for the inclusive $t\bar{t}$ asymmetry bin scan. The uncertainties are statistical.

For each $p_{T,t\bar{t}}$, $m_{t\bar{t}}$ and $\beta_{Z,t\bar{t}}$ differential bin, similar scans were repeated but taking into account migrations between the differential bins (as can be seen in Figures 7.2, 7.3 and 7.4) in addition to the $\Delta|y|$ bins. Changing the bin edge, x_b, in differential bin b can lead to a different linearity in differential bin a when its bin edge, x_a, is kept constant. This is most significant between adjacent differential bins. The bin scanning was therefore conducted such that for each scan of x_a, the adjacent bin edges were also scanned and the set of edges giving the best linearity in all bins was chosen.

With the proposed bin edges, the verification tests of 300 pseudo-experiments for the Protos and linearly reweighted points are shown in Tables 7.5 and 7.6. For both reweighting methods, the biases are small with respect to the overall $A_C^{t\bar{t}}$ uncertainties (shown in Section 7.8) so these bin edges were used for the analysis. The biases from Protos (as opposed to linear) reweighting were included as an uncertainty on $A_C^{t\bar{t}}$ since they are generally a little larger, include effects from the full-systematic uncertainties (though in practise these have negligible impact on the biases), and are based on a BSM model the analysis could be sensitive to.

Should the measured asymmetry be much greater in magnitude than the SM expectation, the effect from the offset bias becomes negligible and the slope bias is significant. In this case, the bias from linear reweighting would be greater and may be used as the uncertainty. The bias would be large with respect to the overall $A_C^{t\bar{t}}$ uncertainty but in the worst-case scenarios (of slopes around 0.9), the bias uncertainty would be 10% of the $A_C^{t\bar{t}}$ central value (itself large), meaning a precise measurement of its value could still be made. However, from previous LHC analyses (see Figures 5.12 and 5.13), no significant deviations were expected from the SM predictions.

| | $A_C^{t\bar{t}}$ | x | Protos reweighting | | | |
			Slope	Offset	|Bias|	$\frac{\|Bias\|}{Total\ unc.}$ (%)
Inclusive	0.0036	0.5	0.998±0.002	0.0000±0.0001	<0.0001	<0.1
$p_{T,t\bar{t}} \in [0, 30]$ GeV	0.0090	0.6	1.009±0.009	0.0017±0.0002	0.0017	12.6
$p_{T,t\bar{t}} \in [30, 120]$ GeV	0.0003	0.5	1.003±0.007	-0.0015±0.0002	0.0015	12.3
$p_{T,t\bar{t}} \in [120, \infty]$ GeV	0.0012	0.4	0.970±0.009	0.0013±0.0003	0.0013	8.6
$m_{t\bar{t}} \in [0, 500]$ GeV	0.0035	0.4	0.986±0.010	0.0007±0.0002	0.0006	4.4
$m_{t\bar{t}} \in [500, 750]$ GeV	0.0039	0.6	0.995±0.004	0.0002±0.0001	0.0002	2.3
$m_{t\bar{t}} \in [750, 1000]$ GeV	0.0049	1.0	1.012±0.011	0.0013±0.0004	0.0014	6.5
$m_{t\bar{t}} \in [1000, 1500]$ GeV	0.0046	0.9	1.008±0.019	0.0000±0.0007	<0.0001	<0.1
$m_{t\bar{t}} \in [1500, \infty]$ GeV	0.0104	0.9	0.978±0.080	0.0017±0.0026	0.0015	1.1
$\beta_{Z,t\bar{t}} \in [0.0, 0.3]$	0.0002	0.3	0.987±0.028	0.0003±0.0004	0.0003	1.3
$\beta_{Z,t\bar{t}} \in [0.3, 0.6]$	0.0016	0.3	0.988±0.009	0.0002±0.0002	0.0002	1.5
$\beta_{Z,t\bar{t}} \in [0.6, 0.8]$	0.0029	0.5	1.011±0.006	-0.0004±0.0002	0.0003	3.1
$\beta_{Z,t\bar{t}} \in [0.8, 1.0]$	0.0081	0.7	0.997±0.005	0.0013±0.0001	0.0013	15.1

Table 7.5 Linearity results with Protos reweighting of $A_C^{t\bar{t}}$ for the best bin edges, x. 300 pseudo-experiments with full-systematic uncertainties were used in the unfolding. The slopes, offsets and biases (for the expected asymmetries given in the second column) are shown. The last column shows the biases as a percentage of the total $A_C^{t\bar{t}}$ uncertainties, determined in Section 7.8.

	$A_C^{t\bar{t}}$	x	Linear reweighting			
			Slope	Offset	|Bias|	$\dfrac{\|Bias\|}{Total\ unc.}$ (%)
Inclusive	0.0036	0.5	0.935±0.003	0.0002±0.0001	<0.0001	<0.1
$p_{T,t\bar{t}} \in [0, 30]$ GeV	0.0090	0.6	0.934±0.011	0.0012±0.0002	0.0006	4.5
$p_{T,t\bar{t}} \in [30, 120]$ GeV	0.0003	0.5	0.950±0.010	-0.0008±0.0002	0.0008	6.8
$p_{T,t\bar{t}} \in [120, \infty]$ GeV	0.0012	0.4	0.922±0.014	0.0004±0.0002	0.0004	2.5
$m_{t\bar{t}} \in [0, 500]$ GeV	0.0035	0.4	0.950±0.015	0.0007±0.0002	0.0006	3.9
$m_{t\bar{t}} \in [500, 750]$ GeV	0.0039	0.6	0.921±0.004	0.0001±0.0001	0.0002	3.0
$m_{t\bar{t}} \in [750, 1000]$ GeV	0.0049	1.0	0.973±0.012	0.0013±0.0003	0.0012	5.8
$m_{t\bar{t}} \in [1000, 1500]$ GeV	0.0046	0.9	0.888±0.023	-0.0023±0.0007	0.0032	8.3
$m_{t\bar{t}} \in [1500, \infty]$ GeV	0.0104	0.9	0.917±0.100	0.0016±0.0026	0.0008	0.6
$\beta_{Z,t\bar{t}} \in [0.0, 0.3]$	0.0002	0.3	0.955±0.047	-0.0010±0.0003	0.0010	5.0
$\beta_{Z,t\bar{t}} \in [0.3, 0.6]$	0.0016	0.3	0.972±0.012	0.0001±0.0002	<0.0001	0.2
$\beta_{Z,t\bar{t}} \in [0.6, 0.8]$	0.0029	0.5	0.990±0.007	-0.0006±0.0002	0.0007	6.3
$\beta_{Z,t\bar{t}} \in [0.8, 1.0]$	0.0081	0.7	0.919±0.005	0.0012±0.0001	0.0006	6.5

Table 7.6 Linearity results with linear reweighting of $A_C^{t\bar{t}}$ for the best bin edges, x. 300 pseudo-experiments without systematic uncertainties were used in the unfolding. The format is the same as in Table 7.5.

7.5.2 Binning Optimisation for Dilepton $\Delta|\eta|$

As for $t\bar{t}$ $\Delta|y|$, x values were scanned for the inclusive and differential dilepton $\Delta|\eta|$ bins, initially with 100 pseudo-experiments for each Protos point without systematic uncertainties. The inclusive slopes and offsets are shown in Figure 7.19.

All of the bin edges give slopes of 0.9 or less, which would lead to a large bias with respect to the total uncertainty if the unfolded data gave an asymmetry much larger than the MC expectation. An attempt to reduce the bias was to split $\Delta|\eta|$ into more than four bins. Table 7.7 shows the slopes and offsets for these cases.

Fig. 7.19 The slopes (left) and offsets (right) against x for the inclusive leptonic asymmetry bin scan with 100 pseudo-experiments. The uncertainties are statistical.

$\Delta|\eta|$ binning	Slope	Offset
6 bins: $\pm$ [0, 1.4, 2.2, 5]	0.787 ± 0.003	0.00049 ± 0.00005
6 bins: $\pm$ [0, 1.4, 2.5, 5]	0.825 ± 0.002	0.00036 ± 0.00004
10 bins: $\pm$ [0, 0.2, 0.6, 1, 1.5, 5]	0.936 ± 0.003	-0.00003 ± 0.00004
20 bins: $\pm$ [0, 0.1, 0.2, 0.4, 0.6, 0.8, 1, 1.2, 1.5, 1.8, 5]	0.953 ± 0.003	-0.00006 ± 0.00004
24 bins: $\pm$ [0, 0.1, 0.2, 0.4, 0.6, 0.8, 1, 1.2, 1.5, 1.8, 2, 2.5, 5]	0.868 ± 0.002	0.00011 ± 0.00004
30 bins: $\pm$ [0, 0.1, 0.2, 0.3, 0.4, 0.5, 0.6, 0.8, 1, 1.1, 1.2, 1.5, 1.8, 2, 2.5, 5]	0.869 ± 0.003	0.00039 ± 0.00004

Table 7.7 Slopes and offsets for additional bins in $\Delta|\eta|$. The binning in the square brackets is symmetrical between positive and negative $\Delta|\eta|$ and is identical at reconstructed- and truth-level. 100 pseudo-experiments were performed without systematic uncertainties.

The 20 bin configuration does give better linearity but this becomes worse again for the 24 and 30 bin configurations. In all cases the slope is less than one so it is clear the bias is coming from another source. One possible source is from a detector acceptance effect. As described in Section 3.4, the inner detector and electromagnetic calorimeter only cover the phase space $|\eta| < 2.5$ and the muon system $|\eta| < 2.7$ (though selection was for $|\eta| < 2.5$) and so all leptons fall within $|\eta| < 2.5$ (see Sections 6.3.1 and 6.3.2). Therefore, $|\Delta|\eta|| = ||\eta_{l^+}| - |\eta_{l^-}|| < 2.5$. Although this also applies to the $t\bar{t}$ events, the jets can

be reconstructed up to $|y| < 4.9$ so it is possible to reconstruct top quarks in the range $|\Delta|y|| < 4.9$. The acceptance effect is shown in Figure 7.20, where the cut-off at $|\Delta|\eta|| < 2.5$ can be seen in the ratio plot.
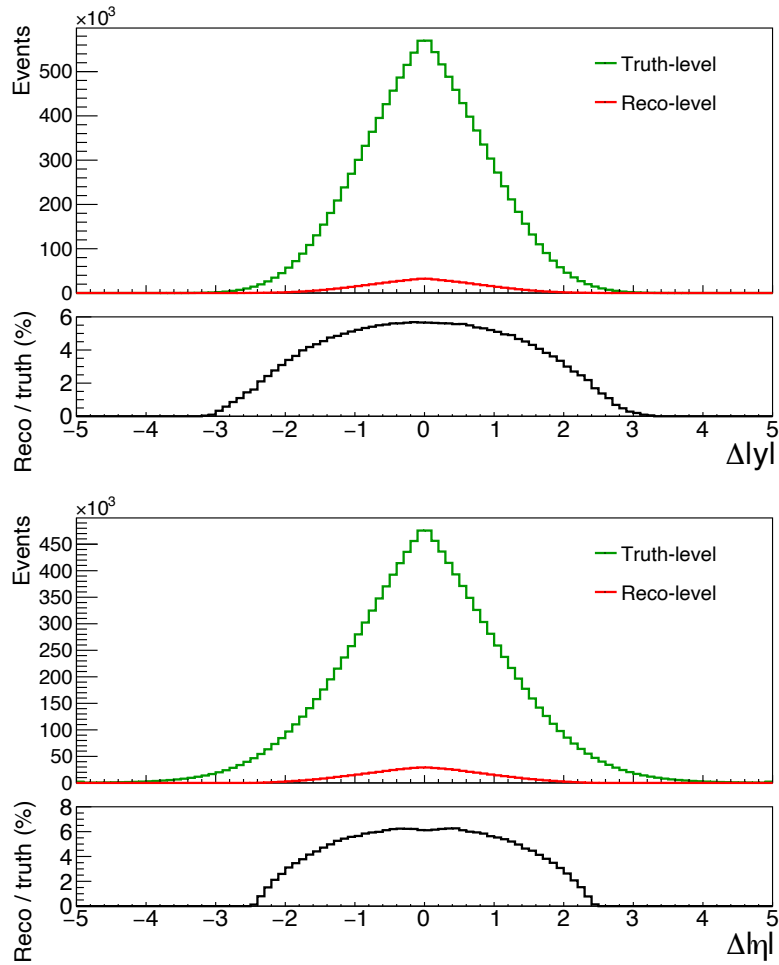
Fig. 7.20 The reconstructed- and truth-level $t\bar{t}$ $\Delta|y|$ (upper plot) and dilepton $\Delta|\eta|$ (lower plot) distributions. All four channels are merged for display purposes. Ratios are shown at the bottom of each plot.

Approximately 2% of the truth-level events fall in $\Delta|\eta| < -2.5$ and a further 2% in $\Delta|\eta| > 2.5$. If these truth events are reweighted with the Protos +4% asymmetry, this changes to 1.85% and 2.16% for $\Delta|\eta| < -2.5$ and $\Delta|\eta| > 2.5$, respectively. However, the lack of detector acceptance means these events are not propagated to reconstructed-level. The response

matrices therefore have probabilities of zero for $|\Delta|\eta|| > 2.5$ regardless of changes in truth-level asymmetry at $|\Delta|\eta|| > 2.5$. For the Protos $+4\%$ asymmetry, the unfolded asymmetry will therefore be less than the actual truth-level value. To see this effect in FBU, the 6 bin configuration, $[-5, -2.5, -1.4, 0, 1.4, 2.5, 5]$ (applied at reconstructed- and truth-level), was studied. Since there are no events in the outermost bins at reconstructed-level, there are no preferred numbers of truth-level events in the unfolding for these bins, meaning all possibilities in the flat prior distribution, $[0, 2\tilde{t}_j]$ are equally likely. The posterior distributions for the outermost two truth bins for the Protos $+4\%$ asymmetry can be seen in the upper plots of Figure 7.21. The mean value is simply the expected SM $\tilde{t}_j$ and not the expected Protos value. Hence the unfolded asymmetry is smaller than expected. For the Protos -4% asymmetry, the same effect is observed whereby the outer truth bins again match the SM expectation, which leads to a more positive unfolded asymmetry than expected. This can be seen in the lower plots of Figure 7.21. Table 7.8 shows a summary of the expected truth-level and unfolded A_C^{ll} values for the Protos $+4\%$ and -4% asymmetries in this 6 bin configuration.
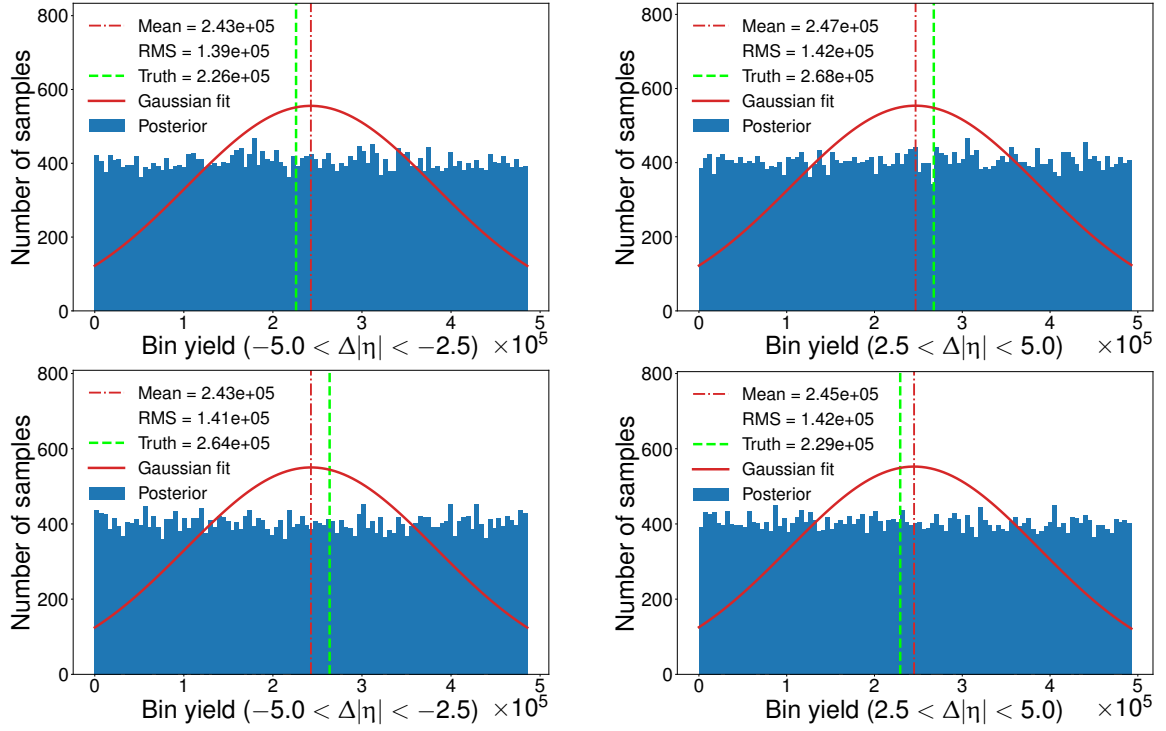
Fig. 7.21 Unfolded outer bin posterior distributions in $[-5, -2.5]$ (left) and $[2.5, 5]$ (right) for the $+4\%$ (upper) and -4% (lower) Protos reweighting working points. No reconstructed-level events occur in these bins. A clearly unsuitable Gaussian fit (red curve) to the flat posterior distribution yields a mean (red vertical line) that does not overlap with the truth Protos expectation (green vertical line).

Additional Protos asymmetry	Expected truth A_C^{ll}	Unfolded A_C^{ll}
$+4\%$	0.04546 ± 0.00006	0.0217 ± 0.0163
-4%	-0.03843 ± 0.00006	-0.0175 ± 0.0165

Table 7.8 The expected truth-level and unfolded A_C^{ll} values for the 6 bin configuration.

A 4 bin configuration, $[-5, -1.4, 0, 1.4, 5]$, was also considered. Here, reconstructed-level events can fall in the outer bins and so the posterior distributions should be Gaussian. However, the response in bin $[1.4, 5]$ is a smearing of the response in $[1.4, 2.5]$ and the zero response in $[2.5, 5]$, so the unfolded truth event counts (and hence asymmetries) still lie

closer to the SM expectations rather than the Protos expectations.
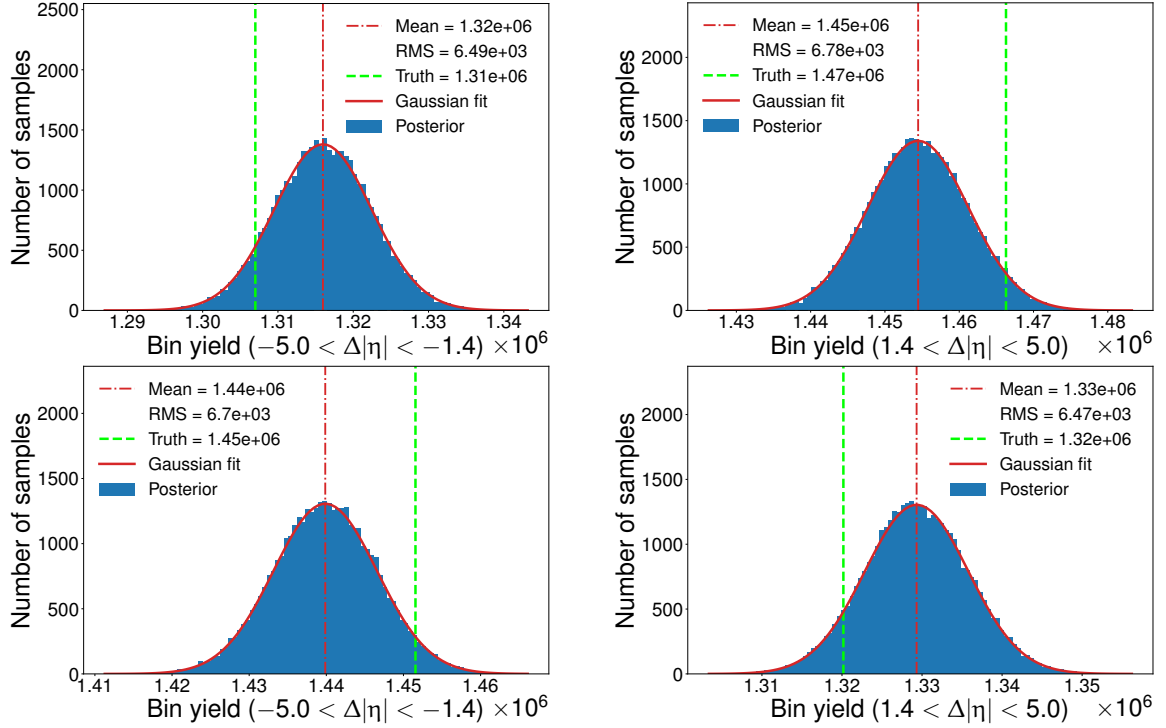
Fig. 7.22 Unfolded outer bin posterior distributions in $[-5, -1.4]$ (left) and $[1, 4, 5]$ (right) for the $+4\%$ (upper) and -4% (lower) Protos reweighting working points. Since there are reconstructed-level events, the unfolded posterior distributions are Gaussian but their means do not reflect the expected Protos truth values.

It is this effect that caused the slopes of the unfolded against truth A_C^{ll} values to be less than one in the bin scans. The unfolded Protos $+4\%$ and -4% outer truth bins are shown in the upper and lower plots of Figure 7.22, respectively. Table 7.9 shows a summary of the expected truth-level and unfolded A_C^{ll} values for the Protos $+4\%$ and -4% asymmetries in this 4 bin configuration.

Additional Protos asymmetry	Expected truth A_C^{ll}	Unfolded A_C^{ll}
$+4\%$	0.04546 ± 0.00006	0.0234 ± 0.0012
-4%	-0.03843 ± 0.00006	-0.0192 ± 0.0012

Table 7.9 The expected truth-level and unfolded A_C^{ll} values for the 4 bin configuration.

To combat the bias, it was decided to calculate the A_C^{ll} values in the reduced phase space of $|\Delta|\eta|| < 2.5$ to ensure there was always detector acceptance for the events at truth-level. Bin scans were repeated, this time with just 20 pseudo-experiments per Protos working point without systematic uncertainties for a quick test, and the slopes and offsets can be seen in Figure 7.23.
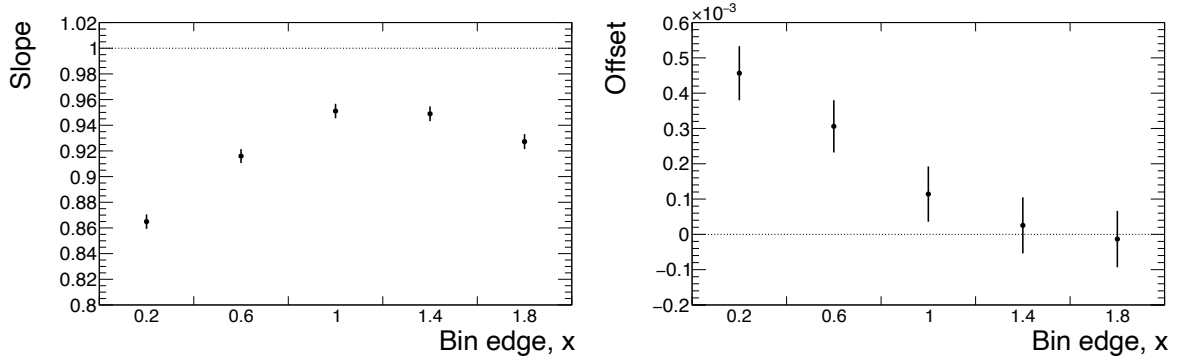
Fig. 7.23 The slopes (left) and offsets (right) against x for the inclusive leptonic asymmetry bin scan with 20 pseudo-experiments in the reduced phase space, $|\Delta|\eta|| < 2.5$. The varied bin edges are identical at truth- and reconstructed-level. The uncertainties are statistical.

There is a large improvement with respect to Figure 7.19 but the slopes are still less than one. FBU allows the truth- and reconstructed-level binning to differ, so the best bin edge from the slope and offset plots, $x = 1.4$, was kept constant at reconstructed-level and a scan of just the truth bins was undertaken. The results are shown in Figure 7.24. From interpolating the plot, a truth bin edge at $x = 0.9$ was likely to give the best slope and a good offset. This was verified with 300 full-systematic pseudo-experiments for each Protos point and 300

statistical-only pseudo-experiments for each linear reweighting point. The process was also repeated for the differential bins in dilepton m, p_T and β_Z. The final reconstructed- and truth-level bin edges with their slopes, offsets and biases for the Protos and linear reweighting methods are shown in Tables 7.10 and 7.11, respectively. Good linearity is obtained with both methods, yielding small expected biases that are in good agreement between the two methods.
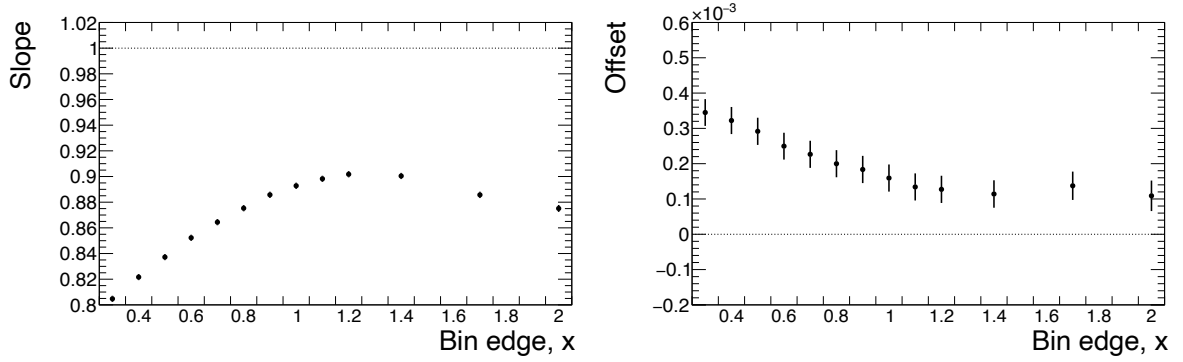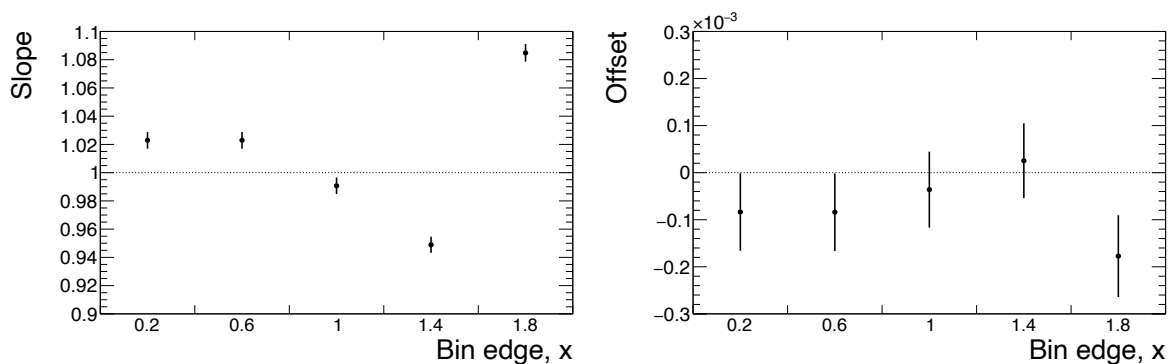

Fig. 7.24 The slopes (left) and offsets (right) against x for the inclusive leptonic asymmetry bin scan with 20 pseudo-experiments in the reduced phase space, $|\Delta|\eta|| < 2.5$. The bin edges are kept constant at $x = 1.4$ at reconstructed-level and varied only at truth-level. The uncertainties are statistical.

	A_C^{ll}	x	Protos reweighting			
			Slope	Offset	|Bias|	$\frac{\|Bias\|}{\text{Total unc.}}$ (%)
Inclusive	0.0019	1.4 (0.9)	0.999±0.002	0.0000±<0.0001	<0.0001	1.5
$p_{T,l\bar{l}} \in [0, 20]$ GeV	0.0015	1.6 (1.0)	1.008±0.009	0.0003± 0.0001	0.0003	4.9
$p_{T,l\bar{l}} \in [20, 70]$ GeV	0.0017	1.4 (0.9)	0.996±0.003	-0.0001±<0.0001	0.0001	4.1
$p_{T,l\bar{l}} \in [70, \infty]$ GeV	0.0022	1.2 (0.6)	1.002±0.003	-0.0001±<0.0001	0.0001	3.7
$m_{l\bar{l}} \in [0, 200]$ GeV	0.0016	1.2 (0.6)	1.001±0.002	0.0000±<0.0001	<0.0001	<0.1
$m_{l\bar{l}} \in [200, 300]$ GeV	0.0036	1.6 (1.0)	0.999±0.005	0.0001± 0.0001	0.0001	1.2
$m_{l\bar{l}} \in [300, 400]$ GeV	0.0049	1.6 (1.2)	0.984±0.009	-0.0002± 0.0002	0.0003	3.7
$m_{l\bar{l}} \in [400, \infty]$ GeV	0.0057	1.6 (1.2)	0.980±0.014	0.0009± 0.0002	0.0008	6.0
$\beta_{Z,l\bar{l}} \in [0.0, 0.3]$	0.0001	0.8 (0.9)	0.969±0.008	-0.0001± 0.0001	0.0001	4.6
$\beta_{Z,l\bar{l}} \in [0.3, 0.6]$	0.0008	1.6 (1.4)	1.002±0.004	0.0001± 0.0001	0.0001	4.7
$\beta_{Z,l\bar{l}} \in [0.6, 0.8]$	0.0018	1.8 (1.0)	1.004±0.003	-0.0003± 0.0001	0.0003	9.0
$\beta_{Z,l\bar{l}} \in [0.8, 1.0]$	0.0040	1.8 (1.4)	0.988±0.003	0.0004± 0.0001	0.0003	11.1

Table 7.10 Linearity results with Protos reweighting of A_C^{ll} for the best bin edges, x. The best reconstructed-level edge is shown without brackets and the best truth-level edge within brackets. 300 pseudo-experiments with full-systematic uncertainties were used in the unfolding. The slopes, offsets and biases (for the expected asymmetries given in the second column) are shown. The last column shows the biases as a percentage of the total A_C^{ll} uncertainties, determined in Section 7.8.

	A_C^{ll}	x	Linear reweighting			
			Slope	Offset	|Bias|	$\frac{\|Bias\|}{\text{Total unc.}}$ (%)
Inclusive	0.0019	1.4 (0.9)	0.991±0.001	0.0000±<0.0001	<0.0001	2.2
$p_{T,l\bar{l}} \in [0, 20]$ GeV	0.0015	1.6 (1.0)	1.004±0.005	0.0002± 0.0001	0.0002	2.6
$p_{T,l\bar{l}} \in [20, 70]$ GeV	0.0017	1.4 (0.9)	0.988±0.002	-0.0001±<0.0001	0.0002	7.4
$p_{T,l\bar{l}} \in [70, \infty]$ GeV	0.0022	1.2 (0.6)	0.994±0.002	0.0000±<0.0001	<0.0001	1.0
$m_{l\bar{l}} \in [0, 200]$ GeV	0.0016	1.2 (0.6)	0.991±0.001	0.0000±<0.0001	<0.0001	2.0
$m_{l\bar{l}} \in [200, 300]$ GeV	0.0036	1.6 (1.0)	0.991±0.003	0.0002± 0.0001	0.0001	3.1
$m_{l\bar{l}} \in [300, 400]$ GeV	0.0049	1.6 (1.2)	0.973±0.006	-0.0002± 0.0001	0.0004	4.1
$m_{l\bar{l}} \in [400, \infty]$ GeV	0.0057	1.6 (1.2)	0.981±0.009	0.0006± 0.0002	0.0005	4.2
$\beta_{Z,l\bar{l}} \in [0.0, 0.3]$	0.0001	0.8 (0.9)	0.967±0.004	-0.0001± 0.0001	0.0001	3.9
$\beta_{Z,l\bar{l}} \in [0.3, 0.6]$	0.0008	1.6 (1.4)	0.996±0.002	0.0001± 0.0001	0.0001	2.0
$\beta_{Z,l\bar{l}} \in [0.6, 0.8]$	0.0018	1.8 (1.0)	1.000±0.002	-0.0002± 0.0001	0.0002	7.2
$\beta_{Z,l\bar{l}} \in [0.8, 1.0]$	0.0040	1.8 (1.4)	0.986±0.002	0.0003± 0.0001	0.0003	8.8

Table 7.11 Linearity results with linear reweighting of A_C^{ll} for the best bin edges, x. 300 pseudo-experiments without systematic uncertainties were used in the unfolding. The format is the same as in Table 7.10.

7.6 Treatment of Systematic Uncertainties

Before processing with FBU, the systematic uncertainties were transformed to remove unnecessary effects, statistical fluctuations and to be compatible with the framework. The following sections describe these modifications and their manipulation within FBU.

7.6.1 Signal Modelling Normalisation

For all of the signal-modelling uncertainties (described in Section 6.8.2), their overall normalisations with respect to the expected nominal (unshifted) events were removed. This is since the asymmetries from Equations 5.8 and 5.9 are calculated as fractions. Normalisation effects in the signal cancel between the numerator and denominator. Thus, only the shape effect of the systematic uncertainty across the $\Delta|y|$ and $\Delta|\eta|$ bins with respect to the nominal expectation needs to remain.

However, a signal modelling uncertainty can alter the acceptance of the signal to enter a certain channel. In removing the normalisation effect from the signal modelling systematic uncertainties, this freedom is significantly reduced. To resolve this, new relative normalisation uncertainties were created in three of the four channels: $ee + \mu\mu \geq (2\ b\text{-tag})$, $e\mu\ (1\ b\text{-tag})$ and $e\mu \geq (2\ b\text{-tag})$. An additional degree of freedom exists in the simultaneous fitting of events in the reconstructed-level bins across all the channels so there are four degrees of freedom in total. The three new NPs were given flat prior distributions between 0% and 200% of the expected normalisation in that channel. The intention was for the FBU fitting procedure to greatly constrain the normalisation ranges relative to the large prior distributions.

7.6.2   Bootstrapping

It is possible for statistical fluctuations to occur in the systematic uncertainties due to limited MC sample sizes. A bootstrapping method [186] was used, where for each systematically shifted and nominal event, 100 random weights from a Poisson distribution of $P(\lambda = 1)$ were generated. Each weight then contributed to a new histogram, giving 100 replicas of both the systematically shifted and nominal $\Delta|y|$ or $\Delta|\eta|$ distributions. The run and event numbers were used as random seeds for generating the weights to ensure the events in the shifted and nominal distributions behaved in a correlated way. For each replica, the relative difference between the shifted and nominal distribution in each bin was calculated. The mean relative difference over the replicas was taken as the systematic uncertainty and the standard deviation as the statistical uncertainty. The following algorithm was then applied:

- For each $\Delta|y|$ or $\Delta|\eta|$ bin, calculate the significance, σ, of the systematic uncertainty events minus the nominal events, with respect to the statistical uncertainty.

- If any of the four bins differ by more than 2σ, the systematic uncertainty for that sample is significant, so do not modify the uncertainty.

- If all of the bins differ by less than 2σ, merge the four bins, and recalculate the systematic shift with respect to nominal.

- If the merged shift differs by more than 2σ, set the systematic uncertainty in all four bins to this merged value, effectively removing the shape but keeping the normalisation of the uncertainty.

- If the merged shift differs by less than 2σ, the systematic uncertainty is likely a statistical fluctuation so set all four bins of the uncertainty to zero.

This was undertaken for all the signal and background samples separately that are affected by the systematic uncertainties. The criterion of 2σ was used rather than 1σ due to there being four bins. In binomial statistics, the probability that a fluctuation will pass the 2σ threshold is
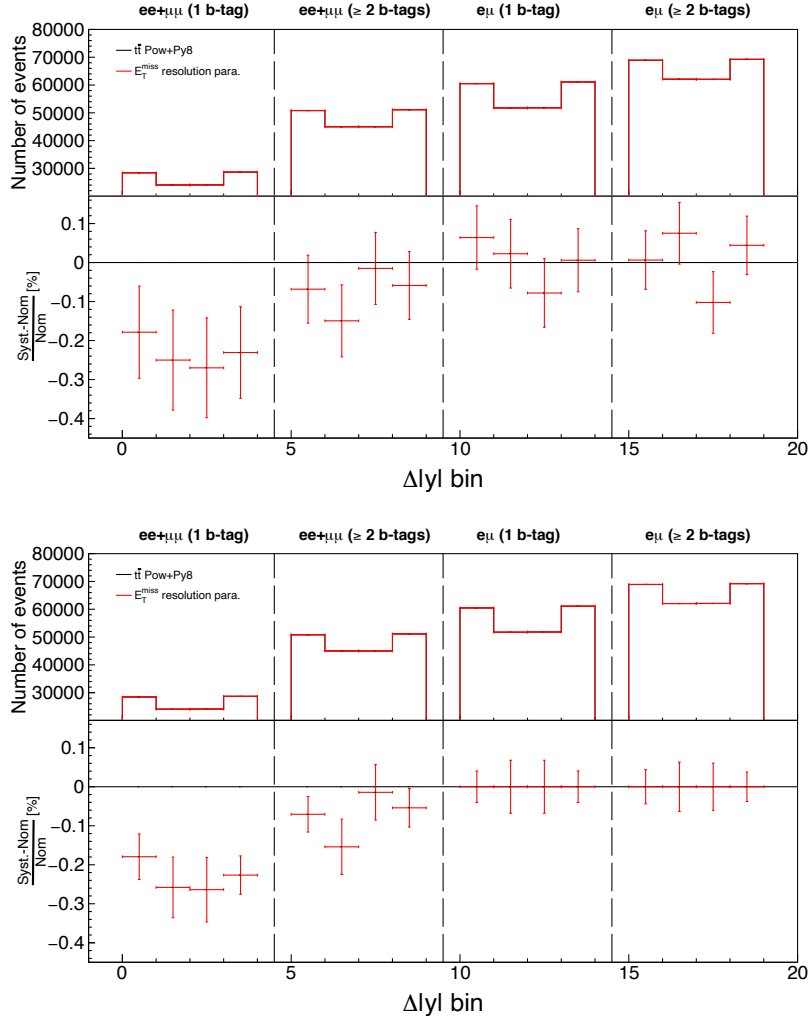
Fig. 7.25 The parallel E_T^{miss} resolution systematic uncertainty on the $t\bar{t}$ signal before (upper plot) and after (lower plot) bootstrapping for the four $\Delta|y|$ bins in each channel of the inclusive case. The x-axis refers to the bin number with a gap of one bin between each channel.

$1 - 0.95^4 = 19\%$. It is therefore unlikely a true statistical fluctuation will pass the bootstrap criteria. For 1σ, this is $1 - 0.68^4 = 79\%$ so the majority of statistical fluctuations would be greater than the threshold and not be affected by the bootstrapping method. An example of bootstrapping for the parallel E_T^{miss} resolution uncertainty (described in 6.8.1.9 and labelled "E_T^{miss} resolution para.") is shown in Figure 7.25. For the two $e\mu$ channels, all four bins in $\Delta|y|$ for the uncertainty fall within 2σ of the nominal expected MC so the bins were merged to remove the shape effect. The merged shift with respect to nominal was still less than 2σ

so the uncertainty was set to zero in these channels. For the $ee + \mu\mu$ channels, the shifts in the individual $\Delta|y|$ bins are sufficiently large so the uncertainty was not bootstrapped.

7.6.3 Symmetrisation

FBU does not allow asymmetric up and down variations of systematic uncertainties. For two-sided systematic uncertainties such as the jet energy scale NPs, the average of the up and down variation was taken as a symmetric two-sided systematic variation on the nominal sample. For one-sided systematic uncertainties such as the jet energy resolution NPs and h_{damp}, the difference between the shifted variation and the nominal sample was taken as the uncertainty and symmetrised.

7.6.4 Signal Statistical Uncertainties

The likelihood fitting does not incorporate statistical uncertainties in the MC signal events. This was resolved by smearing the bins of the response matrix 500 times according to Poisson statistics to give 500 matrices. The unfolding was then repeated for each smeared matrix and a distribution of A_{C} values obtained. The standard deviation of the distribution was taken as the signal MC statistical uncertainty and added in quadrature to the overall A_{C} uncertainty. Figure 7.26 shows an example for the inclusive $A_{\mathrm{C}}^{t\bar{t}}$ case. Summaries of the smearing results are shown later in Tables 7.12 and 7.13.
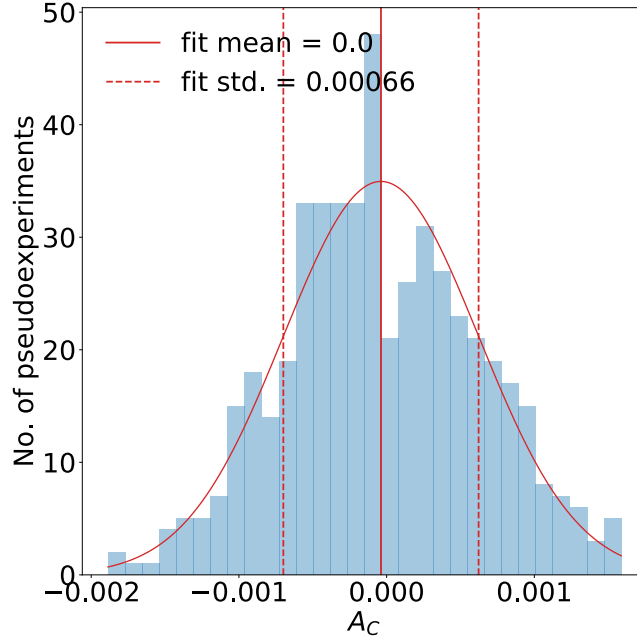
Fig. 7.26 An example distribution of $A_C^{t\bar{t}}$ in the inclusive case for 500 smeared response matrix unfoldings. The histogram is shifted to centre on zero and a Gaussian fit yields the mean and standard deviation shown by the red vertical lines.

7.6.5 Background Statistical Uncertainties

As for the signal, FBU does not account for statistical uncertainties in the MC background samples. Since the reconstructed-level background MC is used directly in the likelihood, each background $\Delta|y|$ or $\Delta|\eta|$ bin, i, was multiplied by an additional NP (γ_i parameter). The sampling of each γ_i value was controlled by a Poisson prior probability distribution based on the background bin's statistical uncertainty. Equation 7.10 was modified to become:

$$b_i(\boldsymbol{\theta}_o, \boldsymbol{\theta}_{bn}, \boldsymbol{\gamma}) = \gamma_i b_i(\boldsymbol{\theta}_o, \boldsymbol{\theta}_{bn}) \times \text{Poisson}(\tau_i | \gamma_i \tau_i), \qquad (7.14)$$

where $\tau_i = (b_i(0)/\delta b_i)^2$, and $b_i(0)$ and δb_i is the MC background yield and its statistical uncertainty, respectively.

7.6.6 Pulls and Constraints

As described in Section 7.2.5, the NP posterior distribution of a systematic uncertainty can be narrower (or occasionally wider) than its prior distribution in the FBU likelihood fitting. This means that the uncertainty has been constrained and its effect is smaller (or larger in rare cases) on the overall charge asymmetry uncertainty, compared with the initial expectation. The mean value of the NP posterior distribution can also be displaced (pulled) from the prior distribution's mean, which is centred on zero. This has the effect of shifting the MC expectation up or down. The pulls and constraints act to increase the likelihood in the FBU fitting procedure. Figure 7.27 shows an example pull and constraint for a JER NP in the inclusive case, where the ATLAS data (rather than MC simulation) were unfolded. The mean of the posterior distribution is pulled slightly in the negative direction by 0.067 relative to the prior distribution, which shifts the expected number of events down. The posterior distribution is also narrower than the prior distribution, constrained by a factor of 0.87, so will have a smaller effect on the overall $A_{\mathrm{C}}^{t\bar{t}}$ uncertainty had its prior value been kept.
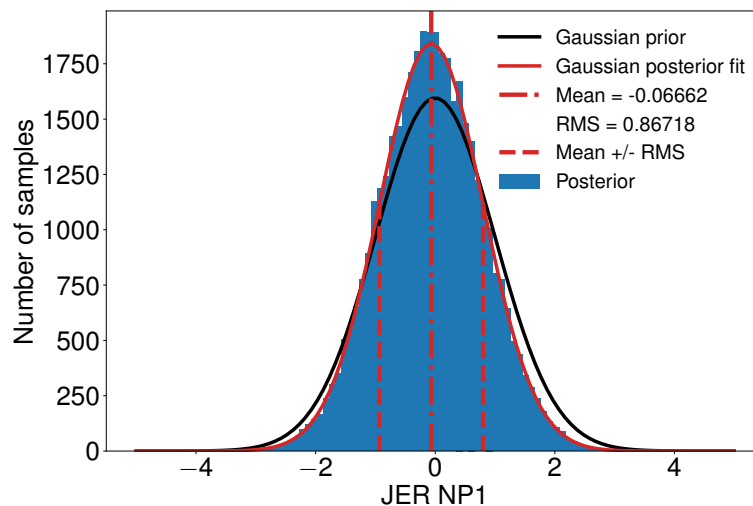
Fig. 7.27 A jet energy resolution uncertainty ("JER NP1") in the inclusive $t\bar{t}$ case, where the ATLAS data have been unfolded. The Gaussian prior distribution (with a standard deviation of one on the *x*-axis) is shown in black and the constrained posterior distribution in blue with a fitted Gaussian is shown in red.

To visualise the effects from all of the NPs, the unfolded $\Delta|y|$ and $\Delta|\eta|$ truth distributions were folded back to reconstructed-level with the SM response matrices, the backgrounds added on, the pulls included, and resultant systematic uncertainties shown. These are known as post-marginal plots. There should be good agreement between the ATLAS data and folded values if the likelihood fitting has worked and not introduced bias. In addition, reconstructed-level plots where FBU was not run and the systematic uncertainties were simply summed in quadrature for the expected MC reconstructed-level bins were created. These are known as pre-marginal plots. Here, the data-MC agreement may not be as good. In both sets of plots, the background MC statistical uncertainties are included in the light grey uncertainty band (as they are accounted for the in the FBU γ_i parameters) but the signal MC statistical uncertainties are not since they do not directly go into the likelihood. Figures 7.28 – 7.35 show the comparisons for the inclusive and differential bins in $\Delta|y|$ and $\Delta|\eta|$.
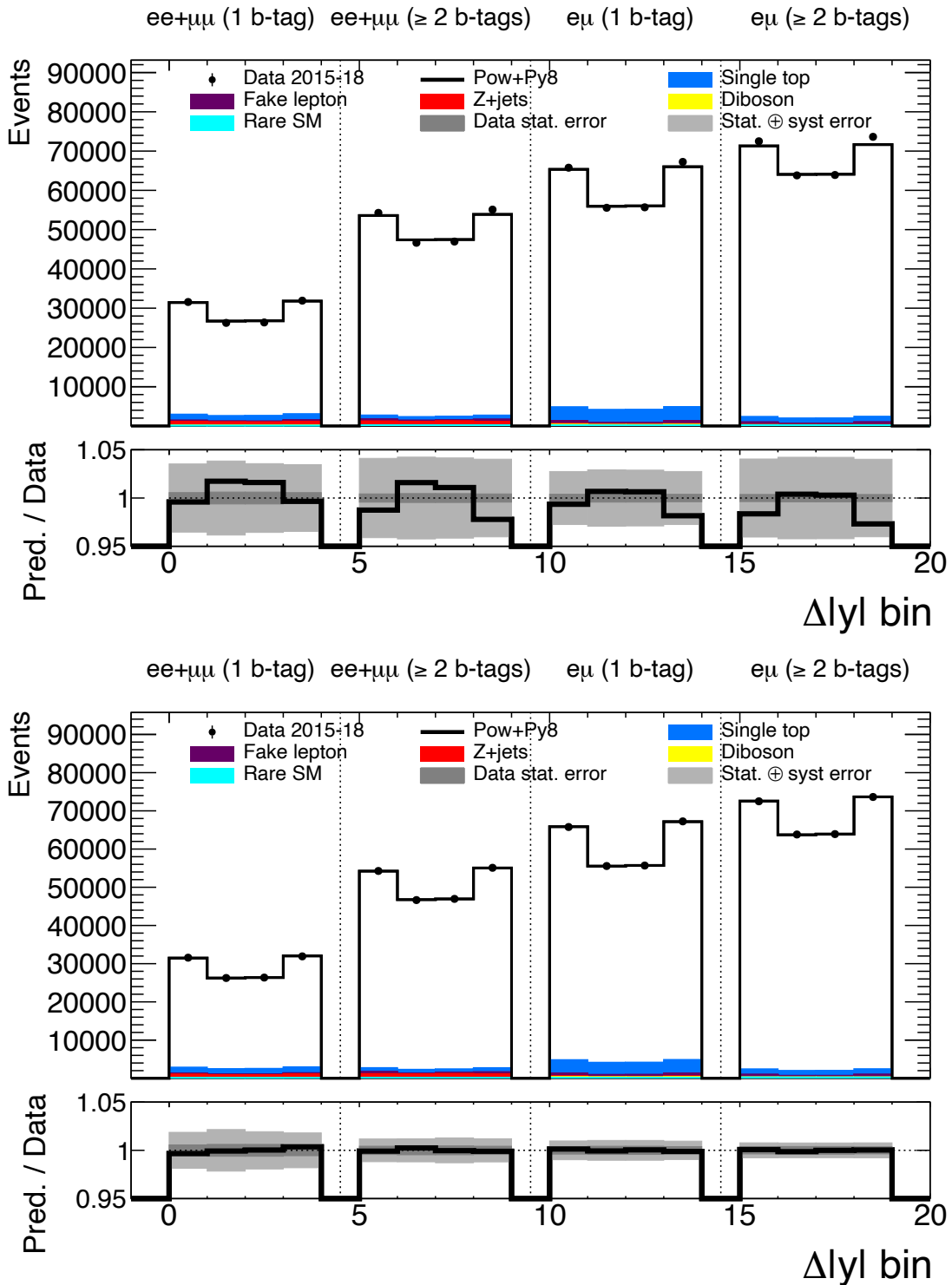
Fig. 7.28 Pre-marginal (upper plot) and post-marginal (lower plot) events in the inclusive $\Delta|y|$ bins. The four channels are shown side-by-side. The *x*-axis refers to the bin number with a gap of one bin between each channel.
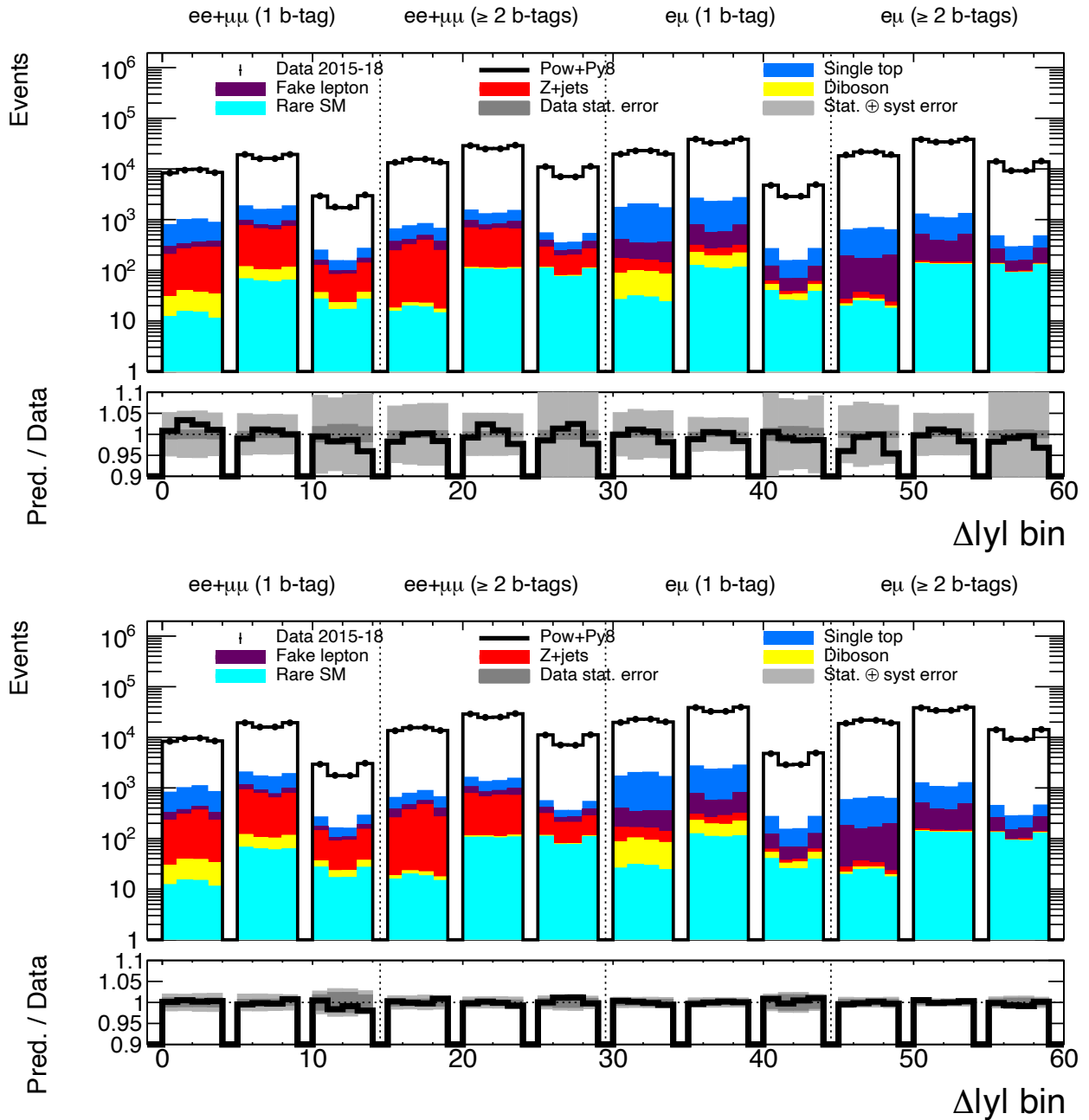
Fig. 7.29 Pre-marginal (upper plot) and post-marginal (lower plot) events in the $\Delta|y|$ bins across the three $p_{T,t\bar{t}}$ bins per channel. The x-axis refers to the bin number with a gap of one bin between each differential distribution and channel.
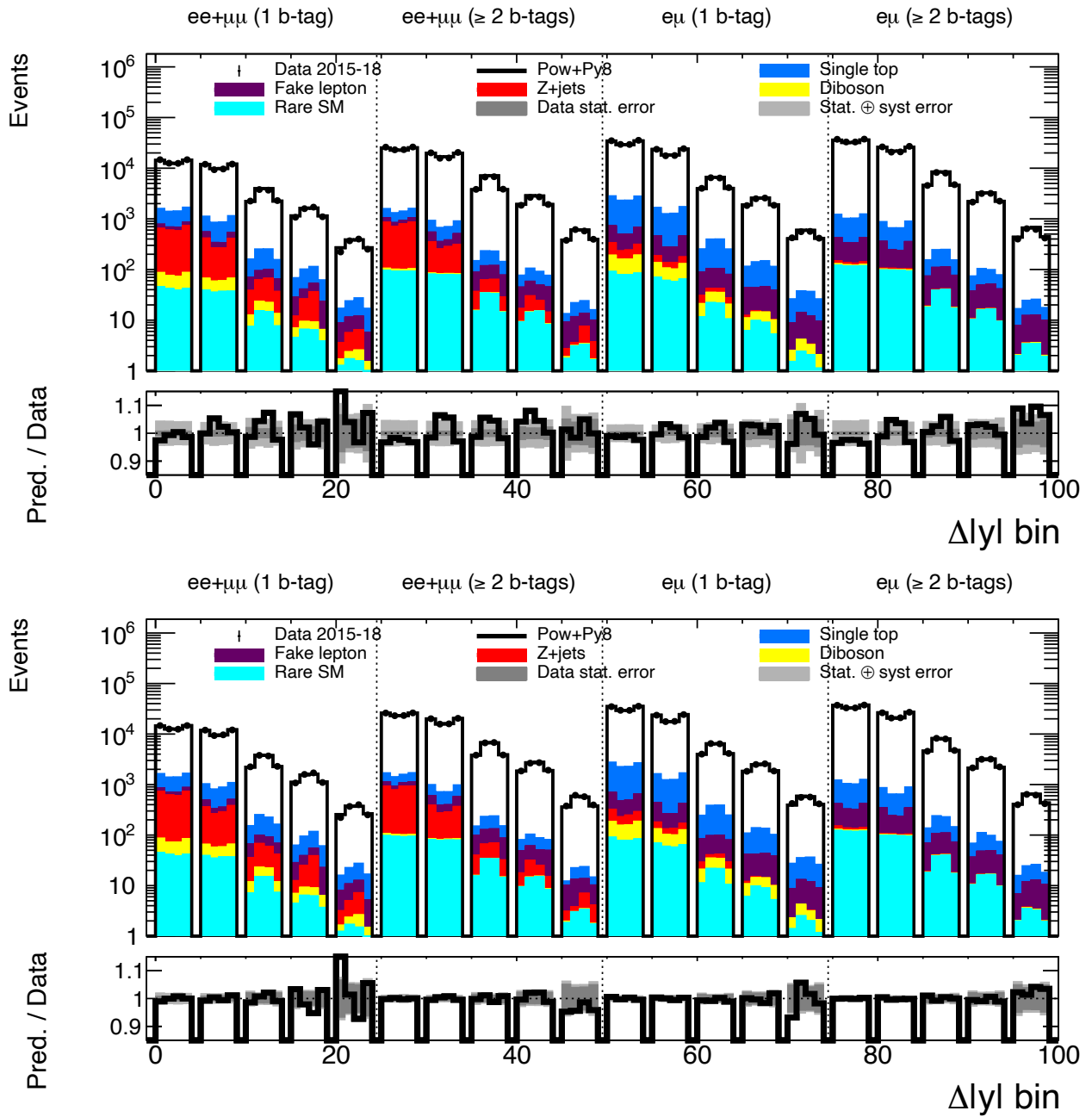
Fig. 7.30 Pre-marginal (upper plot) and post-marginal (lower plot) events in the $\Delta|y|$ bins across the five $m_{t\bar{t}}$ bins per channel.
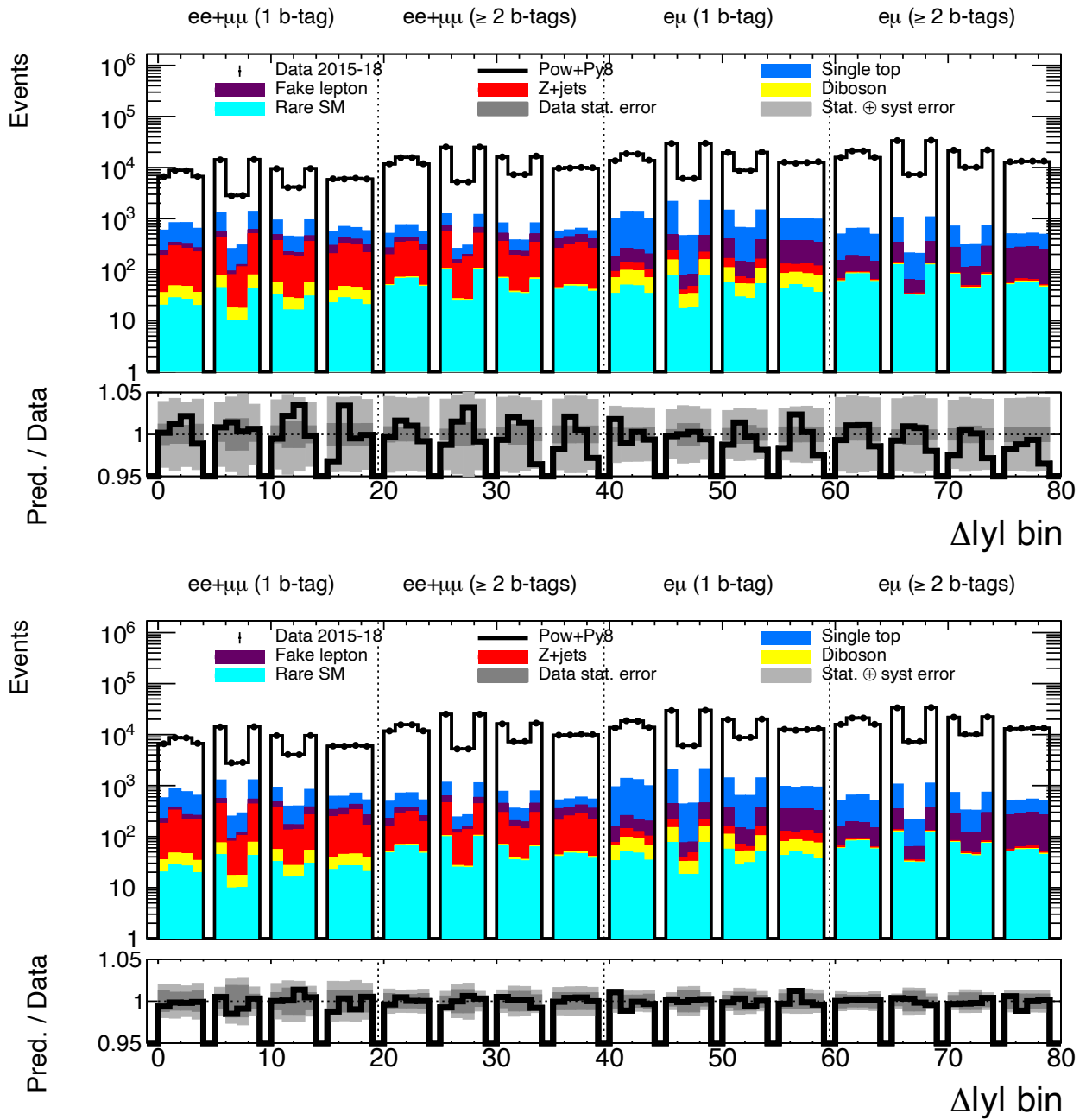
Fig. 7.31 Pre-marginal (upper plot) and post-marginal (lower plot) events in the $\Delta|y|$ bins across the four $\beta_{Z,t\bar{t}}$ bins per channel.
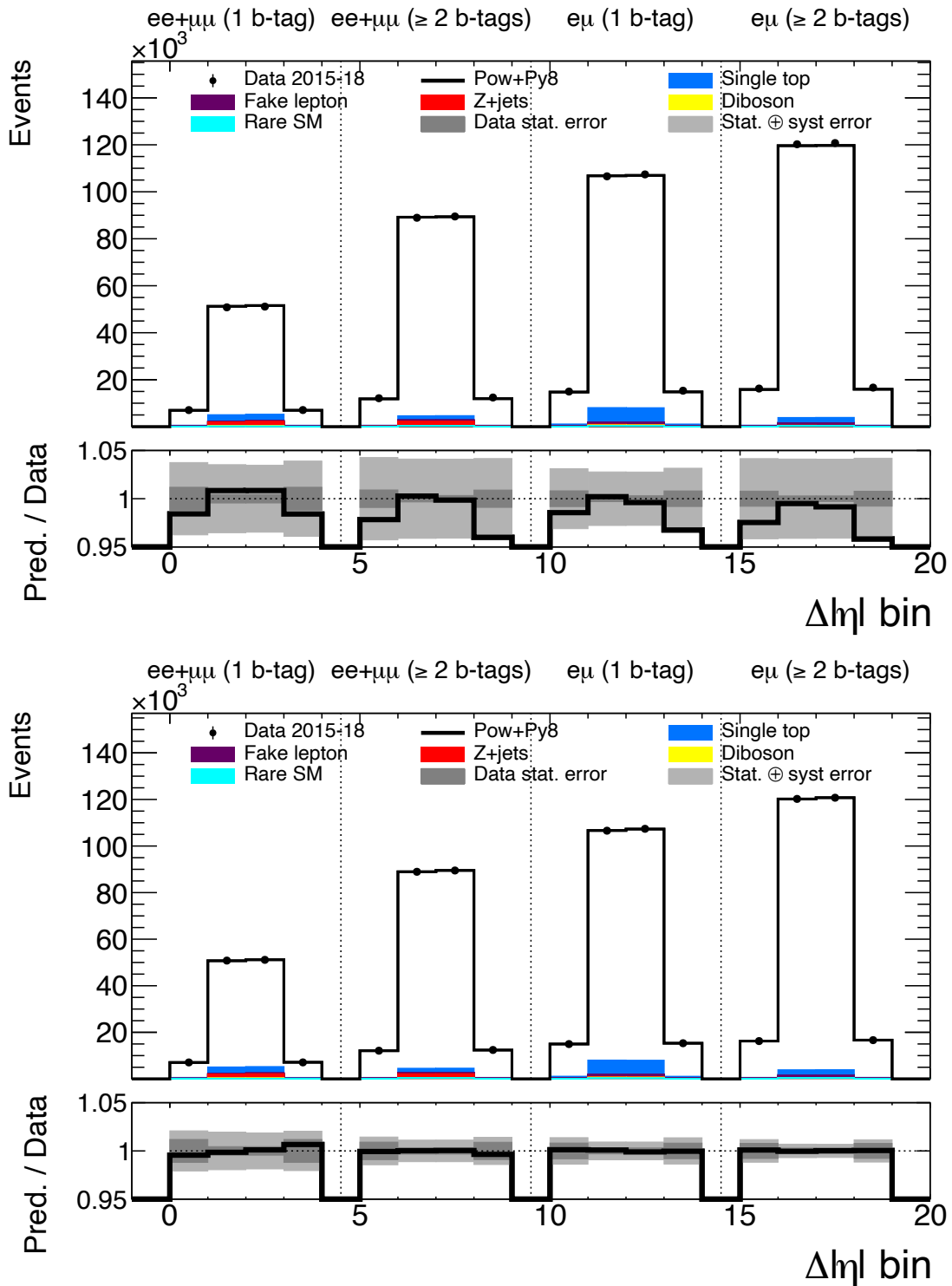
Fig. 7.32 Pre-marginal (upper plot) and post-marginal (lower plot) events in the inclusive $\Delta|\eta|$ bins.
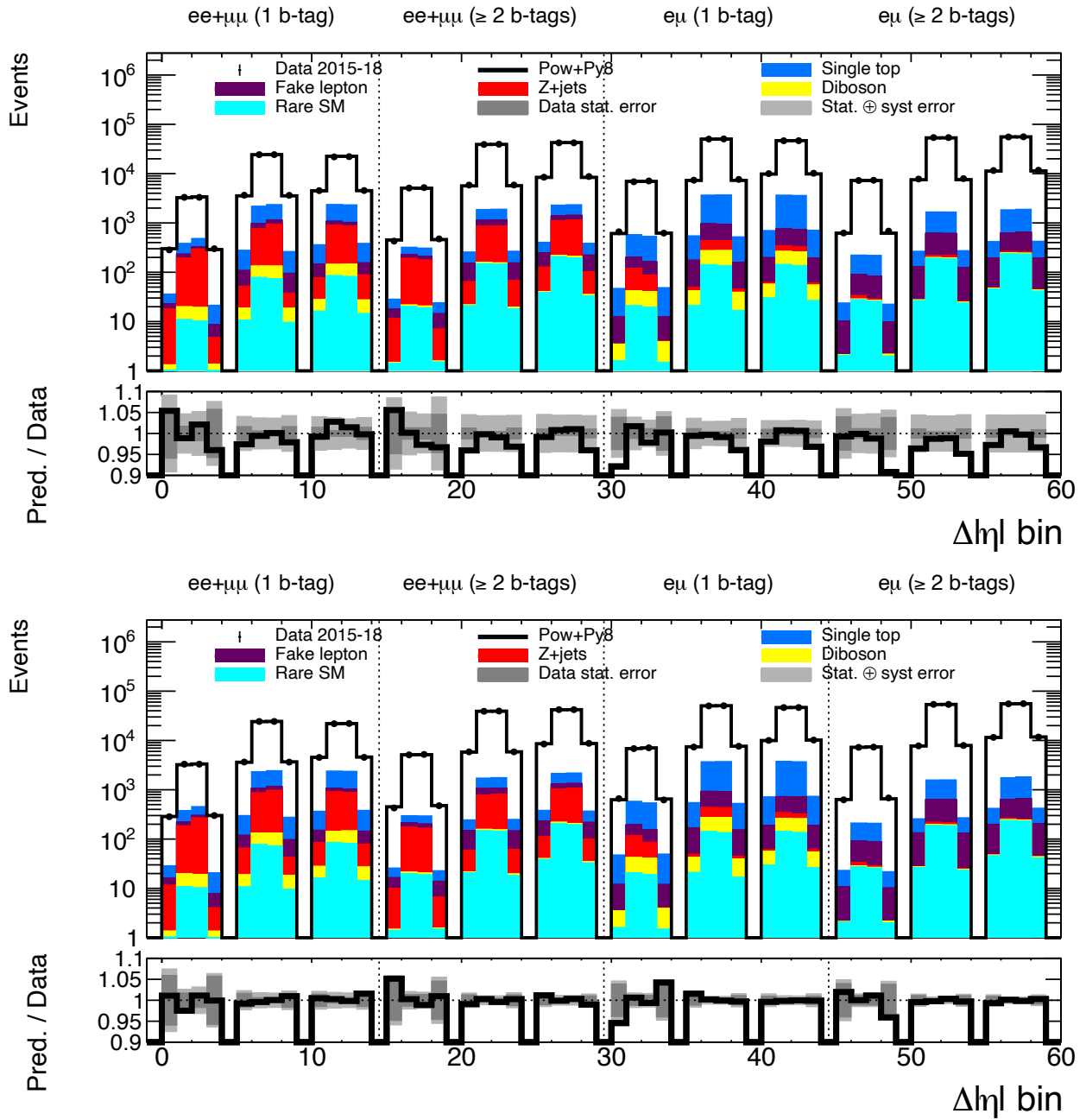
Fig. 7.33 Pre-marginal (upper plot) and post-marginal (lower plot) events in the $\Delta|\eta|$ bins across the three $p_{T,l\bar{l}}$ bins per channel.
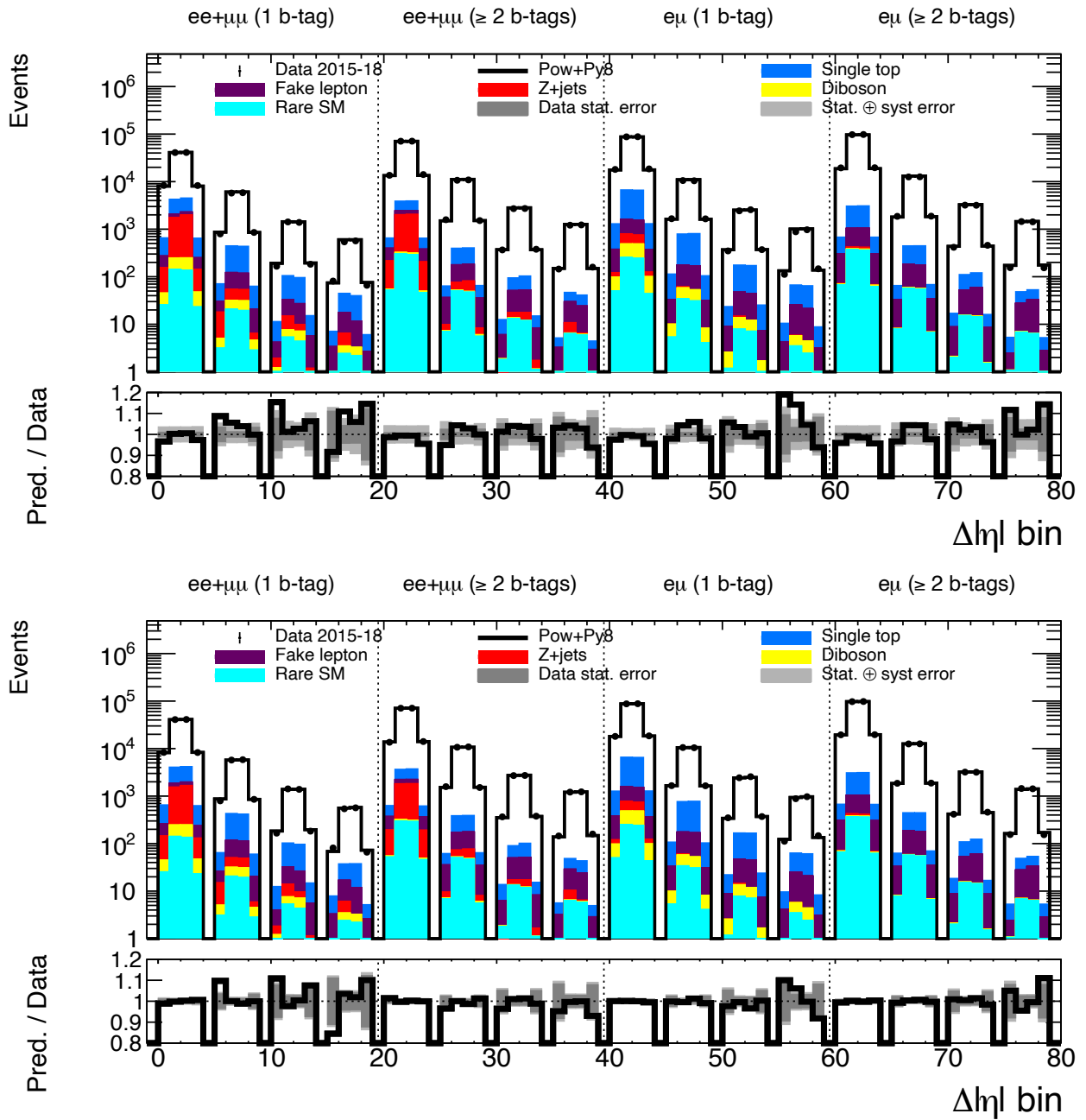
Fig. 7.34 Pre-marginal (upper plot) and post-marginal (lower plot) events in the $\Delta|\eta|$ bins across the four $m_{l\bar{l}}$ bins per channel.
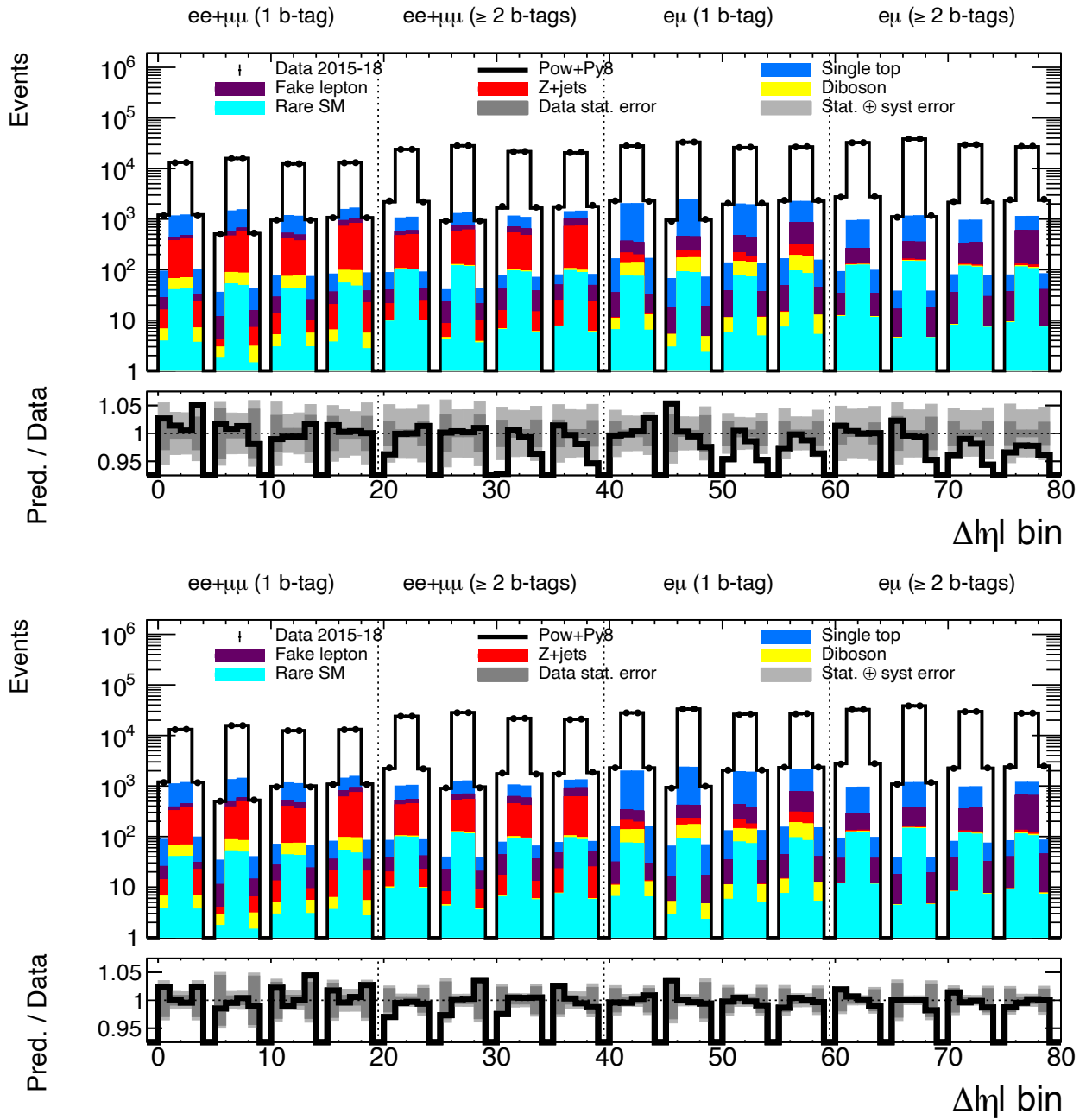
Fig. 7.35 Pre-marginal (upper plot) and post-marginal (lower plot) events in the $\Delta|\eta|$ bins across the four $\beta_{Z,l\bar{l}}$ bins per channel.

In comparing the pre-marginal and post-marginal ratio plots, the systematic uncertainties are greatly reduced, particularly in the $\Delta|y|$ bins, which suffer from greater fluctuations than in the $\Delta|\eta|$ bins, due to the complications in $t\bar{t}$ reconstruction. The reductions come about due to constraints and correlations between the NPs in the likelihood sampling. Shifts in the post-marginal folded events with respect to the pre-marginal MC expectations can be clearly seen in the inclusive plots, with upward shifts for the outer two $\Delta|y|$ and $\Delta|\eta|$ bins and downward shifts for the inner two bins. Moreover, the data in the positive bins looks to be even greater than in the negative bins, compared with the MC predictions, already suggesting that the data asymmetries are larger than the predictions at reconstructed-level. Across the differential bins such as the four $m_{l\bar{l}}$ bins in Figure 7.34, the overall normalisations in the post-marginal plots are adjusted, with the low $m_{l\bar{l}}$ bins shifted up and the high $m_{l\bar{l}}$ bins shifted down.

In general, there is excellent data-MC agreement within uncertainties following the FBU fitting procedure, even with the pulls and reductions in the systematic uncertainties. One can be confident that the pulls and constraints do not bias the charge asymmetry since they come about due to information gained in combining the channels. Should the unfolded data asymmetry not be consistent with the SM, the stress tests from Section 7.5 demonstrate the asymmetries are in good agreement with the injected BSM asymmetries.

7.7 Systematic Uncertainty Ranking

In order to determine which systematic uncertainties were the most important for charge asymmetry following the FBU procedure, a ranking procedure was performed. The pull (P) and constraint (C) in each NP's posterior distribution compared with its prior distribution was first obtained from the nominal full-systematic unfolding results. Then, for each NP, its individual effect on A_C was determined with the following algorithm:

- Set the NP's θ_k value to $P+1$ (pre-marginal up variation) or $P-1$ (pre-marginal down variation).

- Perform unfolding for each variation, freezing θ_k in the likelihood at its set value (for the NP under study) but letting the θ_k values of all the other NPs float as usual.

- Calculate the difference between the new A_C value and the nominal full-systematic A_C value for both the up and down variation ($\Delta A_C^{\text{up, pre}}$ and $\Delta A_C^{\text{down, pre}}$).

- Repeat the unfolding for the constrained variations of the NP, freezing θ_k at $P+C$ (post-marginal up variation) or $P-C$ (post-marginal down variation). Again, calculate the the difference in A_C compared with the nominal A_C value for each variation ($\Delta A_C^{\text{up, post}}$ and $\Delta A_C^{\text{down, post}}$).

The systematic uncertainty variations were then plotted and ranked according to the average post-marginal difference:

$$\frac{1}{2} \times (|\Delta A_C^{\text{up, post}}| + |\Delta A_C^{\text{down, post}}|). \tag{7.15}$$

Figures 7.36 and 7.37 show the 20 highest ranked systematic uncertainties for the $A_C^{t\bar{t}}$ and A_C^{ll} inclusive cases, respectively, where the MC simulation and data were unfolded. The blue bars are for the events being shifted up by the NPs and the red bars for the events being shifted down. The pre-marginal results are given by the empty bars and the post-marginal results by the filled bars. For the background γ_i NPs (where i refers to the bin number) and signal normalisation NPs, the pre-marginal bars are not shown since their values are intentionally large to give the fitting procedure freedom to constrain them. The purple and green points show the nominal full-systematic unfolding pulls of the NPs. Purple corresponds to a positive pull and green a negative pull. For most NPs, if there were no pull, the point would be centred at zero on the plots. However, for the background γ_i NPs and signal normalisation NPs, a centering at $+1$ would correspond to no pull. The error bars on the points show the

magnitude of the nominal full-systematic unfolding constraint. An error bar spanning -1 to $+1$ means there is no constraint.
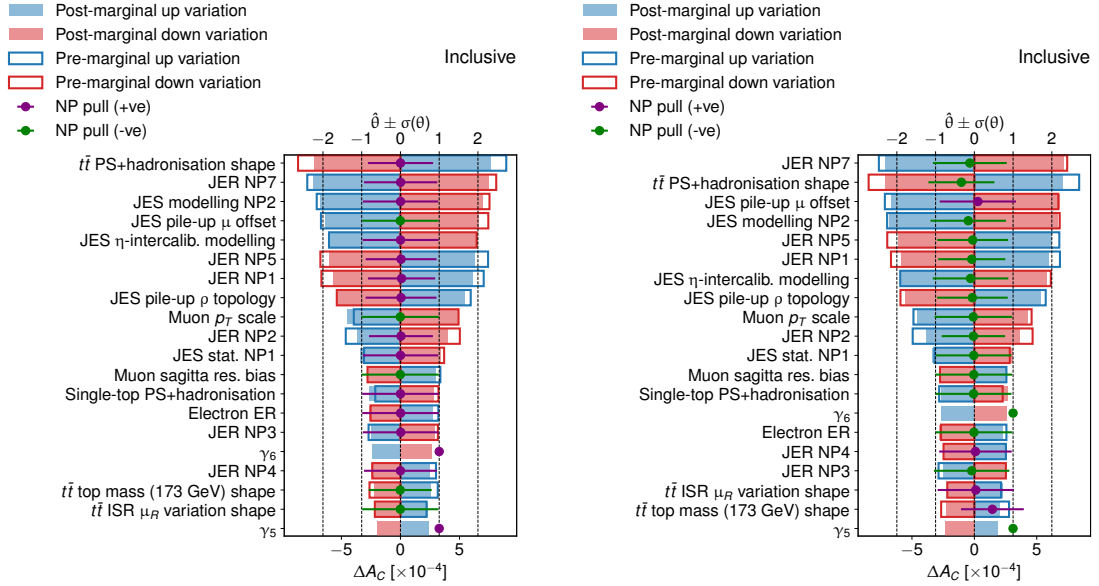
Fig. 7.36 The 20 highest ranked NPs (according to the post-marginal results) in the inclusive $t\bar{t}$ asymmetry. Left: unfolding in MC simulation. Right: unfolding in data.
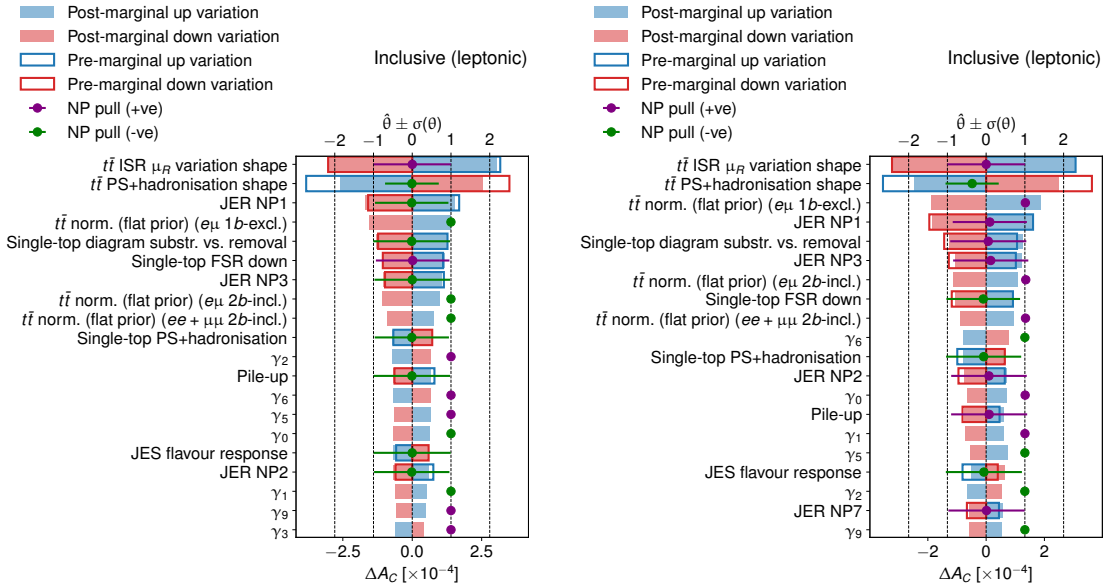
Fig. 7.37 The 20 highest ranked NPs (according to the post-marginal results) in the inclusive leptonic asymmetry. Left: unfolding in MC simulation. Right: unfolding in data.

The ordering of the systematic uncertainty ranking is similar in the MC simulation and data unfolding. There are only very small pulls in the plots on the left since there is perfect mapping of the truth-level to reconstructed-level events through the response matrix, so there should be minimal shifts in the MC. For data, there is a not a perfect mapping, so the likelihood fit can shift the numbers of folded events through systematic uncertainty pulls.

In the $t\bar{t}$ asymmetries, the highest ranked systematic uncertainties are typically the signal modelling, JES and JER NPs. The purple and green error bars show that the parton shower and hadronisation signal modelling uncertainty is constrained, which leads to an important reduction in the overall FBU uncertainty because of its high rank. The JES and JER uncertainties are high up because of large migrations between bins in the $\Delta|y|$ distributions where the $t\bar{t}$ systems are reconstructed using information from jet kinematics.

For the leptonic asymmetries, the effect from the systematic uncertainties is typically smaller than on the $t\bar{t}$ asymmetries. This is because the JER and JES uncertainties, for example, cause few migrations between $\Delta|\eta|$ bins and mostly affect the event selection. The γ_i factors now appear higher in ranking. Figure 7.38 shows the MC background statistical uncertainties for the $\Delta|\eta|$ bins of the four channels in the inclusive leptonic case. It can be seen that the Z + jets uncertainties are dominant for the $ee + \mu\mu$ channels and will be the largest contribution to the γ_i NPs. This adds further motivation for applying the large E_T^{miss} selection cuts.

The $t\bar{t}$ signal normalisation uncertainties are also significant for the leptonic asymmetries. These are similar in magnitude to those in the $t\bar{t}$ asymmetries, but the other systematic uncertainties are smaller so the normalisation uncertainties shift up in the ranking. However, as indicated by the γ_i uncertainties and from the overall uncertainties discussed later in Table 7.13, the statistical uncertainties are dominant for the leptonic asymmetries and the
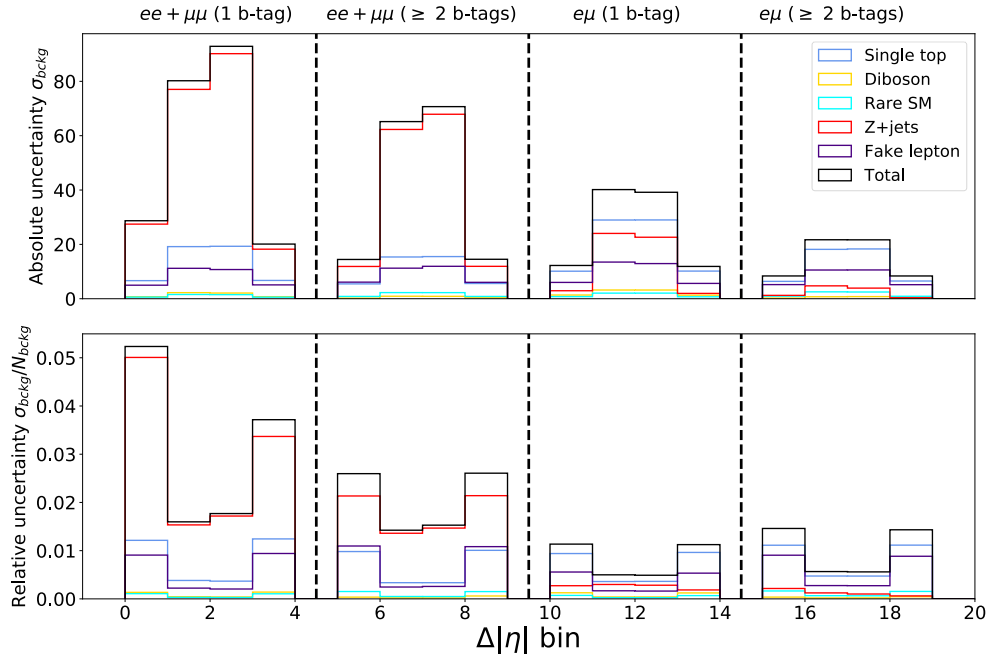
Fig. 7.38 The MC statistical uncertainties for the individual backgrounds (coloured lines) and the total background (black lines). The upper plot shows the absolute uncertainties and the lower plot the uncertainties as a fraction of the background events. Each group of four bins corresponds to the $\Delta|\eta|$ bin content in a channel.

systematic uncertainties have little effect on the overall A_C^{ll} uncertainties.

Whilst not so much the case for the inclusive cases, the top quark mass modelling systematic uncertainty was very highly ranked and constrained in the differential bins. Example systematic uncertainty ranking plots for the unfolded MC simulation in the $p_{T,t\bar{t}}$ and $m_{t\bar{t}}$ bins are shown in Figures 7.39 and 7.40.

Being a physical quantity, the constraint could be interpreted as a precise measurement on the top mass, with its prior uncertainty of $173 - 172.5 = 0.5$ GeV being greatly reduced. For an analysis not focussing on a top mass measurement, it was important to understand this constraint. Firstly, the 173 GeV mass point was used to define the uncertainty as it gave the largest change in events across $\Delta|y|$ and $\Delta|\eta|$ as opposed to 171, 172 and 174 GeV, and
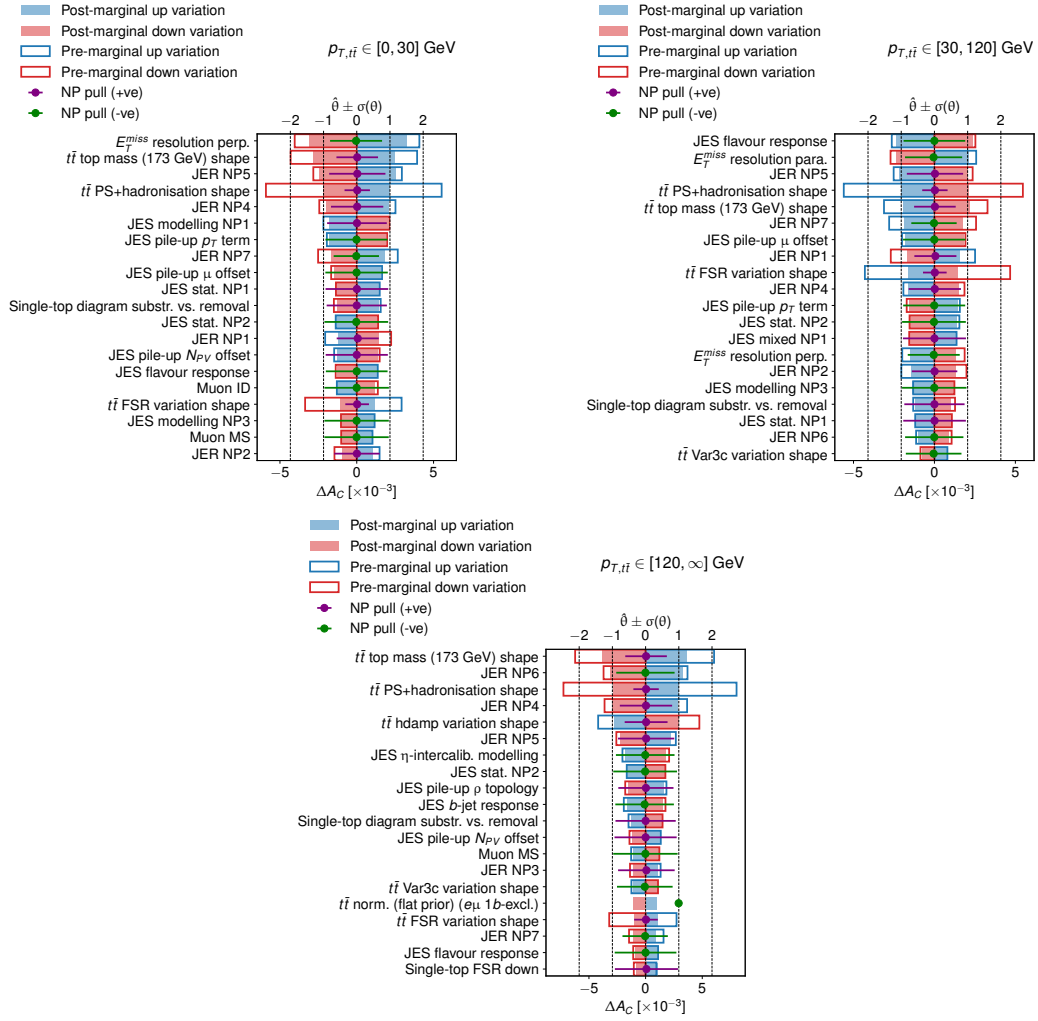
Fig. 7.39 The 20 highest ranked NPs for the three $p_{T,t\bar{t}}$ bins, just for the unfolded MC simulation.

it was also made shape-only. The variation of the systematic uncertainty across $\Delta|y|$ for the four channels in the $p_{T,t\bar{t}}$ and $m_{t\bar{t}}$ bins is shown in Figure 7.41. Almost all bins of the uncertainty are set to zero due to bootstrapping except for a few outliers. FBU was able to use this information to place a large constraint on the uncertainty but not set it to zero.

It is likely the bins not meeting the bootstrap criteria do show large statistical fluctuations in reality. To see if charge asymmetry was truly dependent on top mass, unfolding tests were undertaken on all the mass points. For each 171, 172, 173 and 174 GeV variation, 100
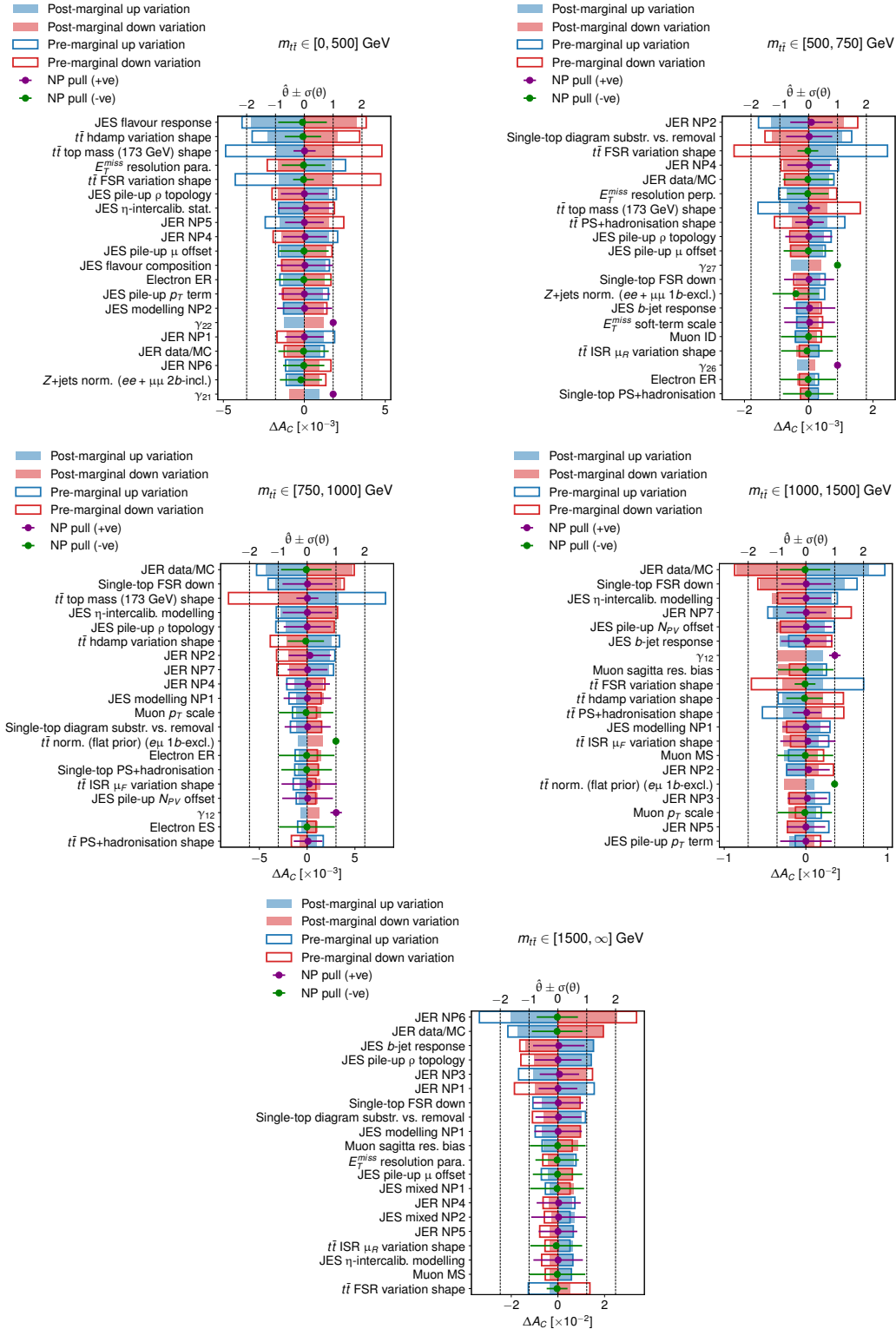
Fig. 7.40 The 20 highest ranked NPs for the five $m_{t\bar{t}}$ bins, just for the unfolded MC simulation.
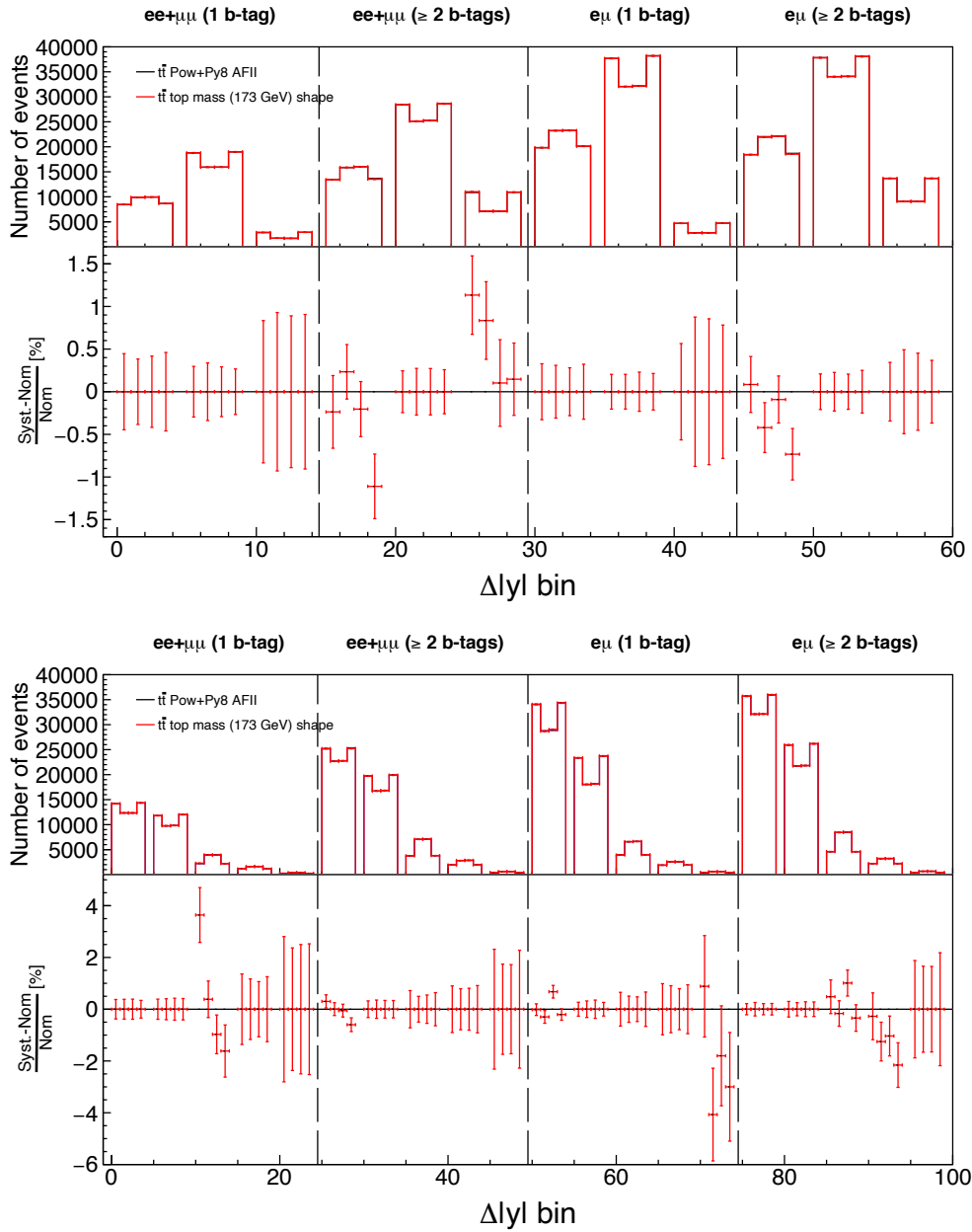
Fig. 7.41 The 173 GeV top mass shape systematic uncertainty after bootstrapping for the $t\bar{t}$ signal MC. For each channel, a group of four $\Delta|y|$ bins shows the events in each differential $p_{T,t\bar{t}}$ bin (upper plot) and $m_{t\bar{t}}$ bin (lower plot).

pseudo-experiments were created, based on their AFII simulation. Each pseudo-experiment was a smearing of the $\Delta|y|$ or $\Delta|\eta|$ bin content according to a Gaussian function based on the bin's MC statistical uncertainty. The AFII 172.5 GeV baseline was then subtracted from each

pseudo-experiment and the difference added to the full-simulation 172.5 GeV nominal $t\bar{t}$ sample. Unfolding with the full-simulation response matrix (without including the systematic uncertainties) was then undertaken to give 100 results for each mass point. The mean and standard deviation of the distribution of the unfolded results for that mass point was taken as the A_C value and uncertainty. The unfolded results were compared with the truth-level MC values for the mass. Figure 7.42 shows these results for the $p_{T,t\bar{t}}$ and $m_{t\bar{t}}$ bins, as well as the reconstructed-level asymmetries. The full-simulation 172.5 GeV points are also shown but without error bars since they are included in the uncertainties of the other mass points.

Across all differential bins, there is no dependence on the truth-level asymmetry with top mass. The unfolded asymmetries do show some variation (following the shape of the reconstructed-level asymmetries), likely due to migrations between the differential bins, but there is no obvious trend with top mass and the statistical uncertainties are large. Given these results, as well as the fact that the 173 GeV mass points typically show the largest variations across $\Delta|y|$ compared with the other mass points, and that even in the 173 GeV case, most of the bins were set to zero through bootstrapping, it was decided (in the approval process) to drop the top mass uncertainty altogether. However, this is subject to change, especially when new mass samples of higher statistics are available.
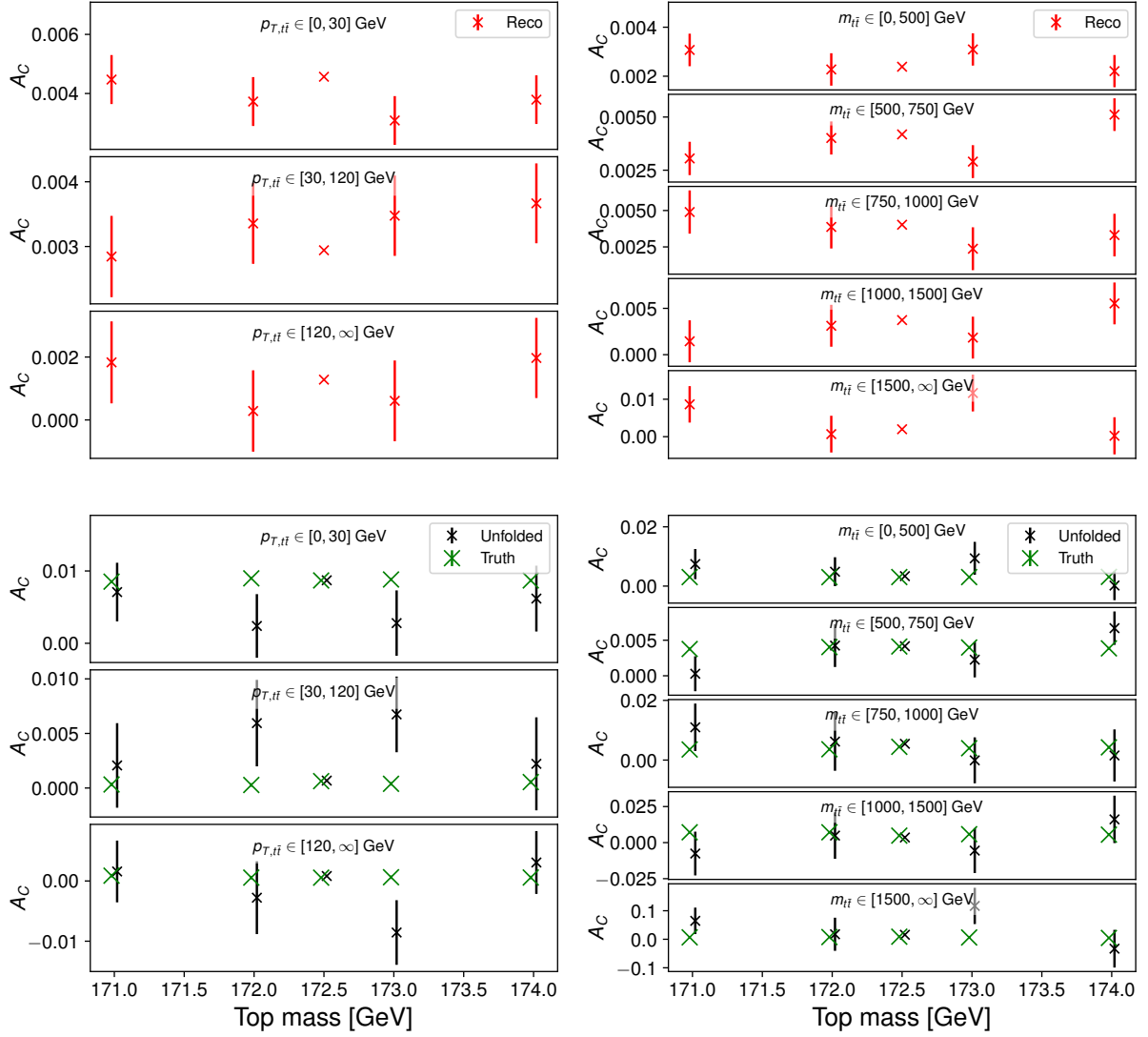
Fig. 7.42 Reconstructed-level $A_C^{t\bar{t}}$ values (red points in upper plots), and unfolded and truth-level $A_C^{t\bar{t}}$ values (black and green points in lower plots) against top quark mass for the $p_{T,t\bar{t}}$ (left) and $m_{t\bar{t}}$ (right) bins.

7.8 Expected Charge Asymmetries

Tables 7.12 and 7.13 show the breakdown of the expected unfolded $A_C^{t\bar{t}}$ and A_C^{ll} values with their uncertainties, respectively. In all cases, the statistical uncertainties are the largest sources of uncertainty. This is in great part due to the correlations and constraints placed on

the systematic uncertainties from the FBU likelihood method, which from the pre-marginal plots in Section 7.6.6 would otherwise be more similar in size to the statistical uncertainties. The systematic uncertainties are smallest for the A_C^{ll} values since they have only a small impact on the event selection and mostly affect the reconstructed $t\bar{t}$ (rather than dilepton) quantities. The biases and statistical uncertainties in the response matrices only make small contributions to the overall uncertainties when summed in quadrature with the unfolding uncertainties, although the bias uncertainties will scale with the A_C values in data, where the linearity test slopes (see Section 7.5) are not equal to one.

The unfolded asymmetries are fully consistent with the truth-level asymmetries (also given in Tables 7.12 and 7.13) showing the FBU technique gives good closure. The expected asymmetries are small (typically less than 1%). The leptonic asymmetries are typically smaller than the $t\bar{t}$ asymmetries (a factor of 1.8 smaller in the inclusive case) but the uncertainties are also smaller (a factor of 2.9 in the inclusive case). Clear trends are seen across the differential bins, with increasing asymmetry for $m_{t\bar{t}}$, $\beta_{Z,t\bar{t}}$, $p_{T,l\bar{l}}$, $m_{l\bar{l}}$ and $\beta_{Z,l\bar{l}}$, but decreasing asymmetry for $p_{T,t\bar{t}}$. However, in all the $t\bar{t}$ asymmetries, the uncertainties pass through zero asymmetry, suggesting there may be limited sensitivity to charge asymmetry if the A_C values in data match those of the SM. This is particularly the case for the last $m_{t\bar{t}}$ bin, which has a very large statistical uncertainty due to very few expected events at high invariant mass. Nonetheless, in the combination with results from the lepton + jets channel, the uncertainties are reduced significantly (see Section 8.3). Furthermore, if the data lie greatly above or below the expectations, their uncertainty bands may not pass through zero, demonstrating a discrepancy with the SM.

	Expected truth		Expected unfolded					
	$A_C^{t\bar{t}}$	Stat. unc.	$A_C^{t\bar{t}}$	Stat. unc.	Syst. unc.	Bias unc.	Response matrix unc.	Total unc.
Inclusive	0.00351	0.00006	0.0036	0.0033	0.0023	<0.0001	0.0007	0.0041
$p_{T,t\bar{t}} \in [0, 30]$ GeV	0.00854	0.00009	0.009	0.011	0.008	0.002	0.002	0.014
$p_{T,t\bar{t}} \in [30, 120]$ GeV	0.00062	0.00008	<0.001	0.009	0.007	0.001	0.002	0.012
$p_{T,t\bar{t}} \in [120, \infty]$ GeV	0.00076	0.00014	0.001	0.012	0.007	0.001	0.003	0.015
$m_{t\bar{t}} \in [0, 500]$ GeV	0.00296	0.00007	0.003	0.012	0.008	0.001	0.002	0.014
$m_{t\bar{t}} \in [500, 750]$ GeV	0.00413	0.00010	0.0039	0.0060	0.0027	0.0002	0.0012	0.0066
$m_{t\bar{t}} \in [750, 1000]$ GeV	0.00473	0.00022	0.005	0.019	0.009	0.001	0.004	0.021
$m_{t\bar{t}} \in [1000, 1500]$ GeV	0.00502	0.00040	0.005	0.035	0.014	<0.001	0.007	0.038
$m_{t\bar{t}} \in [1500, \infty]$ GeV	0.0083	0.0011	0.01	0.13	0.04	<0.01	0.03	0.14
$\beta_{Z,t\bar{t}} \in [0.0, 0.3]$	-0.00023	0.00012	<0.001	0.018	0.009	<0.001	0.004	0.021
$\beta_{Z,t\bar{t}} \in [0.3, 0.6]$	0.00127	0.00011	0.002	0.012	0.007	<0.001	0.002	0.014
$\beta_{Z,t\bar{t}} \in [0.6, 0.8]$	0.00283	0.00012	0.003	0.009	0.005	<0.001	0.002	0.011
$\beta_{Z,t\bar{t}} \in [0.8, 1.0]$	0.00851	0.00010	0.0081	0.0069	0.0045	0.0013	0.0015	0.0085

Table 7.12 Summary of the expected truth-level and expected unfolded $A_C^{t\bar{t}}$ values and uncertainties (using NLO Powheg + Pythia8 MC) for the inclusive and differential measurements. The unfolded total uncertainties (accounting for rounding errors) include the statistical and systematic uncertainties from the FBU sampling, as well as the biases from the Protos linearity tests (calculated assuming the SM $A_C^{t\bar{t}}$ values) and statistical fluctuations in the response matrices added in quadrature.

	Expected truth		Expected unfolded					
	A_C^{ll}	Stat. unc.	A_C^{ll}	Stat. unc.	Syst. unc.	Bias unc.	Response matrix unc.	Total unc.
Inclusive	0.00192	0.00006	0.0019	0.0012	0.0006	<0.0001	0.0002	0.0014
$p_{T,ll} \in [0, 20]$ GeV	0.00163	0.00022	0.0015	0.0064	0.0026	0.0003	0.0012	0.0070
$p_{T,ll} \in [20, 70]$ GeV	0.00171	0.00008	0.0017	0.0020	0.0008	0.0001	0.0004	0.0022
$p_{T,ll} \in [70, \infty]$ GeV	0.00223	0.00009	0.0022	0.0018	0.0006	0.0001	0.0004	0.0019
$m_{ll} \in [0, 200]$ GeV	0.00168	0.00006	0.0016	0.0014	0.0005	<0.0001	0.0003	0.0015
$m_{ll} \in [200, 300]$ GeV	0.00361	0.00022	0.0036	0.0040	0.0011	0.0001	0.0008	0.0042
$m_{ll} \in [300, 400]$ GeV	0.00489	0.00043	0.0049	0.0083	0.0019	0.0003	0.0017	0.0087
$m_{ll} \in [400, \infty]$ GeV	0.00592	0.00061	0.006	0.012	0.003	0.001	0.002	0.013
$\beta_{Z,ll} \in [0.0, 0.3]$	0.00006	0.00013	0.0001	0.0028	0.0012	0.0001	0.0005	0.0031
$\beta_{Z,ll} \in [0.3, 0.6]$	0.00066	0.00012	0.0008	0.0024	0.0007	0.0001	0.0005	0.0026
$\beta_{Z,ll} \in [0.6, 0.8]$	0.00182	0.00013	0.0018	0.0026	0.0009	0.0003	0.0005	0.0028
$\beta_{Z,ll} \in [0.8, 1.0]$	0.00402	0.00010	0.0040	0.0028	0.0011	0.0003	0.0006	0.0031

Table 7.13 Summary of the expected truth-level and expected unfolded A_C^{ll} values and uncertainties (using NLO Powheg + Pythia8 MC) for the inclusive and differential measurements. The format is the same as in Table 7.12.

7.9   ATLAS Data Charge Asymmetries

Following optimisation of the analysis using the simulated MC, the ATLAS data were unfolded. The unfolded (and expected NLO Powheg + Pythia8 truth-level) $A_C^{t\bar{t}}$ and A_C^{ll} values together with a breakdown of their uncertainties are shown in Tables 7.14 and 7.15, respectively. These are preliminary results and small changes could arise as the approval process continues.

The bias uncertainties were determined using the data A_C central values, and the slopes and offsets from Protos reweighting (see Equation 7.13). These are similar in magnitude to the expected MC bias uncertainties shown in Tables 7.12 and 7.13. They make negligible contributions to the overall uncertainties, which are again dominated by statistical uncertainties. Bias uncertainties were also calculated for the linear reweighting model but are similar to the Protos uncertainties. Therefore, the Protos biases were used since they are based on a physical BSM theory.

Figures 7.43 and 7.44 show the unfolded data asymmetries with their statistical and total error bars plotted along with the NLO Powheg + Pythia8 truth-level asymmetries (red bands). Higher order truth-level asymmetries were also produced with fixed-order calculations at NNLO in the perturbative expansion of α_s in QCD, and NLO electroweak (EW) corrections [187, 188] for the $t\bar{t}$ asymmetries. They were also produced at NLO in QCD with NLO EW corrections [189] for the leptonic asymmetries (including the $|\Delta|\eta|| < 2.5$ requirements). The higher order values are shown in Tables 7.16 and 7.17, and plotted in Figures 7.43 and 7.44 (green bands).

	Expected truth		Data unfolded					
	$A_C^{t\bar{t}}$	Stat. unc.	$A_C^{t\bar{t}}$	Stat. unc.	Syst. unc.	Bias unc.	Response matrix unc.	Total unc.
Inclusive	0.00351	0.00006	0.0081	0.0033	0.0022	<0.0001	0.0007	0.0041
$p_{T,t\bar{t}} \in [0, 30]$ GeV	0.00854	0.00009	0.001	0.011	0.007	0.002	0.002	0.013
$p_{T,t\bar{t}} \in [30, 120]$ GeV	0.00062	0.00008	0.017	0.010	0.008	0.001	0.002	0.013
$p_{T,t\bar{t}} \in [120, \infty]$ GeV	0.00076	0.00014	-0.006	0.012	0.007	0.001	0.003	0.014
$m_{t\bar{t}} \in [0, 500]$ GeV	0.00296	0.00007	-0.005	0.011	0.008	0.001	0.002	0.014
$m_{t\bar{t}} \in [500, 750]$ GeV	0.00413	0.00010	0.0204	0.0061	0.0027	0.0001	0.0012	0.0068
$m_{t\bar{t}} \in [750, 1000]$ GeV	0.00473	0.00022	-0.019	0.019	0.008	0.001	0.004	0.021
$m_{t\bar{t}} \in [1000, 1500]$ GeV	0.00502	0.00040	0.084	0.037	0.014	0.001	0.007	0.040
$m_{t\bar{t}} \in [1500, \infty]$ GeV	0.0083	0.0011	-0.16	0.14	0.04	0.01	0.03	0.15
$\beta_{Z,t\bar{t}} \in [0.0, 0.3]$	-0.00023	0.00012	-0.011	0.018	0.010	<0.001	0.004	0.020
$\beta_{Z,t\bar{t}} \in [0.3, 0.6]$	0.00127	0.00011	0.002	0.012	0.007	<0.001	0.002	0.014
$\beta_{Z,t\bar{t}} \in [0.6, 0.8]$	0.00283	0.00012	0.011	0.009	0.006	<0.001	0.002	0.011
$\beta_{Z,t\bar{t}} \in [0.8, 1.0]$	0.00851	0.00010	0.0183	0.0068	0.0044	0.0013	0.0015	0.0083

Table 7.14 Summary of the expected NLO Powheg + Pythia8 MC truth-level and data unfolded $A_C^{t\bar{t}}$ values and uncertainties for the inclusive and differential measurements. The unfolded total uncertainties (accounting for rounding errors) include the statistical and systematic uncertainties from the FBU sampling, as well as the biases from the Protos linearity tests (calculated assuming the data $A_C^{t\bar{t}}$ values) and statistical fluctuations in the response matrices added in quadrature.

	Expected truth		Data unfolded					
	A_C^{ll}	Stat. unc.	A_C^{ll}	Stat. unc.	Syst. unc.	Bias unc.	Response matrix unc.	Total unc.
Inclusive	0.00192	0.00006	0.0058	0.0012	0.0006	<0.0001	0.0002	0.0014
$p_{T,l\bar{l}} \in [0, 20]$ GeV	0.00163	0.00022	0.0172	0.0063	0.0026	0.0005	0.0012	0.0069
$p_{T,l\bar{l}} \in [20, 70]$ GeV	0.00171	0.00008	0.0039	0.0020	0.0007	0.0001	0.0004	0.0022
$p_{T,l\bar{l}} \in [70, \infty]$ GeV	0.00223	0.00009	0.0054	0.0018	0.0006	0.0001	0.0004	0.0019
$m_{l\bar{l}} \in [0, 200]$ GeV	0.00168	0.00006	0.0058	0.0014	0.0005	<0.0001	0.0003	0.0015
$m_{l\bar{l}} \in [200, 300]$ GeV	0.00361	0.00022	0.0022	0.0041	0.0014	0.0001	0.0008	0.0044
$m_{l\bar{l}} \in [300, 400]$ GeV	0.00489	0.00043	0.0145	0.0083	0.0024	0.0005	0.0017	0.0089
$m_{l\bar{l}} \in [400, \infty]$ GeV	0.00592	0.00061	0.020	0.012	0.003	0.001	0.002	0.013
$\beta_{Z,l\bar{l}} \in [0.0, 0.3]$	0.00006	0.00013	-0.0012	0.0028	0.0011	0.0001	0.0005	0.0030
$\beta_{Z,l\bar{l}} \in [0.3, 0.6]$	0.00066	0.00012	0.0047	0.0024	0.0007	0.0001	0.0005	0.0026
$\beta_{Z,l\bar{l}} \in [0.6, 0.8]$	0.00182	0.00013	0.0060	0.0026	0.0009	0.0002	0.0005	0.0028
$\beta_{Z,l\bar{l}} \in [0.8, 1.0]$	0.00402	0.00010	0.0092	0.0028	0.0011	0.0003	0.0006	0.0030

Table 7.15 Summary of the expected NLO Powheg + Pythia8 MC truth-level and data unfolded A_C^{ll} values and uncertainties for the inclusive and differential measurements. The format is the same as in Table 7.14.

	NNLO QCD + NLO EW $A_C^{t\bar{t}}$
Inclusive	$0.0064^{+0.0005}_{-0.0006}$
$p_{T,t\bar{t}} \in [0, 30]$ GeV	$0.0150^{+0.0006}_{-0.0046}$
$p_{T,t\bar{t}} \in [30, 120]$ GeV	$0.0008^{+0.0028}_{-0.0011}$
$p_{T,t\bar{t}} \in [120, \infty]$ GeV	$0.0044^{+0.0030}_{-0.0013}$
$m_{t\bar{t}} \in [0, 500]$ GeV	$0.0055^{+0.0006}_{-0.0006}$
$m_{t\bar{t}} \in [500, 750]$ GeV	$0.0072^{+0.0006}_{-0.0006}$
$m_{t\bar{t}} \in [750, 1000]$ GeV	$0.0079^{+0.0004}_{-0.0006}$
$m_{t\bar{t}} \in [1000, 1500]$ GeV	$0.0096^{+0.0009}_{-0.0009}$
$m_{t\bar{t}} \in [1500, \infty]$ GeV	$0.0094^{+0.0015}_{-0.0011}$
$\beta_{Z,t\bar{t}} \in [0.0, 0.3]$	$0.0011^{+0.0005}_{-0.0004}$
$\beta_{Z,t\bar{t}} \in [0.3, 0.6]$	$0.0023^{+0.0006}_{-0.0004}$
$\beta_{Z,t\bar{t}} \in [0.6, 0.8]$	$0.0042^{+0.0003}_{-0.0003}$
$\beta_{Z,t\bar{t}} \in [0.8, 1.0]$	$0.0146^{+0.0012}_{-0.0014}$

Table 7.16 Summary of the $A_C^{t\bar{t}}$ values and uncertainties calculated at NNLO in QCD and NLO in EW theory [188]. The uncertainties include variations in the μ_R and μ_F scales by factors of two and numerical integration errors.

	NLO QCD + NLO EW A_C^{ll}
Inclusive	$0.0040^{+0.0002}_{-0.0001}$
$p_{T,l\bar{l}} \in [0, 20]$ GeV	$0.0026^{+0.0002}_{-0.0002}$
$p_{T,l\bar{l}} \in [20, 70]$ GeV	$0.0034^{+0.0001}_{-0.0000}$
$p_{T,l\bar{l}} \in [70, \infty]$ GeV	$0.0050^{+0.0002}_{-0.0003}$
$m_{l\bar{l}} \in [0, 200]$ GeV	$0.0033^{+0.0001}_{-0.0001}$
$m_{l\bar{l}} \in [200, 300]$ GeV	$0.0084^{+0.0002}_{-0.0001}$
$m_{l\bar{l}} \in [300, 400]$ GeV	$0.0108^{+0.0003}_{-0.0006}$
$m_{l\bar{l}} \in [400, \infty]$ GeV	$0.0120^{+0.0009}_{-0.0002}$
$\beta_{Z,l\bar{l}} \in [0.0, 0.3]$	$0.0022^{+0.0001}_{-0.0001}$
$\beta_{Z,l\bar{l}} \in [0.3, 0.6]$	$0.0016^{+0.0001}_{-0.0000}$
$\beta_{Z,l\bar{l}} \in [0.6, 0.8]$	$0.0034^{+0.0000}_{-0.0001}$
$\beta_{Z,l\bar{l}} \in [0.8, 1.0]$	$0.0069^{+0.0003}_{-0.0003}$

Table 7.17 Summary of the A_C^{ll} values and uncertainties calculated at NLO in QCD and NLO in EW theory [189]. The uncertainties include variations in the μ_R and μ_F scales by factors of two and numerical integration errors.
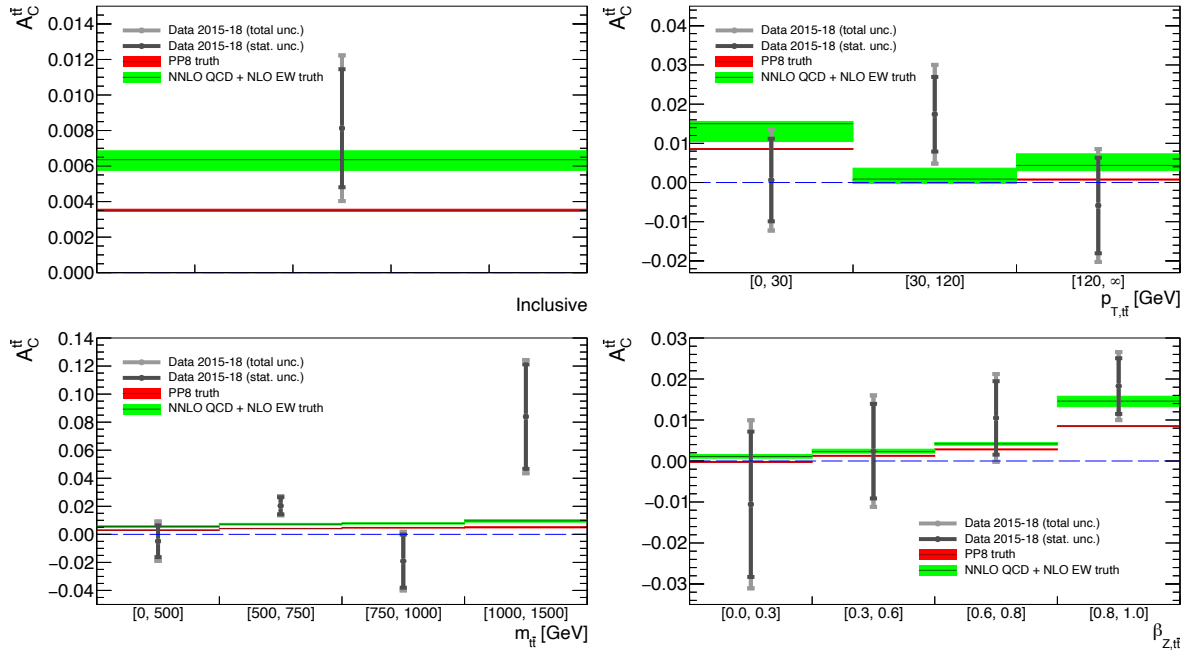
Fig. 7.43 The data $A_C^{t\bar{t}}$ values and uncertainties. Clockwise from the upper left are the asymmetries in the inclusive, $p_{T,t\bar{t}}$, $\beta_{Z,t\bar{t}}$ and $m_{t\bar{t}}$ bins. The highest $m_{t\bar{t}}$ bin is not shown due to its large uncertainty. The unfolded asymmetries are shown with the grey points, where the dark grey error bars are the statistical uncertainties and the light grey bars the total uncertainties including the systematic uncertainties, bias and response matrix statistical fluctuations. The red bands show the MC truth-level asymmetries from NLO Powheg + Pythia8 (PP8). The green bands show higher order calculations (NNLO in QCD and NLO in EW theory).

For the inclusive asymmetries, excesses are seen above zero to 2.0σ and 4.1σ for $A_C^{t\bar{t}}$ and A_C^{ll}, respectively, giving strong evidence for charge asymmetry in the latter case. The excesses above the NLO Powheg + Pythia8 truth-level asymmetries are 1.1σ and 2.8σ, respectively. However, with the higher order calculations, there is better agreement with the data to 0.4σ and 1.3σ. In the differential bins, the unfolded data are typically consistent with the truth-level expectations. The asymmetry in the first $p_{T,l\bar{l}}$ bin does differ from the higher order expectation by 2.1σ, however. For the $\beta_{Z,t\bar{t}}$ and $\beta_{Z,l\bar{l}}$ bins, an increasing trend can be seen going from left to right and the slope in the central values is greater in the data than the truth-level expectations (for both NLO Powheg + Pythia8 and the higher order calculations). The $m_{t\bar{t}}$ bins show no clear trend but there is a possible increase in charge asymmetry with $m_{l\bar{l}}$. No trend in asymmetry is seen across the $p_{T,t\bar{t}}$ bins but the $p_{T,l\bar{l}}$ bins
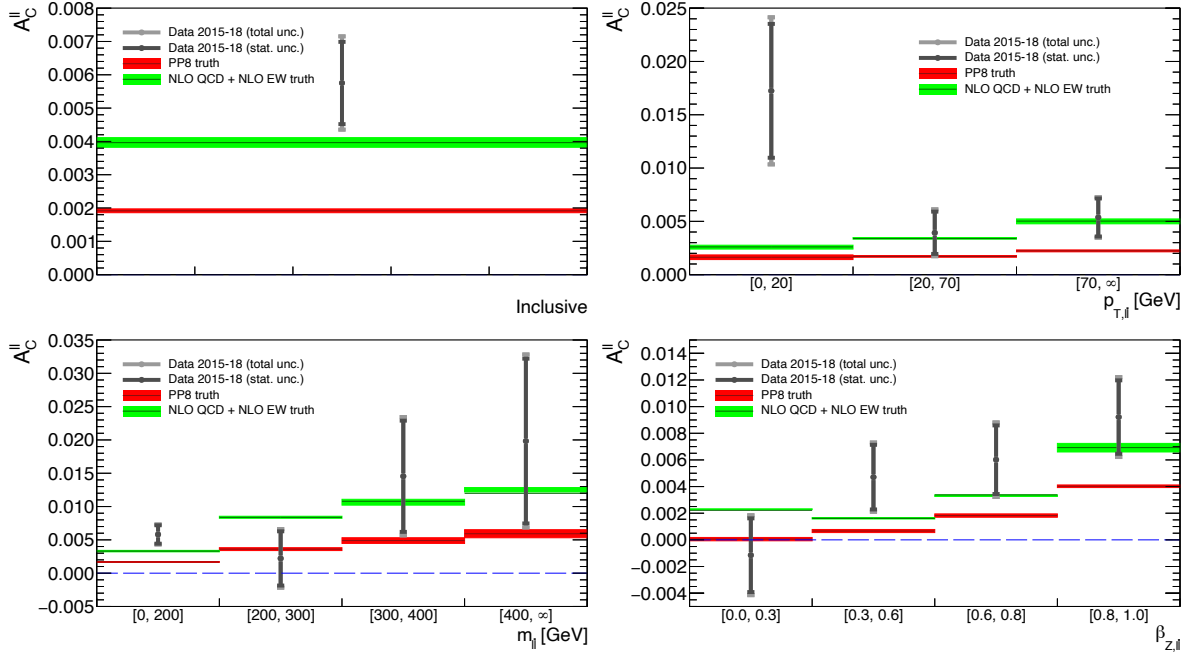
Fig. 7.44 The data A_C^{ll} values and uncertainties. Clockwise from the upper left are the asymmetries in the inclusive, $p_{T,l\bar{l}}$, $\beta_{Z,l\bar{l}}$ and $m_{l\bar{l}}$ bins. The format is the same as in Figure 7.43 but with the green bands showing the higher order calculations at NLO in QCD and NLO in EW theory.

all exhibit positive asymmetries. The unfolded data are in better agreement with the higher order theory calculations in general.

7.10 Cross-Checks of Inclusive A_C^{ll} Result

The disagreement between the unfolded data and red MC band in the inclusive A_C^{ll} measurement is perhaps not too surprising given the disagreement at reconstructed-level shown in the pre-marginal plot of Figure 7.32. In merging the four channels, the reconstructed-level leptonic asymmetry in data is $A_C^{ll} = 0.0039 \pm 0.0012$ and the NLO Powheg + Pythia8 expectation is $A_C^{ll} = 0.00102 \pm 0.00022$, where the uncertainties are statistical. For comparison, the reconstructed-level $t\bar{t}$ inclusive asymmetry in data is $A_C^{t\bar{t}} = 0.0052 \pm 0.0012$ and the NLO Powheg + Pythia8 expectation is $A_C^{t\bar{t}} = 0.00201 \pm 0.00022$, so there is a discrepancy here, too. Since the inclusive leptonic asymmetry shows the largest discrepancy, a test was

performed to check the robustness of the unfolded result. Different $\Delta|\eta|$ bins were trialled to see how they affected the asymmetry, similar to the linearity tests in Section 7.5, but using the actual data rather than simulated BSM predictions. The data were smeared 300 times according to Poisson statistics in separate pseudo-experiments. Each pseudo-experiment was unfolded (without systematic uncertainties) for the given binning configuration. The means and standard deviations of the A_C^{ll} values for each configuration are shown in Table 7.18.

In increasing the number of bins, there is only a small decrease in A_C^{ll} but all values are fully consistent within their statistical errors. The decrease is likely due to statistical fluctuations and biases since the binning is not optimised except in the 4 bin case. As an example, a Protos-reweighted linearity test was performed for the 22 bin case and the A_C^{ll} value corrected. The asymmetry increased from 0.0051 ± 0.0012 to 0.0053 ± 0.0012. One can therefore be confident the unfolded data value is accurate. The improved agreement with the higher order theory calculation adds further weight to this.

$\Delta|\eta|$ binning	A_C^{ll}
4 bins of analysis: $\pm$ [0, 1.4 (0.9), 2.5]	0.0055 ± 0.0012
8 bins: $\pm$ [0, 0.2, 0.6, 1, 2.5]	0.0054 ± 0.0012
18 bins: $\pm$ [0, 0.1, 0.2, 0.4, 0.6, 0.8, 1, 1.2, 1.5, 2.5]	0.0054 ± 0.0013
22 bins: $\pm$ [0, 0.1, 0.2, 0.4, 0.6, 0.8, 1, 1.2, 1.5, 1.8, 2.0, 2.5]	0.0051 ± 0.0012
28 bins: $\pm$ [0, 0.1, 0.2, 0.3, 0.4, 0.5, 0.6, 0.8, 1, 1.1, 1.2, 1.5, 1.8, 2, 2.5]	0.0053 ± 0.0014

Table 7.18 Unfolded inclusive A_C^{ll} values in data for different binning configurations. The data were smeared according to Poisson statistics in 300 separate pseudo-experiments and unfolding without systematic uncertainties was performed. The means and standard deviations of the pseudo-experiments were taken as the A_C^{ll} values and uncertainties, respectively. The binning in the square brackets is symmetrical between positive and negative $\Delta|\eta|$. It is identical at reconstructed- and truth-level, except for the 4 bin case used in the analysis, where the reconstructed-level inner bin edge is shown outside brackets and the truth-level edge inside brackets.

Conclusions and Combination of the Dilepton and Lepton + Jets Channel

8.1 Conclusions of Dilepton Channel Charge Asymmetry

The charge asymmetry in top quark pair production was measured in the dilepton channel using 139 fb^{-1} of data from $\sqrt{s} = 13$ TeV pp collisions in the ATLAS detector. The $t\bar{t}$ events were reconstructed with the Neutrino Weighting algorithm, which uses kinematic quantities from recorded jets, charged leptons and missing transverse energy from undetectable neutrinos in the detector. The leptons were split into ee, $e\mu$ and $\mu\mu$ pairs, which also included τ leptons decaying to electrons and muons. The ee and $\mu\mu$ channels were merged. The data were further split into the case of exactly one jet being b-tagged, and greater than or equal to two jets being b-tagged in the event.

The events were rebinned into four $\Delta|y|$ bins for each channel with a binning optimisation method and unfolded with Fully Bayesian Unfolding to truth-level using response matrices to account for limited detector acceptance and reconstruction inefficiencies. The unfolding

method enabled the separate channels to be combined and systematic uncertainties to be included in a likelihood method, resulting in posterior distributions of charge asymmetries. The means and standard deviations of the distributions were taken as the charge asymmetry values and uncertainties, respectively. The asymmetries were calculated for the reconstructed $t\bar{t}$ pairs and also for the two leptons from the $t\bar{t}$ decays, which have smaller expected asymmetries but smaller associated uncertainties. In both cases, the asymmetries were measured inclusively across all the data, and in bins of $t\bar{t}$ (or dilepton) invariant mass, transverse momentum and velocity in the direction along the beampipe. The systematic uncertainties were constrained and correlations between them accounted for in the unfolding, which reduced the overall charge asymmetry uncertainties.

For the leptonic asymmetries, large unfolding biases were encountered in stress tests of BSM asymmetries. This was determined to be due to lack of detector acceptance for leptons at $|\eta| > 2.5$, meaning there was no sensitivity to enhancements in charge asymmetry at $|\Delta|\eta|| > 2.5$. It was therefore decided to work in the reduced phase-space of $|\Delta|\eta|| < 2.5$ for the leptonic asymmetries. Uncertainties due to the remaining small biases in the leptonic and $t\bar{t}$ asymmetries were added in quadrature to the overall charge asymmetry uncertainties. Statistical uncertainties from the response matrices were also added in quadrature to the overall uncertainties.

The predicted truth-level asymmetries at $\sqrt{s} = 13$ TeV are small (between 0% and +1%) in the NLO Powheg + Pythia8 simulation. In the inclusive $t\bar{t}$ case, the $A_C^{t\bar{t}}$ expectation is 0.00351 ± 0.00006. This is smaller than the $\sqrt{s} = 7$ TeV (0.0123 ± 0.0005 [116]) and 8 TeV (0.0111 ± 0.0004 [121]) NLO predictions by 71% and 68%, respectively. The decrease is due to an enhanced contribution from gg fusion as energy increases (see Section 5.2),

which dilutes the asymmetry.

Comparing the unfolded data results in the dilepton channel, the total uncertainty in the 13 TeV inclusive $t\bar{t}$ measurement (0.0081 ± 0.0041) is less than the total uncertainty in the 7 TeV (0.021 ± 0.030 [116]) and 8 TeV (0.021 ± 0.0016 [121]) measurements by 86% and 75%, respectively. Therefore, the decrease in uncertainty at 13 TeV compared with 7 and 8 TeV is greater than the decrease in expected asymmetry, giving a better overall sensitivity. Improvements are also seen with respect to the 7 and 8 TeV CMS results. The sensitivities of the leptonic asymmetries are also improved with respect to the former ATLAS and CMS results. The Run 1 $A_C^{t\bar{t}}$ and A_C^{ll} values are summarised in Figure 5.12.

For the inclusive A_C^{ll} measurement, strong evidence of non-zero charge asymmetry was observed to 4.1σ. No evidence had been seen in the 7 and 8 TeV results. Furthermore, the unfolded data lie 2.8σ away from the NLO Powheg + Pythia8 prediction so there will be interest to understand the discrepancy. The higher order NLO QCD + NLO EW prediction does however lead to better agreement with the data to 1.3σ.

It was possible to use more bins across the differential measurements than at $\sqrt{s} = 7$ TeV and 8 TeV due to the large 139 fb^{-1} dataset. For instance, five $m_{t\bar{t}}$ bins were used at 13 TeV compared with two bins ([0, 500] GeV and [500, ∞] GeV) at 8 TeV. In the 13 TeV results, the $A_C^{t\bar{t}}$ values do not show any obvious trend across the $m_{t\bar{t}}$ bins, but there is a clear increasing pattern in the $\beta_{Z,t\bar{t}}$ and $\beta_{Z,l\bar{l}}$ distributions. The slopes of the central values are slightly greater than the truth-level predictions (in the lower order MC) so further investigation will be of interest.

The largest sources of uncertainty in the charge asymmetries were due to statistical uncertainties in the data, particularly for the leptonic asymmetries and highest $m_{t\bar{t}}$ bins. These are reduced in the combination with the lepton + jets channel (see Section 8.3).

8.2 Charge Asymmetry in the Lepton + Jets Channel

As shown by the pie chart in Figure 5.4, $t\bar{t}$ decay through the lepton + jets channel ($t\bar{t} \to W^+b\, W^-\bar{b} \to l^+\nu_l b\, q\bar{q}\bar{b}$ or $q\bar{q}b\, l^-\bar{\nu}_l\bar{b}$) has a larger branching ratio than for the dilepton channel. However, with more jets, multijet QCD backgrounds are more important so the event selection is less pure in the signal.

The event signature required for the leptonically-decaying top (or antitop) quark was an isolated lepton (electron or muon), missing transverse momentum (for the neutrino) and one jet. For the hadronically-decaying top (or antitop), either three jets with distance parameter, $R = 0.4$ [140], were required (resolved topology), or a single large jet with $R = 1.0$ (boosted topology). The boosted topology occurs due to the hadronically-decaying top or antitop quark having a very large p_T, such that the b quark produced in association with the W boson and the two quarks from the W decay overlap to produce a single cluster of large area in the hadronic calorimeter.

For the resolved and boostod topoologies, the electron and muon events were further split into 1 b-tag and ≥ 2 b-tag channels, giving a total of eight channels. These were then combined in the FBU framework. The preliminary data results [190] are shown in Figure 8.1.

In the inclusive case, the measured data yields $A_C^{t\bar{t}} = 0.0060 \pm 0.0015$ giving strong evidence of charge asymmetry to a significance of 4.0σ. This is almost twice the value of the truth-level NLO Powheg + Pythia8 MC prediction of $A_C^{t\bar{t}} = 0.00356 \pm 0.00005$, with a
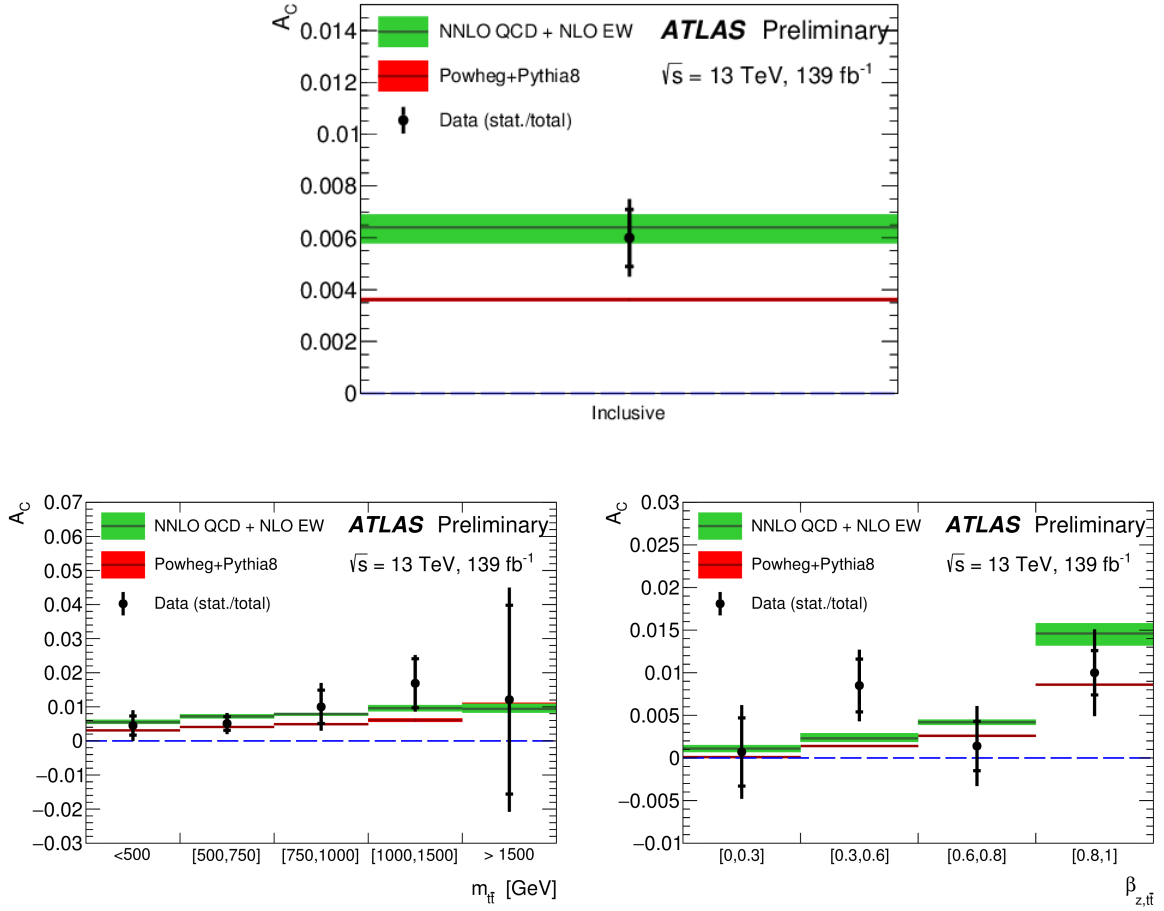
Fig. 8.1 The $A_C^{t\bar{t}}$ values and uncertainties for the lepton + jets channel [190]. Upper plot: inclusive asymmetry. Lower plots: Asymmetries in the $m_{t\bar{t}}$ bins (left) and $\beta_{Z,t\bar{t}}$ bins (right). The unfolded asymmetries are shown with the black points, where the inner bar is the statistical error and the outer bar the total error including the FBU uncertainty with systematic uncertainties, bias and response matrix statistical fluctuations. The red bands show the MC truth-level asymmetries from Powheg + Pythia8. The green bands show higher order predictions (NNLO in QCD and NLO in EW theory).

small disagreement to 1.6σ. However, the NNLO QCD + NLO EW inclusive prediction of

$$A_C^{t\bar{t}} = 0.0064_{-0.0006}^{+0.0005}$$ (see Table 7.16) is in good agreement with the data to 0.2σ.

Across the $m_{t\bar{t}}$ and $\beta_{Z,t\bar{t}}$ bins[1], the data-MC agreement is good and the precision is limited by

the statistics of the data. As for the dilepton channel, there appears to be a slight increasing

---

[1]The $p_{T,t\bar{t}}$ bins were not considered in these results but are now included for the combination with the dilepton channel.

209

asymmetry with $\beta_{Z,t\bar{t}}$. Across the $m_{t\bar{t}}$ bins, there is also an increase in asymmetry, not seen in the dilepton channel, which suffers from large statistical uncertainties at high $m_{t\bar{t}}$. In comparison with the ATLAS lepton + jets results at $\sqrt{s} = 7$ TeV and 8 TeV (see Figure 5.12), the inclusive uncertainties are 87% [113] and 70% [118] smaller, respectively, showing a large improvement. This is enhanced in the combination with the dilepton channel.

8.3 Dilepton and Lepton + Jets Channel Combination

It is simple within the FBU framework to combine the six dilepton and eight lepton + jets channels through Equation 7.12 for the $t\bar{t}$ asymmetries. The reconstructed- and truth-level binning was kept the same across all channels and is identical to that in Table 7.5. All of the experimental systematic uncertainties common to the channels were correlated between the channels, as well as the majority of the $t\bar{t}$ signal modelling and single top background normal-isation uncertainties. However, the other background normalisation uncertainties were kept uncorrelated between the dilepton and lepton + jets channels since the relative contributions to the backgrounds from various processes differ and the uncertainties were determined by different methods. The expected unfolded sensitivities for the combination (and the individual lepton + jets and dilepton channels for comparison) are shown in Table 8.1, as well as the expected truth-level values, all determined with NLO Powheg + Pythia8 MC. The table does not yet include the response matrix statistical uncertainties or the bias uncertainties and may not be the final setup, though some conclusions can be drawn. The data are yet to be unfolded.

For all bins, the expected unfolded asymmetries are consistent between the dilepton and lepton + jets channels, and the uncertainties are reduced in the combination. They are also consistent with the truth-level values, as expected for the simulation. In the inclusive case, the addition of the dilepton channel reduces the uncertainty by 12%. A similar trend is seen for the differential bins, with a 19% reduction in the uncertainty for the highest $p_{T,t\bar{t}}$ bin. The

decreases occur due to the extra statistics gained ($\sim 20\%$ more from the dilepton channel) and more constraining power in the systematic uncertainties when the joint fitting of the channels is performed in FBU.

Measurement	Bin	Expected truth		Expected unfolded			
		$A_{\mathrm{C}}^{t\bar{t}}$	Stat. unc.	Channel	$A_{\mathrm{C}}^{t\bar{t}}$	Stat. unc.	Stat. + syst. unc.
Inclusive		0.00351	0.00006	Lepton + jets	0.0036	0.0011	0.0017
				Dilepton	0.0036	0.0033	0.0041
				Combination	0.0035	0.0011	0.0015
$p_{T,t\bar{t}}$	[0, 30] GeV	0.00854	0.00009	Lepton + jets	0.0086	0.0034	0.0044
				Dilepton	0.009	0.011	0.014
				Combination	0.0086	0.0032	0.0040
	[30, 120] GeV	0.00062	0.00008	Lepton + jets	0.0007	0.0027	0.0037
				Dilepton	<0.001	0.009	0.012
				Combination	0.0007	0.0026	0.0033
	[120, ∞] GeV	0.00076	0.00014	Lepton + jets	0.0004	0.0047	0.0064
				Dilepton	0.001	0.012	0.014
				Combination	0.0004	0.0043	0.0052
$m_{t\bar{t}}$	[0, 500] GeV	0.00296	0.00007	Lepton + jets	0.0030	0.0029	0.0038
				Dilepton	0.003	0.012	0.014
				Combination	0.0029	0.0028	0.0034
	[500, 750] GeV	0.00413	0.00010	Lepton + jets	0.0042	0.0020	0.0025
				Dilepton	0.0039	0.0060	0.0065
				Combination	0.0040	0.0019	0.0022
	[750, 1000] GeV	0.00473	0.00022	Lepton + jets	0.0049	0.0047	0.0056
				Dilepton	0.005	0.019	0.021
				Combination	0.0047	0.0045	0.0051
	[1000, 1500] GeV	0.00502	0.00040	Lepton + jets	0.0055	0.0071	0.0084
				Dilepton	0.005	0.035	0.038
				Combination	0.0055	0.0068	0.0080
	[1500, ∞] GeV	0.0083	0.0011	Lepton + jets	0.007	0.022	0.026
				Dilepton	0.01	0.13	0.14
				Combination	0.008	0.022	0.025
$\beta_{Z,t\bar{t}}$	[0.0, 0.3]	-0.00023	0.00012	Lepton + jets	<0.0001	0.0040	0.0049
				Dilepton	<0.001	0.018	0.020
				Combination	<0.0001	0.0039	0.0046
	[0.3, 0.6]	0.00127	0.00011	Lepton + jets	0.0015	0.0032	0.0037
				Dilepton	0.002	0.012	0.013
				Combination	0.0016	0.0029	0.0034
	[0.6, 0.8]	0.00283	0.00012	Lepton + jets	0.0026	0.0029	0.0036
				Dilepton	0.003	0.009	0.011
				Combination	0.0026	0.0027	0.0033
	[0.8, 1.0]	0.00851	0.00010	Lepton + jets	0.0084	0.0027	0.0041
				Dilepton	0.0081	0.0069	0.0083
				Combination	0.0085	0.0025	0.0033

Table 8.1 Summary of the expected truth-level and expected unfolded $A_{\mathrm{C}}^{t\bar{t}}$ values and uncertainties (using NLO Powheg + Pythia8 MC) for the lepton + jets channel, the dilepton channel and their combination. The uncertainties do not yet include the statistical fluctuations in the response matrices and the bias uncertainties.

8.4 Outlook

The results for the $t\bar{t}$ charge asymmetries can be viewed in the context of Effective Field Theories (EFTs) [109]. EFTs yield an extension to the SM by expanding the Lagrangian around a new energy scale, Λ^{-2}, which is beyond the reach of the LHC:

$$\mathscr{L}_{\text{eff}} = \mathscr{L}_{\text{SM}} + \frac{1}{\Lambda^2}\sum_i C_i O_i + \mathscr{O}\left(\frac{1}{\Lambda^4}\right), \tag{8.1}$$

where $\mathscr{L}_{\text{eff}}$ is the modified Lagrangian and $\mathscr{L}_{\text{SM}}$ the SM Lagrangian. The O_i are dimension-6 operators that are invariant under $SU(3) \times SU(2) \times SU(1)$ transformations and built from SM fields. The C_i are dimensionless coupling factors (Wilson coefficients) that encode the effects of BSM physics in low-energy observables and are regularly interpreted in the Warsaw basis [191]. These will be zero if the SM is complete.

In hadron colliders, charge asymmetry is sensitive to four Wilson coefficients: C_u^1, C_u^2, C_d^1 and C_d^2 [192, 193]. These are reduced to two coefficients by assuming the couplings to up- and down-type quarks are equal: $C^1 = C_u^1 = C_d^1$ and $C^2 = C_u^2 = C_d^2$, which is valid in BSM models such as axigluon exchange [105]. The charge asymmetry is affected by the difference, $C^- = C^1 - C^2$, which can be rewritten in terms of the couplings and masses of new states. For example, the axigluon state is related to C^- by the following relation [194]:

$$\frac{C^-}{\Lambda^2} = -4\frac{g_s^2}{m_A^2}, \tag{8.2}$$

where g_s is the strong QCD coupling ($\alpha_s = g_s^2/4\pi$) and m_A is the axigluon mass.

The operators were applied using the MG5_aMC [135] generator and bounds placed on the coefficients through the combined dilepton and lepton + jets $A_C^{t\bar{t}}$ expected results. Fig-
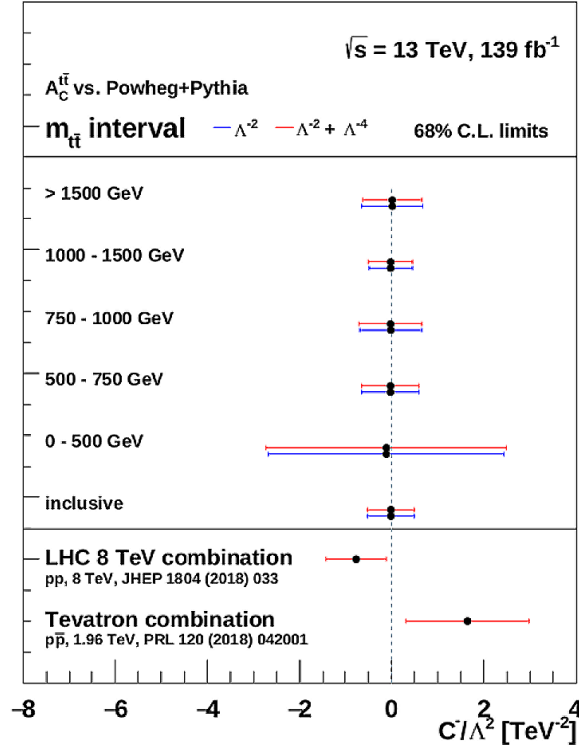
Fig. 8.2 The expected 13 TeV Powheg + Pythia8 limits on the C^-/Λ^2 coefficient with the dilepton and lepton + jets channel combination for the inclusive case and five $m_{t\bar{t}}$ bins. The blue bars show the coefficient at order Λ^{-2} and the red bars with a correction at Λ^{-4}. The bottom two results are those extracted from 8 TeV LHC data [115] and 1.96 TeV Tevatron data [111].

ure 8.2 shows the expected bounds on C^-/Λ^2 where the input data is the unfolded NLO Powheg + Pythia8 SM spectrum, in which the C^- value will be zero. The inclusive and differential $m_{t\bar{t}}$ values are shown, where the limited number of data events at high $m_{t\bar{t}}$ is offset by the higher $t\bar{t}$ production through $q\bar{q}$ annihilation, maintaining strong sensitivity. The inclusive expectations show tighter limits can be set on C^-/Λ^2 than those determined from the 8 TeV LHC and 1.96 TeV Tevatron data.

In conclusion, the individual dilepton and lepton + jets data results, calculated with the full Run 2 ATLAS dataset at $\sqrt{s} = 13$ TeV, as well as the expected results in their combination, show marked improvements in sensitivity to charge asymmetry and BSM models compared

with previous results. The uncertainties are dominated by statistical uncertainties in the data. These would be reduced if combined with the $\sqrt{s} = 13$ TeV data at CMS in the future. For instance, at 8 TeV, the ATLAS lepton + jets inclusive $A_C^{t\bar{t}}$ result (0.0090 ± 0.0049 [118]) combined with the CMS lepton + jets $A_C^{t\bar{t}}$ (0.0033 ± 0.0042 [119]) gave a final result of $A_C^{t\bar{t}} = 0.0055 \pm 0.0034$ [115]. This is a reduction of 31% in the total uncertainty with respect to the ATLAS result and 19% with respect to the CMS result.

It is clear from this thesis how interesting the preliminary results are at 13 TeV thanks to the excellent precision obtained. The FBU framework was of significant importance in reducing the systematic uncertainties, combining channels and giving unbiased results in unfolding the data. The final results (likely to be the world's most precise upon release) will lead to a deeper understanding of the top quark once the paper is released, even if they agree in most part with the Standard Model.

Beyond Run 2, the collision energy in the LHC during Run 3 will be $\sqrt{s} = 13$ TeV but may increase to 14 TeV. A dataset of 300 fb^{-1} is expected for each of ATLAS and CMS. There will therefore be no or little dilution in the expected asymmetry and a large increase in statistics. This should increase to 3000 fb^{-1} at an energy of $\sqrt{s} = 14$ TeV when the LHC is upgraded to the High Luminosity LHC (HL-LHC) [195] with the possibility of probing even finer differential bins.

References

[1] Dalton J., "A New System of Chemical Philosophy," William Dawson & Sons, London (1808).

[2] Mendeleev D. I., "The principles of chemistry," Collier, New York (1901).

[3] Thomson J. J., "On the structure of the atom: an investigation of the stability and periods of oscillation of a number of corpuscles arranged at equal intervals around the circumference of a circle; with application of the results to the theory of atomic structure," Philos. Mag. 7 39 (1904).

[4] Rutherford E. *et al.*, "The Scattering of α and β Particles by Matter and the Structure of the Atom," Philos. Mag. 6 21 (1911).

[5] Bohr N., "On the Constitution of Atoms and Molecules," Phil. Mag. Ser. 6 26 1 (1913).

[6] Heisenberg W. Z. "On the Perceptual Content of Quantum Theoretical Kinematics and Mechanics," Zeitschrift Für Physik 43 172 (1927).

[7] Chadwick J., "Possible Existence of a Neutron," Nature 129 312 (1932).

[8] Anderson C. D., "The Apparent Existence of Easily Deflectable Positives," Science 76 238 (1932).

[9] Stückelberg E. C., G., "The significance of proper time in wave mechanics," Helv. Phys. Acta. 14 322 (1941).

[10] Feynman R. P., "The Theory of positrons," Phys. Rev. 76 749 (1949).

[11] Englert C. *et al.*, Lecture notes for the 2017 HEP School for Experimental High Energy Physics Students 03-15 September 2017. Technical Report, RAL-TR-2017-009. See https://stfc.ukri.org/research/particle-physics-and-particle-astrophysics/hep-summer-school. Accessed 28 January 2019.

[12] 13th Annual Fermilab-CERN Hadron Collider Physics Summer School 20-31 August 2018. See https://indico.fnal.gov/event/17113. Accessed 28 January 2019.

[13] Thomson M., "Modern Particle Physics," Cambridge University Press, Cambridge (2013).

[14] Halzen F. and Martin A. D., "Quarks and Leptons: An Introductory Course in Modern Particle Physics," John Wiley & Sons, Inc., Hoboken (1984).

[15] Griffiths D., "Introduction to Elementary Particles, Second Edition," Wiley-VCH, Weinheim (2008).

[16] Lattes C., Occhialini G. and Powell C., "Observations on the Tracks of Slow Mesons in Photographic Emulsions," Nature 160 453 (1947).

[17] M. Tanabashi *et al.* (Particle Data Group), Phys. Rev. D 98 030001 (2018) and 2019 update.

[18] Gell-Mann M., "The interpretation of the new particles as displaced charge multiplets," Phys. Rev. 92 883 (1956); Nuovo Cimento 4 no.S2 848 (1956).

[19] Nakano T. and Nishijima K., "Charge Independence for V-particles," Prog. Theor. Phys. 10 581 (1953).

[20] Gell-Mann M. and Ne'eman Y., "The Eightfold Way," Benjamin, New York (1964).

[21] Akash J., "Symmetries in Particle Physics."
See https://www.researchgate.net/publication/27980646. Accessed 2 February 2019.

[22] Barnes V. E. *et al.*, "Observation of a Hyperon with Strangeness -3," Phys. Rev. Lett. 12 204 (1964).

[23] Gell-Mann M., "A schematic model of baryons and mesons," Phys. Rev. Lett. 8 214 (1964).

[24] Zweig G., "An SU(3) model for strong interaction symmetry and its breaking," CERN-TH-412 (1964).

[25] Pauli W., "The Connection Between Spin and Statistics," Phys. Rev. 58 716 (1940).

[26] Glashow S. L., Iliopoulos J. and Maiani L., "Weak Interactions with Lepton-Hadron Symmetry," Phys. Rev. D 2 1285 (1970).

[27] Aubert J. *et al.*, "Experimental Observation of a Heavy Particle J," Phys. Rev. Lett. 33 1404 (1974).

[28] Augustin J. E. *et al.*, "Discovery of a Narrow Resonance in e^+e^- Annihilation," Phys. Rev. Lett. 33 1406 (1974).

[29] Kobayashi M., Maskawa T., "CP Violation in the Renormalizable Theory of Weak Interaction," Prog. Theor. Phys. 49 652 (1973).

[30] Culligan G. *et al.*, "Longitudinal Polarization of the Electrons from the Decay of Unpolarized Positive and Negative Muons," Proc. Phys. Soc. 73 169 (1959).

[31] Wu C. S. *et al.*, "Experimental Test of Parity Conservation in Beta Decay," Phys. Rev. 105 1413 (1957).

[32] Christenson J. H., Cronin J. W., Fitch V. L. and Turlay R., "Evidence for the 2π Decay of the K_2^0 Meson," Phys. Rev. Lett. 13 138 (1964).

[33] Herb S. W. *et al.*, "Observation of a Dimuon Resonance at 9.5 GeV in 400 GeV Proton-Nucleus Collisions," Phys. Rev. Lett. 39 252 (1977).

[34] CDF Collaboration, "The CDF Detector: An Overview," Nucl. Instrum. Meth. A 271 387 (1988).

[35] CDF Collaboration, "Observation of Top Quark Production in $\bar{p}p$ Collisions," Phys. Rev. Lett. 74 2626 (1995), [hep-ex/9503002].

[36] D0 Collaboration, "The D0 Detector," Nucl. Instrum. Meth. A 338 185 (1994).

[37] D0 Collaboration, "Observation of the Top Quark," Phys. Rev. Lett. 74 2632 (1995), [hep-ex/9503003].

[38] Wilson R. R., "The Tevatron," FERMILAB-TM-0763 (1978).

[39] Glashow S. L., "Partial Symmetries of Weak Interactions," Nucl. Phys. 22 579 (1961).

[40] Goldstone J., Salam A. and Weinberg S., "Broken Symmetries," Phys. Rev. 127 965 (1962).

[41] Weinberg S., "A Model of Leptons," Phys. Rev. Lett. 19 1264 (1967).

[42] UA1 Collaboration, "Experimental Observation of Isolated Large Transverse Energy Electrons with Associated Missing Energy at $\sqrt{s} = 540$ GeV," Phys. Lett. 122 B 103 (1983).

[43] UA2 Collaboration, "Observation of Single Isolated Electrons of High Transverse Momentum in Events with Missing Transverse Energy at the CERN anti-p p Collider," Phys. Lett. 122 B 476 (1983).

[44] UA1 Collaboration, "Experimental Observation of Lepton Pairs of Invariant Mass Around 95 GeV/c^2 at the CERN SPS Collider," Phys. Lett. 126 B 398 (1983).

[45] UA2 Collaboration, "Evidence for $Z^0 \rightarrow e^+ e^-$ at the CERN anti-p p Collider," Phys. Lett. 129 B 130 (1983).

[46] Brout R. and Englert F., "Broken Symmetry and the Mass of Gauge Vector Mesons," Phys. Rev. Lett. 13 321 (1964).

[47] Higgs P. W., "Broken Symmetries and the Masses of Gauge Bosons," Phys. Rev. Lett. 13 508 (1964).

[48] Guralnik G. S., Hagen C. R. and Kibble T. W. B., "Global Conservation Laws and Massless Particles," Phys. Rev. Lett. 13 585 (1964).

[49] Ellis J., "Higgs Physics," CERN-PH-TH-2013-315, [arXiv:1312.5672 [hep-ph]].

[50] ATLAS Collaboration, "Observation of a new particle in the search for the standard model Higgs boson with the ATLAS detector at the LHC," Phys. Lett. B 716 (2012), [arXiv:1207.7214 [hep-ex]].

[51] CMS Collaboration, "Observation of a new boson at a mass of 125 GeV with the CMS experiment at the LHC," Phys. Lett. B 716 (2012), [arXiv: 1207.7235 [hep-ex]].

[52] Randle-Conde, A., "Feynman diagram maker." See https://www.aidansean.com/feynman. Accessed 2 February 2019.

[53] Planck Collaboration, "Planck 2013 results. XVI. Cosmological parameters," Astron. Astrophys. **571** (2014), A16, [arXiv:1303.5076 [astro-ph.CO]].

[54] NASA/CXC/K.Divona. See http://chandra.harvard.edu/resources/illustrations/darkmatter.html. Accessed 12 April 2019.

[55] Degrassi G. *et al.*, "Higgs mass and vacuum stability in the Standard Model at NNLO," JHEP 1208 098 (2012), [arXiv:1205.6497 [hep-ph]].

[56] Baer H. *et al.*, "Radiative natural supersymmetry: Reconciling electroweak fine-tuning and the Higgs boson mass," Phys. Rev. D 87 no.11 115028 (2013), [arXiv:1212.2655 [hep-ph]].

[57] Evans L. and Bryant P., "LHC machine," JINST 3 S08001 (2008).

[58] Myers S., "The LEP collider, from design to approval and commissioning," CERN-91-08, CERN-YELLOW-91-08.

[59] Benedikt M. *et al.*,"LHC Design Report. 3. The LHC injector chain," CERN-2004-003-V-3.

217

[60] Science and Technologies Facilities Council, UK Research and Innovation. See https://stfc.ukri.org/research/particle-physics-and-particle-astrophysics/large-hadron-collider/cern-accelerator-complex. Accessed 29 April 2019.

[61] Burnet J. P., "Putting it into Practice," CERN Yellow Report, CERN-2015-003, [arXiv:1607.01596 [physics.acc-ph]].

[62] Taking a Closer Look at LHC. See https://www.lhc-closer.es/taking_a_closer_look_at_lhc/0.magnetic_multipoles. Accessed 24 May 2019.

[63] ALICE Collaboration, "The ALICE experiment at the CERN LHC," JINST 3 S08002 (2008).

[64] LHCb Collaboration, "The LHCb Detector at the LHC," JINST 3 S08005 (2008).

[65] CMS Collaboration, "The CMS experiment at the CERN LHC," JINST 3 S08004 (2008).

[66] ATLAS Collaboration, "The ATLAS Experiment at the CERN Large Hadron Collider," JINST 3 S08003 (2008).

[67] ATLAS Outreach. "ATLAS Fact Sheet: To raise awareness of the ATLAS detector and collaboration on the LHC." ATLAS Brochure (2010). See https://cds.cern.ch/record/1457044. Accessed 29 May 2019.

[68] ATLAS Experiment - Public Results, Luminosity Public Results Run 2. See https://twiki.cern.ch/twiki/bin/view/AtlasPublic/LuminosityPublicResultsRun2. Accessed 29 May 2019.

[69] Zachary M. and the Atlas Collaboration, "Simulation of Pile-up in the ATLAS Experiment," J. Phys.: Conf. Ser. 513 022024 (2014).

[70] ATLAS Experiment - Public Results, ATLAS Stand-Alone Event Displays. See https://twiki.cern.ch/twiki/bin/view/AtlasPublic/EventDisplayStandAlone. Accessed 29 May 2019.

[71] Pernegger H., "The Pixel Detector of the ATLAS experiment for LHC Run 2," JINST 10 no.6 C06012 (2015).

[72] Pequenao J., "Computer generated image of the ATLAS inner detector." See https://cds.cern.ch/images/CERN-GE-0803014-01. Accessed 28 May 2019.

[73] Potamianos K., "The upgraded Pixel detector and the commissioning of the Inner Detector tracking of the ATLAS experiment for Run 2 at the Large Hadron Collider," PoS EPS-HEP2015 261 (2015), [arXiv:1608.07850 [physics.ins-det]].

[74] ATLAS Collaboration, "Operation and performance of the ATLAS semiconductor tracker,", JINST 9 P08009 (2014), [arXiv:1404.7473 [hep-ex]].

[75] Mindur B. [ATLAS Collaboration], "ATLAS Transition Radiation Tracker (TRT): Straw tubes for tracking and particle identification at the Large Hadron Collider," Nucl. Instrum. Meth. A 845 257 (2017).

[76] Universität Bonn. See https://www.hep1.physik.uni-bonn.de/research/index/copy_of_atlas-pixel-detector-ibl/re-commissioning-of-the-4-layer-atlas-pixel-detector. Accessed 30 May 2019.

[77] DESY. See http://www.desy.de/f/students/lectures2011/lec3.pdf. Accessed 3 June 2019.

[78] Grupen C. and Shwartz B., "Particle Detectors, Second Edition," Cambridge University Press, Cambridge (2008).

[79] ATLAS Collaboration, "ATLAS muon spectrometer: Technical design report," CERN-LHCC-97-22, ATLAS-TDR-10.

[80] Amram N. *et al.*, "Streamlined Calibrations of the ATLAS Precision Muon Chambers for Initial LHC Running," Nucl. Instrum. Meth. A 671 40 (2012), [arXiv:1103.0797 [physics.ins-det]].

[81] Pequenao J., Event Cross Section in a computer generated image of the ATLAS detector. See https://cds.cern.ch/record/1096081. Accessed 28 May 2019.

[82] Gaillard M., "CERN Data Centre passes the 200-petabyte milestone." See https://home.cern/news/news/computing/cern-data-centre-passes-200-petabyte-milestone. Accessed 28 August 2019.

[83] ATLAS Collaboration, "Performance of the ATLAS Trigger System in 2015," Eur. Phys. J. C 77 no.5 317 (2017), [arXiv:1611.09661 [hep-ex]].

[84] Nedden M. zur [ATLAS Collaboration], "The LHC Run 2 ATLAS trigger system: design, performance and plans," JINST 12 C03024 (2017), [arXiv:1611.09661 [hep-ex]].

[85] Achenbach R. *et al.*, "The ATLAS Level-1 Calorimeter Trigger," JINST 3 P03001 (2008).

[86] Anulli F. *et al.*, "The Level-1 Trigger Muon Barrel System of the ATLAS experiment at CERN," JINST 4 P04010 (2009).

[87] Trigger Physics Menu. See https://twiki.cern.ch/twiki/bin/viewauth/Atlas/TriggerPhysicsMenu. Accessed 21 December 2019.

[88] Simioni E., "The Topological Processor for the future ATLAS Level-1 Trigger: from design to commissioning," [arXiv:1406.4316 [physics.ins-det]].

[89] Müller F. [ATLAS Collaboration], "Upgrade of the ATLAS Level-1 calorimeter trigger," ATL-DAQ-SLIDE-2014-772.

[90] Eisenhandler E. F., "ATLAS Level-1 Calorimeter Trigger Algorithms," ATL-DAQ-2004-011, ATL-COM-DAQ-2004-014, CERN-ATL-DAQ-2004-011.

[91] Brun R. and Rademakers F., ROOT - An Object Oriented Data Analysis Framework, Proceedings AIHENP'96 Workshop, Lausanne, Sep. 1996, Nucl. Inst. & Meth. in Phys. Res. A 389 81 (1997). See also http://root.cern.ch. Accessed 31 August 2019.

[92] ATLAS Collaboration, "Electron efficiency measurements with the ATLAS detector using the 2015 LHC proton-proton collision data," ATLAS-CONF-2016-024.

[93] ATLAS Experiment - Public Results, Public Egamma Trigger Plots for Collision Data. See https://twiki.cern.ch/twiki/bin/view/AtlasPublic/EgammaTriggerPublicResults. Accessed 31 August 2019.

[94] Song T. and Berrehrah H., "Hadronization time of heavy quarks in nuclear matter," Phys. Rev. C 94 no.3 034901 (2016), [arXiv:1601.04449 [nucl-th]].

[95] Kohn F., "Measurement of the charge asymmetry in top quark pair production in pp collision data at $\sqrt{s} = 7$ TeV using the ATLAS detector," [arXiv:1204.0952 [hep-ex]].

[96] NNPDF Collaboration, "Parton distributions for the LHC Run II," JHEP 1504 040 (2015), [arXiv:1410.8849 [hep-ph]].

[97]   Bärnreuther P., "Top Quark Pair Production at the LHC."
       See https://core.ac.uk/download/pdf/36448208.pdf. Accessed 30 November 2019.

[98]   Heinson A., "Useful Diagrams of Top Signals and Backgrounds." See
       https://www-d0.fnal.gov/Run2Physics/top/top_public_web_pages/top_feynman_diagrams.html.
       Accessed 9 December 2019.

[99]   ATLAS Collaboration, "Measurement of the top quark mass in the $t\bar{t} \rightarrow$ lepton + jets channel
       from $\sqrt{s} = 8$ TeV ATLAS data and combination with previous results," Eur. Phys. J. C 79 no.4
       290 (2019), [arXiv:1810.01772 [hep-ex]].

[100] CMS Collaboration, "Measurement of the top quark mass using proton-proton data at $\sqrt{s} = 7$
       and 8 TeV," Phys. Rev. D 93 no.7 072004 (2016), [arXiv:1509.04044 [hep-ex]].

[101] LHCTopWG Summary Plots.
       See https://twiki.cern.ch/twiki/bin/view/LHCPhysics/LHCTopWGSummaryPlots. Accessed 18
       December 2019.

[102] Czakon M., Fiedler P. and Mitov A., "Total Top-Quark Pair-Production Cross Section at Hadron
       Colliders Through $O(\alpha_S^4)$," Phys. Rev. Lett. 110 252004 (2013), [arXiv:1303.6254 [hep-ph]].

[103] ATLAS Collaboration, "Measurements of top-quark pair spin correlations in the $e\mu$ channel at
       $\sqrt{s} = 13$ TeV using pp collisions in the ATLAS detector," [arXiv:1903.07570 [hep-ex]].

[104] CMS Collaboration, "Measurement of the top quark polarization and $t\bar{t}$ spin correlations using
       dilepton final states in proton-proton collisions at $\sqrt{s} = 13$ TeV," Phys. Rev. D 100 no.7 072002
       (2019), [arXiv:1907.03729 [hep-ex]].

[105] Antuñano O., Kühn J. H. and Rodrigo G., "Top quarks, axigluons, and charge asymmetries at
       hadron colliders," Phys. Rev. D 77 014003 (2008), [arXiv:0709.1652v1 [hep-ph]].

[106] Aguilar-Saavedra J. A. *et al.*, "Asymmetries in top quark pair production at hadron colliders,"
       Rev. Mod. Phys. 87 421 (2015), [arXiv:1406.1798 [hep-ph]].

[107] Rosner J. L., "Prominent decay modes of a leptophobic Z'," Phys. Lett. B 387 113 (1996),
       [hep-ph/9607207].

[108] Ferrario P. and Rodrigo G., "Massive color-octet bosons and the charge asymmetries of top
       quarks at hadron colliders," Phys. Rev. D 78 094018 (2008), [arXiv:0809.3354 [hep-ph]].

[109] Buckley A. *et al.*, "Constraining top quark effective theory in the LHC Run II era," JHEP 1604
       015 (2016), [arXiv:1512.03360 [hep-ph]].

[110] Kühn J. H. and Rodrigo G., "Forward-backward and charge asymmetries at Tevatron and the
       LHC," [arXiv:1411.4675 [hep-ph]].

[111] CDF and D0 Collaborations, "Combined Forward-Backward Asymmetry Measurements in
       Top-Antitop Quark Production at the Tevatron," Phys. Rev. Lett. 120 no.4 042001 (2018),
       [arXiv:1709.04894 [hep-ex]].

[112] CDF Collaboration, "Evidence for a Mass Dependent Forward-Backward Asymmetry in Top
       Quark Pair Production," Phys. Rev. D 83 112003 (2011), [arXiv:1101.0034 [hep-ex]].

[113] ATLAS Collaboration, "Measurement of the top quark pair production charge asymmetry in
       proton-proton collisions at $\sqrt{s} = 7$ TeV using the ATLAS detector," JHEP 02 107 (2014),
       [arXiv:1311.6724 [hep-ex]].

[114] CMS Collaboration, "Inclusive and differential measurements of the $t\bar{t}$ charge asymmetry in
       proton-proton collisions at $\sqrt{s} = 7$ TeV," Phys. Lett. B 717 129 (2012), [arXiv:1207.0065

[hep-ex]].

[115] ATLAS and CMS Collaborations, "Combination of inclusive and differential $t\bar{t}$ charge asymmetry measurements using ATLAS and CMS data at $\sqrt{s} = 7$ and 8 TeV," JHEP 04 033 (2018), [arXiv:1709.05327 [hep-ex]].

[116] ATLAS Collaboration, "Measurement of the charge asymmetry in dileptonic decays of top quark pairs in pp collisions at $\sqrt{s} = 7$ TeV using the ATLAS detector," JHEP 05 061 (2015), [arXiv:1501.07383 [hep-ex]].

[117] CMS Collaboration, "Measurements of the $t\bar{t}$ charge asymmetry using the dilepton decay channel in pp collisions at $\sqrt{s} = 7$ TeV," JHEP 04 191 (2014), [arXiv:1402.3803 [hep-ex]].

[118] ATLAS Collaboration, "Measurement of the charge asymmetry in top-quark pair production in the lepton-plus-jets final state in pp collision data at $\sqrt{s} = 8$ TeV with the ATLAS detector," Eur. Phys. J. C 76 no.2 87 (2016), [arXiv:1509.02358 [hep-ex]].

[119] CMS Collaboration, "Measurement of the charge asymmetry in top quark pair production in pp collisions at $\sqrt{s} = 8$ TeV using a template method," Phys. Rev. D 93 no.3 034014 (2016), [arXiv:1508.03862 [hep-ex]].

[120] CMS Collaboration, "Inclusive and differential measurements of the $t\bar{t}$ charge asymmetry in pp collisions at $\sqrt{s} = 8$ TeV," Phys. Lett. B 757 154 (2016), [arXiv:1507.03119 [hep-ex]].

[121] ATLAS Collaboration, "Measurements of the charge asymmetry in top-quark pair production in the dilepton final state at $\sqrt{s} = 8$ TeV with the ATLAS detector," Phys. Rev. D 94 032006 (2016), [arXiv:1604.05538 [hep-ex]].

[122] CMS Collaboration, "Measurements of $t\bar{t}$ charge asymmetry using dilepton final states in pp collisions at $\sqrt{s} = 8$ TeV," Phys. Lett. B 760 365 (2016), [arXiv:1603.06221 [hep-ex]].

[123] ATLAS Collaboration, "Measurement of the charge asymmetry in highly boosted top-quark pair production in $\sqrt{s} = 8$ TeV pp collision data collected by the ATLAS experiment," Phys. Lett. B 756 52 (2016), [arXiv:1512.06092 [hep-ex]].

[124] GEANT4 Collaboration, "GEANT4: A Simulation toolkit," Nucl. Instrum. Meth. A 506 250 (2003).

[125] Alioli S. *et al.*, "A general framework for implementing NLO calculations in shower Monte Carlo programs: the POWHEG BOX," JHEP 1006 043 (2010), [arXiv:1002.2581 [hep-ph]].

[126] Sjöstrand T. *et al.*, "An Introduction to PYTHIA 8.2," Comput. Phys. Commun. 191 159 (2015), [arXiv:1410.3012 [hep-ph]].

[127] NNPDF Collaboration, "Parton distributions with LHC data," Nucl. Phys. B 867 244 (2013), [arXiv:1207.1303 [hep-ph]].

[128] ATLAS Collaboration, "ATLAS Pythia 8 tunes to 7 TeV data," ATL-PHYS-PUB-2014-021.

[129] Czakon M. and Mitov A., "Top++: A Program for the Calculation of the Top-Pair Cross-Section at Hadron Colliders," Comput. Phys. Commun. 185 2930 (2014), [arXiv:1112.5675 [hep-ph]].

[130] ATLAS Collaboration, "Studies on top-quark Monte Carlo modelling for Top 2016," ATL-PHYS-PUB-2016-020.

[131] Frixione S. *et al.*, "Single-top hadroproduction in association with a W boson," JHEP 0807 029 (2008), [arXiv:0805.3067 [hep-ph]].

[132] Gleisberg T. and Hoeche S., "Comix, a new matrix element generator," JHEP 0812 039 (2008), [arXiv:0808.3674 [hep-ph]].

[133] Cascioli F., Maierhofer P. and Pozzorini S., "Scattering Amplitudes with Open Loops," Phys. Rev. Lett. 108 111601 (2012), [arXiv:1111.5206 [hep-ph]].

[134] Bothmann E. *et al.*, "Event Generation with Sherpa 2.2," SciPost Phys. 7 no.3 034 (2019), [arXiv:1905.09127 [hep-ph]].

[135] Alwall J. *et al.*, "The automated computation of tree-level and next-to-leading order differential cross sections (MadGraph5_aMC@NLO), and their matching to parton shower simulations," JHEP 1407 079 (2014), [arXiv:1405.0301 [hep-ph]].

[136] ATLAS Collaboration, "Electron reconstruction and identification in the ATLAS experiment using the 2015 and 2016 LHC proton-proton collision data at $\sqrt{s} = 13$ TeV," Eur. Phys. J. C 79 no.8 639 (2019), [arXiv:1902.04655 [physics.ins-det]].

[137] ATLAS Collaboration, "Electron and photon performance measurements with the ATLAS detector using the 2015-2017 LHC proton-proton collision data," JINST 14 no.12 P12006 (2019), [arXiv:1908.00005 [hep-ex]].

[138] ATLAS Collaboration, "Muon reconstruction performance of the ATLAS detector in proton-proton collision data at $\sqrt{s} = 13$ TeV," Eur. Phys. J. C 76 no.5 292 (2016), [arXiv:1603.05598 [hep-ex]].

[139] Lampl W. *et al.*, "Calorimeter clustering algorithms: Description and performance," ATL-LARG-PUB-2008-002.

[140] Cacciari M., Salam G. P. and Soyez G., "The anti-k_t jet clustering algorithm," JHEP 0804 063 (2008), [arXiv:0802.1189 [hep-ph]].

[141] Cacciari M., Salam G. P. and Soyez G., "The Catchment Area of Jets," JHEP 0804 005 (2008), [arXiv:0802.1188 [hep-ph]].

[142] ATLAS Collaboration, "Jet energy scale measurements and their systematic uncertainties in proton-proton collisions at $\sqrt{s} = 13$ TeV with the ATLAS detector," Phys. Rev. D 96 no.7 072002 (2017), [arXiv:1703.09665 [hep-ex]].

[143] ATLAS Collaboration, "Performance of pile-up mitigation techniques for jets in pp collisions at $\sqrt{s} = 8$ TeV using the ATLAS detector," Eur. Phys. J. C 76 no.11 581 (2016), [arXiv:1510.03823 [hep-ex]].

[144] ATLAS Collaboration, "Optimisation and performance studies of the ATLAS b-tagging algorithms for the 2017-18 LHC run," ATL-PHYS-PUB-2017-013.

[145] ATLAS Collaboration, "Measurements of b-jet tagging efficiency with the ATLAS detector using $t\bar{t}$ events at $\sqrt{s} = 13$ TeV," JHEP 1808 089 (2018), [arXiv:1805.01845 [hep-ex]].

[146] ATLAS Collaboration, "ATLAS b-jet identification performance and efficiency measurement with $t\bar{t}$ events in pp collisions at $\sqrt{s} = 13$ TeV," Eur. Phys. J. C 79 no.11 970 (2019), [arXiv:1907.05120 [hep-ex]].

[147] Hoecker A. *et al.*, "TMVA - Toolkit for Multivariate Data Analysis," PoS ACAT 040 (2007), [arXiv:physics/0703039 [physics.data-an]].

[148] Good Run Lists For Analysis Run 2.
See https://twiki.cern.ch/twiki/bin/view/AtlasProtected/GoodRunListsForAnalysisRun2. Accessed 21 December 2019.

[149] ATLAS Collaboration, "Performance of electron and photon triggers in ATLAS during LHC Run 2," Eur. Phys. J. C 80 no.1 47 (2020), [arXiv:1909.00761 [hep-ex]].

[150] ATLAS Collaboration, "Performance of the ATLAS muon triggers in Run 2," CERN-EP-2020-031. [arXiv:2004.13447 [hep-ex]].

[151] Meyer J. M., "Measurement of the Top Quark Mass using Dilepton Events and a Neutrino Weighting Algorithm with the D0 Experiment at the Tevatron (Run II)." See http://lss.fnal.gov/cgi-bin/find_paper.pl?thesis-2007-65. Accessed 15 January 2020.

[152] Erdmann J. *et al.*, "A likelihood-based reconstruction algorithm for top-quark pairs and the KLFitter framework," Nucl. Instrum. Meth. A 748 18 (2014), [arXiv:1312.5595 [hep-ex]].

[153] Richter-Was E., Froidevaux D. and Poggioli L., "ATLFAST 2.0 a fast simulation package for ATLAS," ATL-PHYS-98-131, ATL-COM-PHYS-98-011, CERN-ATL-PHYS-98-131.

[154] ATLAS Collaboration, "Luminosity determination in pp collisions at $\sqrt{s} = 13$ TeV using the ATLAS detector at the LHC," ATLAS-CONF-2019-021.

[155] Van der Meer S., "Calibration of the Effective Beam Height in the ISR," CERN-ISR-PO-68-31.

[156] Grafström P. and Kozanecki W., "Luminosity determination at proton colliders," Prog. Part. Nucl. Phys. 81 97 (2015).

[157] Buttinger W., "Extended Pileup Reweighting."
See https://twiki.cern.ch/twiki/bin/viewauth/AtlasProtected/ExtendedPileupReweighting. Accessed 18 February 2020.

[158] ATLAS Collaboration, "Tagging and suppression of pileup jets with the ATLAS detector," ATLAS-CONF-2014-018.

[159] ATLAS Collaboration, "Monte Carlo Calibration and Combination of In-Situ Measurements of Jet Energy Scale, Jet Energy Resolution and Jet Mass in ATLAS," ATLAS-CONF-2015-037.

[160] ATLAS Collaboration, "Jet energy scale measurements and their systematic uncertainties in proton-proton collisions at $\sqrt{s} = 13$ TeV with the ATLAS detector," Phys. Rev. D 96 no.7 072002 (2017), [arXiv:1703.09665 [hep-ex]].

[161] ATLAS Collaboration, "Measurement of b-tagging efficiency of c-jets in $t\bar{t}$ events using a likelihood approach with the ATLAS detector," ATLAS-CONF-2018-001.

[162] ATLAS Collaboration, "Calibration of light-flavour jet b-tagging rates on ATLAS proton-proton collision data at $\sqrt{s} = 13$ TeV," ATLAS-CONF-2018-006.

[163] ATLAS Collaboration, "Muon reconstruction performance of the ATLAS detector in 2016," ATL-PHYS-PROC-2017-246.

[164] ATLAS Collaboration, "Electron and photon energy calibration with the ATLAS detector using 2015-2016 LHC proton-proton collision data," JINST 14 P03017 (2019), [arXiv:1812.03848 [hep-ex]].

[165] ATLAS Collaboration, "Performance of missing transverse momentum reconstruction with the ATLAS detector using proton-proton collisions at $\sqrt{s} = 13$ TeV," Eur. Phys. J. C 78 no.11 903 (2018), [arXiv:1802.08168 [hep-ex]].

[166] ATLAS Collaboration, "E_T^{miss} performance in the ATLAS detector using 2015-2016 LHC pp collisions," ATLAS-CONF-2018-023.

[167] Bahr M. *et al.*, "Herwig++ Physics and Manual," Eur. Phys. J. C 58 639 (2008), [arXiv:0803.0883 [hep-ph]].

[168] Bellm J. *et al.*, "Herwig 7.0/Herwig++ 3.0 release note," Eur. Phys. J. C 76 no.4 196 (2016), [arXiv:1512.01178 [hep-ph]].

[169] Harland-Lang L. A. *et al.*, "Parton distributions in the LHC era: MMHT 2014 PDFs," Eur. Phys. J. C 75 no.5 204 (2015), [arXiv:1412.3989 [hep-ph]].

[170] Rojo J., "PDF4LHC recommendations for Run II," PoS DIS 2016 018 (2016), [arXiv:1606.08243 [hep-ph]].

[171] Dulat S. *et al.*, "New parton distribution functions from a global analysis of quantum chromo-dynamics," Phys. Rev. D 93 no.3 033006 (2016), [arXiv:1506.07443 [hep-ph]].

[172] Aliev M. *et al.*, "HATHOR: HAdronic Top and Heavy quarks crOss section calculatoR," Comput. Phys. Commun. 182 1034 (2011), [arXiv:1007.1327 [hep-ph]].

[173] Kant P. *et al.*, "HATHOR for single top-quark production: Updated predictions and uncertainty estimates for single top-quark production in hadronic collisions," Comput. Phys. Commun. 191 74 (2015), [arXiv:1406.4403 [hep-ph]].

[174] ATLAS Collaboration, "Multi-Boson Simulation for 13 TeV ATLAS Analyses," ATL-PHYS-PUB-2017-005.

[175] Frixione S. *et al.*, "Electroweak and QCD corrections to top-pair hadroproduction in association with heavy bosons," JHEP 1506 184 (2015), [arXiv:1504.03446 [hep-ph]].

[176] ATLAS Collaboration, "Measurements of top quark spin observables in $t\bar{t}$ events using dilepton final states in $\sqrt{s} = 8$ TeV pp collisions with the ATLAS detector," JHEP 1703 113 (2017), [arXiv:1612.07004 [hep-ex]].

[177] Volker B., "Unfolding methods in high-energy physics experiments," DESY-84-118.

[178] Cowan G., "A survey of unfolding methods for particle physics," Conf. Proc. C 0203181 248 (2002).

[179] Choudalakis G., "Fully Bayesian Unfolding," [arXiv:1201.4612 [physics.data-an]].

[180] Cowan G., Statistical Data Analysis," Oxford University Press, Oxford (1998).

[181] Diaconis P., "The Markov Chain Monte Carlo Revolution," Bull. Amer. Math. Soc. (N. S.) 46 179 (2009), MR 2476411.

[182] Hoffman M. D. and Gelman A., "The No-U-Turn Sampler: Adaptively Setting Path Lengths in Hamiltonian Monte Carlo," JMLR 15 (2014), [arXiv:1111.4246 [stat.CO]].

[183] McElreath R., "Markov Chains: Why Walk When You Can Flow?" See http://elevanth.org/blog/2017/11/28/build-a-better-markov-chain/. Accessed 1 April 2020.

[184] Salvatier J., Wiecki T. V. and Fonnesbeck C. "Probabilistic programming in Python using PyMC3," PeerJ Computer Science 2:e55 (2016). [arXiv:1507.08050v1 [stat.CO]].

[185] Aguilar-Saavedra J. A., "Protos - PROgram for TOp Simulations, MC Generator." See http://jaguilar.web.cern.ch/jaguilar/protos. Accessed 1 April 2020.

[186] Bohm G. and Zech G., "Introduction to Statistics and Data Analysis for Physicists," 2nd Rev. Ed. Verlag Deutsches Elektronen-Synchrotron, Hamburg (2014).

[187] Czakon M. *et al.*, "Top-quark charge asymmetry at the LHC and Tevatron through NNLO QCD and NLO EW," Phys. Rev. D 98 no.1 014003 (2018), [arXiv:1711.03945 [hep-ph]].

[188] Centre for Precision Studies in Particle Physics.
See http://www.precision.hep.phy.cam.ac.uk/results. Accessed 1 April 2020.

[189] Bernreuther W. and Si Z.-G. Values provided through private communication. See also "Top quark and leptonic charge asymmetries for the Tevatron and LHC," Phys. Rev. D 86 030426 (2012), [arXiv:1205.6580 [hep-ph]].

[190] ATLAS Collaboration, "Inclusive and differential measurement of the charge asymmetry in $t\bar{t}$ events at 13 TeV with the ATLAS detector," ATLAS-CONF-2019-026.

[191] Grzadkowski B. *et al.*, "Dimension-Six Terms in the Standard Model Lagrangian," JHEP 1010 085 (2010), [arXiv:1008.4884 [hep-ph]].

[192] Rosello M. P. and Vos M., "Constraints on four-fermion interactions from the $t\bar{t}$ charge asymmetry at hadron colliders," Eur. Phys. J. C 76 no.4 200 (2016), [arXiv:1512.07542 [hep-ex]].

[193] Zhang C. and Willenbrock S., "Effective-Field-Theory Approach to Top-Quark Production and Decay," Phys. Rev. D 83 034006 (2011), [arXiv:1008.3869 [hep-ph]].

[194] Degrande C. *et al.*, "Non-resonant New Physics in Top Pair Production at Hadron Colliders," JHEP 1103 125 (2011), [arXiv:1010.6304 [hep-ph]].

[195] Bernius C. "HL-LHC prospects from ATLAS and CMS," ATL-PHYS-PROC-2019-023.

MC Samples

The $t\bar{t}$ MC signal samples used in the dilepton and lepton + jets channels are summarised in Table A.1. Alternative ATLFAST 2.0 (AFII) [153] simulation samples are also shown. The MC background samples are shown in Tables A.2 and A.3. All three tables show the MC generators, theoretical cross-sections and k-factors (scale factors which account for higher order corrections to the Feynman diagrams) for each sample, which have unique dataset IDs (DSIDs).

DSID	Filter	Generator	Cross-section (pb)	k-factor	Simulation
		Nominal samples			
410472	dilepton	Powheg + Pythia8.230	76.95	1.1398	Full
410470	lepton + jets	Powheg + Pythia8.230	396.87	1.1398	Full
		Alternative samples			
410472	dilepton	Powheg + Pythia8.230	76.95	1.1398	AFII
410470	lepton + jets	Powheg + Pythia8.230	396.87	1.1398	AFII
410482	dilepton	Powheg + Pythia8.230 $h_{\mathrm{damp}} = 3.0\,m_t$	76.94	1.1398	AFII
410480	lepton + jets	Powheg + Pythia8.230 $h_{\mathrm{damp}} = 3.0\,m_t$	320.01	1.1398	AFII
410558	dilepton	Powheg+Herwig7.04	77.00	1.1391	AFII
410557	lepton + jets	Powheg+Herwig7.04	320.185	1.1392	AFII
411045	lepton + jets	Powheg + Pythia8.230 $m_t = 171$ GeV	324.337	1.1455	AFII
411046	lepton + jets	Powheg + Pythia8.230 $m_t = 172$ GeV	324.337	1.1416	AFII
411049	lepton + jets	Powheg + Pythia8.230 $m_t = 173$ GeV	315.625	1.1378	AFII
411050	lepton + jets	Powheg + Pythia8.230 $m_t = 174$ GeV	307.224	1.1340	AFII
411053	dilepton	Powheg + Pythia8.230 $m_t = 171$ GeV	80.107	1.1455	AFII
411054	dilepton	Powheg + Pythia8.230 $m_t = 172$ GeV	77.947	1.1416	AFII
411057	dilepton	Powheg + Pythia8.230 $m_t = 173$ GeV	75.856	1.1378	AFII
411058	dilepton	Powheg + Pythia8.230 $m_t = 174$ GeV	73.831	1.1455	AFII

Table A.1 Summary of the signal MC samples.

DSID	Process	Generator	Cross-section (pb)	k-factor	Simulation
		Single top			
410658	t-channel top	Powheg + Pythia8.230	36.993	1.00	Full
410659	t-channel antitop	Powheg + Pythia8.230	22.175	1.00	Full
410644	s-channel top	Powheg + Pythia8.230	2.0268	1.015	Full
410645	s-channel antitop	Powheg + Pythia8.230	1.2676	1.015	Full
410646	tW process DR lepton + jets top	Powheg + Pythia8.230	37.936	0.945	Full
410647	tW process DR lepton + jets antitop	Powheg + Pythia8.230	37.906	0.946	Full
410648	tW process DR dilepton top	Powheg + Pythia8.230	3.9968	0.945	Full
410649	tW process DR dilepton antitop	Powheg + Pythia8.230	3.9940	0.946	Full
		Single top - alternative samples			
410658	t-channel top	Powheg + Pythia8.230	36.993	1.00	AFII
410659	t-channel antitop	Powheg + Pythia8.230	22.175	1.00	AFII
410644	s-channel top	Powheg + Pythia8.230	2.0268	1.015	AFII
410645	s-channel antitop	Powheg + Pythia8.230	1.2676	1.015	AFII
410646	tW process DR lepton + jets top	Powheg + Pythia8.230	37.936	0.945	AFII
410647	tW process DR lepton + jets antitop	Powheg + Pythia8.230	37.906	0.946	AFII
410648	tW process DR dilepton top	Powheg + Pythia8.230	3.9968	0.945	AFII
410649	tW process DR dilepton antitop	Powheg + Pythia8.230	3.9940	0.946	AFII
410654	tW process DS lepton + jets top	Powheg + Pythia8.230	36.925	0.971	Full
410655	tW process DS lepton + jets antitop	Powheg + Pythia8.230	37.662	0.952	Full
410656	tW process DS dilepton top	Powheg + Pythia8.230	3.8926	0.967	Full
410657	tW process DS dilepton antitop	Powheg + Pythia8.230	3.9698	0.948	Full
411033	t-channel top	Powheg+Herwig7.04	37.017	1.193	AFII
411032	t-channel antitop	Powheg+Herwig7.04	22.194	1.184	AFII
411034	s-channel top	Powheg+Herwig7.04	2.0279	1.016	AFII
411035	s-channel antitop	Powheg+Herwig7.04	1.2687	1.016	AFII
411036	tW process DR lepton + jets top	Powheg+Herwig7.04	37.958	0.9448	AFII
411037	tW process DR lepton + jets antitop	Powheg+Herwig7.04	37.929	0.9448	AFII
411038	tW process DR dilepton top	Powheg+Herwig7.04	3.9991	0.9412	AFII
411039	tW process DR dilepton antitop	Powheg+Herwig7.04	3.9963	0.9419	AFII

Table A.2 Summary of the single top t-channel, s-channel and tW associated production processes. The tW DR (Diagram Removal) and DS (Diagram Subtraction) processes are discussed in Sections 6.1.2 and 6.8.3.1.

Table A.3 Summary of the other background processes.

DSID	Process	Generator	Cross-section (pb)	k-factor	Simulation
W + jets					
364156-69	$W \to \mu\nu$	Comix+OpenLoops+Sherpa2.2.1	20472.488	0.9702	Full
364170-83	$W \to e\nu$	Comix+OpenLoops+Sherpa2.2.1	20476.908	0.9702	Full
364184-97	$W \to \tau\nu$	Comix+OpenLoops+Sherpa2.2.1	20507.226	0.9702	Full
Z + jets					
364100-13	$Z \to \mu\mu$	Comix+OpenLoops+Sherpa2.2.1	2138.730	0.9751	Full
364114-27	$Z \to ee$	Comix+OpenLoops+Sherpa2.2.1	2137.697	0.9751	Full
364128-41	$Z \to \tau\tau$	Comix+OpenLoops+Sherpa2.2.1	2138.015	0.9751	Full
Z + jets (low mass: 10 GeV $< m_{ll} <$ 40 GeV)					
364198-203	$Z \to \mu\mu$	Comix+OpenLoops+Sherpa2.2.1	2465.673	0.9751	Full
364204-209	$Z \to ee$	Comix+OpenLoops+Sherpa2.2.1	2466.284	0.9751	Full
364210-215	$Z \to \tau\tau$	Comix+OpenLoops+Sherpa2.2.1	2468.6697	0.9751	Full
Diboson					
363355	1 lepton	Comix+OpenLoops+Sherpa2.2.1	15.564	0.27976	Full
363356	1 lepton	Comix+OpenLoops+Sherpa2.2.1	15.563	0.13961	Full
363357-60, 363489	1 lepton	Comix+OpenLoops+Sherpa2.2.1	159.104	1.00	Full
364250, 364253-55	2 and 3 leptons	Comix+OpenLoops+Sherpa2.2.2	21.613	1.00	Full
Rare SM					
410155	$t\bar{t}W$	MG5_aMC2.3.3+Pythia8.210	0.5483	1.10	Full
410156	$t\bar{t}Z \to \nu\nu$	MG5_aMC2.3.3+Pythia8.210	0.15499	1.11	Full
410157	$t\bar{t}Z \to q\bar{q}$	MG5_aMC2.3.3+Pythia8.210	0.52771	1.11	Full
410218	$t\bar{t}Z \to ee$	MG5_aMC2.3.3+Pythia8.210	0.036888	1.12	Full
410219	$t\bar{t}Z \to \mu\mu$	MG5_aMC2.3.3+Pythia8.210	0.036895	1.12	Full
410220	$t\bar{t}Z \to \tau\tau$	MG5_aMC2.3.3+Pythia8.210	0.036599	1.12	Full
345873	$t\bar{t}H$ all-jets (2015-17 MC)	Powheg + Pythia8.230	0.23082	1.00	Full
346343	$t\bar{t}H$ all-jets (2018 MC)	MG5_aMC2.6.0+Pythia8.230	0.23082	1.00	Full
345874	$t\bar{t}H$ lepton + jets (2015-17 MC)	Powheg + Pythia8.230	0.22276	1.00	Full
346344	$t\bar{t}H$ lepton + jets (2018 MC)	MG5_aMC2.6.0+Pythia8.230	0.22276	1.00	Full
345875	$t\bar{t}H$ dilepton (2015-17 MC)	Powheg + Pythia8.230	0.05343	1.00	Full
346345	$t\bar{t}H$ dilepton (2018 MC)	MG5_aMC2.6.0+Pythia8.230	0.05343	1.00	Full
410560	tZ	MG5_aMC2.3.3+Pythia8.212	0.24037	1.00	Full
410408	tWZ	MG5_aMC2.3.3+Pythia8.212	0.016046	1.00	Full

Cut Flow Tables

Tables B.1 – B.6 show how the cuts in Section 6.6 affect the number of data and MC events (signal and background) for each channel. The pre-selection field includes the requirements of a primary vertex, two oppositely charged leptons with their p_T and flavour requirements, at least two jets with their p_T requirements, and flags to identify fake and τ lepton candidates. The MC event numbers are scaled to the same luminosity as the data, and multiplied by the process cross-sections, the k-factors and correctional reweighting factors.

Table B.1 Cut flows for the ee (1 b-tag) channel. The $t\bar{t}$ Powheg + Pythia8 (Pow+Py8) signal is split whereby the W bosons decay directly into electrons or muons (no τ case), and where one or both W bosons decay through a τ lepton into an electron or muon (τ case).

Sample	Data		$t\bar{t}$ Pow+Py8 (no τ)		$t\bar{t}$ Pow+Py8 (τ)		Single top		Z + jets		Diboson		Rare SM		Fake lepton	
Initial	2139711		1133501		1133501		59957		769436		18029		10533		1986049	
Pre-selection	-1472849	666862	-909319	224182	-1107286	26215	-46712	13245	-445132	324304	-14717	3311	-7914	2619	-1972404	13644
$\lvert m_{ll} - m_Z \rvert > 10$ GeV	-377818	289044	-30074	194108	-4156	22059	-1606	11639	-279952	44352	-2465	846	-1414	1205	-8132	5512
$E_T^{\text{miss}} > 60$ GeV	-152454	136590	-84271	109837	-8757	13302	-4951	6689	-41277	3075	-458	388	-459	746	-3013	2498
$m_{ll} > 15$ GeV	-1128	135462	-719	109118	-82	13220	-35	6653	-174	2901	-3	385	-5	741	-22	2476
1 b-tagged jet	-63073	72389	-52299	56819	-6259	6961	-2032	4621	-405	2496	-29	356	-388	352	-1011	1466
NW weight > 0	-19884	52505	-14555	42265	-1745	5216	-1860	2762	-1262	1235	-223	133	-171	182	-483	982
Passed events		52505		42265		5216		2762		1235		133		182		982

Table B.2 Cut flows for the ee (≥ 2 b-tag) channel.

Sample	Data		$t\bar{t}$ Pow+Py8 (no τ)		$t\bar{t}$ Pow+Py8 (τ)		Single top		Z + jets		Diboson		Rare SM		Fake lepton	
Initial	2139711		1133501		1133501		59957		769436		18029		10533		1986049	
Pre-selection	-1472849	666862	-909319	224182	-1107286	26215	-46712	13245	-445132	324304	-14717	3311	-7914	2619	-1972404	13644
$\lvert m_{ll} - m_Z \rvert > 10$ GeV	-377818	289044	-30074	194108	-4156	22059	-1606	11639	-279952	44352	-2465	846	-1414	1205	-8132	5512
$E_T^{\text{miss}} > 30$ GeV	-66217	222827	-26337	167770	-2714	19345	-1543	10096	-27593	16759	-215	631	-157	1048	-1299	4213
$m_{ll} > 0$ GeV	-0	222827	-0	167770	-0	19345	-0	10096	-0	16759	-0	631	-0	1048	-0	4213
≥ 2 b-tagged jets	-124008	98819	-86521	81249	-10072	9272	-7116	2980	-14848	1911	-585	46	-503	545	-2575	1639
NW weight > 0	-6931	91888	-3910	77339	-363	8909	-1158	1822	-750	1162	-22	23	-150	394	-169	1470
Passed events		91888		77339		8909		1822		1162		23		394		1470

Table B.3

Sample	Data		$t\bar{t}$ Pow+Py8 (no τ)		$t\bar{t}$ Pow+Py8 (τ)		Single top		Z + jets		Diboson		Rare SM		Fake lepton	
Initial	2139711		1133501		1133501		59957		769436		18029		10533		1986049	
Pre-selection	-1288134	851577	-854936	278565	-1106585	26916	-43890	16067	-334094	435342	-12182	5846	-7533	2999	-1982574	3475
$|m_{l\bar{l}} - m_Z| > 10$ GeV	-497375	354202	-37529	241036	-4212	22704	-1983	14084	-371274	64068	-4682	1164	-1618	1381	-2700	775
$E_T^{\text{miss}} > 60$ GeV	-190425	163777	-105045	135991	-9192	13512	-6048	8036	-59585	4483	-673	491	-535	846	-536	239
$m_{l\bar{l}} > 15$ GeV	-973	162804	-607	135383	-62	13449	-28	8008	-137	4346	-3	488	-4	841	-2	237
1 b-tagged jet	-75806	86998	-65282	70101	-6408	7042	-2463	5545	-584	3762	-38	450	-447	395	-76	161
NW weight > 0	-23407	63591	-17385	52716	-1719	5323	-2212	3333	-2105	1657	-288	162	-187	207	-56	105
Passed events	63591		52716		5323		3333		1657		162		207		105	

Table B.3 Cut flows for the $\mu\mu$ (1 b-tag) channel.

Table B.4

Sample	Data		$t\bar{t}$ Pow+Py8 (no τ)		$t\bar{t}$ Pow+Py8 (τ)		Single top		Z + jets		Diboson		Rare SM		Fake lepton	
Initial	2139711		1133501		1133501		59957		769436		18029		10533		1986049	
Pre-selection	-1288134	851577	-854936	278565	-1106585	26916	-43890	16067	-334094	435342	-12182	5846	-7533	2999	-1982574	3475
$|m_{l\bar{l}} - m_Z| > 10$ GeV	-497375	354202	-37529	241036	-4212	22704	-1983	14084	-371274	64068	-4682	1164	-1618	1381	-2700	775
$E_T^{\text{miss}} > 30$ GeV	-83811	270391	-32669	208367	-2840	19864	-1905	12179	-39088	24980	-337	826	-184	1197	-276	499
$m_{l\bar{l}} > 0$ GeV	-0	270391	-0	208367	-0	19864	-0	12179	-0	24980	-0	826	-0	1197	-0	499
≥ 2 b-tagged jets	-151219	119172	-106933	101435	-10309	9555	-8548	3631	-22319	2661	-764	62	-570	627	-355	144
NW weight > 0	-8093	111079	-4717	96718	-369	9186	-1402	2228	-1095	1567	-31	31	-176	451	-21	123
Passed events	111079		96718		9186		2228		1567		31		451		123	

Table B.4 Cut flows for the $\mu\mu$ (≥ 2 b-tag) channel.

Table B.5 Cut flows for the $e\mu$ (1 b-tag) channel.

Sample	Data		$t\bar{t}$ Pow+Py8 (no τ)		$t\bar{t}$ Pow+Py8 (τ)		Single top		Z + jets		Diboson		Rare SM		Fake lepton	
Initial	2139711		1133501		1133501		59957		769436		18029		10533		1986049	
Pre-selection	-1532749	606962	-624167	509334	-1079391	54110	-30200	29757	-768368	1068	-16485	1543	-8012	2520	-1979956	6092
$|m_{l\bar{l}} - m_Z| > 0$ GeV	-0	606962	-0	509334	-0	54110	-0	29757	-0	1068	-0	1543	-0	2520	-0	6092
$E_T^{\mathrm{miss}} > 0$ GeV	-0	606962	-0	509334	-0	54110	-0	29757	-0	1068	-0	1543	-0	2520	-0	6092
$m_{l\bar{l}} > 0$ GeV	-0	606962	-0	509334	-0	54110	-0	29757	-0	1068	-0	1543	-0	2520	-0	6092
1 b-tagged jet	-290954	316008	-248848	260486	-26140	27970	-8759	20998	-122	946	-99	1444	-1349	1171	-2482	3610
NW weight > 0	-71750	244258	-57499	202987	-5652	22318	-7239	13759	-332	614	-791	653	-481	690	-1043	2567
Passed events	244258		202987		22318		13759		614		653		690		2567	

Table B.6 Cut flows for the $e\mu$ (≥ 2 b-tag) channel.

Sample	Data		$t\bar{t}$ Pow+Py8 (no τ)		$t\bar{t}$ Pow+Py8 (τ)		Single top		Z + jets		Diboson		Rare SM		Fake lepton	
Initial	2139711		1133501		1133501		59957		769436		18029		10533		1986049	
Pre-selection	-1532749	606962	-624167	509334	-1079391	54110	-30200	29757	-768368	1068	-16485	1543	-8012	2520	-1979956	6092
$|m_{l\bar{l}} - m_Z| > 0$ GeV	-0	606962	-0	509334	-0	54110	-0	29757	-0	1068	-0	1543	-0	2520	-0	6092
$E_T^{\mathrm{miss}} > 0$ GeV	-0	606962	-0	509334	-0	54110	-0	29757	-0	1068	-0	1543	-0	2520	-0	6092
$m_{l\bar{l}} > 0$ GeV	-0	606962	-0	509334	-0	54110	-0	29757	-0	1068	-0	1543	-0	2520	-0	6092
≥ 2 b-tagged jets	-316289	290673	-260577	248757	-27990	26120	-21016	8741	-956	112	-1452	90	-1172	1348	-3614	2478
NW weight > 0	-16817	273856	-11492	237265	-971	25149	-3154	5588	-36	77	-45	45	-312	1036	-223	2255
Passed events	273856		237265		25149		5588		77		45		1036		2255	